Thermal Measurements

The Foundation of Fire Standards

LOUIS A. GRITZO
NORM ALVARES
Editors

ASTM INTERNATIONAL
STP 1427

STP 1427

Thermal Measurements: The Foundation of Fire Standards

L. A. Gritzo and N. Alvares

ASTM Stock Number: STP1427

ASTM
100 Barr Harbor Drive
PO Box C700
West Conshohocken, PA 19428-2959

Printed in the U.S.A.

Library of Congress Cataloging-in-Publication Data

Thermal measurements : the foundation of fire standards / L.A. Gritzo and N. Alvares.
p. cm.
"ASTM stock number: STP1427."
Papers of a conference held Dallas, Tex. Dec. 3, 2001.
ISBN 0-8031-3451-7
1. Fire testing—Standards—Congresses. 2. Materials—Thermal properties—Congresses. 3. Protective coatings—Testing—Instruments—Congresses. I. Gritzo, L. A. II. Alvares, Norman J.

TH9446.3 .T47 2003
628.9'22—dc21

2002038390

Photocopy Rights

Peer Review Policy

Each paper published in this volume was evaluated by two peer reviewers and at least one editor. The authors addressed all of the reviewers' comments to the satisfaction of both the technical editor(s) and the ASTM Committee on Publications.

To make technical information available as quickly as possible, the peer-reviewed papers in this publication were prepared "camera-ready" as submitted by the authors.

The quality of the papers in this publication reflects not only the obvious efforts of the authors and the technical editor(s), but also the work of the peer reviewers. In keeping with long-standing publication practices, ASTM International maintains the anonymity of the peer reviewers. The ASTM International Committee on Publications acknowledges with appreciation their dedication and contribution of time and effort on behalf of ASTM International.

Printed in Bridgeport, NJ
2003

Foreword

This publication, *Thermal Measurements: The Foundation of Fire Standards,* contains papers presented at the symposium of the same name held in Dallas, Texas on 3 December 2001. The symposium was sponsored by ASTM International Committee E05 on Fire Standards. The symposium cochairmen were Louis A. Gritzo, Sandia National Laboratories and Norm Alvares, Fire Science Applications.

Contents

Overview

This book represents the work of presenters at the *Symposium Thermal Measurements: The Foundation of Fire Standards* held on December 3, 2001, as part of the E-5 Fire Standards Committee meeting in Dallas, Texas. Presentations provided information on recent advances in measurements and addressed several significant challenges associated with performing thermal measurements as part of fire standards development, testing and analysis of test results. The testing environment and the results of fire standards tests are almost always based on one or more thermal measurements. Measurements of importance include temperature, heat flux, calorimetry, and gas species concentrations. These measurements are also of primary importance to the experimental validation of computer models of fire and material response.

The widespread application of thermal measurements, their importance to fire standards, and recent technical advances in diagnostic development motivated the organization of this ASTM symposium. The papers contained in this publication represent the commitment of the ASTM E-5.32 Subcommittee of Fire Standards Research to addressing key issues affecting the evolution of fire standards.

Despite frequent and numerous thermal measurements performed in fire standards testing, advances in thermal measurements have been slow to materialize. The most notable advances in measurements are associated with the development of optical diagnostics and techniques and the ability to collect and store large amounts of data. As highlighted in this publication, useful advances are often focused in scope and occur as the result of progress made by individual researchers and fire standard practitioners with specific missions, interests or needs. The ability to present and discuss these accomplishments at the symposium and through this publication broadens the impact of these contributions to fire standards.

Among the significant themes emerging from the presentations at the symposium, and reflected in the papers included herein, are efforts to better characterize the uncertainty associated with using established techniques to perform measurements of primary interest such as temperature, heat flux and calorimetry. In all of these areas, variation in uncertainty resulting from different environments, implementation, and techniques has yet to be fully characterized. Significant contributions in each of the areas, have been realized and are included in this publication.

Temperature

Despite the frequency of temperature measurement to characterize test environments and material response, challenges remain in consistently performing measurements with quantified uncertainty. Six papers addressed temperature measurement over conditions ranging from thermal fields in furnace environments to thermal response of engulfed objects in large pool fires and measurements of firefighter's clothing. Thermocouples, while straightforward in use and operation, are illustrated as deserving consideration of measurements uncertainty for each specific application.

Heat Flux

Measurements of heat flux are useful for defining the fire thermal field to evaluate material thermal response. Several established gauges have been extensively in fire standards. As with temperature measurements, the resulting uncertainty varies with the gauge design and the environment. The magnitude of this uncertainty, and the need to perform cost-effective experiments and tests, has yielded some new designs and application techniques. No new techniques have been developed recently that have gained widespread acceptance. Significant progress associated with existing methods is highlighted in papers addressing calibration, angular sensitivity, and uncertainty quantification.

Calorimetry and Ignition Energy

Included in the publication are papers on oxygen consumption calorimetry and measurements of ignition energy. Although not as common as heat flux and temperature measurements, these parameters often are very important in fire standards, for the role they play in the initiation, growth, and spread of fire environments.

Although widely acknowledged as central to fire development and growth, heat release rate measurements are often taken as having low uncertainties as compared to other measured values. Evaluation of oxygen consumption is therefore a timely topic for consideration.

Uncertainty in the measurements of ignition energy is also explored in this publication. Modern diagnostics and tools allow a closer look at legacy methods and techniques for performing these measurements.

Summary

The papers included in this publication represent progress on a range of thermal measurement topics the scope of material is indicative of the challenge to perform high quality measurements for every fire standards application. Specifically, improvements in the quantification of measurement uncertainty for these environments is promising and holds the key for advancing the thermal measurements that serve as the foundation of fire standards.

William M. Pitts,[1] Emil Braun,[2] Richard D. Peacock,[3] Henri E. Mitler,[4] Erik L. Johnsson,[5] Paul A. Reneke,[6] and Linda G. Blevins[7]

Temperature Uncertainties for Bare-Bead and Aspirated Thermocouple Measurements in Fire Environments

Reference: Pitts, W. M., Braun, E., Peacock, R. D., Mitler, H. E., Johnsson, E. L., Reneke, P. A., and Blevins, L. G., **"Temperature Uncertainties for Bare-Bead and Aspirated Thermocouple Measurements in Fire Environments,"** *Thermal Measurements: The Foundation of Fire Standards, ASTM STP 1427*, L. A. Gritzo and N. J. Alvares, Eds., ASTM International, West Conshohocken, PA, 2002.

Abstract

Two common approaches for correcting thermocouple readings for radiative heat transfer are aspirated thermocouples and the use of multiple bare-bead thermocouples with varying diameters. In order to characterize the effectiveness of these approaches, two types of aspirated thermocouples and combinations of bare-bead thermocouples with different diameters were used to record temperatures at multiple locations during idealized enclosure fires, and the results were compared with measurements using typical bare-bead thermocouples.

The largest uncertainties were found for thermocouples located in relatively cool regions subject to high radiative fluxes. The aspirated thermocouples measured significantly lower temperatures in the cool regions than the bare-bead thermocouples, but the errors were only reduced by 80–90 %. A simple model for heat transfer processes in bare-bead and aspirated thermocouples successfully predicts the experimental trends.

The multiple bare-bead thermocouples could not be used for temperature correction because significant temperature fluctuations were present with time scales comparable to the response times of the thermocouples.

[1]Research Chemist, Building and Fire Research Laboratory, National Institute of Standards and Technology, MS 8662, Gaithersburg, MD 20899-8662

[2]Retired from the Building and Fire Research Laboratory, National Institute of Standards and Technology, Gaithersburg, MD

[3]Chemical Engineer, Building and Fire Research Laboratory, National Institute of Standards and Technology, MS 8664, Gaithersburg, MD 20899-8664

[4]Guest Researcher, Building and Fire Research Laboratory, National Institute of Standards and Technology, MS 8664, Gaithersburg, MD 20899-8664

[5]Mechanical Engineer, Building and Fire Research Laboratory, National Institute of Standards and Technology, MS 8662, Gaithersburg, MD 20899-8662

[6]Computer Scientist, Building and Fire Research Laboratory, National Institute of Standards and Technology, MS 8664, Gaithersburg, MD 20899-8664

[7]Senior Member of Technical Staff, Combustion Research Facility, Sandia National Laboratories, P.O. Box 969, MS 9052, Livermore, CA 94551-0969

Keywords: aspirated thermocouple, enclosure, fire tests, measurement uncertainties, temperature measurement, thermocouple

Introduction

Gas-phase temperature is the most ubiquitous measurement recorded in fire environments and plays a central role in understanding fire behavior. Generally, either bare-bead or sheathed thermocouples are employed. While it is recognized that such thermocouples are subject to significant systematic errors when used in fire environments, e.g., see [*1*], in most fire studies uncertainties for temperature measurements are not estimated or reported.

The work summarized here has been undertaken to characterize the errors in temperature measurements that can occur when bare-bead thermocouples are used in fire environments and to assess the potential of two approaches--aspirated thermocouples and the use of multiple thermocouples having different diameters--to reduce these errors.

Thermocouple Response Equations

Thermocouples are made by joining two dissimilar metal wires to form a junction. When a thermocouple junction is at a different temperature than the opposite ends of the two wires, a potential voltage difference develops across the open ends. If the open ends are held at a known temperature, the measured voltage can be related to the temperature of the junction.

In general, the thermocouple junction temperature can be determined with a great deal of accuracy. The difficulty is that the junction temperature is not necessarily equal to the local surrounding gas temperature that is usually the quantity of interest. This point is discussed extensively in the literature. (e.g., see [*2*] and [*3*]) For steady-state conditions, differences between the junction and local surroundings temperatures can result from 1) radiative heating or cooling of the junction, 2) heat conduction along the wires connected to the junction, 3) catalytic heating of the junction due to radical recombination reactions at the surface, and 4) aerodynamic heating at high velocities. Radiative effects are particularly important in fire environments and will be the focus of much of what follows.

The final steady-state temperature achieved by a thermocouple junction in contact with a gas results from a balance between all of thc heat transfer processes adding energy to or removing energy from the junction. However, for analysis purposes it is typical to isolate those processes that are expected to be most dominant. Such an approach greatly simplifies the mathematical analysis. When considering the effects of radiative heat transfer on a thermocouple junction temperature it is typical to assume a steady state and only consider convective and radiative heat transfer processes. With these assumptions the difference between the gas temperature (T_g) and the junction temperature (T_j) can be approximated as

$$T_g - T_j = \frac{\sigma\varepsilon}{h_c}\left(T_j^4 - T_s^4\right), \qquad (1)$$

where h_c is the convective heat transfer coefficient between the gas and junction, ε is the probe emissivity, and Φ is the Stefan-Boltzmann constant. T_s is the effective temperature of the surroundings for the junction. Values of h_c are usually obtained from heat transfer correlations written in terms of the Nusselt number (Nu) defined as $h_c d/k$, where d is the wire diameter and k is the gas conductivity. Numerous correlations are available for Nu. A commonly used expression from Collis and Williams can be written as

$$Nu\left(\frac{T_m}{T_j}\right)^a = A + BRe^n = A + B\left(\frac{Ud}{\nu}\right)^n \qquad (2)$$

for small diameter wires. [4] T_m is the film temperature defined as the absolute value of $0.5(T_g\text{-}T_j)$, Re is the Reynolds number defined as indicated for local gas flow velocity, U, and kinematic viscosity,<, and a, A, B, and n are constants having values of -0.17, 0.24, 0.56, and 0.45, respectively.

Equation (2) is based on results for heat transfer to a cylinder in a cross flow. In the literature heat transfer correlations for spheres are sometimes used since practical thermocouple wires are typically joined at beads, with approximately spherical shapes, that are two to three times larger than the wires used to form the junction. However, it has been demonstrated that thermal conduction rapidly spreads heat along the wires such that the presence of the bead is a minor perturbation on the local temperature present at the junction. [5,6] The spherical approximation only becomes valid for much larger junction-to-wire diameter ratios. [7]

Substituting Eq. (2) into Eq. (1), neglecting the small temperature dependence in Eq. (2), and assuming that U is sufficiently large that A can be ignored allows Eq. (1) to be rewritten as

$$T_g - T_j \sim \frac{d^{0.55}}{U^{0.45}}\left(T_j^4 - T_s^4\right), \qquad (3)$$

which demonstrates that the difference between a thermocouple reading and the actual gas temperature (i.e., the error in the gas temperature measurement) increases for larger diameter thermocouples, while it is reduced by increasing the gas flow velocity over the junction.

Equation (3) allows two common approaches for reducing the effects of radiation on thermocouple measurements of gas temperature to be understood. The first is the use of an aspirated thermocouple in which the gas to be measured is pumped through a solid structure containing the thermocouple. The solid serves to radiatively shield the thermocouple from its surroundings. The shield is heated/cooled by radiation to a temperature that is intermediate between T_g and T_s and, due to the strong dependence of radiation on temperature, significantly reduces the effects of radiation at the junction. The gas flow over the shield and thermocouple increases convective heat transfer and brings both surfaces closer to the actual gas temperature. Equation (3) indicates that the absolute value of $(T_g\text{-}T_j)$ becomes smaller as the aspiration velocity is increased. In practice, pumping capability and/or aerodynamic heating limit the maximum velocities that can be employed for aspirated thermocouples. The second approach is to record temperatures

with several thermocouples having different diameters and to extrapolate the results to zero diameter. Equation (3) shows that such an extrapolation should provide a good estimate for the actual gas temperature.

Thus far, the discussion has been in terms of steady-state heat transfer. The behavior is more complicated if the local gas temperature is changing since the convective heat transfer rate between a gas and thermocouple junction is finite. Most analyses of thermocouple time response only consider convective heat transfer and the thermal inertia of the thermocouple material. Other heat transfer processes such as radiation and conduction are assumed to be second order effects. With these and other assumptions, the time constant, ϑ, for the response of a thermocouple, can be written as

$$\tau = \frac{\rho_j C_j d}{4 h_c}, \qquad (4)$$

where Δ_j is the density of the thermocouple material and C_j is the heat capacity. Using Eq. (2), it can be shown that ϑ should increase as $d^{1.55}$ and decrease with increasing gas velocity as $U^{0.45}$. The transient response of the thermocouple is written as

$$T_g - T_j = \tau \frac{dT_j}{dt}, \qquad (5)$$

where t is time. Significant instantaneous errors can occur when large gas temperature fluctuations occur on time scales less than or comparable to ϑ. Note that if values of ϑ are known, Eq. (5) offers a means to correct measured values of T_j for finite thermocouple time response.

Experimental

A practical approach for characterizing the errors associated with the use of thermocouples for gas measurements in fire environments has been adopted. Measurements using bare-bead thermocouples typical of those employed at NIST for fire tests, several types of aspirated thermocouples, and combinations of thermocouples having different diameters were recorded at multiple locations in a set of controlled and repeatable enclosure fires and the results compared. Note that a drawback of this approach is that the actual gas temperature can never be known with certainty.

The tests were performed in a 40 %-scale model (0.97 m × 0.97 m × 1.46 m) of a proposed standard ASTM enclosure for fire testing [*8*] , which is very similar to the ISO Fire Tests - Full-Scale Room Test for Surface Products (ISO 9705). The enclosure includes a single doorway (0.48 m wide × 0.81 m high) that was sized using ventilation scaling. [*9*] The enclosure includes a false floor, and, as a result, the base of the doorway is raised approximately 42 cm above the laboratory floor. The enclosure has been described in detail elsewhere. [*10*] Two fuels were employed. For the majority of fires natural gas was burned using a 15.2 cm diameter gas burner positioned at the center of the room near the floor. Nominal heat-release rates (based on fuel-flow rates) were chosen to generate conditions of fully ventilated burning (100 kW), near-stoichiometric

burning (200 kW), and strongly under ventilated burning (400 kW). Natural gas burns fairly cleanly with little soot production. A heavily sooting fuel, liquid heptane, was also burned to assess the effects of varying soot levels on thermocouple measurements. The heptane fires grew naturally on a 21.7 cm diameter pool burner located near the floor at the center of the enclosure. Eventually they achieved flashover, reaching maximum heat-release rates on the order of 700 kW to 800 kW.

Temperature measurements for several types of thermocouples were compared. These included two types of double-shield aspirated probes based on a design described by Glawe et al. (designated as their "Probe 9"). [*11*] These probes were configured such that gas was aspirated over inside surfaces of both shields and the thermocouple. The outer shield had an inner diameter of 0.77 cm, while the inner-shield diameter was 0.56 cm. A type K (alumel/chromel) bead thermocouple constructed from 0.51 mm diameter wire was placed along the centerline within the inner shield. The difference between the two probes was the location of the opening through which the gas was aspirated. For the first, the opening was at the end of the outer shield, while in the second it was on the side. Pumps equipped with water and particle traps were used to draw gases through 0.32 cm^2 openings into the probes at volume flow rates of 18.9 L/min, based on room temperature pumping.

A group (referred to as Combination I) of bare-bead Type K thermocouples with different diameters, which were located close together (within 2 cm), were also tested. Commercial thermocouples formed from wires having diameters of 0.127 mm, 0.254 mm, and 0.381 mm with bead sizes two to three times the wire diameter were used. The length-to-diameter ratios for these thermocouples ranged from approximately 20 to 65. For mounting and connection purposes, the commercial thermocouples were spot welded to the appropriate 0.25 mm diameter leads of Type K commercial glass-insulated thermocouple wire. The exposed lengths of the 0.25 mm diameter wire were each approximately 4 mm. Two additional types of thermocouples, typical of those used during routine full-scale testing at NIST, were tested. These were formed by welding exposed 5 mm lengths of the 0.25 mm diameter alumel and chromel wires to form a bead (current practice, referred to as "NIST typical") or a cross (earlier practice).

Comparisons of the response for the above three types of thermocouples (two aspirated and Combination I) were made by repeating nominally identical fire tests while recording temperature measurements at ten locations using a given type. Reproducibility was assessed by repeated tests for each type. Measurement locations included six heights (7.6 cm, 22.9 cm, 38.1 cm, 53.3 cm, 68.6 cm, and 78.7 cm) above the floor along the centerline of the doorway and locations in the upper (80 cm above floor) and lower (24 cm above floor) layers in the front and rear of the enclosure (20 cm from end and side walls).

Limited measurements were also made using two additional temperature probes. The first was a single-shield aspirated thermocouple based on the design of Newman and Croce. [*12*] This is the most widely used type of aspirated thermocouple for fire testing and is recommended by the ASTM Standard Guide for Room Fire Experiments (E 603 – 98a). ASTM E 603 – 98a claims the approach allows "accurate temperature measurement based on the thermocouple voltage alone." The second was a group (referred to as Combination II) of commercial bare-bead thermocouples formed from wires having diameters of 0.025 mm, 0.051 mm, and 0.127 mm (length-to-diameter ratios ranging

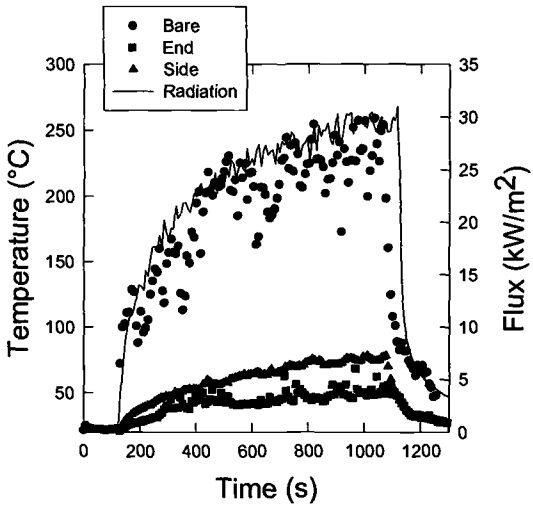

Fig. 1– *Temperatures measured in the lower layer of the enclosure doorway with end- and side-aspirated thermocouples and a 0.25 mm diameter bare-bead thermocouple are shown for 400 kW natural-gas fires. Radiative heat flux was measured at floor level.*

from 65 to 320) mounted like the Combination I probes. These probes were only tested at the two locations in the rear of the enclosure for the natural-gas fires.

Additional measurements made during the fire tests included heat-release-rate measurements by oxygen calorimetry, upper- and lower-layer doorway velocities (11 and 74 cm above the floor) by bidirectional probe, and radiative heat flux by a Schmidt-Boelter heat flux gauge positioned to look upwards at floor level in the center of the doorway. For the vast majority of fire tests, measurements were acquired with a computer-controlled data acquisition system that averaged the readings over a line cycle (1/60 s) and recorded data for a single sensor every 8 s. Total times for individual fire tests varied from 900 s to 1500 s. In experi-ments where the smallest variable-diameter thermocouples were used, a separate PC-based data acquisition system allowed data to be recorded at either 7 Hz or 1000 Hz.

Results

Figure 1 compares temperature time records for 400 kW natural gas fires, recorded 23 cm above the floor in the doorway, for the two types of double-shield aspirated thermocouples with the results for a NIST typical bare-bead thermocouple. The radiative heat flux measured by the floor-mounted radiometer is also shown. The temperature measurement position is in the lower layer of the doorway, where the bi-directional probe indicates that air is flowing into the enclosure with a velocity on the order of 1 m/s. The actual temperature at the measurement point is unknown, but is expected to be on the order of room temperature or . 22 EC if the air entering the enclosure is not preheated before passing through the doorway. This temperature represents a lower limit, but should be a good estimate since the air temperature rise associated with absorption of the imposed heat flux by water vapor, the only significant absorber in ambient air, is estimated to be less than 1 EC [*13*], and the doorway is well removed from heated surfaces that could warm the incoming air.

Burning was observed along the interface between the upper and lower layers as well as in the plume exiting the doorway, which explains the temporally increasing radiative heat flux. Thus the measurement location is a relatively cool location subject to

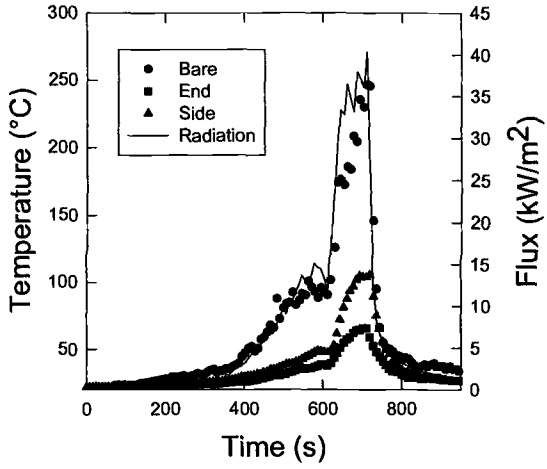

Fig. 2–*Temperatures recorded in the lower layer of the enclosure doorway with end- and side-aspirated and 0.254 mm bare-bead thermocouples are shown for heptane fires. Radiative heat flux was measured at floor level.*

a significant radiative heat flux. During the test, the bare-bead thermocouple recorded temperatures approaching a maximum of 250 EC and had a time dependence very similar to that for the radiant flux. For long times the error in the bare-bead temperature measurement due to radiation is on the order of 225 EC or roughly 75 % in terms of absolute temperature.

The two aspirated thermocouples measured significantly reduced temperatures as compared to the bare-bead thermocouple, but the temperature still increased with radiant heat flux. The two probes recorded different results, with the end-opening configuration approaching a maximum of 50 EC and the side-opening probe 75 EC, i.e. 25 EC and 50 EC above ambient, respectively. Assuming the air is actually at the ambient temperature, it is concluded that the use of the double-shield aspirated thermocouples has reduced the error due to radiation by 80 % to 90 % as compared to the bare-bead thermocouple. It is evident that the effectiveness of the aspirated thermocouples depends on the location of the opening, and the recorded temperatures cannot be error free. For this location the opening for the side-aspirated probe was facing into the doorway towards the fire and heated surfaces, while the end-aspirated probe faced the cool lower doorframe. This suggests that the different temperatures recorded by the two probes are due primarily to the limited view factors associated with the openings for the shielded thermocouples.

Figure 2 shows the corresponding results for heptane-fueled fires. The time bases have been shifted to match the heptane burnout times. Radiation fluxes are somewhat higher than for natural-gas fires due to the higher soot loading. The behaviors of the aspirated thermocouples are consistent with those found using natural gas.

Figure 3 compares the responses for the two types of double-shield aspirated and the bare 0.25 mm diameter thermocouples in the door way upper layer at a height of 68.6 cm above the floor for 400 kW natural-gas fires. At this location the probes should be immersed in hot gas and radiate to cooler surroundings. The figure indicates that the two aspirated probes measure similar temperatures that are somewhat higher than observed by the bare thermocouple. Averages taken over 400 s to 1000 s time periods yield 988 EC, 1003 EC, and 902 EC for the end-aspirated, side-aspirated, and bare thermocouples, respectively. These findings indicate that the bare thermocouple is reading at least 90 EC low due to the effects of radiative heat losses. This represents an absolute temperature error of approximately 7 %.

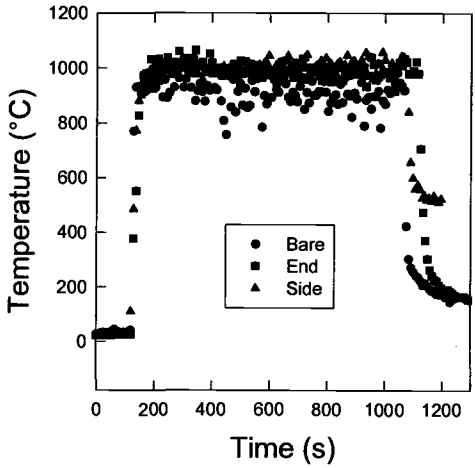

Fig. 3–*Temperatures recorded in the upper layer of the doorway with end- and side-aspirated thermocouples and a 0.254 mm bare-bead thermocouple are shown for 400 kW natural-gas fires.*

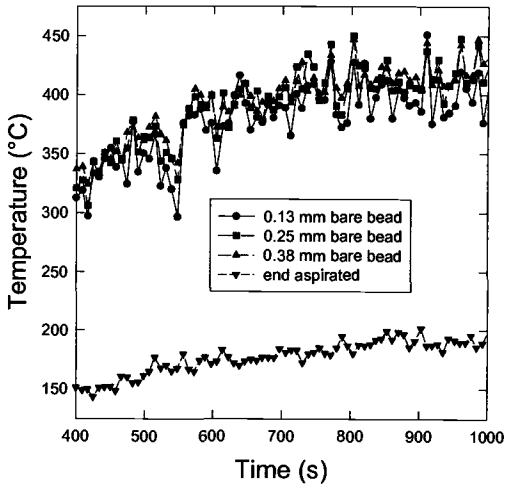

Fig. 4–*Temperatures recorded with three bare-bead thermocouples having the indicated diameters and an end-aspirated probe are shown. The measurements are for the lower-layer location in the rear of the enclosure during a 400 kW natural-gas fire.*

An example of results using the Combination I bare-bead thermocouples is shown in Fig. 4 for measurements in the lower layer at the rear of the enclosure. For comparison purposes, temperatures recorded by an end-aspirated probe are also included. Several conclusions are immediately obvious. First, each of the bare-bead thermocouples is recording temperatures that are much higher (roughly 200 EC) than measured by the aspirated thermocouple. In this radiative environment it is expected that lower temperatures will be recorded by smaller diameter thermocouples. This trend is barely discernable in the data, being somewhat hidden by differences in time responses for the thermocouples, which decrease with diameter, to temperature fluctuations.

Such convolution is more evident for data recorded with the set of smallest thermocouples. Figure 5 shows the results for data recorded at 8 Hz over a short time period in the rear of the upper layer for a 400 kW natural-gas fire. The temperature fluctuations are much larger than the variations in thermocouple response due to the use of different diameters and depend strongly on the thermocouple time constants. The presence of a diameter dependence for both the time response and radiation correction means that a simple correction for radiation is not feasible. It should be noted that the fluctuations evident in Fig. 5 are much larger than those measured with the larger thermocouples, indicating that the limited time response of thermocouples of a size typically used for fire testing can result in significant errors in instantaneous temperature.

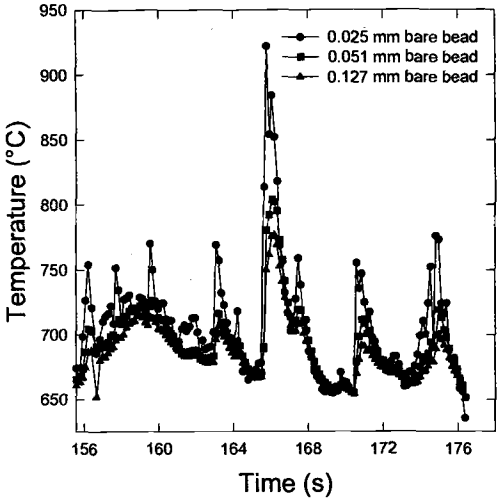

Fig. 5–*Simultaneous temperatures recorded in the rear of the upper layer of the enclosure using three small thermocouples are shown for a short period during a 400 kW natural-gas fire.*

Discussion

The findings of this investigation demonstrate that instantaneous and time-averaged temperature measurements recorded in fire environments using bare-bead thermocouples can have significant systematic errors due to both radiative heat transfer and finite time response. In principle, it should be possible to correct for such uncertainties when sufficient knowledge of thermocouple properties and the environment is available. However, such properties as the local radiative environment, the local gas velocity and composition, and the thermocouple surface emissivity are difficult to measure, and, in practice, such correction does not appear to be feasible. Perhaps the best approach is for a researcher to estimate the various properties along with uncertainty ranges and use error propagation to estimate the resulting uncertainty range for the measurement. It is the responsibility of the researcher to assess whether or not the resulting uncertainty limits meet the requirements of the experimental design.

The largest relative temperature errors are found for cool gases in the presence of strong radiation fields. Errors associated with measurements for a hot gas with the thermocouple radiating to cooler surroundings are significant, but relatively smaller.

The use of aspirated thermocouples can significantly reduce temperature measurement errors due to radiative effects as compared to bare-bead thermocouples. However, it has been found in this study, and elsewhere, that aspirated thermocouples are not 100 % effective, and that significant differences between actual and measured temperatures can still be present. This finding contradicts the suggestion of Newman and Croce [*12*] and the assertion in ASTM E 603- 98a that such uncertainties can be considered to be insignificantly small. It should be mentioned that many researchers, e.g., see [*14*], have recommended that aspirated thermocouples be operated with the highest aspiration velocities possible (on the order of 100 m/s) as opposed to values of less than 10 m/s commonly recommended for fire tests. It is clear that the use of higher velocities will further reduce the errors associated with aspirated thermocouple measurements in fire environments. It should be remembered that there are potential penalties associated with aspirated thermocouple use including increased volume and temporal averaging as well as the environmental perturbations associated with the high pumping speeds and large probe size.

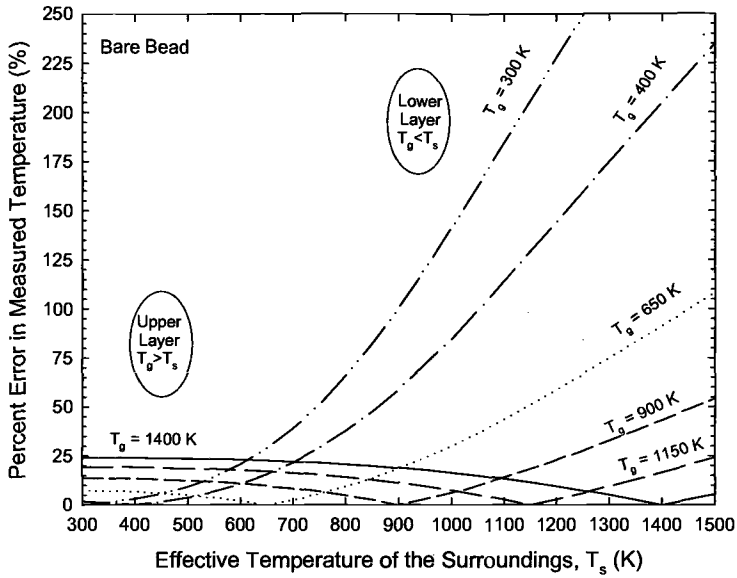

Fig. 6–*Calculated percentage errors for an idealized bare-bead thermocouple with 1.5 mm diameter bead are shown as functions of gas and effective surroundings temperatures.*

The lack of a strong dependence of thermocouple temperature on thermocouple wire diameter evident in Figs. 4 and 5 requires further comment. It is known that thermal conduction to the prongs supporting a thermocouple can change the temperature of the junction as well as its response time. Estimates of the required length-to-diameter ratio necessary to completely eliminate effects of conduction are generally on the order of 200. [*5,15*] For the small diameter Combination II thermocouples used for the data shown in Fig. 5, the length-to-diameter ratio ranges from 65 to 320. This suggest that while conduction may play some role, its effects on the both the time response and junction temperature should be relatively small. Thus the time variation of the relative ordering and magnitudes of the recorded temperatures for the different thermocouples shown in this figure must be due to a coupling of the different thermocouple time responses and the temporal temperature fluctuations present in the gas. Similar behaviors are evident for the larger diameter thermocouples shown in Fig. 4, but heat conduction to the 0.25 mm diameter wire supports may play a more complicated role since length-to-diameter ratios vary from 20 to 64 for the Combination I thermocouples. Such a coupling may partially explain the relatively small variations in measured temperature with thermocouple diameter. However, it is also clear that changes in time response are responsible for the temporal variations in relative temperature ordering for the three thermocouples.

As part of this study, idealized models for the relevant heat transfer processes for bare-bead and single- and double-shield thermocouples in typical fire environments have been developed as discussed in detail elsewhere. [*16,17*] Figure 6 shows calculated

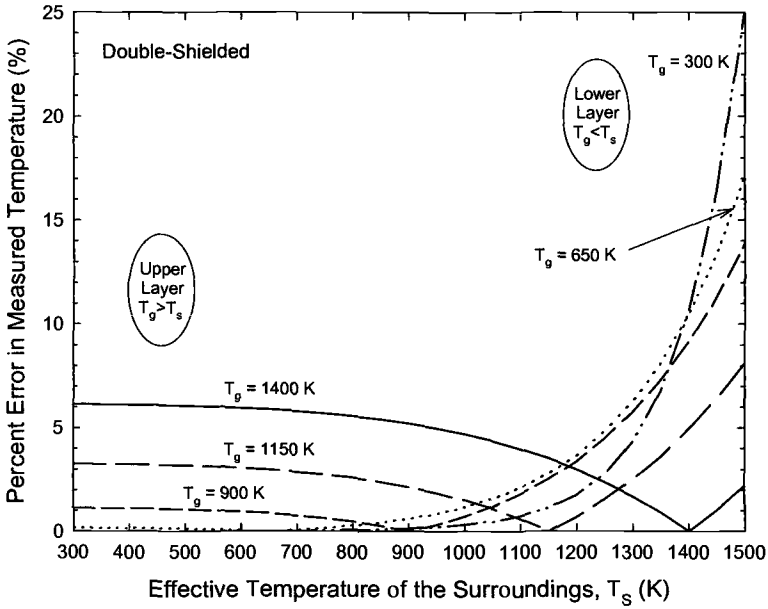

Fig. 7–*Calculated percentage errors for an idealized double-shield aspirated thermocouple are shown as functions of gas and effective surroundings temperatures.*

responses for a 1.5 mm diameter bare-bead thermocouple. The calculated behaviors are qualitatively similar to those observed experimentally. The largest relative errors occur for cool gases in highly radiative environments.

Similar results for a model of a double-shield aspirated thermocouple are shown in Fig. 7. Comparison with Fig. 6 indicates that for given gas and effective surroundings temperatures the calculated errors are reduced considerably for the aspirated probe. This is consistent with the current experimental results. Inspection of Fig. 7 also shows that the calculated percentage errors for the aspirated probe remain significant for conditions encountered in real fires. This conclusion is also consistent with current experimental findings.

Calculations were also carried out for a single-shield probe similar to that described by Newman and Croce. [*12*] The results of these calculations indicate that the double-shield probe is more effective at minimizing differences between actual and measured temperatures. These calculations provide additional evidence that contrary to the current recommendations of ASTM E 603 – 98a, significant temperature measurement errors may still be present for single-shield aspirated thermocouples.

Based on the current results, it is concluded that extrapolation of temperature measurements to zero diameter for close groupings of bare-bead thermocouples having different diameters is not a viable approach for correcting thermocouple results in fire environments due to the strong temporal temperature fluctuations present and the variable

finite time responses of the thermocouples. This conclusion is also at variance with the recommendations of ASTM E 603 – 98a. It is possible that techniques being developed for dynamic measurements of thermocouple time constants, e.g., see [*18*], combined with high-speed data acquisition might allow future development of this approach.

Summary

The current investigation has shown that, for conditions frequently present in enclosure fires, temperatures recorded with bare thermocouples have large errors due to the radiative environment. Errors in terms of absolute temperature as high as 75 % were observed in the lower layer and 7 % in the upper layer. The use of aspirated thermocouples reduces the error by 80 % to 90 %, but with the cost of increased complexity and reduced spatial and temporal resolution. The use of bare-bead thermocouples having different diameters as a means for correcting for radiative effects is not appropriate when implemented using typical fire measurement approaches. It is possible that this approach could be effectively used if more elaborate data acquisition and analysis approaches are employed.

References

[1] Jones, J. C., "On the Use of Metal Sheathed Thermocouples in a Hot Gas Layer Originating from a Room Fire," *Journal of Fire Sciences*, Vol. 13, No. 4, July-August 1995, pp. 257-260.

[2] Moffatt, E. M., "Methods of Minimizing Errors in the Measurement of High Temperatures in Gases," *Instruments*, Vol. 22, No. 2, February 1949, pp.122-132.

[3] Moffat, R. J., "Gas Temperature Measurement," *Temperature: Its Measurement and Control in Science and Industry. Part 2.*, A. I. Dahl, Ed., Reinhold, New York, 1962, pp. 553-571.

[4] Collis, D. C. and Williams, M. J., "Two-Dimensional Convection from Heated Wires at Low Reynolds Numbers," *Journal of Fluid Mechanics*, Vol. 6, No. 4, October 1959, pp. 357-384.

[5] Bradley, D. and Matthews, K. J., "Measurement of High Gas Temperatures with Fine Wire Thermocouples," *Journal of Mechanical Engineering Science*, Vol. 10, No. 4, October 1968, pp. 299-305.

[6] Hayhurst, A. N. and Kittelson, D. B., "Heat and Mass Transfer Considerations in the Use of Electrically Heated Thermocouples of Iridium Versus an Iridium/Rhodium Alloy in Atmospheric Pressure Flames," *Combustion and Flame*, Vol. 28: No. 4, 1977, pp. 301-317.

[7] Hibshman, II, J. R., *An Experimental Study of Soot Formation in Dual Mode Laminar Wolfhard-Parker Flames*, Master's Thesis, Department of Mechanical Engineering, Virginia Polytechnic Institute and State University, June, 1998.

[8] "Proposed Method for Room Fire Test of Wall and Ceiling Materials and Assemblies," American Society for Testing and Materials, Philadelphia, PA, November 1982, pp. 1618-1638.

[9] Quintiere, J. G., "Scaling Applications in Fire Research," *Fire Safety Journal*, Vol. 15, No. 1, 1989, pp. 3-29.

[10] Bryner, N. P., Johnsson, E. L., and Pitts, W. M., "Carbon Monoxide Production in Compartment Fire: Reduced-Scale Enclosure Facility," Internal Report NISTIR 5568, National Institute of Standards and Technology, Gaithersburg, MD, September 1994.

[11] Glawe, G. E., Simmons, F. S., and Stickney, T. M., "Radiation and Recovery Corrections and Time Constants of Several Chromel-Alumel Thermocouple Probes in High-Temperature, High-Velocity Gas Streams," NACA-TN3766, National Advisory Committee for Aeronautics, Washington, DC, October 1956.

[12] Newman, J. S. and Croce, P. A., "Simple Aspirated Thermocouple for Use in Fires," *Journal of Fire and Flammability*, Vol. 10, No. 4, 1979, pp. 326-336.

[13] Hottel, H. C., in McAdams, W. H., *Heat Transmission*, 2nd Ed., McGraw-Hill, New York, 1942, pp. 64-67.

[14] Land, T. and Barber, R., "The Design of Suction Pyrometers," *Transactions of the Society of Instrument Technology*, Vol. 6, No. 3, September 1954, pp. 112-130.

[15] Heitor, M. V., and Moreira, A. L. N., "Thermocouples and Sample Probes for Combustion Studies," *Progress in Energy and Combustion Science*, Vol. 19, No. 3, 1993 pp. 259-278.

[16] Blevins, L. G. and Pitts, W. M., "Modeling of Bare and Aspirated Thermocouples in Compartment Fires," Internal Report NISTIR 6310, National Institute of Standards and Technology, Gaithersburg, MD, April 1999.

[17] Blevins, L. G. and Pitts, W. M., "Modeling of Bare and Aspirated Thermocouples in Compartment Fires," *Fire Safety Journal*, Vol. 33, No. 4, November 1999, pp. 239-259.

[18] Tagawa, M. and Ohta, Y., "Two-Thermocouple Probe for Fluctuating Temperature Measurement in Combustion – Rational Estimation of Mean and Fluctuating Time Constants," *Combustion and Flame*, Vol. 109, No. 4, June 1997, pp. 549-560.

J. Clifford Jones[1]

Suggestions Towards Improved Reliability of Thermocouple Temperature Measurement in Combustion Tests

REFERENCE: Jones, J. C., **"Suggestions Towards Improved Reliability of Thermocouple Temperature Measurement in Combustion Tests,"** *Thermal Measurements: The Foundation of Fire Standards, ASTM STP 1427*, L. A. Gritzo and N.J. Alvares, Eds., ASTM International, West Conshohocken, PA, 2002.

ABSTRACT: Two common forms of combustion testing—oven heating tests for spontaneous combustion propensity of coals and carbons, and temperature measurements in 'simulated room fires'—are discussed in terms of thermocouple uncertainty. For oven heating tests, radiation effects on thermocouple accuracy are examined and examples, from the recent research literature, of unjustifiable claims of thermocouple accuracy in such tests are given and discussed. For simulated room fires, very detailed calculations based on heat balance at the thermocouple tip are performed, and it is shown how unsuspected radiation effects can entail significant errors. Means of eliminating, or at least of significantly reducing, these errors is given in detail. The approach is applicable to steady or to non-steady conditions.

KEYWORDS: thermocouples, combustion testing, radiation error

General Introduction

Thermocouple thermometry has been widely practised for about a century. The author has spent over 20 years in experimental research in the area of fuels and combustion, and thermocouples are featured in a great deal of this work. Most of those years were spent in Australia, and it is fair to say that Australia has produced a number of eminent thermocouple experts. One of these is N.A. Burley, who was largely responsible for the development of the Type N (nicrosil/nisil) thermocouple, the most recent thermocouple type to have received 'letter designation'. There are, in 2002, still only eight letter-designated types: Types J, K, T, E and N, which are base-metal types, and Types S, R and B which are noble-metal types. Another Australian thermocouples expert is R. Bentley, who has written a specialised monograph on thermocouples [1] and, perhaps more importantly, was one of the investigators responsible, in the 1960s, for rejection of the 'e.m.f. at the tip' notion, of which more will be mentioned later in this article.

[1] Senior Lecturer, Department of Engineering, University of Aberdeen, Aberdeen AB24 3UE, UK.

This paper is an attempt to articulate weakness in thermoelectric thermometry and, where possible suggest solutions. Often in combustion applications, gas temperatures are measured; therefore this paper will focus principally on thermocouples in gaseous environments.

The paper will be structured in the following way. First, there will be a brief discussion of the classical 'Laws of Thermoelectric Thermometry'. Next, some specific cases of the application of thermocouples to investigations in fuels and combustion which are possibly unreliable will be described. The reason for the unreliability will be identified and tentative recommendations for improved procedures made.

The Laws of Thermoelectric Thermometry

It has been known since the mid-1960s [2] that the classical notion that a thermocouple e.m.f. is at the tip, where the two dissimilar metals are in contact, is incorrect and that e.m.f. develops along the thermoelements where the temperature changes. So, if a thermocouple is at the same temperature all the way along its length there is no e.m.f. in it. This has been reiterated by Bentley [1,3] as well as by the present author [4,5,6] who has sought to familiarise the combustion community with the true nature of the thermocouple e.m.f. The classical 'Laws of Thermoelectricity' are given in Table 1 below. *They were based on empirical observation and accepted as such are correct.* They have however sometimes been interpreted in terms of the 'e.m.f. at the tip' notion and such interpretations are flawed. In Table 1 below are the Laws of Thermoelectricity, which include the traditional interpretation according to the e.m.f. at the tip notion as well as what the author sees as ideas pointing towards a sounder interpretation in view of the true nature of the e.m.f. distribution.

TABLE 1— *Laws of thermoelectricity: classical and modern interpretations.*

'Law' of Thermoelectricity*	Interpretation on the 'e.m.f. at the Tip' Notion.	Pointers Towards a Sounder Interpretation
'Law of homogeneous metals': A thermoelectric current cannot be sustained in a circuit of a single homogeneous material, however varying in cross section, by the application of heat alone.	Two 'dissimilar metals' are required for there to be an e.m.f.	There will be e.m.f.'s where the temperature changes along the length of the metal wire. However, an e.m.f. reading taken at any one point in a closed loop of a single metal with temperature changes along it will be zero as the e.m.f.'s on either side of the point will cancel each other out.
'Law of intermediate metals': The algebraic sum of the thermoelectric forces in a circuit composed of any number of dissimilar metals is zero if all of the circuit is at a uniform temperature	Each 'junction e.m.f.' has an equal and opposite one.	If the circuit is at a uniform temperature no thermal e.m.f.'s develop at all.

TABLE 1— continued.

'Law of successive or intermediate temperatures': If two dissimilar homogeneous metals produce a thermal e.m.f. of E_1 when the junctions are at temperatures T_1 and T_2, and a thermal e.m.f. of E_2 when the junctions are at T_2 and T_3, the e.m.f. generated when the junctions are at T_1 and T_3 will be $E_1 + E_2$.	$E_1 = J_2 - J_1$ where J denotes 'junction e.m.f.' $E_2 = J_3 - J_2$ $\Downarrow$ $E_2 + E_1 = J_3 - J_1$	The e.m.f. developed by each of the two thermoelements depends only on the temperatures at their ends. Any e.m.f.'s due to intermediate temperatures do not contribute to the net e.m.f.

*Quoted from [7]

Some Difficulties in the Use of Thermocouples in Combustion Testing

Introduction

What is perhaps required is an appreciation in temperature measurement of any sort is that the sensing device, be it a thermocouple, a resistance temperature detector (RTD), or a simple mercury-in-glass thermometer, constitutes a perturbation to the site of the measurement. In other words, the situation with and without the sensor is not the same and skilled judgement is sometimes required to assess how close the thermocouple reading is to the temperature at the site of interest in the absence of the sensor. It can therefore be most imprudent simply to take a thermocouple reading at face value. The reading might be a satisfactory measure of the temperature of interest, but such a conclusion has to be reasoned carefully and not simply assumed.

What also has to be understood is that a thermocouple even when previously unused has an uncertainty of a degree or so due to inhomogeneity of the thermoelements. A common choice of thermocouple configuration in combustion (and indeed many other) applications is the mineral insulated metal-sheathed (MIMS) thermocouple, in which the thermoelements are contained within a sheath (usually 310 stainless steel) and the space in the sheath not occupied by wire is filled with magnesium oxide. These are supplied in sheath diameters from half a millimetre upwards, and the intrinsic uncertainty in the reading from such a thermocouple in new condition is ± 2.2K or 0.75 of one percent of the reading in degrees centigrade, whichever is larger. The 'internal cold junction compensation' at the recorder might well add a fraction of one degree to this error as of course will wear and tear during use, for example, migration of small amounts of manganese from the sheath to the thermoelements. According to Bentley [1], the ultimate level of accuracy which can be obtained in thermoelectric thermometry is, at temperatures up to 250°C, ± 0.05 % of the temperature. This level of accuracy cannot necessarily be obtained with just any thermocouple even when brand new: thermocouples calibrated to this degree of accuracy first have to be scanned to confirm the homogeneity of the thermoelements, then follows a lengthy calibration procedure using reference thermocouples which are reserved for calibration purposes as required by the National Association of Testing Authorities (NATA) and other bodies which issue standards for thermocouple calibration. The combustion scientist may not get involved in thermocouple calibration at this level, but may take the tolerance given by the supplier and apply it to the estimation of uncertainties of measured temperatures.

Oven Tests for Spontaneous Heating

Introduction

In the world of transportation safety of such materials as coal, coke, adsorbent carbons and cellulosic materials there are standard tests, authorised by such bodies as the UN, IMCO and ISO, for assessing the propensity of particular examples of such substances to 'spontaneous combustion'. Such tests have been in use since the 'seventies, and results for a particular material might sometimes be expected to stand up in law if, for example, there has been a fire on board a ship carrying such materials. The author has been closely involved in R&D into such testing procedures for some years and numerous publications (e.g., [8]) have resulted. This is the framework within which some of his deliberations on thermoelectric thermometry have taken place. In all of its forms, the test for spontaneous heating propensity uses a small gauze container (typically a 10 cm cube) of the substance of interest, which is heated isothermally in a recirculating air oven; set temperatures are up to about 200°C. The *sample* temperature is followed by means of an immersed thermocouple, but in extrapolation of the test result to predict the behaviour of large stockpiles, according to the principles of ignition theory, it is the *oven* temperature which is required. Let us therefore analyse heat balance at the tip of a thermocouple placed in the 'work space' of an air oven.

Energy Balance at the Thermocouple Tip

The steady-state energy balance is expressed by the following equation:

$$h(T_g - T_t) = \varepsilon\sigma(T_t^4 - T_w^4) \qquad (1)$$

where h = convection coefficient ($W\ m^{-2}K^{-1}$)
T_g = gas (air) temperature (K)
T_t = thermocouple tip temperature (K)
T_w = oven wall temperature (K)
ε = emissivity of the thermocouple tip
σ = Stefan's constant ($5.7 \times 10^{-8}\ W\ m^{-2}K^{-4}$)

The equation assumes, entirely justifiably, that the thermocouple tip is minute in comparison with the internal volume of the oven, so that no radiation from the tip is reflected back to it. The oven walls, of which the thermocouple tip has a 'view', are at temperature T_w where:

$$T_g > T_w$$

Before inserting some appropriate numbers into the equation, so that the difference between the thermocouple reading T_t and the true gas temperature T_g might be estimated for a typical oven heating test, two other thermal influences which in principle operate will be identified. One is the obvious possibility that heat leakage down the thermocouple wires and also, if a metal-sheathed thermocouple is used, down the sheath, will cause cooling of the thermocouple tip and hence a reading which is too low. MIMS thermocouples of 1.5 mm sheath diameter are a common

choice for this sort of work. In these, the thermoelement wires are of diameter 250 μm and the sheath of thickness 230 μm. In an oven heating test, the thermocouple is likely to be immersed into the oven to an extent of at least 100 sheath diameters (i.e., 15 cm) and all the way along the immersed part the thermocouple sheath is receiving heat from the oven by forced convection. The situation therefore approximates closely to there being a flat temperature profile along the thermocouple from the tip to the oven exit, whereupon there is a step change to room temperature. The tip is therefore thermally buffered from the leakage which takes place at the exit only, so no errors due to conduction leakage are *in these circumstances* expected.

Another influence is conversion of kinetic energy to thermal at the thermocouple tip. A full energy balance at a thermocouple tip requires consideration of this even if (as turns out to be the case) its effect is negligible. The extent to which a thermocouple tip responds to the kinetic energy depends upon the recovery factor (symbol α) and can be approximated from the Prandtl number. In Appendix 1 to this paper, a relevant calculation for a thermocouple tip is presented. The calculation indicates clearly that in this application kinetic energy effects are of no importance. It therefore appears that a thermocouple measuring the temperature of an air oven can be analysed according to convection and radiation only, in which case equation 1 suffices for an estimation of accuracy. Returning to this equation:

$$h(T_g - T_t) = \varepsilon\sigma(T_t^4 - T_w^4)$$

imagine an oven 'set' at 200°C, i.e., a MIMS thermocouple in the oven, immersed to 100 sheath diameters, reads 200°C. The oven has forced-air recirculation, and in unpublished work based on measurements made in one of the ovens in his own laboratory the author has calculated a value of 30 W $m^{-2}K^{-1}$ for the convection coefficient h between the air in the oven and the tip of a 1.5 mm sheath diameter MIMS thermocouple; this is certainly the expected order of magnitude for fairly mild forced convection such as an air oven affords. In the same piece of unpublished work it was confirmed that for most of their area the internal walls are about 2 K below the temperature reading at the thermocouple. The other quantity required is the emissivity, difficult to estimate. However stainless steel having received no polishing after manufacture can have an emissivity as high as 0.5 [1] and this can only increase through tarnishing, so a value of 0.5 will be used in the calculation that follows. Rearranging equation 1:

$$(T_g - T_t) = (\varepsilon\sigma/h)(T_t^4 - T_w^4) \qquad (2)$$

Putting, then, $T_t = 473K$, $T_w = 471K$, $h = 30$ W $m^{-2}K^{-1}$ and $\varepsilon = 0.5$ gives:

$$(T_g - T_t) = 0.8 \text{ K}$$

that is, the thermocouple tip is 0.8 K below the gas temperature. So *even without considering the calibration uncertainties* there is an error of the order of one degree due to radiation effects.

Literature Reports at Odds with the Conclusions from Energy Balance

Table 2 below cites two claims, published in the *very recent* peer-reviewed literature, in respect of oven temperature measurement in combustion testing of the sort under discussion.

TABLE 2—*Difficulties with oven temperature measurements in recently reported work.*

Ref.	Details	Comments
[11]	(a) A claim that a base-metal thermocouple was supplied with a tolerance of ± 0.2K.	(a) Unlikely
	(b) A claim that two such thermocouples in an oven at about 200°C, connected 'back to back' to measure a temperature difference were calibrated to ± 0.02K	(b) Impossible. The most stringent calibration possible could not give better than ± 0.1 K.
[12]	Calibration in liquid nitrogen (−196°C) of a MIMS thermocouple subsequently used at temperatures of around 200°C.	No reason why a thermocouple within spec. at oven temperatures should also be within spec. at cryogenic temperatures. More seriously, the exposure to liquid nitrogen would introduce mechanical strain into the thermoelements, negating the effect of annealing during manufacture and causing loss of calibration.

Temperature Measurements in 'Simulated Room Fires'

Introduction

Frequently in research into the fire safety of enclosures such as airport lounges, shopping malls and aircraft interiors, a 'thermocouple tree' is positioned in hot gases and the thermocouple readings at the respective positions taken to be the gas temperature at those positions. The author has twice [13,14] published comments on research papers where this approach has been taken. In the work under discussion in [13] MIMS type K thermocouples were standing in a 'burn room'which had been deliberately ignited in order to study fire dynamics. Temperature histories were recorded at various positions in the burn room, these having maxima in the region of 1000°C (1273K). The maxima are broad, and on this basis conditions were taken [13] to be 'quasi steady' so that equation 1 can be applied in order to give insights into the accuracy of the thermocouple readings. Importantly from the point of view of thermocouple accuracy, passage of gas past the thermocouples was by natural drift only, attributable to buoyancy forces in which temperature differences play a part. In fact such flow past something the size of a thermocouple tip is likely to be such that natural and forced convection *both* have to be considered, and this approach will be taken herein.

Analysis of Errors

Imagine that in the situation similar to that outlined in the previous paragraph, a thermocouple standing in burnt gas itself transparent to thermal radiation is reading 900 K, and that the walls were some 25K lower, i.e., at 875 K. We make an initial estimate of the convection coefficient as 20 W $m^{-2}K^{-1}$. Since the tip is standing in burnt gas, it will have experienced deposition of particulate and will therefore have a high emissivity, perhaps approximating closely to a black body ($\varepsilon = 1$). Inserting these figures into equation 1 gives:

$$(T_g - T_t) = (1 \times 5.7 \times 10^{-8} /20)\{900^4 - 875^4\} = 199 \text{ K}$$

The radiation error involved if the walls are a mere 25K below the gas is therefore so large as to make the thermocouple reading impractical. Repeating the calculation with $T_t = 600$ K and $T_w = 575$ K gives:

$$(T_g - T_t) = 58 \text{ K}$$

In archival journals and in conference proceedings, (e.g., [15]) thermocouple readings taken under such conditions continue to be reported. The next section will suggest possible means of improvement, and will focus on the above calculations as examples of thermocouple measurements requiring correction.

An Approach to Heat Transfer Corrections to Thermocouples in Gases

The Importance of Wall Temperatures

In order to use Equation 1 to estimate the error in the reading of 900K in the measurement described in the previous section, two quantities are required: T_w and h. The simple approach to correction to be described in this section requires at least a rough measurement of the former: a means, to some extent novel, of arriving at a good estimate for the latter will be fully explained.

It is recommended that, once a thermocouple for gas measurement (or an assembly thereof) is installed, half a dozen or so further thermocouples are placed with their tips in intimate contact with the closest surface, that which is in 'sight' of the thermocouple tips in the gas, and that the signals from these are followed. The user might choose to use the lowest value or some suitably averaged value of the output from these thermocouples to represent T_w for calculation purposes. There is clearly scope for R&D in ascertaining at what vertical heights relative to that of the thermocouple in the gas the wall thermocouples should be to give the most reliable value of T_w. A point to which we shall return is that, because of its much higher thermal inertia, the wall will vary in temperature much more slowly than the gas. The quantity T_w might therefore approximate to a constant value for the duration of the gas temperature readings; this also requires R&D.

Convection Coefficients

We proceed according to the hypothesis above that both forced and natural convection will contribute significantly to heat transfer from gas to thermocouple tip. In this section, the calculation performed above where the gas was at 900K and the walls at 875K will be reconsidered for several possible convection scenarios. Whereas

a value of 20 W m^{-2} K^{-1} was assumed previously, a value will be calculated for each of the scenarios and afterwards an attempt will be made to draw some broadly based conclusions. First, we present convection coefficients and their calculation.
Natural convection depends upon the Grashof number Gr:

$$Gr = \frac{g\beta(T_g - T_t)d^3}{v^2} Pr$$

where d (in the case under discussion) = thermocouple tip diameter
g = acceleration due to gravity (9.81 m s^{-2})
β = 'compressibility factor' = $[(T_t + T_g)/2]^{-1}$ (K^{-1})
v = kinematic viscosity (m^2 s^{-1})

and a correlation for a spheres receiving heat by natural convection is [16]:

$$Nu = h_N d/k = 2 + 0.43\ (GrPr)^{1/4}$$

where: Nu is the Nusselt number, Pr is the Prandtl number, h_N is the coefficient of natural convection and k is the gas thermal conductivity at the mean of the gas and surface temperatures. This is valid in the range:

$$1 < Gr < 10^5$$

Note that the product GrPr is the Rayleigh number Ra, therefore the above equation can be re-written:

$$Nu = h_N d/k = 2 + 0.43\ Ra^{1/4}$$

For forced convection, the relevant dimensionless group of the Reynolds number Re:

$$Re = ud/v$$

where: u = linear speed of the gas (m s^{-1}), other symbols as previously defined. A widely used correlation for forced convection past a sphere is [17]:

$$Nu = h_F d/k = 2 + 0.6Re^{0.5}Pr^{0.333}$$

where h_F is the coefficient of forced convection. The correlation is valid for Re in the range 1 to 10^5 and Pr in the range 0.6 to 400.

The relative importance of natural and forced convection depends on the quotient:

$$Gr/Re^2$$

A value of this in excess of 10 indicates that natural convection dominates and that forced convection is fairly insignificant. The treatment herein is directed at examining the effects, in terms of heat transfer to a thermocouple tip, of various flow conditions. The following values of the properties of the post-combustion gas at the temperatures of interest will suffice.

$$\nu = 10^{-4}\ m^2\ s^{-1}$$
$$Pr = 0.7$$
$$k = 0.07\ W\ m^{-1}K^{-1}$$
$$\beta = 10^{-3}\ K^{-1}$$

Against this background, three sets of flow conditions in the previously considered example – gas at 900K and walls at 875 K – will be considered.

Scenario 1— Post-combustion gas flowing past the thermocouple tip, of diameter 5 mm, at a speed of about 2 cm s^{-1}.

Here we have:

$$Re = (5 \times 10^{-3} \times 0.02 / 10^{-4}) = 1$$

In estimating Gr we need a value for ΔT, the difference between tip and gas temperature, and this is not known. Putting the value of 199 K calculated on the basis of the assumed convection coefficient of 20 W $m^{-2}K^{-1}$ gives:

$$Gr = [9.81 \times 10^{-3} \times 199 \times (5 \times 10^{-3})^3/(10^{-4})^2] = 24$$

and:

$$Gr/Re^2 = 24$$

It is clear that flow is in a regime where natural convection dominates and the correlation:

$$Nu = h_N d/k = 2 + 0.43\ Ra^{1/4}$$

applies with Gr = 24 and Pr = 0.7, giving:

$$Nu = 2.9 = 5 \times 10^{-3}\ h_N/0.07 \Rightarrow h_N = 40\ W\ m^{-2}K^{-1}$$

Returning to the situation where the gas was at 900K and the walls at 875 K:

$$(T_g - T_t) = (1 \times 5.7 \times 10^{-8} / 40)\{900^4 - 875^4\} = 100\ K$$

The Grashof number recalculated with this value of $(T_g - T_t)$ is 12, the Nusselt number 2.7 and the convection coefficient 38 W $m^{-2}K^{-1}$ and the temperature difference 95 K. The difference between 40 and 38 W $m^{-2}K^{-1}$ is insignificant. Convection correlations such as those used herein, being based partly on dimensional analysis and partly on experimental results, are not accurate enough to distinguish one from the other. Further iterations are therefore not necessary.

The message of this calculation is that with slow movement of gas and a bulky thermocouple tip, natural convection will dominate. The assumptions have been made that the tip is spherical and 'black.' In practice, the thermocouple tip could be made black. From knowledge of the tip diameter, a correction can be made provided that the flow speed 'u' is known. It ought not to be difficult to determine this, from

anemometer readings at the cooled gas on exit and application of the continuity equation.

Scenario 2— Post-combustion gas flowing past the thermocouple tip, of diameter 3 mm, at a speed of about 5 cm s^{-1}.

Here we have:

$$Re = (3 \times 10^{-3} \times 0.05 / 10^{-4}) = 1.5$$

Putting as before the value of 199 K calculated on the basis of the assumed convection coefficient of 20 W $m^{-2}K^{-1}$ gives:

$$Gr = [9.81 \times 10^{-3} \times 199 \times (3 \times 10^{-3})^3/(10^{-4})^2] = 5.2$$

From which,

$$Gr/Re^2 = 2.3$$

and clearly both natural and forced convection have to be considered here. The natural component, coefficient h_N, is calculable from:

$$Nu = h_N d/k = 2 + 0.43\,(GrPr)^{1/4} \Rightarrow Nu = 2.6$$

and the forced component h_F from:

$$Nu = h_F d/k = 2 + 0.6Re^{0.5}Pr^{0.333} \Rightarrow Nu = 2.7$$

These can be combined according to:

$$Nu_{FN}^3 = Nu_F^3 + Nu_N^3 \Rightarrow Nu_{FN} = 3.3,\ h_{FN} = 78\ W\ m^{-2}K^{-1}$$

$$(T_g - T_t) = (1 \times 5.7 \times 10^{-8} / 78)\{900^4 - 875^4\} = 51\ K$$

It is now necessary to iterate by putting this value of $(T_g - T_t)$ into the expression for the Grashof number and recalculating Nu_N:

$$Gr = [9.81 \times 10^{-3} \times 51 \times (3 \times 10^{-3})^3/(10^{-4})^2] = 1.4$$

$$Nu_N = h_N d/k = 2 + 0.43\,(GrPr)^{1/4} = Nu = 2.4$$

$$Nu_{FN}^3 = Nu_F^3 + Nu_N^3 \Rightarrow Nu_{FN} = 3.2,\ h_{FN} = 75\ W\ m^{-2}K^{-1}$$

and further iteration is unnecessary. The total convection coefficient is then 75 W $m^{-2}K^{-1}$, from which:

$$(T_g - T_t) = (1 \times 5.7 \times 10^{-8} / 75)\{900^4 - 875^4\} = 53\ K$$

and the following points should be noted:

(i) The values of Re and Gr are all such that the correlations used are valid.

(ii) Strictly speaking the iterations should involve revision of the quantities ν, Pr, k and β. However changes required to these would be very small and, having regard to the fact that correlations for Nu seldom yield convection coefficients to a greater degree of reliability than ± 15%, are not worth making in this illustrative presentation. Computer programs for future implementation of these ideas could include such refinements if they were thought necessary.

(iii) A fairly small change in conditions - a slightly smaller thermocouple bead diameter and a slightly faster flow speed of gas - have changed the thermal regime at the thermocouple from one of natural convection only to one where natural and forced convection contribute about equally to the total heat transfer to the tip. In the former case the radiation error was about 100 K and in the latter 35K. In each case the correction is calculable if the flow speed of the gas is known and the thermocouple tip can be taken to be 'black'. However the sensitivity of the actual thermocouple reading to such conditions has to be fully appreciated.

Scenario 3— Post-combustion gas flowing past the thermocouple tip, of diameter 0.75 mm, at a speed of about 25 cm s^{-1}.

Here:

$$Re = (0.75 \times 10^{-3} \times 0.25 / 10^{-4}) = 1.9$$

Putting as before the value of 199 K calculated on the basis of the assumed convection coefficient of 20 W $m^{-2}K^{-1}$ gives:

$$Gr = [9.81 \times 10^{-3} \times 199 \times (0.75 \times 10^{-3})^3/(10^{-4})^2] = 0.08$$

From which,

$$Gr/Re^2 = 0.023$$

indicating that forced convection dominates. The Grashof number is outside the range to which the correlation previously used applies, but that is immaterial since forced convection dominates therefore no attempt need be made to use the correlation for natural convection.

The relevant correlation is:

$$Nu = h_F d/k = 2 + 0.6Re^{0.5}Pr^{0.333} \Rightarrow Nu = 2.7 \quad h_F = 255 \text{ W m}^{-2}\text{K}^{-1}$$

Putting this into the heat balance equation for the thermocouple tip gives:

$$(T_g - T_t) = (1 \times 5.7 \times 10^{-8} / 255)\{900^4 - 875^4\} = 16 \text{ K}$$

Putting this value for the temperature difference into the expression for the Grashof number gives:

$$Gr = 0.007, Gr/Re^2 = 0.002$$

confirming that forced convection is the dominant mode of heat transfer.

The three scenarios above are for a range of conditions encompassing natural convection only, combined natural and forced convection and forced convection only. The results are summarised in Table 3 below, and it can be seen that as forced convection becomes more dominant the convection coefficient becomes larger therefore the radiation error becomes smaller. It is approaching being negligible in scenario 3. Very often experiments are carried out without any knowledge of the flow regime.

TABLE 3— *Summary of calculations for convection coefficients at a thermocouple tip.*

Gas at 900 K, walls at 875K ⇓	Re	Gr After Iteration	Gr/Re^2	Total Convection Coefficient/W $m^{-2}K^{-1}$	$(T_g - T_t)$/K
Scenario 1. $u = 2$ cm s^{-1} $d = 5$ mm	1	12	12	38	95
Scenario 2. $u = 5$ cm s^{-1} $d = 3$ mm	1.5	1	0.4	75	53
Scenario 3. $u = 25$ cm s^{-1} $d = 0.75$ mm	1.9	0.007	0.002	255	16

A Possible "Short Cut" if the Flow Speed of Gas is Not Known

The correlations for forced or natural convection as applied in the previous section all reduce to:

$$Nu = hd/k \approx 2.7$$

where h may be h_F or h_N, and this suggests a means of obtaining a rough idea of the convection coefficient if the flow speed 'u' is not known: it is reasonable to assume that the bead diameter 'd' will always be known. So for example in our scenario 1 above $d = 5 \times 10^{-3}$ m and $k = 0.07$ W $m^{-1}K^{-1}$ therefore:

$$h = 2.5 \times 0.07/5 \times 10^{-3} = 38 \text{ W } m^{-2}K^{-1}$$

For the regime where both forced and natural are significant the simplified relationship is:

$$Nu_{FN} = (2.7^3 + 2.7^3)^{0.33333} = 3.4$$

Taking a simple mean of the value for Nu for forced or natural convection (2.7 in each case) and that for forced and natural (3.4) gives a 'general-purpose' value of 2.9. Values of the convection coefficient and the temperature error so calculated are compared in Table 4 below with the values obtained from the more detailed treatment in the previous section. In each case, the approximate approach developed herein gives a very reasonable estimate of the radiation error.

TABLE 4— *Comparisons of convection coefficients and radiation corrections from detailed and approximate (Nu =2.9) approaches.*

Gas at 900 K, walls at 875K ⇓	Convection coefficient from detailed treatment/ $W\ m^{-2}K^{-1}$	$(T_g - T_t)$ from detailed treatment/K	Convection coefficient from approximate treatment/ $W\ m^{-2}K^{-1}$	$(T_g - T_t)$ from approximate treatment/K
Scenario 1. $u = 2\ cm\ s^{-1}$ $d = 5\ mm$	38	95	41	97
Scenario 2. $u = 5\ cm\ s^{-1}$ $d = 3\ mm$	75	53	68	59
Scenario 2. $u = 25\ cm\ s^{-1}$ $d = 0.75\ mm$	255	16	271	15

Comments and Recommendations

The calculations above have shown:

(a) that radiation errors can be very large and depend strongly upon two factors, the thermocouple tip dimension and the flow speed of gas. The first of these is easily ascertained, but not the second.

(b) that if knowledge of the flow speed of gas is obtainable detailed correction for radiation errors is straightforward. It is not a major undertaking to determine the flow speed by anemometric measurements on the cooled exit gas and application of the continuity condition.

(c) if convection to the tip is either in the wholly natural regime or in the wholly forced regime a very straightforward calculation is possible to estimate the convection coefficient without knowledge of the gas flow speed. If convection is in a regime where both forced and natural contributions are significant, correction is equally straightforward.

The author urges that further calculations be performed with a view to implementation of these ideas in the routine measurement of gas temperatures in simulated fires. Scope for extension of the calculations as they relate to steady conditions exists in terms of three factors: thermocouple bead shape, thermocouple bead width variation through deposition of particles and, most fundamentally, opacity of the atmosphere in which the thermocouple is immersed.

There remains of course the fact that all of the analysis above is for steady conditions, whereas conditions are usually non-steady in such measurements.

However a 'quasi-steady' approximation is often adequate in which case the above treatment applies. In particular, fires in the post-flashover regime often have close to steady temperatures. An algorithm has however been developed to extend the approach herein for a spherical thermocouple bead in a transparent atmosphere to improve thermocouple accuracy in non-steady measurements, and this is fully explained in the following section.

An Algorithm to Extend the Approach to Non-Steady Temperatures

Calculation of the Biot Number as a Preliminary

This first requires knowledge of the Biot number (Bi) at the thermocouple tip, defined as:

$$Bi = h(V/A)/\mathbf{k}$$

where **k** is the thermal conductivity of the thermocouple material (an emboldened symbol being used to distinguish it from the thermal conductivity of the gas contacting the thermocouple, which features previously), V the volume of the tip and A its area. Taking as illustrative numbers those from scenario 1:

$V/A = r/3$ where r is the thermocouple bead radius

$$\Downarrow$$

$$V/A = 8 \times 10^{-4}$$

Putting $\mathbf{k} \approx 15$ W m^{-1}K^{-1} and $h = 41$ W m^{-2}K^{-1} gives:

$$Bi = 2 \times 10^{-3}$$

This very low value suggests that a single temperature rather than a distributed one can be taken to apply to the thermocouple tip: a value of Bi no higher than about 0.1 would be sufficient to ensure this. It is doubtful whether any investigator has ever questioned that a single temperature rather than a distributed one applies to a thermocouple tip in the light of its inevitably very small size, but for the algorithm which follows demonstration of this is desirable.

The Algorithm

The non-steady heat balance at the tip is then:

$$c\rho(V/A)\frac{dT_t}{dt} = h(T_t - T_g) - \varepsilon\sigma(T_t^4 - T_w^4)$$

where: c is the heat capacity of the thermocouple material (J kg^{-1}K^{-1}) and ρ its density (kg m^{-3}), other symbols as previously defined. The substitutions:

$$V/A = d/6$$

and,

$$h = 2.9k/d$$

where k is the thermal conductivity of gas, can be made. The point has already been made that the walls will vary in temperature much more slowly than the gas, so use of a suitably measured single value of T_w will suffice although, of course, extension incorporating a slowly varying T_w is in principle possible.

Concluding Remarks

This paper has focused on two routine examples of thermocouple usage in combustion testing and identified weaknesses in both which, it is hoped, ASTM will note in future deliberations on methods of temperature measurement.

References

[1] "Theory and Practice of Thermoelectric Thermometry," Springer Verlag (1998), and previous editions thereof published by CSIRO, Australia.

[2] Bentley R. E., "Understanding Thermoelectricity," Australian Institute of Physics Seminar, Sydney, August 1966.

[3] Bentley R., "The distributed nature of e.m.f. in thermocouples and its consequences," *Australian Journal of Instrumentation and Control*, December 1982.

[4] Jones J. C., "Combustion Science: Principles and Practice," pp. 292–299, 'Appendix on the use of thermocouples,' Millennium Books, Sydney, 1993.

[5] Jones J. C., "Some points to remember in thermocouple utilisation Part 1," European Process Engineer, November 1998, pp. 117–119.

[6] Jones J. C., "A combustion scientist's view of thermocouple temperature measurement," *Seminar on Advanced Sensors and Instrumentation Systems for Combustion Processes*, pp. 11/1–11/4, Institution of Electrical Engineers, London, 2000.

[7] "Manual on the Use of Thermocouples in Temperature Measurement," 1981 Edition, ASTM International, West Conshohocken, PA.

[8] Jones J. C., "A new and more reliable test for propensity of coals and carbons to spontaneous heating," *Journal of Loss Prevention in the Process Industries*, Vol. 13, 2000, pp. 69–71.

[9] Moffatt R. J., "Gas Temperature Measurement," *in* Herzfeld G.E. (Ed.), *Temperature: Its Measurement and Control in Science and Industry*, Reinhold, New York, 1962.

[10] Gerrard P., Sanyo-Gallenkamp, Loughborough UK, personal communication.

[11] Chen X. D., "On basket methods for obtaining exothermic reactivity of solid materials," *Trans. I. Chem.E.*, Part B, Vol. 77, 1999, pp. 187–192.

[12] (a) Nugroho Y. S., McIntosh A. C., Gibbs B. M., "Low-temperature oxidation of single and blended coals," *Fuel,* Vol. 79, 2000, pp. 1951–1961.

(b) Nugroho Y. S., McIntosh A.C., Gibbs B. M., "On the interpretation of oxidation studies of single and blended coals," *Fuel,* Vol. 80, 2001, pp. 1983–1985.

[13] Jones J. C., "On the use of metal sheathed thermocouples in a hot gas layer originating from a room fire," *Journal of Fire Sciences,* Vol. 13, 1995, pp. 257–260.

[14] Jones J. C., "On the measurement of temperatures in simulated room fires," *Journal of Fire Sciences*, Vol. 16, 1998, pp. 3–6.

[15] Richardson L. J., *Proceedings of the 24th International Conference on Fire Safety 20-33 Product Safety Corporation*, West Virginia, 1997.

[16] Holman J. P., "Heat Transfer," McGraw-Hill, New York, any available edition.

[17] Geankoplis C. J., "Transport Processes and Unit Operations," 2nd Edition, Allyn and Bacon, 1993.

Appendix 1— Examination of the effect of kinetic energy recovery on a thermocouple tip.

Moffatt [9] gives the following equation for the temperature effect of the extent of recovery of kinetic energy:

$$T_J = T_T\{1 - (1 - \alpha)\frac{[(\gamma - 1)/2]\,M^2}{1 + [(\gamma - 1)/2]\,M^2}\}$$

where T_T is the thermocouple tip temperature, T_J the gas stream temperature, α = recovery factor, γ the ratio of principal specific heats (= 1.4 for air) and M the Mach number. According to a leading manufacturer of fan-assisted ovens such as those widely used in the tests under discussion [10], the speed with which gas will flow past a thermocouple tip inside such an oven will be in the range 1-10 m s^{-1}, i.e., up to Mach 0.03. For forced convection under turbulent conditions, the correlation is:

$$\alpha = Pr^{1/3}$$

where Pr is the Prandtl number, is a reasonable approximation, and for air at oven temperatures Pr = 0.7, giving $\alpha = 0.89$. Inserting this into the above equation, together with a value of 1.4 for γ gives:

$$T_J = 0.99998T_T$$

James T. Nakos[1]

Understanding The Systematic Error of a Mineral-Insulated, Metal Sheathed (MIMS) Thermocouple Attached to a Heated Flat Surface

Reference: Nakos, J. T., "Understanding The Systematic Error of a Mineral-Insulated, Metal Sheathed (MIMS) Thermocouple Attached to a Heated Flat Surface," Thermal Measurements: The Foundation of Fire Standards, ASTM STP 1427, L. A. Gritzo and N.J. Alvares, Eds., ASTM International, West Conshohocken, PA, 2002.

Abstract: Uncertainty assessments of temperature measurements performed at Sandia National Laboratories fire test facilities typically focus on measurements using mineral-insulated, metal sheathed (MIMS), ungrounded junction, chromel-alumel (Type K) thermocouples (TCs). These TCs are used to observe the temperatures of both heat sources and test objects in hydrocarbon fuel fires and simulated fires (typically up to 1200°C). Among the sources of uncertainty, errors associated with TC installation often prove to be dominant. For example, ungrounded junction, MIMS TCs have a systematic error when mounted on a flat steel plate (a commonly used configuration) when attempting to measure the plate temperature. A (relatively simple) model of an ungrounded junction MIMS TC mounted on a flat steel plate was developed. The purpose of this model is not to correct TC readings. Rather, it is to qualitatively understand the systematic error associated with the measurement and find ways to reduce the error through more effective mounting procedures or use of different junction types (e.g., grounded junction). Experimental data showing the errors are presented, as are details of the model and model versus experimental data comparisons.

Key Words: fire testing, thermocouples, MIMS thermocouples, errors, uncertainty, hydrocarbon fuel fires, simulated fire tests, computer model.

Introduction:

Fire testing has been performed for over 30 years at Sandia National Laboratories fire test facilities in support of certification/qualification of high consequence systems and recently in support of computer model validation efforts related to the ASCI (Accelerated Strategic Computing Initiative) program. A majority of the measurements

[1] Principal Member of Technical Staff, Fire Science and Technology Department 09132, MS 0555, P.O. Box 5800, Sandia National Laboratories, Albuquerque, NM, 87185.

Sandia is a multiprogram laboratory operated by Sandia Corporation, a Lockheed Martin Company, for the United States Department of Energy under contract DE-AC04-94-AL85000.

at the fire test facilities has been made by thermocouples (TCs). In fires, TCs are deployed in the fire plume and on objects in the fire. In simulated fires, TCs are also used to measure the heat source temperature. Due to high temperature requirements (e.g.1200°C), mineral-insulated, metal-sheathed (MIMS) TCs are most often used. Otherwise, the TCs normally don't survive the test. In an effort to obtain the best temporal response, the smaller diameter TCs are desirable, so 0.16 cm (1/16 inch) diameter TCs are used. This size is a good compromise between ruggedness and response. In the temperature range of interest, Type K (chromel-alumel) TCs are most appropriate. To reduce electrical noise, to protect the integrity of individual measurements, and to allow the use of resistance measurements as diagnostics, ungrounded TCs are normally employed. Alloy 600 sheaths are used because other materials (e.g., stainless steel) react with combustion products.

Uncertainty assessments of temperature measurements at these test facilities are important, because the measurements are used to both qualify hardware and to validate computer models. In the first case, data are subject to review by regulatory agencies and a statement of the data quality is needed. In the second case, a statement of the uncertainty bounds is needed to allow proper comparisons with model predictions. Among the sources of uncertainty, errors associated with TC installation often prove to be dominant. For example, ungrounded junction, MIMS TCs have a systematic error when mounted on a flat steel plate (a commonly used configuration) when measuring the plate temperature.

The purpose of this paper is to present experimental data showing the systematic error in a specific application common to many simulated fire tests, then to provide a model of the behavior of the TC to better understand the error, and finally to provide some suggestions that will reduce the error. Data were gathered from a series of experiments performed for the U.S. Coast Guard, Hughes Associates, and Ktech Corp. on a "Furnace Characterization Unit."

Test Setup and Experimental Data

Simulated fire applications require a heat source with carefully controlled temperatures. In a typical simulated fire test, quartz infrared lamps (6 kW each) are used to heat a flat stainless steel or inconel plate to a known and carefully controlled temperature (See Figure 1). The flat plate is painted with high emissivity black paint, ($\varepsilon = 0.85$); therefore, one can approximate the plate boundary condition (BC) as a constant temperature gray body with an emissivity of 0.85. For example, if one wants to simulate a 10CFR71 regulatory fire ([1]) the plate temperature is set to 800°C.

Each quartz infrared lamp is about 30 cm long and 1 cm diameter and is composed of a tungsten filament surrounded by a fused quartz envelope. The space between the filament and the quartz is filled with a halogen gas. Up to 63 lamps are mounted in a panel that has a water-cooled, highly reflective surface. Several individual panels (each about 117 cm tall and 30 cm wide) are mounted side-by-side to be able to heat test units of various sizes. Figure 1 shows a sketch of the side view of the setup.

Proper control of the test requires accurate measurement of the plate temperature. This is accomplished by mounting MIMS TCs on the flat plate at carefully chosen locations. The plate is made of SS or inconel and is normally about 0.16 cm (1/16 inch) thick. Therefore, the plate thickness and TC diameters are the same. The TCs are mounted on the side of the plate facing the test unit (not the side facing the lamps).

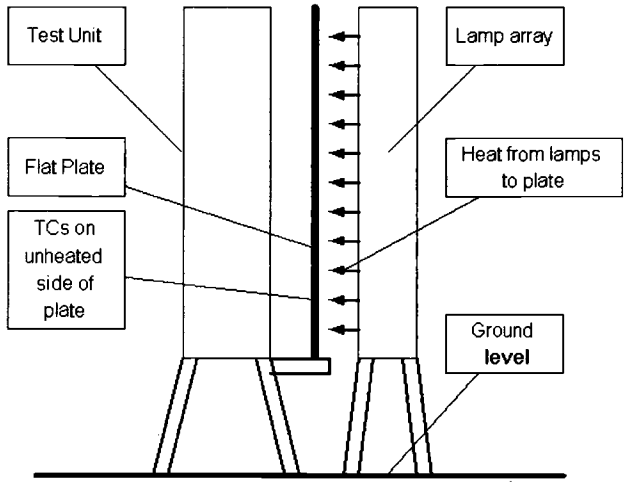

Fig. 1—*Side View of the Radiant Heat Test Setup*

The 0.16 cm diameter, inconel sheathed, ungrounded junction, Type K, TCs are most often used in this type of application. From previous work (e.g., [2], [3]) it is generally accepted that a more accurate measurement of the plate temperature is made via an intrinsically mounted TC where each of the two wires (chromel and alumel) are individually spot welded to the surface being measured (i.e., the plate). Although there is an error when using intrinsically mounted TCs, the error is much less than the sheathed TCs. Therefore, it is assumed that the "true" plate temperature is that measured by the intrinsically mounted TCs. It is worth repeating that intrinsically mounted TCs are not normally used because they are not robust and can fail at these temperatures. To estimate the systematic error of the sheathed TCs we mounted an intrinsic TC adjacent to each sheathed TC (20 pairs total) on the flat plate and measured the temperature difference.

There were 20 sheathed-intrinsic TC pairs on the flat plate, which was 100 cm (40 inches) square and 0.16 cm (1/16 inch) thick. The sheathed TCs were labeled TC1-TC21 and the intrinsic TCs were labeled TC22-TC41. (TC21 did not have a matching intrinsic TC). There were three rows of TCs on the plate, one row 10.2 cm from the top, one row 10.2 cm from the bottom, and the last in the middle 50 cm from the top or bottom. Each TC pair was mounted so the measuring junctions were co-located within about 0.64 cm

(0.25 in). The TC sheaths were held in place using thin (0.0076 mm [0.003 in]) nichrome straps spot-welded to the plate; in addition, the tip of the ungrounded junction TCs were covered with an additional strap that covered the tip. The intrinsic TC wires were individually spot-welded to the plate. The remainder of the intrinsic TC sheath was held in place with nichrome straps. Figure 2 shows a sketch of a typical sheathed TC/intrinsic TC pair mounting at the measuring junctions.

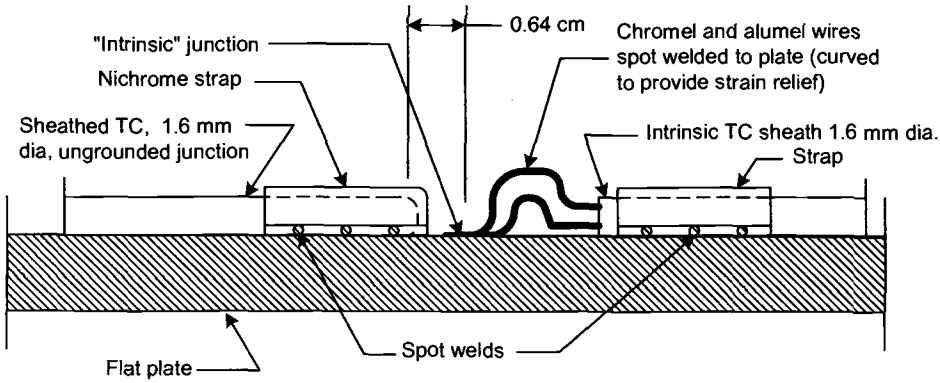

Fig. 2—*Typical Sheathed and Intrinsic TC Pair Mounting Scheme*

The flat plate temperature was raised from ambient to 900°C according to a prescribed temperature profile, which simulates growth of a fire in a ship compartment defined by the International Maritime Organization [4]:

$$T = [345^* \log_{10}(8^*t+1)] + 20 \qquad (1)$$

where
t = time (minutes) and
T = temperature in Celsius

Control TCs were used as feedback to the automatic power control system. Figure 3 shows the desired plate temperature profile, a linear approximation, and control TC9, TC11, and 13. A linear approximation of the log profile was used as input to the power control system. As can be seen, the plate temperature profile closely matched the desired profile. TC9, TC11, and TC13 were sheathed TCs to be sure the control system operated properly. Additional detailed regarding the experiments can be found in reference [5].

Figures 4 and 5 show difference data between the intrinsic and sheathed TCs (i.e., intrinsic TC value – sheathed TC value). Figure 4 is for the entire test, and Figure 5 for the first 10 minutes. Difference data for the remaining TC pairs are not shown here to

conserve space, but the results in Figures 4 and 5 are representative of all of the reliable data (see Table 1 below). Note that several intrinsic TCs failed during this test(TC28, 35, and 36).

As can be seen, the intrinsic TCs read higher than the sheathed TCs during the time when the plate was being heated, i.e., up to about 42 minutes. The inference is that the sheathed TCs read lower than the "true" plate temperature and this difference is a measure of the systematic error of the sheathed TCs.

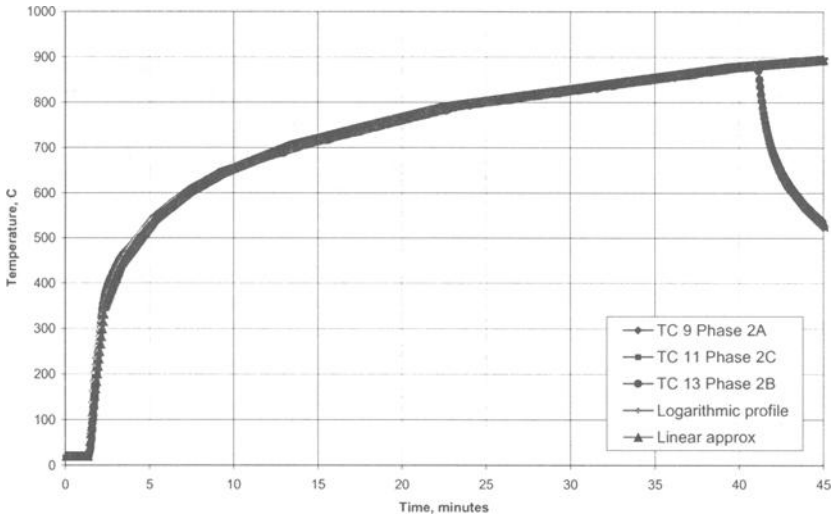

Fig. 3—*Flat Plate Temperature Profile (10/27/99 test)*

Typical of all the plots, the error rapidly rises as the plate temperature begins its rise, then peaks (maximum of about 50°C), then drops quickly to a much lower value, then slowly rises to another lower peak (12-25°C) and finally stabilizes to a constant value. At 42 minutes the error drops quickly to a negative value because power to the lamps was turned off so the plate began to cool. Errors during cool-down will not be discussed here.

Table 1 summarizes the errors from the 20 pairs of TCs. Shown are peak errors, minimum errors, errors just before the power was turned off (i.e., "long term" errors), time to peak error and time to minimum error. There is considerable variability in the results. For example, peak errors range from 19.4-48.8°C with an average of 37.6°C, minimum errors range from 4.6-19.8°C with an average of 13.1°C, and long-term errors from 11-26°C with an average of 18°C. Times to peak error range from 0.25-0.70 min

and time to minimum ranges from 1.35-2.45 min. However, the qualitative behavior is consistent: the error rises rapidly, drops rapidly, and then stabilizes.

The errors just before the plate temperature begins to cool (11-26°C of a maximum of 900°C) are small on a relative basis, but early when the plate temperature is low, the error is higher. For example, at the 10 minute time, TC17 reads about 650°C (same as in Figure 3) and the error from Figure 5 is about 20°C or about a 2.2% error. At very early times, when the error peaks, the temperature of TC17 is about 350°C and the error is 47°C, or about 7.5%. These errors need to be known and included when analyzing the error budget available for the test. Another consideration is if one uses sheathed TC

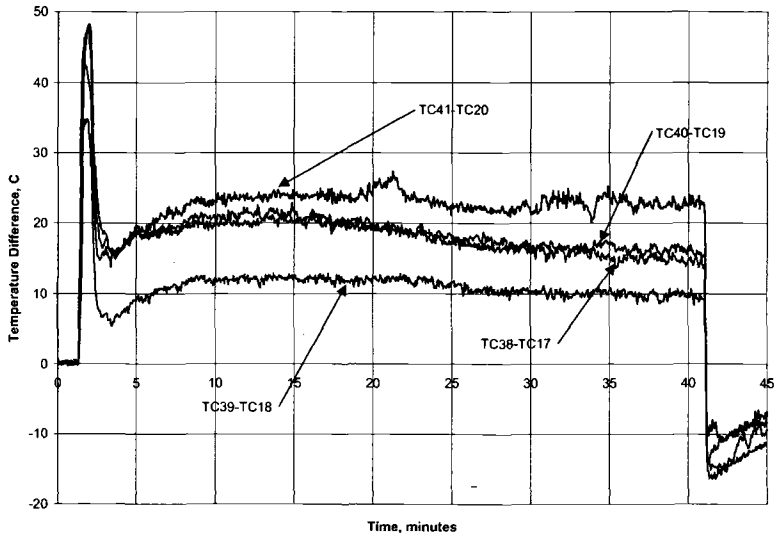

Fig. 4—*Temperature Differences, Intrinsic-Sheathed TCs (0-70 min)*

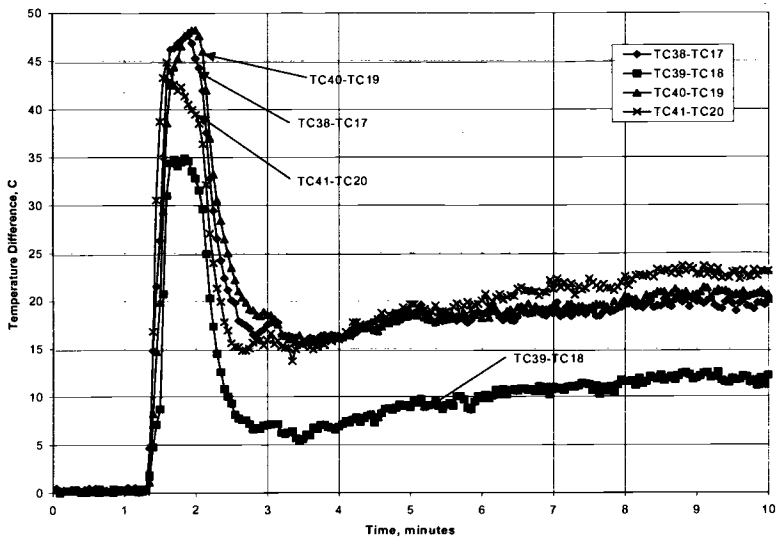

Fig. 5—*Temperature Differences, Intrinsic-Sheathed TCs (0-10 min)*

values to estimate heat flux (σT^4); the heat flux error is about 4x the temperature error so can be about 30% in error at low temperatures.

Table 1—*Summary of Experimental Errors*

TC pair	Peak Error, C	Minimum Error, C	Long Term Error, C	Time[1] to Peak Error from 'Zero', min	Time[1] to Min Error from 'Zero', min
TC22-TC1	19.4	4.6	11	0.30	1.65
TC23-TC2	29.8	10.1	16	0.30	1.95
TC24-TC3	40.0	14.2	19	0.55	2.00
TC25-TC4	31.4	9.7	14	0.60	2.15
TC26-TC5	47.3	19.8	26	0.55	1.45
TC27-TC6	45.7	17.6	23	0.60	2.40
TC28-TC7	TC failed	TC failed	TC failed	TC failed	TC failed
TC29-TC8	32.2	12.3	16	0.35	2.40
TC30-TC9	32.8	13.2	20	0.35	1.50
TC31-TC10	43.1	19.5	25	0.40	1.35
TC32-TC11	33.3	11.4	17	0.60	2.25
TC33-TC12	48.8	17.8	23	0.40	1.85
TC34-TC13	31.8	13.2	20	0.70	2.45
TC35-TC14	TC failed	TC failed	TC failed	TC failed	TC failed
TC36-TC15	TC failed	TC failed	TC failed	TC failed	TC failed
TC37-TC16	27.1	6.4	11	0.25	1.55
TC38-TC17	47.7	16.5	15	0.60	1.55
TC39-TC18	34.9	6.6	11	0.55	1.50
TC40-TC19	48.2	15.4	17	0.65	2.40
TC41-TC20	44.9	13.7	24	0.30	2.05
Average	37.6	13.1	18	0.47	1.91
Maximum	48.8	19.8	26	0.70	2.45
Minimum	19.4	4.6	11	0.25	1.35

[1]Zero time is 1.3 minutes, when TCs began to rise.

Even though great care and consistent procedures were used to mount the TC pairs, large variations in error occurred. Also, several of the intrinsic TCs failed. In summary, if sheathed TCs are used to measure the temperature of a flat plate, systematic errors of 2% up to about 7.5% can occur. The temperatures indicated by the sheathed TCs are lower than the true plate temperature.

Geometry of MIMS TCs

In an effort to understand the underlying sources of the systematic error shown in Figures 4 and 5, a model was developed. However, first it was necessary to section a number of used MIMS TCs so we could obtain a better understanding of the internal geometry. Reference [6] summarizes the dimensions found by sectioning 9 TCs. Additional TCs were sectioned as part of this effort.

In Figure 6, the ungrounded junction end of a MIMS TC (1.6 mm diameter) was sectioned to expose the bead where the two wires (chromel and alumel) were welded together. As can be seen, the end of the TC sheath contains no MgO insulation - the insulation stops before it gets to the bead. As such, the sheath shields the bead from the temperature source.

ASTM E608/E 608M [7] recommends methods of MIMS TC fabrication, including repacking the tip with MgO insulation when the junction is formed. Before the outer sheath tip is installed on the sheath, MgO is should be added to cover the formed junction. It is possible that when sectioning the TCs, the re-packed insulation fell out because it was at a lesser density than the original MgO. However, after sectioning more than 6 TCs for this project, there was no obvious residue of MgO in the tip. Therefore, an uncovered bead (no MgO in the tip) was used to develop the model. The mounting geometry is shown in Figure 2 and again in Figure 7. To improve thermal contact, a nichrome strip is placed over the tip of the TC and spot welded to the plate so the tip is entirely covered.

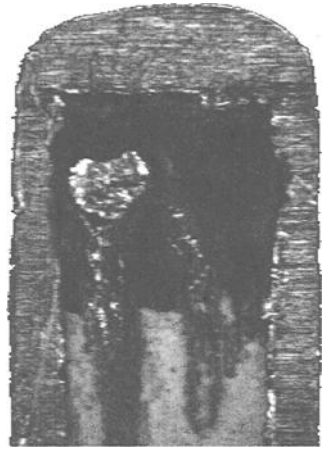

Fig. 6—*Photograph of Sectioned1.6 mm Diameter Sheathed TC*

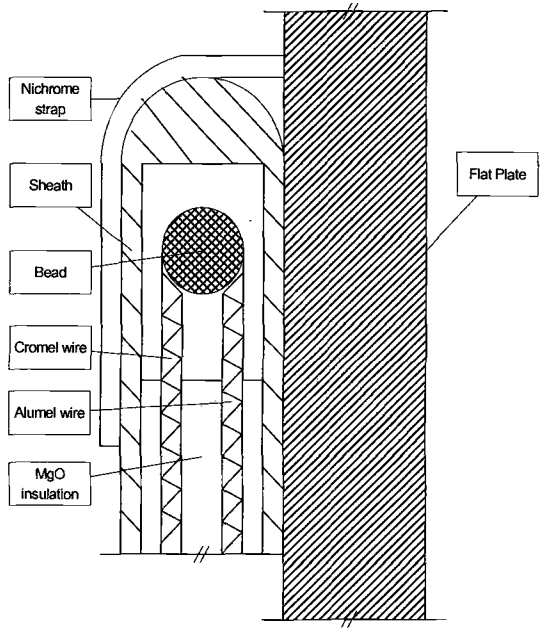

Fig. 7—*Sectional View of MIMS TC, Flat Plate and Nichrome Strap*

Computer Model

The "true" plate temperature T_p was assumed known via the intrinsic TCs. The test unit temperature is designated T_a, the bead temperature is T_b, and the sheath temperature is T_s. It is desired to find the bead temperature T_b, of the MIMS TC because that is what will be recorded by the data acquisition system.

Assumptions are as follows:

- Radiation and conduction are the only means of heat transfer considered; convection is assumed to be second order.
- The flat plate is painted on both sides with black paint of emissivity 0.85 (typical of Pyromark® black paint); the test unit is assumed to have emissivity of 1.0 (to make the analysis simpler).
- The flat plate and test unit are large (i.e., infinite) compared with the TC diameter.
- The flat plate, test unit, and ambient are assumed to be isothermal.
- The flat plate and test unit temperatures are assumed to be equal and increasing with time for purposes of calculating the radiative heat transfer to the sheath.
- The magnesium oxide insulation does not extend to the tip, so the bead is not covered with insulation – air is between the inside of the sheath and the bead. Therefore, the bead receives energy from the sheath via radiation, and gains energy via conduction through the lead wires.
- Bead properties are assumed to be a 50% linear combination of chromel and alumel properties. Properties can be found in reference [9].
- The bead and sheath respond as lumped masses.
- Assumed shapes for the sheath tip and bead are spherical. Volume to area ratios were calculated for both a sphere and a cylinder and the difference was less than 5%, a second order effect for this analysis.
- The sheath material was Alloy 600, a nickel based material.
- The TC tip is completely surrounded by the nichrome strap, so the tip is shielded from the environment.

The method used to estimate the bead temperature begins with assuming there are four surfaces at uniform but rising temperature: the flat plate, the sheath, the bead, and test unit. The model estimates the bead temperature using both radiation and conduction. The radiative contribution is evaluated by separating the problem into two parts: a) outside the sheath, and b) inside the sheath.

Radiative Contribution

Outside the sheath - The sheath at the tip (average thickness 0.165mm or 0.0065") cannot "see" the test unit because it is covered by the nichrome strap (0.076 mm thick [0.003"]), but nonetheless is affected by the test unit temperature. Therefore, the test unit will be included in the analysis.

The radiosity (J) can be used to formulate the problem [8]:

$$q_i = A_i(J_i - \sum_{j=1}^{n} J_j F_{i-j}) \quad (2)$$

where

J_i = radiosity, W/m^2

q_i = net rate of heat loss from surface i, watts

F_{i-j} = view factor, surface i to j

A_i = area of surface i, m^2

Writing equation (2) for the three surfaces outside the sheath we obtain the following:

$$Plate: q_p / A_p = J_p - J_p F_{p-p} - J_s F_{p-s} - J_a F_{p-a} \quad (3)$$

$$Sheath: q_s / A_s = J_s - J_p F_{s-p} - J_s F_{s-s} - J_a F_{s-a} \quad (4)$$

$$TestUnit: q_a / A_a = J_a - J_p F_{a-p} - J_s F_{a-s} - J_a F_{a-a} \quad (5)$$

Where the subscripts 'p', 's', and 'a' refer to the plate, sheath, and test unit.

Because the plate is flat, the sheath is convex, and the test unit is assumed to be flat, the view factors from those surfaces to themselves are identically zero:

$$F_{a-a} = F_{s-s} = F_{p-p} = 0 \quad (6)$$

Because the plate and test unit are much larger than the TC sheath (1 m vs 1.6 mm), the view factors from the plate to sheath and test unit to sheath are negligible. Also, the plate and the test unit are assumed to be large. These assumptions result in the following:

$$F_{a-s} \cong 0, F_{p-s} \cong 0$$

$$F_{p-a} = 1, F_{a-p} = 1 \quad (7)$$

For the assumed geometry, one can approximate the configuration as three surfaces: an infinite flat plate at T_p, another infinite flat plate (test unit) at T_a, and the sheath at T_s. Using view factor algebra and noting that the sheath is convex, the view factor of the sheath to the plate is the same as from the sheath to the test unit:

$$F_{s-p}+F_{s-a} = 1, \quad F_{s-p} = F_{s-a} = 1/2. \quad (8)$$

Therefore, equations (3)-(5) reduce to the following:

$$q_p / A_p = J_p - J_a \qquad (9)$$

$$q_s / A_s = J_s - J_p / 2 - J_a / 2 \qquad (10)$$

$$q_a / A_a = J_a - J_p \qquad (11)$$

For any surface (Kreith [8]):

$$J_i = \rho_i G_i + \varepsilon_i E_{bi} \qquad (12)$$

where

ρ = reflectance
G = irradiation (radiation per unit time incident on a unit surface area), W/m^2
E_b = blackbody emissive power, W/m^2.

For the test unit, the reflectance ρ_i will be assumed = 0 (absorptivity = 1.0), so equation (12) reduces to:

$$J_a = \sigma T_a^4 \qquad (13)$$

Therefore, J_a is known if T_a is known. T_a is the test unit temperature and is known from experimental data.

Now use a second expression for q_i (Kreith [8]):

$$q_i = (A_i \varepsilon_i / (1 - \varepsilon_i))(E_{bi} - J_i) \qquad (14)$$

This assumes all surfaces are gray ($\varepsilon_i = \alpha_i$, and $\rho_i = 1\text{-}\varepsilon_i$) and of uniform temperature. This equation can be written for two of the three surfaces:

$$Plate: q_p / A_p = (\varepsilon_p / (1 - \varepsilon_p))(E_{bp} - J_p) \qquad (15)$$

$$Sheath: q_s / A_s = (\varepsilon_s / (1 - \varepsilon_s))(E_{bs} - J_s) \qquad (16)$$

A similar equation is not needed for J_a because it is known from equation (13). One can substitute equation (9) into equation (15) to eliminate J_p, the result is:

$$q_p / A_p = \varepsilon_p E_{bp} - J_a \qquad (17)$$

Similarly, equation (10) can be substituted into (16) and use (13) to obtain:

$$q_s / A_s = \varepsilon_s (E_{bs} - \varepsilon_p E_{bp} / 2 - \varepsilon_a E_{ba} / 2) = \sigma \varepsilon_s (T_s^4 - \varepsilon_p T_p^4 / 2 - T_a^4 / 2) \qquad (18)$$

This is the net heat loss to the sheath. Because heat is flowing into the sheath, q_s/A_s will be <0, so the heat input to the sheath is the negative of the value in equation (18).

Next, using a lumped analysis, the response of the sheath to the heat input from the plate is: ***change in internal energy = net heat gain*** (from equation (18)):

$$\rho_s c_{ps} V_s \partial T_s / \partial t = \sigma A_s \varepsilon_s (\varepsilon_p T_p^4 / 2 - T_s^4 + T_a^4 / 2) \qquad (19)$$

Solving equation (19) for $\partial T_s/\partial t$ and approximating the partial derivative with a forward difference in time, we obtain:

$$T_s(t+\Delta t) = T_s(t) + (\Delta t \sigma \varepsilon_s / \rho_s c_{ps} (V_s / A_s))(0.85 T_p^4 / 2 - T_s^4 + T_a^4 / 2) \qquad (20)$$

Equation (20) was programmed into a spreadsheet to estimate the sheath temperature as a function of time. T_s at the next time step is estimated from T_s at the past time step.

Inside the sheath - The ratio of the area of the bead (A_b) divided by the area of the sheath (A_s) is part of the analysis. From Figure 6 one could assume the bead is a sphere and the sheath tip as a sphere or cylinder. The geometry of the bead alone is roughly spherical, but with the wires included, it is roughly cylindrical. The geometry of the sheath at the tip is not easily described – a sphere or a cylinder could approximate it. Using measured properties from Black [5], the volume/area ratio was calculated using both a sphere and a cylinder for both the sheath and bead. Results differed by less than 5%, not significant in this model. Therefore, both the sheath and bead were assumed to be spheres.

From [8], the net heat flow between concentric spheres or cylinders can be expressed as follows:

$$q_{s-b} = \sigma A_b (T_s^4 - T_b^4) / ((1/\varepsilon_b) + (A_b / A_s)(1/(\varepsilon_s - 1))) \qquad (21)$$

where A_b is the bead surface area and A_s the sheath inner surface area.

Similar to the sheath analysis, a lumped energy balance on the bead allows one to estimate the transient bead temperature:

$$T_b(t+\Delta t) = T_b(t) + (\Delta t \sigma / \rho_b c_{pb} (V_b / A_b))(T_s^4 - T_b^4) / ((1/\varepsilon_b) + (A_b / A_s)(1/\varepsilon_s - 1))) \qquad (22)$$

Conduction Contribution

Conduction terms for transport from the plate to the sheath, and from the sheath through the insulation to the lead wires to the bead were included in the model. This consisted of adding to equations (19) and (22) a term as follows:

$$q_{cond} = k_{eff} A \partial T / \partial x \quad (23)$$

Where

q_{cond} = heat transfer via conduction
k_{eff} = thermal conductivity, W/m K.

The effective thermal conductivity ('k_{eff}') is affected by contact resistance, material properties of the sheath and strap, the overall contact area between the sheath and plate, and the contact area between the sheath and strap. It is very difficult to accurately estimate these parameters, and therefore k_{eff} in these experiments. Also, the length scale Δx over which the conduction path is relevant is also difficult to accurately establish. The temperature difference ($\partial T \approx \Delta T$) is:

$$T_p - T_s \quad (24)$$

and a conduction heat transfer coefficient is:

$$k_{eff} / \Delta x = h_{cond} \quad (25)$$

This heat transfer coefficient approach has been used in the past to develop time constants for this type of installation [10]. A term of the form shown in equation (23) was added to both equations (20) and (22).

Using equations (1), (20) and (22), one can step through in time, first calculating the next plate temperature, then the next sheath temperature, and finally the next bead temperature. The cycle is then repeated.

Values of 'h_{cond}' (plate to sheath and sheath to bead) were varied so that model results more closely matched measured errors typical of Figure 5. Figure 8 shows results of both the predicted error from the model (radiation and conduction) and the measurements from Figure 5. Values of '$k_{eff}/\Delta x$' used in this data were 0.4 for conduction into the sheath from the plate, and 1.5 for conduction into the bead, within maximum and minimum bounds estimated for the conduction part. Peak errors for both the model and experimental data are about the same because the model was optimized to agree with the data. The late time error was slightly affected by the radiation properties, therefore it was optimized to agree with late time experimental data. The minimum error and timing were not optimized – these parameters agreed (or not) based on tuning the peak error. The minimum error (12.6°C) was within the bounds of the maximum and minimum values shown in Table 1 (4.6-19.8°C).

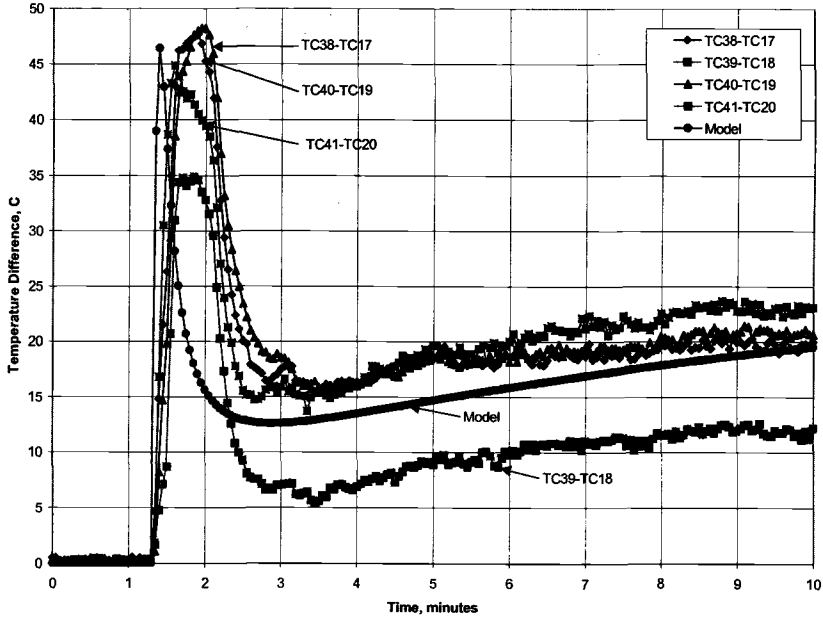

Fig. 8—*Comparison of Model Prediction and Experimental Data*

The minimum error occurred at 1.45 minutes, near the low end but within the bounds in Table 1 (1.35-2.45 minutes). However, agreement is not as good in peak error timing. The model predicts the peak will be reached faster, 0.10 minutes from the beginning, in contrast to the experimental data, which showed the peak was reached between 0.25-0.70 minutes from the start. The model results decline more rapidly than the experimental data. The long term predicted error (about 20°C) is also within the bounds of Table 1 (11-26°C).

A sensitivity analysis was performed on the model results. Values of '$k/\Delta x$', plate emissivity, sheath and bead properties, and volume to area ratios for the sheath and bead were varied to better the agreement with the experimental data. Unfortunately, to obtain good agreement on the maximum error, the peak shifted towards zero and the duration at the peak shortened (more of a spike). This poor timing is likely due to model deficiencies (e.g., the lumped mass assumption and no mesh of actual TC tip geometry) and therefore, better agreement is not possible with this approach.

The relative importance of the radiative and conductive contributions to the total heat transfer to the TC sheath from the plate was estimated from the beginning of the test until the end. Relative contributions shown that conduction plays the major part in the TC response during the early part of the experiment (over 90%) while the relative

contributions are about the same (50% each) at the end. This is expected because at lower temperature differences radiation is less important.

A similar analysis of the heat transfer from the sheath to the bead showed that conduction dominated (almost 100%) at low temperatures but radiation contributed 15% at high temperatures. Therefore, the main sources of error are due to less than perfect thermal contact between the sheath and plate, and that the bead is displaced from the plate.

Although these are satisfying results, this should by no means be construed as a predictive model since multiple approximations were used and values of $k/\Delta x$ were "calibrated" to obtain good agreement with the experimental data. However, the model is useful because it brings out the important elements of the error, provides information related to when conduction and radiation are most important, and methods that can be used to reduce errors (e.g., using straps).

Summary

A model of the response of a mineral-insulated, metal-sheathed (MIMS) thermocouple (TC) using radiative and conductive components was used to study the measured, systematic errors when measuring a rapidly rising flat plate temperature.

Experimental data show that the MIMS TCs systematically under predict the plate temperature by up to 49°C early in the temperature rise. Peak experimental errors were observed at 0.25-0.70 minutes (15-42 seconds) from the beginning of the initial rise and the average was about 28 seconds. The error then rapidly drops to a minimum value and finally slowly rises to an almost steady value (e.g., 11-26°C) as the plate temperature rises to its maximum. The minimum error is reached from 1.35-2.45 minutes (81-147) seconds from the initial rise.

A radiation and conduction model of the TC was developed to better understand the TC behavior. Results showed both modes of heat transfer were important. The thermal contact of the TC tip with the plate is particularly important.

The bead at the TC tip is not surrounded by MgO insulation, but it is believed that this does not affect the response except at late times. Therefore, an error will always be present when using an ungrounded junction MIMS TC. Grounded junction MIMS TCs would reduce this error but other issues (e.g., noise and diagnostics) arise when used. In many cases, the errors such as those shown in Figure 5 may not be significant. However, their existence needs to be known and included in the error or uncertainty budget available for the overall measurement.

Conclusions

Several conclusions from this study are summarized below:

1) MIMS TCs have a systematic error when measuring a flat plate heated as in Figure 1.
2) The bead (i.e., measuring junction) of some MIMS TCs is separated from the sheath via an air gap, not imbedded in MgO insulation as previously thought (see Figure 6).
3) Ungrounded junction MIMS TCs under-predict a plate temperature if the TCs are mounted on the unheated side of the plate.
4) The systematic error rises during the initial, fast rise transient to a maximum, then drops to a minimum, then slowly rises to an almost constant value as the plate temperature rises to its maximum.
5) Both radiation and conduction are important to the TC response.
6) Good thermal contact at the TC tip is important for an accurate measurement. Use of a nichrome strap around the TC tip is an important part of the mounting procedure.
7) The model presented provides guidance on important factors in the TC's response, but it should not be used as a predictive tool because of the approximations used.
8) Main sources of error are bead displacement from the plate and less than perfect thermal contact.

Acknowledgements

The author would like to thank Ned Keltner of Ktech Corp., the U.S. Coast Guard, and Hughes Associates for allowing use of some of the data referenced in the experiments, and the excellent support of the Sandia National Laboratories Radiant Heat Facility technologists Jack Pantuso and Bennie Belone who helped design and complete fabrication and installation of the thermocouples and setup. Thanks also go to Cecily Romero, Walt Gill, Louis Gritzo and Jaime Moya for reviewing and providing valuable comments on the manuscript.

References

[1] Code of Federal Regulations, Energy, 10 Part 71.73, (10CFR71.73), pg 250, January 1, 1999.

[2] Keltner, N.R., and J.V. Beck, "Surface Temperature Measurement Errors," ASME Journal of Heat Transfer, Vol. 105, May 1983, pp 312-318.

[3] "Thermocouple Instrumentation," Technical Memorandum SC-TM-69-372, N.R. Keltner, Radiant Heat and Plasma Division 7323, Sandia National Laboratories, July 1969.

[4] International Maritime Organization (IMO) Resolution A.754(18), Recommendation on Fire Resistance Tests for "A," "B," and "F" Class Divisions, 1993.
[5] Nakos, J.T., Pantuso, J., and Bentz, J., "Final Report – Summary of Thermal Testing of the Furnace Characterization Unit for the Coast Guard," Sandia National Laboratories report SAND2000-1534, June 2000.
[6] Sandia National Laboratories Memorandum from Stephen Black to Walt Gill, "Geometry and Dimensions of 1/16" Diameter Inconel Sheathed Type K Thermocouples," July 6, 1998.
[7] Annual Book of ASTM Standards 2001, Section 14, General Methods and Instrumentation – Temperature Measurement, Vol. 14.03, Standard Specification for MIMS Base Metal Thermocouples, E 608/E 608M-00, Section 6.3.1.
[8] Kreith, Frank, *Principles of Heat Transfer, third edition*, Intext Educational Publishers, 1973.
[9] *Manual on the Use of Thermocouples in Temperature Measurement, Fourth Edition*, ASTM STP 470B, ASTM Publication Code No. (PCN) 28-012093-40, April 1993.
[10] Blanchat, T.K., L.L. Humphries, and W. Gill, "Sandia Heat Flux Gage Thermal Response and Uncertainty Models," Sandia National Laboratories report SAND2000-1111, May 2000.

Annageri V. Murthy,[1] Benjamin K. Tsai,[2] and Robert D. Saunders[3]

Calibration of a Heat Flux Sensor up to 200 kW/m^2 in a Spherical Blackbody Cavity

Reference: Murthy, A. V., Tsai, B. K., and Saunders, R. D., "**Calibration of a Heat Flux Sensor up to 200 kW/m^2 in a Spherical Blackbody Cavity**," *Thermal Measurements: The Foundation of Fire Standards, ASTM STP 1427*, L. A. Gritzo and N. J. Alvares, Eds., ASTM International, West Conshohocken, PA, 2002.

Abstract: This paper presents the results of a comparative study of narrow view-angle and wide view-angle calibrations of a water-cooled Schmidt-Boelter heat-flux sensor. The narrow view-angle calibration, up to a heat flux level of 50 kW/m^2, was conducted using the 25 mm Variable Temperature Blackbody (VTBB) facility. An electrical substitution standard was used as a transfer standard to determine the flux level at the sensor plane. The wide view-angle calibration was conducted by placing the sensor inside the radiating cavity of a spherical blackbody. The calibration in the spherical blackbody is based on the heat-flux derived from the Stefan-Boltzmann equation using the blackbody temperature measured from a type-S thermocouple. The calibration covered an extended range from 50 kW/m^2 to 200 kW/m^2. Results of the calibration of the heat-flux sensor using the two different techniques are presented. A discussion of the problems associated with calibrating sensors at high heat-flux levels by inserting the sensor inside a blackbody cavity is also presented.

Key words: blackbodies; heat-flux; sensors; thermal radiation; transfer calibration

The heat-flux sensor calibration technique currently in use at the National Institute of Standards and Technology (NIST) uses an open-mode approach [1,2]. In this approach, the sensor to be calibrated is placed at a distance away from the radiating aperture of the blackbody, which is a heated graphite tube of 25 mm radiating cavity diameter. The maximum heat-flux when the sensor is located 1.25 cm away from the exit is approximately 50 kW/m^2 at the blackbody operating temperature of about ≈2773 K. The corresponding view-angle subtended at the sensor by the blackbody radiating-aperture is approximately 14°. When the sensor is moved further away, the corresponding maximum heat-flux level and the associated view-angle decrease. The heat-flux at the sensor location is determined by using an electrical substitution radiometer (ESR). This is in

[1] President, Aero-Tech, Inc., 53 Sanlun Lakes Dr., Hampton, VA 23666.
[2] Physical Scientist, Optical Technology Division, NIST, 100 Bureau Dr., Gaithersburg, MD 20899-8441.
[3] President, Saunders Enterprises, 13105 Chestnut Oak Dr., Gaithersburg, MD 20878.

on the radiative properties of the same blackbody. The latter method is used for measurement of low irradiance levels as in narrow view-angle radiance temperature measurements.

The determination of heat-flux using an ESR has the advantage of accounting for radiation reflected from the inner surface of the extension tube normally fitted to the exit of a blackbody and also for possible non-isothermal distribution near the heated end of the blackbody cavity. Also, the ESR calibration, generally considered absolute, can be determined independently with traceability to the High Accuracy Cryogenic Radiometer (HACR), which is an electrical substitution radiometer that serves as the primary standard for optical radiation measurements in the U.S. [3]. All radiance, irradiance and radiance temperature measurements at NIST are based ultimately on electrical substitution radiometry.

The transfer calibration technique using the ESR as a transfer standard falls in the narrow view-angle category. Another approach is to use a wide view-angle measurement. The radiating source, which is not necessarily a blackbody, has to be large and the sensor has to be located in close proximity to the source. The radiance distribution of the source must be known if the heat-flux at the sensor is to be determined using the source characteristics. The angular response of the sensor is also an important factor because of the large view-angle. However, open type sensors with no view restrictors are Lambertian with the angular response close to cosine function. Angular response measurements reported in reference [4] show cosine variation of a Schmidt-Boelter sensor similar to the sensor used in the present experiments. A variation of the wide view-angle approach is possible if the radiant source is a blackbody with large cavity dimensions compared to the sensor size. In this case, the sensor can be placed inside the cavity thus giving 180° (2π sr) field-of-view.

For calibration at high heat-flux levels using thermal radiation, placing the sensor inside the blackbody cavity is the only viable approach [5]. It provides the highest realizable heat-flux from blackbody radiation. However, this approach can pose problems due to convection effects when used to calibrate sensors in the low heat-flux range up to 50 kW/m^2. Sensors used in fire test methods fall in this heat-flux range. If not performed under vacuum conditions, exposure of the sensor surface to hot gas within the blackbody introduces additional heat-flux due to convection. Convection heat-flux can be a significant portion of the total heat-flux in the low heat-flux range. In such situations, the calculation of the heat-flux based purely on blackbody radiation can lead to large errors in calibration. A new technique developed in Sweden avoids the convection problem by placing the sensor in the horizontal plane at the bottom of a cooled enclosure attached to a spherical blackbody aperture [6, 7].

For calibration in the low heat-flux range, the open mode is preferable. However, there have been concerns with the open mode calibration because of its associated narrow view-angle. Some of the observed differences in the calibration by the two methods have been speculatively attributed to view-angle effects. For an open type sensor with a good cosine response, the two methods should give identical calibration within the experimental uncertainty. The preference over a particular mode has to be made from a view to minimize convection effects for a specified heat-flux calibration range. In practical situations of using the heat-flux sensors, the view-angle can range between 0°

and 180°, depending on the application. One of the methods under consideration by the International Standards Organization (ISO) is the cooled enclosure technique developed in Sweden [8]. In this method, the sensor is placed inside a cooled fixture that is attached to the aperture of the spherical blackbody aperture, giving included view-angles of 50° and 90°, depending on the range of calibration.

When the angular response of the sensor is not a cosine function, it is necessary to use the narrow view-angle calibration approach along with the appropriate angular response to determine the heat-flux level. An example of such a situation is presented in reference [8] for the calibration of an elliptical radiometer in a spherical blackbody.

A comparative study of the narrow and wide view-angle calibrations of a heat-flux sensor in two blackbody facilities is presented in this paper. The sensor used for this calibration was a 200 kW/m^2 range water-cooled Schmidt-Boelter type. For the narrow view-angle calibration conducted in a heated graphite-tube blackbody facility, the heat-flux at the sensor was derived from the ESR measurements over the range up to 50 kW/m^2. The wide view-angle (180° field-of-view) calibration, carried out by placing the sensor inside a spherical blackbody cavity, covered an extended range from 50 kW/m^2 to 200 kW/m^2. The heat flux was derived from the measured temperature and using the Stefan-Boltzmann equation. The higher calibration range from 50 kW/m^2 to 200 kW/m^2 was chosen to keep the convection effects small compared to the radiant heat-flux at the sensor surface. The two calibrations in the spherical and variable temperature blackbodies provide a comparison of the narrow and wide view-angle calibrations, and also help to validate the calibration technique in the spherical blackbody up to 200 kW/m^2.

Experiments

The experiments were carried out in a spherical blackbody [9] using a Schmidt-Boelter sensor. Figure 1 shows a schematic layout of the spherical blackbody and the associated accessories. The blackbody cavity is a 0.23 m diameter spherical furnace fitted with a 50.8 mm diameter aperture. The furnace walls are made of clay and are electrically heated. The furnace inner surface is coated with high-temperature black paint. The furnace can be operated continuously up to a maximum temperature of 1373 K. Operation at higher temperatures up to 1446 K is possible for short durations. The cavity temperature is measured by a type-S precision thermocouple. A PID controller maintains the cavity temperature at a set value within 1 K. With the present design, the facility is operated in an upright position with the radiating aperture in the vertical plane.

The cooled fixture attached to the blackbody cavity is comprised of a single-piece water-cooled extension tube with a precision aperture at one end fitted to the radiating cavity of the spherical furnace. The other end of the extension tube serves as an opening for inserting the sensor housing assembly. The inside of the tube is coated with high temperature black paint with an emissivity of about 0.93 to 0.94. The black cooled extension tube minimizes effects of reflected and emitted radiation from the inner surface of the tube.

The calculated aperture total normal emissivity values are 0.9969, 0.9986 and 0.9994 for cavity surface emissivity values of 0.8, 0.90 and 0.95, respectively. Even with the lower value of 0.8 for the emissivity of the blackbody cavity surface coating material, the calculated total emissivity is 0.997. Hence, the radiant heat-flux level at the sensor surface when placed inside the cooled fixture is close to that produced by an ideal blackbody at the cavity temperature.

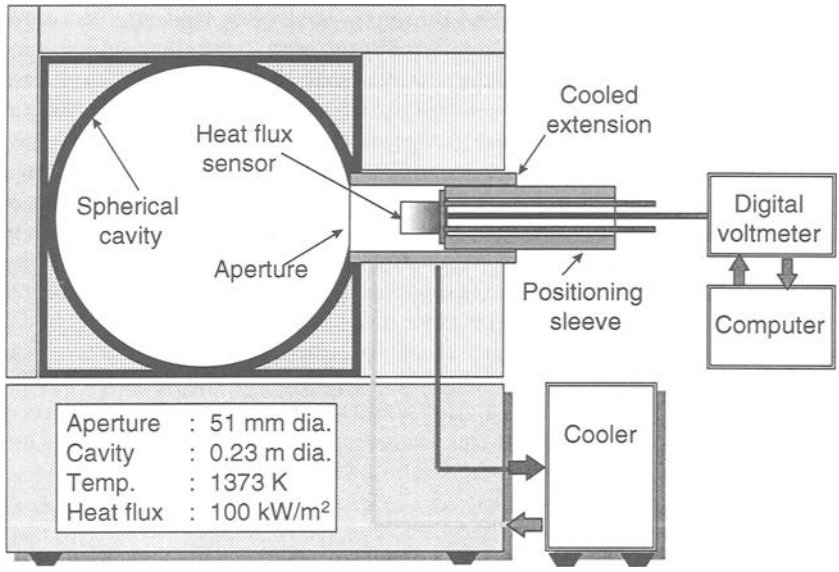

Figure 1 - *Schematic layout of the spherical blackbody and the cooled aperture.*

A stop ring on the inner surface of the tube at a distance of 12.5 mm from the aperture end helps in placing the sensor assembly either inside the blackbody cavity or the cooled fixture at a precise location. In the present experiments, measurements were made with the sensor inserted through the aperture into the blackbody cavity. Four type-K thermocouples, located 90° apart on the inner surface of the tube, midway between the aperture and the stop ring, measure the cooled-fixture temperature. A closed-loop, air-cooled pump cools the radiating aperture and the extension tube by continuously circulating water at a flow rate of 14 L/min at 140 kPa pressure.

Figure 2 shows the test heat-flux sensor mounted on the holder, which is attached to a positioning sleeve. The positioning sleeve slides inside the outer sleeve and helps to locate the sensor plane at different positions. The outer sleeve fits into the blackbody cooled-extension tube up to the aperture stop location. The sensor can be located at a specified distance from the aperture using the stop ring as a reference location. The

positioning sleeve slides inside the outer sleeve and the complete assembly fits into the cooled extension tube from the furnace, forming a closed cooled connection to the blackbody.

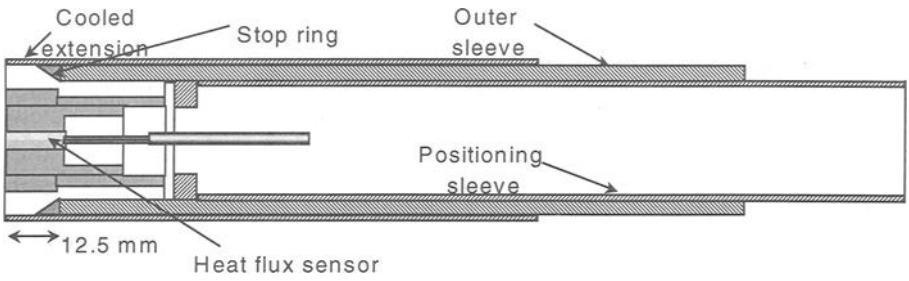

Figure 2 - *Schmidt-Boelter sensor mounted on the positioning sleeve.*

The Schmidt-Boelter type heat-flux sensor used in the present study was placed at three different locations inside the blackbody cavity from the aperture plane. Figures 3a-c show the relative positions of the sensor inside the spherical cavity for the three locations. The first Position 1 is at 0.32 cm inside from the aperture plane. In this position, the sensor plane is nearly flush with the inner surface of the heated cavity. The other two Positions 2 and 3 are at 2.54 cm and 3.81 cm inside the cavity from the aperture plane, respectively.

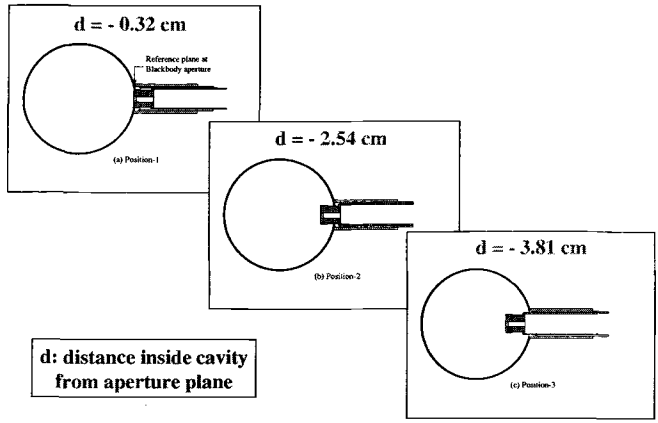

Figure 3 - *Sensor locations inside the spherical cavity: distance from aperture plane a) - 0.32 cm (Position 1), b) - 2.54 cm (Position 2), and c) - 3.81 cm (Position 3). Cavity diameter: 22.9 cm.*

Results and Discussion

Figure 4 shows the results of open-mode transfer technique calibration of the Schmidt-Boelter sensor used in the present experiments. The calibration was carried out, in the range 0 kW/m^2 to 50 kW/m^2, in the 25 mm VTBB facility using the electrical substitution radiometer reference standard [10]. The measured responsivity of the sensor was 0.070 mV/(kW/m^2), with a relative expanded uncertainty of 2 % (coverage factor $k = 2$).

The present measurements were made in the spherical blackbody over the temperature range from 700 °C to 1080 °C, giving a corresponding blackbody radiation from 50 kW/m^2 to 190 kW/m^2. The temperature of the blackbody was increased gradually to the set value. After stabilization of the temperature at the set value, the sensor-holder assembly was inserted into the blackbody cavity through the water-cooled sight tube. The measurements were made after allowing for the initial transients to settle. The output of the sensor was recorded for a period of 30 s to 85 s.

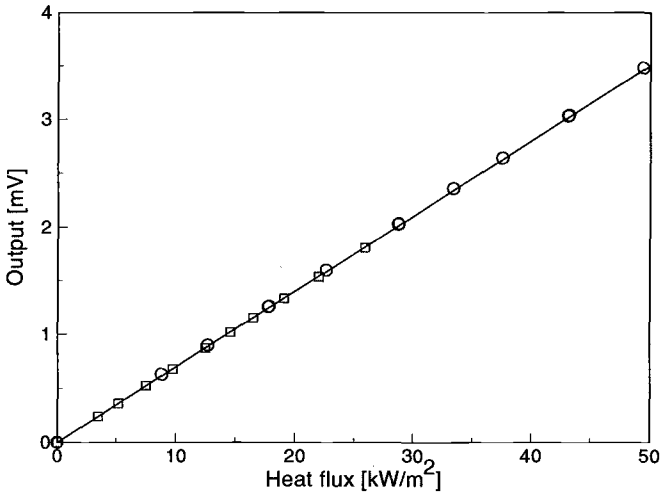

Figure 4 - *Results of open-mode transfer technique calibration of Schmidt-Boelter sensor in the 25 mm VTBB [10].*

The radiating surface area of the spherical cavity is much larger than the sensor-assembly. Hence, the presence of the sensor inside the cavity has no significant effect on the radiation field. Figure 5 shows the typical sensor output for different blackbody temperatures, when the sensor was positioned at a distance of 2.54 cm from the aperture

plane inside the cavity. The steady sensor signal output during the measurement interval suggests nearly equilibrium thermal environment inside the cavity.

Of the three locations of the sensor, the location close to the aperture plane (Position 1) is chosen to demonstrate the effect of the cooled aperture and possibility of a non-isothermal region on the cavity surface close to the aperture. The other two positions (Positions 2 and 3) are well inside the cavity, and also sufficiently far away from the radiating surface.

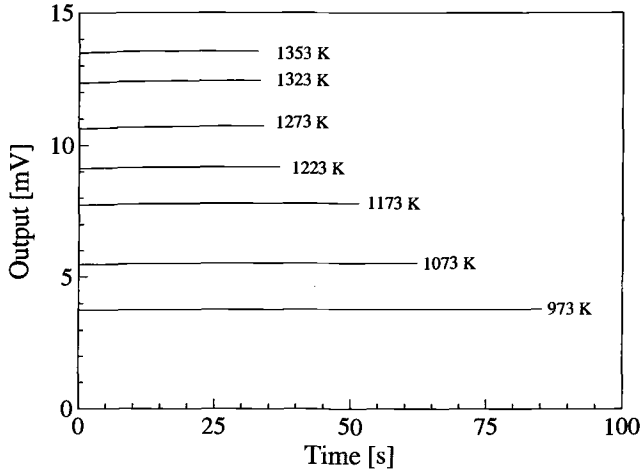

Figure 5 - *Schmidt-Boelter sensor output record for different blackbody temperatures.*

Figure 6 shows the responsivity plots of the sensor for all three positions of the sensor. The plot shows the measured sensor output [mV] for different heat-flux levels obtained by operating the blackbody at different temperatures. The heat-flux level was calculated using the Stefan-Boltzmann equation. The calculated responsivity at these positions using linear regression to the measured data is shown in Table 1. The measured responsivity of 0.0698 mV/(kW/m^2) to 0.0703 mV/(kW/m^2), given by the slope of the linear-fit for the data, at Positions 2 and 3 corresponding to locations inside the cavity, appear to agree. The average measured responsivity of 0.0701 mV/(kW/m^2) for Positions 2 and 3, also agrees with the open-mode calibration results from the VTBB. However, despite their close agreement, the measured responsivity must be viewed in the context of other unaccounted factors; convection effects, effective emissivity and measurement uncertainty, discussed later. The responsivity measured with the sensor located close to the aperture (Position 1) is lower by about 9 %. One probable explanation [8] for the lower responsivity is the cooling effect of the sensor surface due to the proximity of the cooled fixture and the aperture.

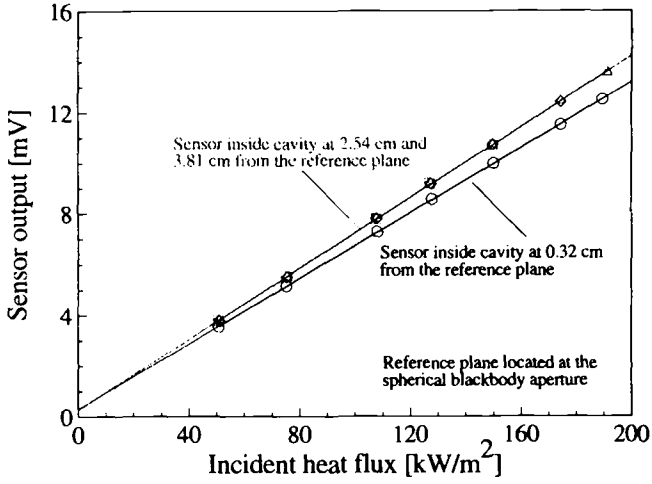

Figure 6 - *Schmidt-Boelter sensor output variation with heat-flux level. Symbols denote different locations of the sensor from the aperture plane. O: - 0.32 cm, □, Δ: - 2.54 cm, and ◇: -3.81 cm.*

Table 1 - *Measured responsivity of Schmidt-Boelter sensor in the spherical blackbody. (Calibration range: 50 kW/m² to 190 kW/m²)*

Sensor Position	Distance cm	Test date	Responsivity mV/(W/cm²)	Regression Factor	Remarks
1	-0.32 cm	01/08/2001	0.645	1.0000	Sensor close to aperture
2	-2.54 cm	01/08/2001	0.704	0.9999	Sensor inside cavity
2	-2.54 cm	01/17/2001	0.698	0.9999	
3	-3.82 cm	01/18/2001	0.701	0.9999	
Open-mode transfer technique			0.700	1.0000	25 mm VTBB data [10]

The intercept of the linear fit on the y-axis is an indication of the convection effects, which must be accounted for when calibrating at lower heat-flux levels. The linearity of the data suggests that the convection heat transfer effect, while may not be small, is not changing significantly over the calibration range from 50 kW/m² to 190 kW/m². The convection heat transfer to the sensor tends to reduce the calculated responsivity based on radiant flux.

As mentioned earlier, the agreement of the responsivity at Positions 2 and 3 inside the cavity is indicative of the nearly uniform blackbody radiation field in the measurement

region. An effective emissivity of 1.0 has been assumed to calculate the heat flux at the sensor location. However, temperature non-uniformity on the cavity surface can reduce the effective emissivity from the assumed value of unity resulting in an increase in the responsivity calibration factor. It is probable that the convection and the non-uniform temperature distribution effects are compensating, resulting in good agreement of the responsivity within the experimental uncertainty. Detailed experiments and calculations are planned to examine these effects more critically.

The linearity of the sensor response is demonstrated by the nearly unity regression factor obtained by the linear regression analysis to the measured data. At higher flux levels, the slope represents the responsivity, because the differential change in sensor output is proportional to the corresponding change in radiant flux. The high degree of linearity suggests the convective heat-flux is not changing significantly over this interval. The convection effects also depend on the orientation of the sensor and the radiating aperture. In the present configuration, they are located in the vertical plane. The blackbody unit is now being modified so that the assembly can be tilted so that the sensor is below the radiating aperture in a horizontal plane.

Convection heat transfer effects

When the sensor is placed inside the spherical cavity, the cooler sensor surface is exposed to the hot gas inside the cavity. This results in heat gain to the sensor surface due to the onset of natural (free) convection because of buoyant forces. The convective heat flux is proportional to the difference between the sensor surface temperature (T_c) and the hot gas temperature (T_g) inside the cavity, and increases nearly linearly with the gas temperature. However, the radiant heat flux, being proportional to T_g^4, increases rapidly with increasing blackbody temperature. The sensor output will be proportional to the total of the radiative and convective flux.

A complete analysis of convection heat transfer at the sensor surface requires extensive computation. However, an estimate over a broad range of operating conditions can be obtained by using the empirical correlation proposed by Churchill and Chu [11] for free convection flows. With the gage placed inside the cavity, the sensor and the cavity surface form an enclosure. However, since the spherical cavity dimension being much larger than the sensor/holder assembly, free-convection theory is a good approximation. The sensor/holder assembly is inserted in to the spherical cavity after stabilization of the temperature. Hence, the holder/sensor surface temperature is assumed to be at the ambient value. The gas temperature at the sensor location in the cavity is unknown. However, assuming it to be equal to the blackbody temperature would represent an upper limit on the severity of convection compared to the radiative flux.

For application of the Churchill-Chu correlation, the sensor/holder diameter was used as the characteristic length. The Raleigh number based on the characteristic length varied from 12×10^4 to 6×10^4 over the blackbody temperature range from 973 K to 1355 K, corresponding to a radiant heat flux range from 50 kW/m^2 to 190 kW/m^2.

Figure 7 shows the sensor output plotted against radiant flux as well as the total flux obtained by adding the calculated convective flux to the radiant flux. The positive intercept of the linear fit on the y-axis for the radiant flux calibration is an indication of

the presence of convection effects. The application of the convection correction results in an apparent zero-offset without significantly affecting the linearity of the sensor response. The linearity suggests that the convection heat transfer effect, while not small, is not changing significantly over the calibration heat flux range from 50 kW/m^2 to 190 kW/m^2.

It may be observed that with convection effects included, the linear fit for the data has a negative intercept possibly due to over-correction for the convection correction. The over-correction is probably due to two reasons. First, the hot gas temperature is likely to be less than the blackbody temperature assumed in the calculations. Secondly, the Churchill-Chu correlation is based on two-dimensional free convection theory. Three-dimensional effects tend to reduce the magnitude of convection heat transfer. It is likely that the slopes of the two curves for radiant and total flux represent the upper and lower bounds for the sensor responsivity. The best estimate [12] for the responsivity is the corresponding mean value of 0.686 mV/(kW/m^2), with an associated uncertainty assuming an appropriate probability distribution function maximum deviation.

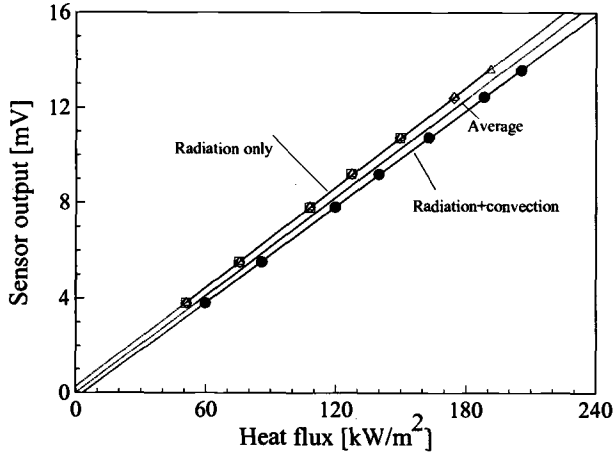

Figure 7 - *Convection heat transfer effect for the Schmidt-Boelter sensor calibration.*

Effective emissivity

When placed inside the cavity, the sensor responds to the hemispherical radiation from the cavity surface. Hence, the effective hemispherical emissivity, rather than the normal emissivity, determines the level of incident radiant flux at the sensor location. This is valid when viewing from location far away from the blackbody. Emissivity is a function of the temperature distribution and the intrinsic emissivity of spherical cavity surface, and the location of the sensor inside the cavity. Figure 8 shows the results of Monte-Carlo calculations for the effective emissivity for different positions of the sensor

and for cavity surface emissivity values of 0.8 and 0.9. These calculations were performed using a blackbody emissivity-modeling program [13].

When the sensor is located far inside close to the radiating surface of the cavity, the effective emissivity is close to the intrinsic emissivity of the cavity surface. As the sensor is moved away from the surface towards the aperture, the effective emissivity gradually increases due to increasing number of reflections. Close to the aperture, the effective emissivity nearly approaches unity for surface emissivity values of 0.8 and 0.9. For sensor Positions 2 and 3 (Table 1), the estimated value is 0.995 (± 0.005).

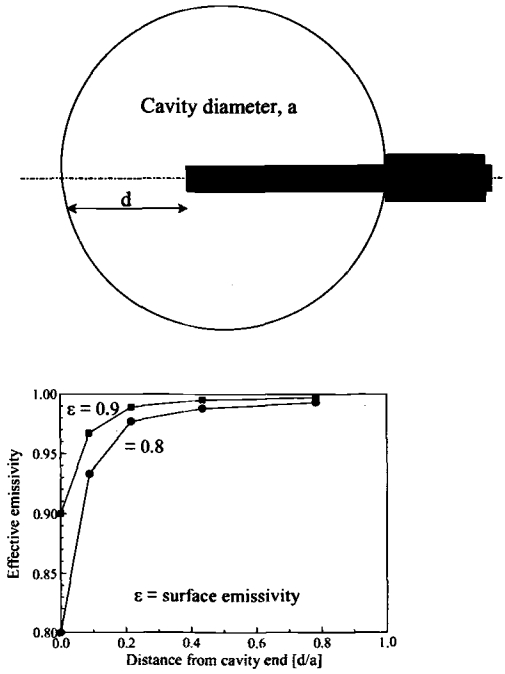

Figure 8 - *Effective hemispherical emissivity calculation for sensor in a spherical cavity.*

Corrections to measured responsivity

Table 2 summarizes the corrections to the measured responsivity for convection and effective emissivity. The corrected value of the responsivity for the present calibration is about 1.6 % lower than the transfer calibration value. The closeness of the responsivity

measured by the two methods suggests that the sensor used in the present tests is nearly Lambertian. A previous test [4] on a similar sensor with the same emissivity coating was found to have nearly Lambertian response. Placing the sensor inside a blackbody cavity is the only viable approach for calibration at high heat flux levels (500 kW/m^2 - 2000 kW/m^2). The agreement between the two calibration methods is encouraging for further developing the technique for use with cylindrical cavity blackbodies, which have a higher temperature capability than the spherical blackbody used in the present study. However, the associated issues related to non-uniform cavity surface temperature distribution, effective emissivity and furnace loading need to be addressed in detail to fully validate the technique.

Table 2 - *Corrections for the measured responsivity*

Mean responsivity (Measured)		**0.700 mV/(W/cm^2)**
Corrections		
Effective emissivity	0.5%	
Natural convection	-1.9%	
Corrected responsivity (SPBB)		**0.689 mV/(W/cm^2)**
Transfer technique (VTBB)		**0.700 mV/(W/cm^2)**

Measurement Uncertainties

The measurement uncertainties associated with the transfer technique calibration in the 25 mm VTBB are discussed in references [1] and [2]. Based on several calibrations of a different Schmidt-Boelter reference sensor, the relative expanded uncertainty in VTBB calibrations is 2 % for a coverage factor of $k = 2$. For the present calibration in the spherical blackbody, the individual uncertainties are discussed below and the values tabulated in Table 3.

Blackbody temperature

The temperature of the blackbody is measured by a type-S thermocouple and is stable to be within ± 1 K. Assuming uniform temperature distribution, the corresponding uncertainty in the radiant heat-flux will be about 0.4 % at the lowest test temperature of 1073 K.

Influence of sensor/holder assembly

The sensor and the holder assembly are placed inside the cavity after stabilization of the blackbody temperature. However, the presence of the assembly reduces the cavity

radiation heat loss through the aperture due to nearly closed aperture opening, which leads to an increase in the furnace temperature. This is observed to introduce an uncertainty of about 1 K in the measured temperature and a corresponding additional uncertainty in the calculated radiant flux.

Alignment error

Not present since the sensor is inside a large cavity.

Sensor reading

The sensor readings are averaged over a period of 30 s to 85 s and the uncertainty in the standard deviation of the mean was less than 0.1%.

Effective emissivity calculations

The upper and lower bounds for the effective emissivity are 1.0 and 0.99, respectively. It is assumed that the true value lies within these bounds with equal probability. Hence, assuming a uniform or rectangular probability distribution [12], the calculated value of the uncertainty is 0.3 %.

Convection correction

The upper and lower bounds for the calculated convection correction are ± 1.9 % of the mean value of the responsivity calculated with and without convection correction. Assuming that it is equally probable for the true value to lie within these bounds, the calculated value of the uncertainty is 1.2 % for a rectangular probability distribution.

Table 3 - *Estimate of uncertainties in heat-flux sensor calibration. (Heat-flux range 50 kW/m^2 to 190 kW/m^2)*

Uncertainty Source	Type	Uncertainty [%]
a. Blackbody temperature	B	0.4
b. Sensor/Holder effect	B	0.4
c. Effective emissivity correction	B	0.3
d. Alignment: Linear	B	0.0
Angular	B	0.0
e. Sensor output reading	A	0.1
f. Convection correction	B	1.2
g. Repeat tests	B	0.6
Relative expanded uncertainty ($U = k \cdot u_c$)	**$k = 2$**	**3.0**

Repeat tests

Several repeat transfer calibration tests in the 25 mm VTBB on a reference sensor has demonstrated a standard deviation 0.6 % of the responsivity of the mean value [4]. This value of uncertainty is conservatively added to other uncertainty components to account for long-term repeatability of the calibration in the spherical blackbody.

Combined uncertainty

The individual uncertainties have been listed in Table 3. The combined uncertainty (u_c) is given by the square root of the sum-of-the-squares of the individual uncertainty components. The relative expanded uncertainty (U) is 3.0 % ($k = 2$).

Traceability of Calibrations

The determined sensor responsivity using the 25 mm VTBB in the range 0 kW/m^2 to 50 kW/m^2 is directly traceable to the NIST high accuracy cryogenic radiometer [2]. For the calibration in the spherical blackbody, in the range from 50 kW/m^2 to 190 kW/m^2, the heat-flux is derived from thermocouple temperature measurements. The thermocouple measurements are also traceable to the NIST through the manufacturer of the blackbody unit. The good agreement between the two different methods for determining the heat-flux at the sensor location and using different field-of-view is encouraging. It must be noted that the narrow view-angle measurement is a primary calibration from which all other calibrations are derived. NIST radiance temperature scale is based on narrow view-angle measurements of blackbody cavities.

Conclusions

A comparative study of the narrow and wide view-angle calibrations of a heat-flux sensor using blackbody radiation is presented. For the narrow view-angle calibration, conducted previously in a heated graphite-tube facility, the sensor was placed away from the blackbody thus minimizing the convection effects. The heat-flux was derived from transfer calibration using a transfer standard electrical substitution radiometer. For the wide view-angle (180°) calibration, the sensor was placed inside a heated spherical blackbody cavity. The heat-flux at the sensor was calculated using Stefan-Boltzmann equation corresponding to the blackbody temperature measured by a thermocouple. The measured responsivity was corrected for convection heat transfer and effective emissivity. The two calibrations appear to agree within the expanded uncertainty of 3 % (coverage factor $k = 2$). While this agreement is encouraging, further work on the non-uniform cavity surface temperature distribution and convection effects is needed to extend the technique for calibration using other blackbody cavity shapes. Tests with the sensor located in the horizontal plane avoid the significant convection heat transfer in the present experiments, and help in assessing the validity of convection corrections.

References

[1] Murthy, A. V., and Tsai, B. K., "Transfer Calibration of Heat Flux Sensors at NIST," HTD-Vol. 345, D.Kaminski, A.M. Smith, and T.F. Smith, Eds. *Proceedings of the National Heat Transfer Conference*, American Society of Mechanical Engineers, Vol. 7, 1997, pp. 81-88.

[2] Murthy, A. V., Tsai, B. K., and Gibson, C. E., "Calibration of High Heat Flux Sensors at NIST," *Journal of Research of the National Institute of Standards and Technology*, Vol. 102, No. 44, 1996, pp. 479-487.

[3] Gentile, T. T., Houston, J. M., Hardis, J. E. Cromer, C. L., and Parr, A. C., "The NIST High Accuracy Cryogenic Radiometer," *Applied Optics*, Vol. 35, 1996, pp. 1056-1068.

[4] Murthy, A. V., Tsai, B. K., and Saunders, R. D., "Transfer Calibration Validation Tests on a Heat Flux Sensor in the 51-mm High-Temperature-Blackbody," *Proceedings of the 47th International Instrumentation Symposium*, 2001.

[5] Brookley, C. E., and Llewellyn, W. E., "Determination of Blackbody Radiance at Temperatures above 2300 °C," *Proceedings of the Seventh Symposium on Temperature*, 1992.

[6] Olsson, S., "Calibration of Thermal Radiometers - The Development of a New Method," SP Report 1989:04, National Testing and Research Institute, SP, Sweden, 1989.

[7] Olsson, S., "Calibration of Radiant Heat Flux Meters - The Development of a Water-Cooled Aperture for use with Blackbody Cavities," SP Report 1991:58, Swedish National Testing and Research Institute, Sweden, 1991.

[8] Persson, B., and I. Wetterlund, I., "Tentative Guidelines for Calibration and Use of Heat Flux Meters," SP report 1997:33, Swedish National Testing and Research Institute, Sweden, 1997.

[9] Murthy, A. V., Tsai, B. K., and Saunders, R. D., "High Heat Flux Sensors Calibration in a Cooled Enclosure," *Proceedings of the 45th International Instrumentation Symposium*, Aerospace Industry and Test Measurement Division, 1999, pp. 91-100.

[10] Murthy, A. V., Tsai, B. K. and Saunders, R. D., "Comparative Calibration of Heat Flux Sensors in Two Blackbody Facilities," *Journal of Research of the National Institute of Standards and Technology*, Vol. 104, No. 5, 1999, pp. 487-494.

[11] Churchill, S. W., and Chu, H. H. S., "Correlating Equations for Laminar and Turbulent Free Convection from a Vertical Plate," *International Journal of Heat and Mass Transfer*, Vol. 18, 1975, pp. 1323-1329.

[12] Taylor, B. N., and Kuyatt, C. E., "Guidelines for Evaluating and Expressing the Uncertainty of NIST Measurement Results," *NIST Technical Note 1297*, 1994.

[13] STEEP3 – User's Guide, "Blackbody emissivity Modeling Program - Ver. 1.3," Virial, Inc., Gaithersburg, MD, 2000.

Ronald L. Alpert, [1]Lawrence Orloff,[1] and John L. de Ris[1]

Angular Sensitivity of Heat Flux Gages

Reference: Alpert, R. L., Orloff, L., and de Ris, J. L., "**Angular Sensitivity of Heat Flux Gages**," *Thermal Measurements: The Foundation of Fire Standards, ASTM STP 1427*, L.A. Gritzo and N.J. Alvares, Eds., ASTM International, West Conshohocken, PA, 2002.

Abstract: The response of a heat flux gage depends on both the angular distribution of the source radiant flux and the angular sensitivity of the coating on a gage's heat-sensing element. The issue becomes important for the calibration of apparatuses designed to test the response of materials subjected to a known level of incident thermal radiation. In this study, the angular sensitivity of several different gage coatings are measured by rotating the gage sensing surface in front of a black body source. Ideally, gage output is proportional to the cosine of the angle of incidence with respect to the normal, known as Lambertian behavior. Some commercial black coatings become non-Lambertian for angles above 60^0 from the surface normal, but other coatings maintain a Lambertian response beyond 70^0. The impact of these differences on the calibration of the Fire Propagation Apparatus and the Cone Calorimeter is evaluated.

Keywords: heat flux, heat flux gage, gage calibration

Introduction

The radiant heat received by a surface depends on both the angular distribution of the incident radiation and the angular sensitivity of the material receiving the radiation. This means that the response of a heat flux gage depends on both the angular distribution of the source radiant flux and the angular sensitivity of the coating of gage's heat-sensing element. The issue becomes important for the calibration of apparatuses designed to test the response of materials subjected to a known amount of incident thermal radiation. Under "ideal" conditions, the radiation incident on the surface is uniform over the complete hemisphere of incident angles and the angular sensitivity of the receiving surface is proportional to the cosine of the angle from the normal (i.e. a Lambertian surface).

[1] Principal research scientist, advanced research scientist and principal research scientist, respectively, Factory Mutual Research, 1151 Boston-Providence Turnpike, Norwood, MA 02062

There are significant differences in the angular distribution of incident radiation when comparing the Cone Calorimeter (ASTM Test Method for Heat and Visible Smoke Release Rates for Materials and Products Using an Oxygen Consumption Calorimeter, E 1354) to the Fire Propagation Apparatus (ASTM Test Methods for Measurement of Synthetic Polymer Material Flammability Using a Fire Propagation Apparatus, E 2058). Such differences are also evident when comparing apparatuses used to calibrate heat flux gages (e.g., hemispherical oven cavities or sources approximating point emitters). One can correct for angular effects once the angular distribution of the incident radiation in the standard fire test and gage calibration apparatuses is known and once the angular sensitivity of the coating on the calibration gage is known.

Information and data on the angular dependence both of emissivity and absorptivity, is generally lacking, especially for nonmetallic surfaces. Much of the information available is from work performed in 1935 by E. Schmidt and E.R.G. Eckert in Germany that is summarized in [1,2]. The summaries in [1,2] contain plots showing that the ratio of hemispherical to normal emittance is approximately 0.96 for high emittance nonmetallic surfaces.

Recent worldwide efforts to make the measurement of heat flux more accurate through improvement in the procedure for calibration of transducers are described in [*3*]. At Factory Mutual Research, heat flux gages are calibrated by placing them at several distances in front of a hot furnace orifice. (Figure 1) illustrates the method of calibration, which is based on first principles rather than transfer from some other device. The radiant heat flux emerging from the orifice is assumed to be σT^4, where σ is the Stefan-Boltzmann constant and T is the temperature of the target inside the furnace. The emissivity of the target cavity is assumed to be unity, i.e., a blackbody. Blackbody radiation temperature is measured by a disappearing filament optical pyrometer viewing the center of the target through the furnace orifice. The gage is cooled by water set to the ambient air temperature to minimize convection errors. Similarly, surfaces viewed by the gage are painted black and cooled with ambient temperature water to minimize errors due to stray radiation. The orifice itself is gold plated with a low emissivity mirror finish. An ambient temperature water-cooled shutter is placed in front of the orifice. The change in gage signal is recorded while the shutter is repeatedly opened and closed under computer-control to eliminate errors in the measurement of the signal voltage. Residual errors are attributable to errors of blackbody temperature measurement (± 2 K) and distance from orifice (± 1mm). These uncertainties each affect the calibration constant less than 0.6%.

Experiment

The apparatus described above (Figure 1) is also used to measure the *angular* sensitivity of different heat flux gage coatings. The heat flux gage is securely mounted in a V-clamp supported on a precision turntable. The sensing element is located on the axis of the turntable and forward of the V-clamp to prevent reflection from the clamp surface to the sensing element. Note that the V-clamp assembly allows the gage sensing element to be precisely on the axis of rotation while still being held securely.

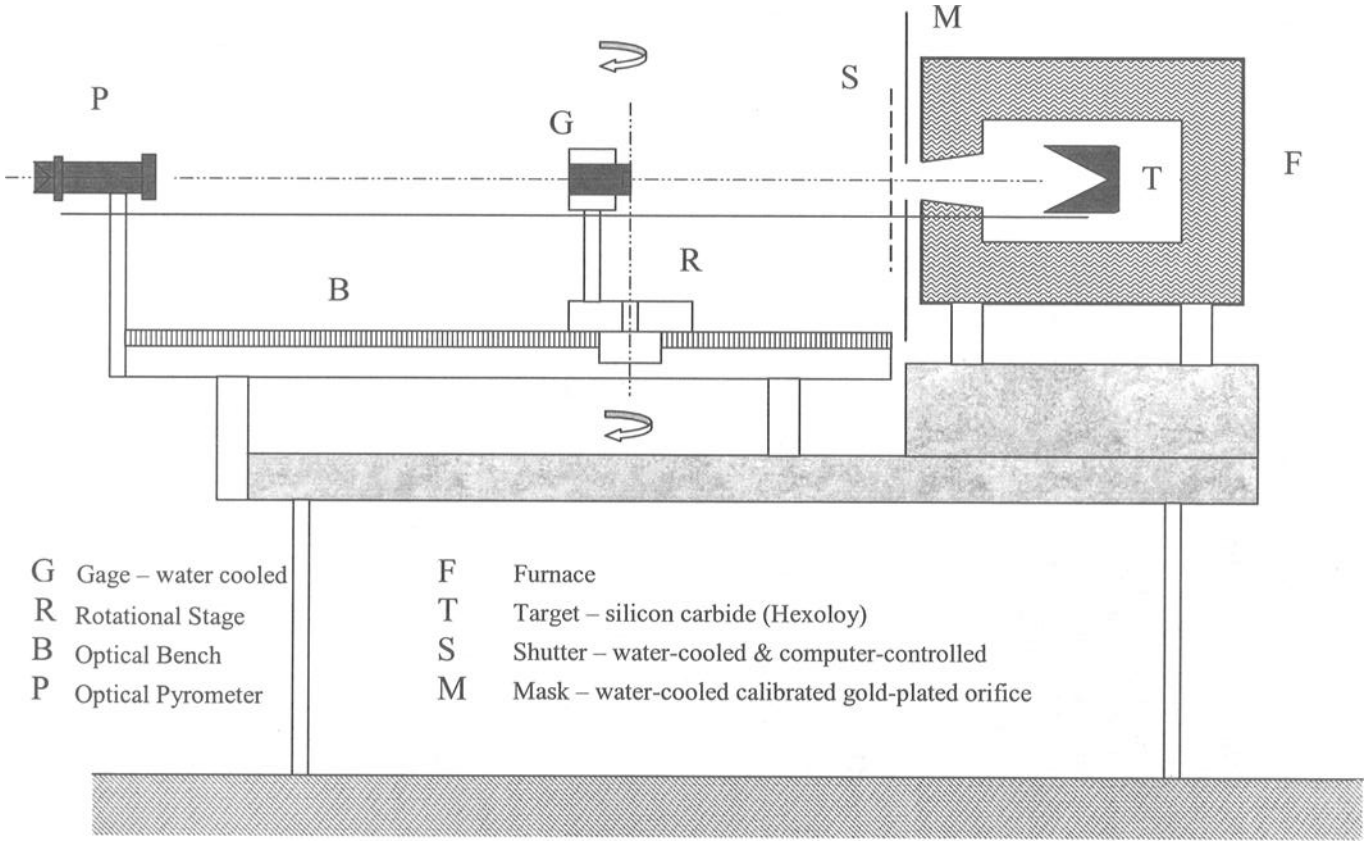

Figure 1. Calibration Apparatus to Obtain Angular Sensitivity

The measurement procedure is as follows. The optical pyrometer, gage, furnace orifice and target are first aligned on the optical rail. The cooling water temperature is adjusted to ambient. The blackbody radiation temperature is measured both before and after the calibration. With a gage positioned 240-mm from the oven aperture, angular sensitivity of different gage coatings is measured by rotating the sensing surface to discrete angular positions, up to ± 90 degrees from the oven normal. At each such angular position, the shutter is opened and closed a total of 6 complete cycles. A cycle consists of a settling time of about 6s and 50 measurements from a voltage amplifier having a gain of 500.12 connected to the gage. Each voltage measurement is taken over a period of 6 line cycles by an integrating digital voltmeter. The 50 readings are averaged and then compared to the previous averaged voltage with the shutter in the opposite position. The 15 complete shutter cycles produce a total of 29 changes in voltage. The changes in voltage have a standard deviation less than 0.6 microvolts. The measurement process at each angular position takes about 15 minutes under computer control.

Measurement Results

In general the angular sensitivities of coatings are not Lambertian (i.e. do not follow a cosine law) and therefore must be measured. (Figures 2a-2d) show the angular sensitivities of typical Schmidt-Boelter and Gardon gages as received from a vendor[2] as well as Gardon gages having Thurmalox[3] and IITRI MH21/IP[4] coatings. Thurmalox is high temperature paint normally used for solar collector applications but also specified in the E 2058 standard for application on test specimens, to ensure complete absorption of external radiation from the apparatus heaters. The IITRI MH21/IP coating has well-documented optical properties and is sometimes used for its exceptionally high normal absorptance (0.979 between 250 –2500 nm wavelengths).

All the angular sensitivity measurements appear to be quite accurate, due to the lack of scatter and consistency with expected behavior. These measurements permit calculation of the ratio of hemispherical to normal absorptance of each of the coatings, as shown in (Table 1). The ratios are all about 0.96, except even higher for the Thurmalox coating. This suggests that the nominal calibration constant of a gage receiving radiation uniformly from all hemispherical directions (e.g., gage inserted into a spherical furnace cavity) should differ by 4% from a calibration obtained from radiation incident only in the normal direction (e.g., gage facing a furnace orifice).

Since the gage output ideally is proportional to the cosine of the angle of incidence with respect to the normal, one clearly sees from (Figures 2a-2d) the angle at which the response no longer follows the idealized Lambertian behavior. The coatings examined here maintain their Lambertian response beyond 70^0 but well below the 90^0 ideal.

---

[2] Medtherm Corporation, P.O. Box 412, Huntsville, AL 35804

[3] The Dampney Company, 85 Paris St., Everett, MA 02149

[4] IIT Research Institute, Chemical Technology Division, Advanced Materials & Coatings Lab, Chicago, IL 60616

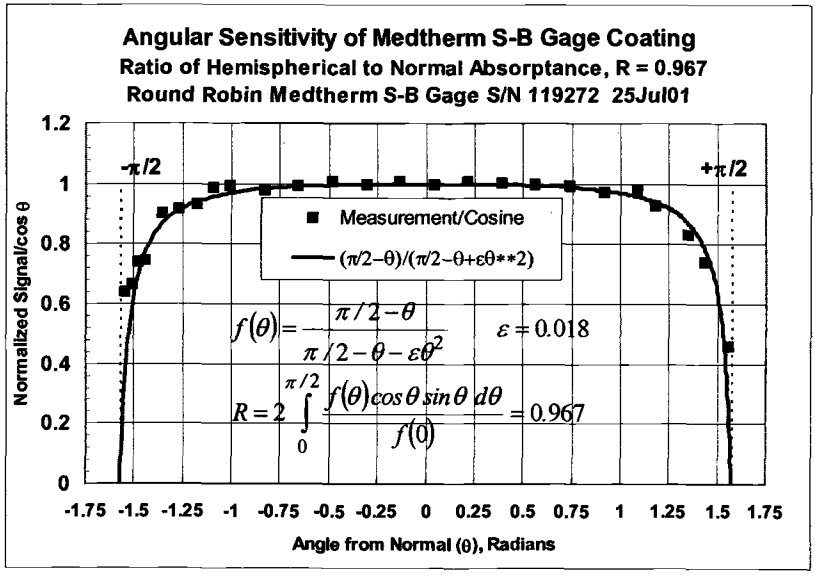

Figure 2a – *Angular Sensitivity of Medtherm Schmidt-Boelter Gage Coating*

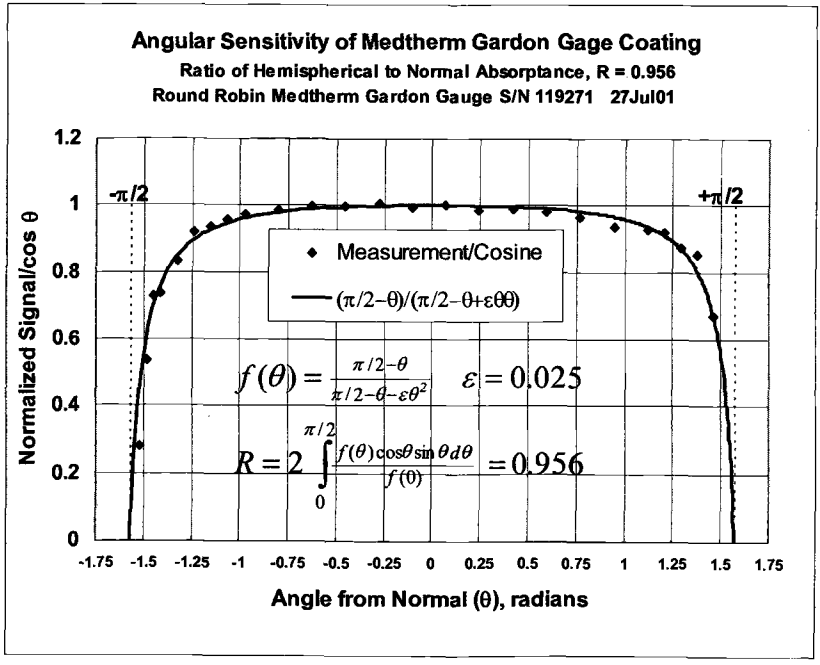

Figure 2b – *Angular Sensitivity of Medtherm Gardon Gage Coating*

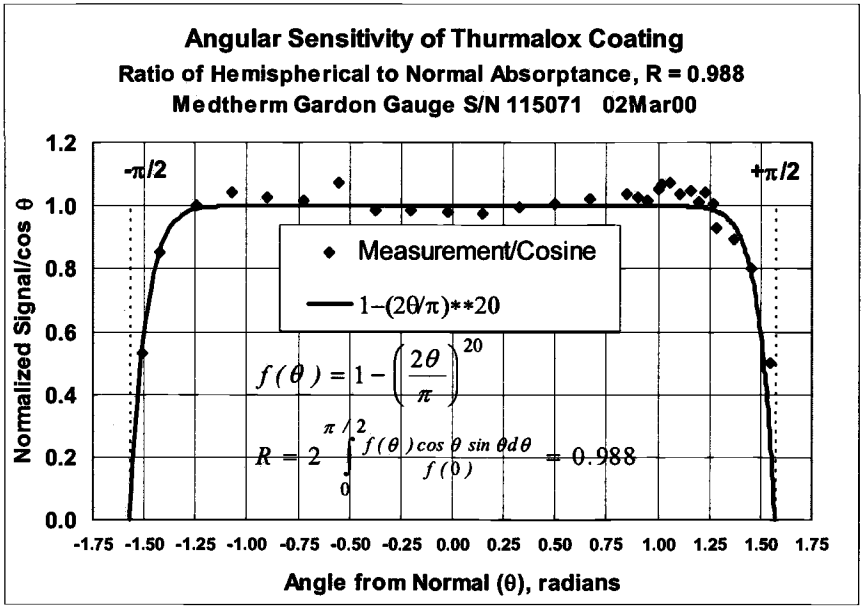

Figure 2c – *Angular Sensitivity of Medtherm Gardon Gage with Thurmalox Coating*

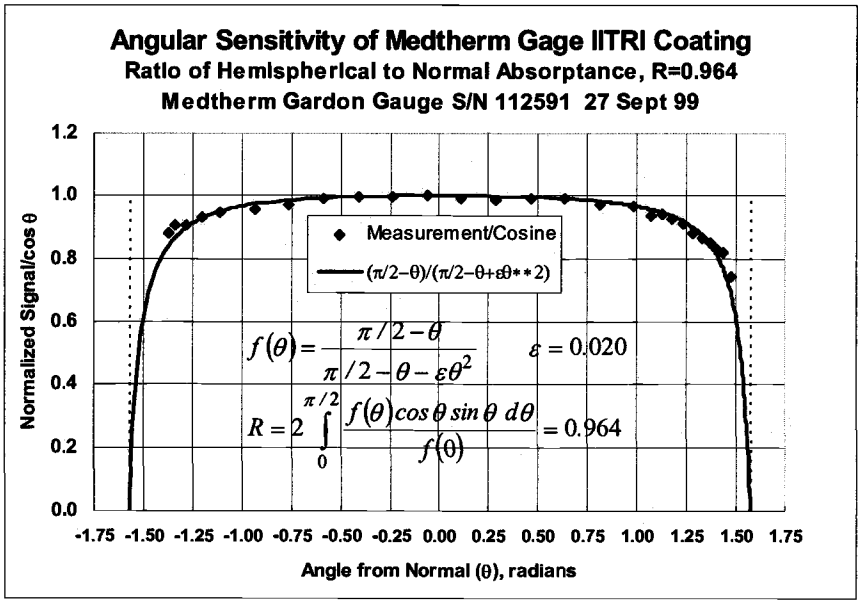

Figure 2d – *Angular Sensitivity of Medtherm Gardon Gage with IITRI MH21/IP Coating*

Table 1 – *Angular Sensitivity of Coatings*

Medtherm Serial #	Type	Coating	Curve Fit	Adjustable Parameter, ε	Ratio of Hemispherical to Normal Absorptance
119272 Round Robin	Schmidt-Boelter	Medtherm S-B Gage Coating	$\frac{\frac{\pi}{2}-\theta}{\frac{\pi}{2}-\theta+\varepsilon\theta}$	0.018	0.967
119271 Round Robin	Gardon	Medtherm Gardon Gage Coating	$\frac{\frac{\pi}{2}-\theta}{\frac{\pi}{2}-\theta+\varepsilon\theta}$	0.025	0.956
115071	Gardon	Thurmalox	$1-\left(\frac{2\theta}{\pi}\right)^{\varepsilon}$	20	0.988
112591	Gardon	IITRI MH21/IP	$\frac{\frac{\pi}{2}-\theta}{\frac{\pi}{2}-\theta+\varepsilon\theta}$	0.020	0.964

Impact of Angular Sensitivity on the Calibration of the Fire Propagation Apparatus and the Cone Calorimeter

Laboratory test apparatus used to measure the behavior of materials in fire environments require calibration of the externally applied heat flux levels. This calibration is generally performed with a Gardon- or Schmidt-Boelter-type gage sensing-surface at a position corresponding to the initial location of the surface of the specimen being tested. During actual testing, the specimen surface of some materials can regress well below the initial location or, conversely, the specimen may expand or intumesce, bringing the surface well above the initial location. It is not unusual for such surface movement to be in the range of 10 to 40 mm. Hence, calibration of the apparatus should include a vertical traverse with the heat flux gage to document the change in incident flux on the specimen as a result of surface regression or expansion. Since a vertical traverse with the heat flux gage will result in variations in the angle of incidence of thermal radiation from the apparatus, there will be an effect due to the angular sensitivity of the gage surface coating. It is therefore instructive to examine how the heat flux absorbed by a gage, and a specimen having the same surface coating as the gage, varies during a vertical traverse calibration.

To determine the spatially integrated heat flux absorbed by the horizontal sensing surface of a calibration gage (or a specimen having the same coating) as a function of elevation from the baseline position during a vertical traverse calibration of a given apparatus, the following integral is evaluated:

$$\dot{q}''(Z) = \int_{\theta_1(Z)}^{\theta_2(Z)} f(\theta)\alpha 2\pi \cos\theta \sin\theta d\theta \qquad (1)$$

where

$2\pi \sin\theta d\theta$ = solid angle subtended between θ and $\theta + d\theta$

$f(\theta)$ = normalized angular sensitivity function plotted in (Figures 2a-2d)

α = assumed constant coating absorptivity

$\theta_1(Z), \theta_2(Z)$ = upper and lower limiting angles, respectively, of the radiant heat source viewed by the gage sensing surface when facing upward, and

Z = height of gage sensing surface above the baseline position.

(Figure 3) below shows $\dot{q}''(Z)$ for a gage in the Fire Propagation Apparatus, calculated using curve fits to data from IITRI MH21/IP (Figure 2d) and Medtherm Flat Black coatings (Figure 2b) on a Gardon heat flux gage. Note that the re-normalized fits do not display the relative sensitivities of individual gages to a normally incident flux. The definitions of the limiting angles and the dimensions used for the calculation are shown in (Figure 4). According to manufacturer specifications, the Medtherm flat black coating has an absorptivity of 92% and the MH21/IP coating has an absorptivity of 97.9%. The curve for an ideal coating having unity absorptivity in the entire field of view is also shown. It can be seen that the chosen baseline position is approximately at the point where absorbed heat flux is least sensitive to changes in surface elevation, independent of the type of gage coating. Note that for the preceding calculations, any small effect of the quartz tube in the Fire Propagation Apparatus is ignored. This tube isolates a controlled specimen gaseous environment (e.g., flows of pure nitrogen, normal air or oxygen enriched air) from the laboratory atmosphere.

(Figure 5) is the corresponding calculation of $\dot{q}''(Z)$ for a gage in the Cone Calorimeter, with the definitions of the limiting angles and dimensions used shown in (Figure 6). It can be seen that the absorbed heat flux is sensitive to decreases in surface elevation from the baseline position, such as would occur during specimen regression but not nearly as sensitive to increases in surface elevation that would occur during specimen expansion.

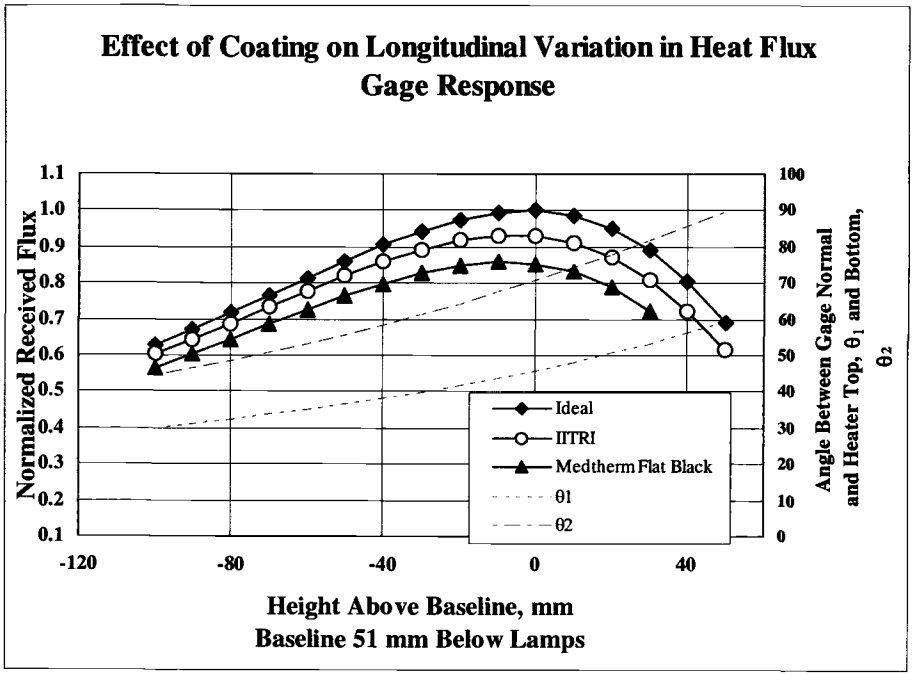

Figure 3 – *Flux Absorbed and Limiting Angles between Gardon Gage and Heat Source as a Function of Gage Height in the Fire Propagation Apparatus (ASTM E 2058) for Ideal ($\alpha = 1$), IITRI MH21/IP ($\alpha = 0.979$) and Medtherm Flat Black ($\alpha = 0.92$) Coatings*

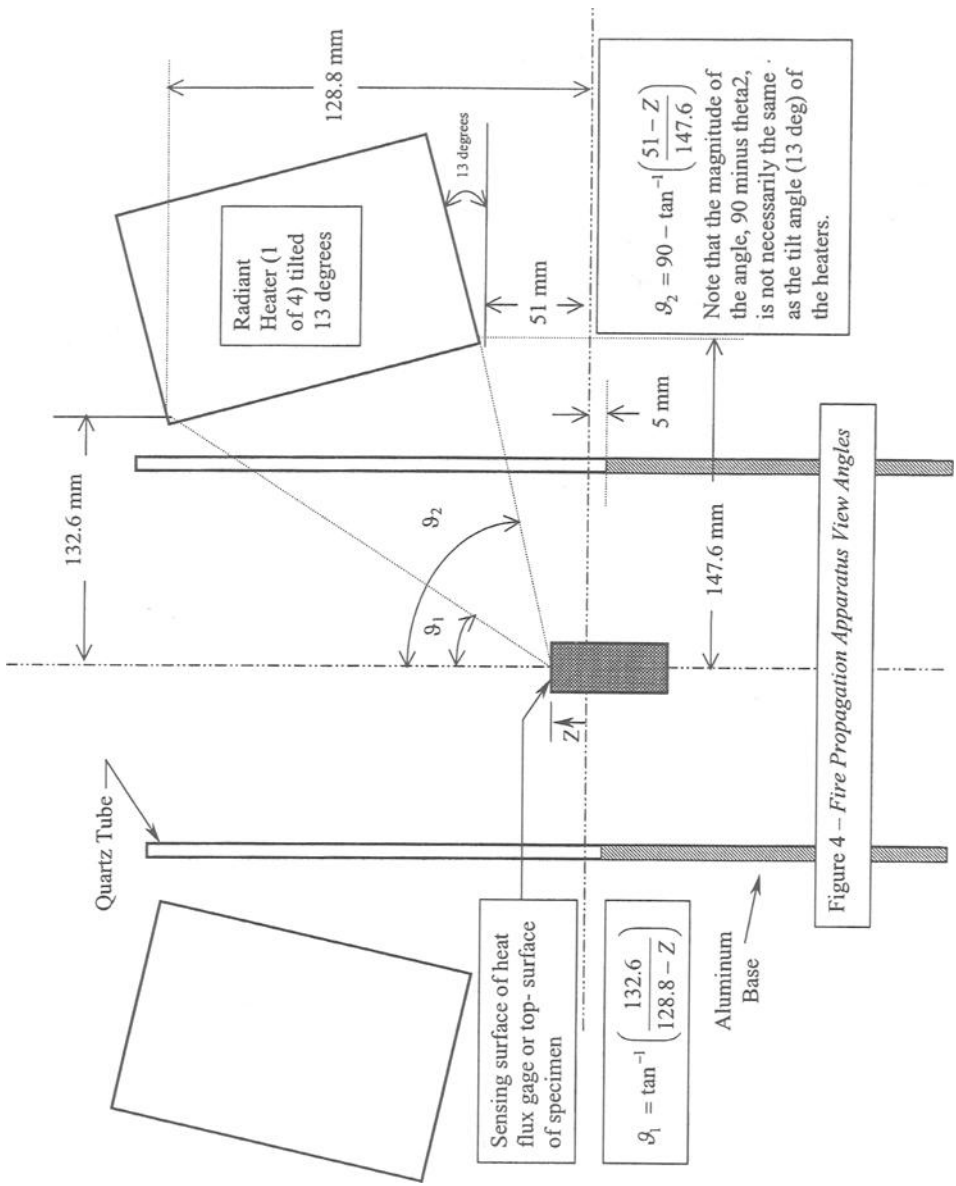

Figure 4 – *Fire Propagation Apparatus View Angles*

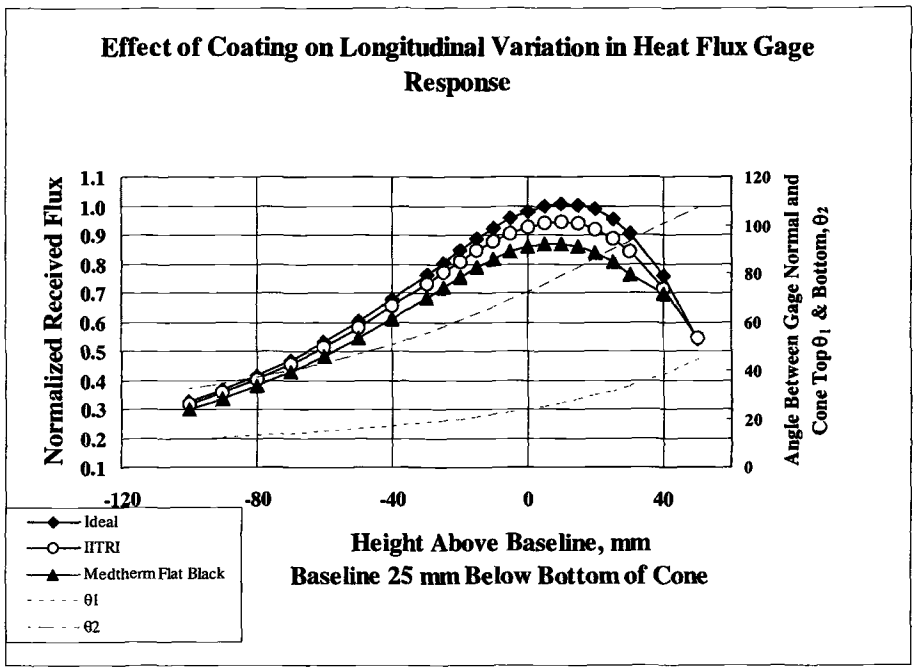

Figure 5 – *Flux to Gardon Gage and Angles between Gage and Heater Body as a Function of Gage Height in Cone Calorimeter (ASTM E 1354) for Ideal ($\alpha = 1$), IITRI MH21/IP ($\alpha = 0.979$) and Medtherm Flat Black ($\alpha = 0.92$) Coatings on Gage Sensing Surface*

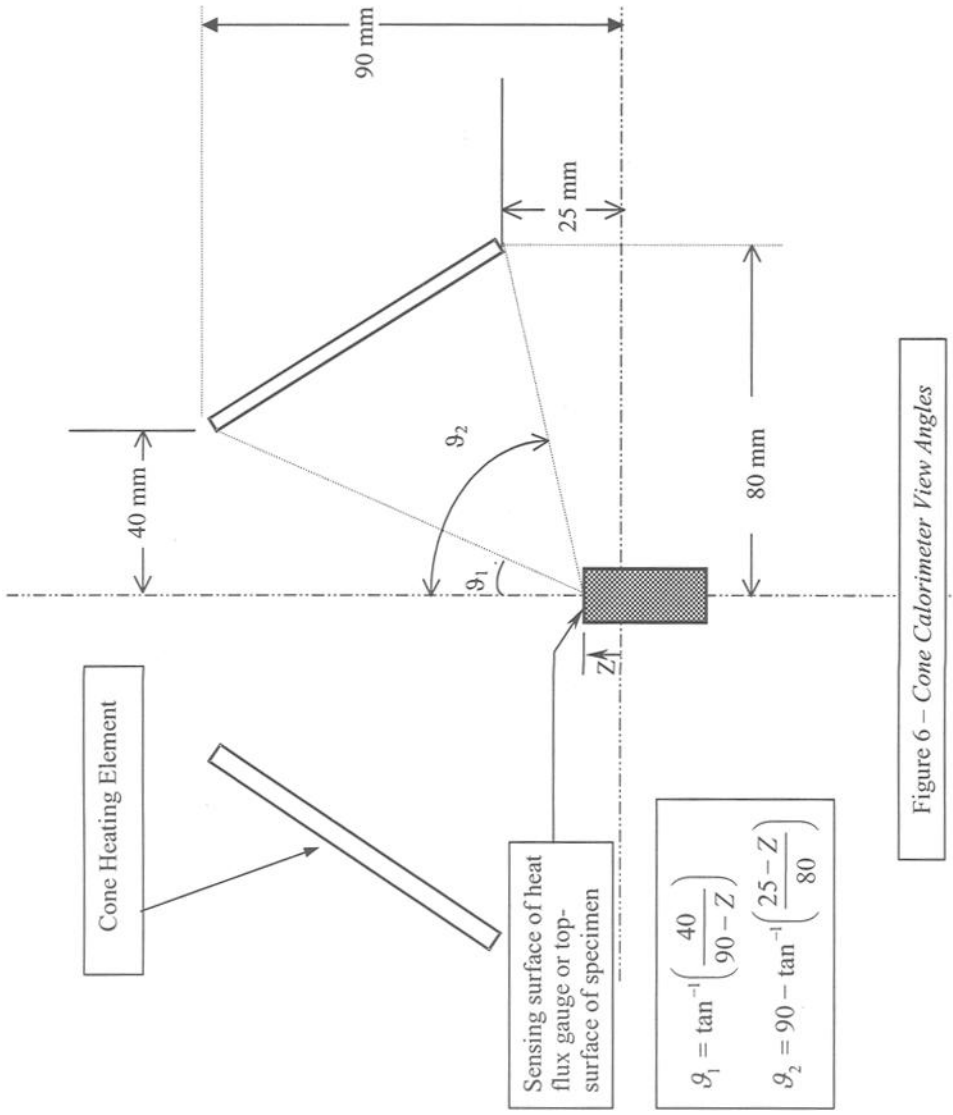

Figure 6 – *Cone Calorimeter View Angles*

Usually, it is desired to calibrate a laboratory fire test apparatus in terms of the magnitude of incident flux externally applied by the apparatus heat source. To determine the incident flux magnitude, however, a correction must be made to account for the difference between the angular distribution of thermal radiation to a calibration gage in the apparatus compared to the angular distribution from a radiant source when the gage itself is calibrated.

For example, if the gage itself is calibrated using radiation incident only in the normal direction, then the following correction factor must be applied to the gage output signal, E to obtain the true incident heat flux:

$$\frac{\int_{\theta_1}^{\theta_2} f(0)\sin\theta\cos\theta d\theta}{\int_{\theta_1}^{\theta_2} f(\theta)\sin\theta\cos\theta d\theta} \qquad (2)$$

where all terms have been defined previously. The correction factor has a value of about 1.05 at the baseline position in the Fire Propagation Apparatus for the IITRI MH21/IP coating.

Conclusions

It is important to be aware of errors that can result from the angular sensitivity of coatings on heat flux gages and the angular distribution of incident radiation from heat sources in the laboratory apparatus being calibrated by such gages. For most coatings on gages calibrated with normally incident radiation, use of (Equation 2) will yield an incident heat flux from the radiant sources in E 1354 or E 2058 the order of 4 or 5% greater than what would be obtained from the gage calibration constant alone. Effects due to the angular distribution of this incident radiation in E 1354 and E 2058 determine how changes in the elevation of the specimen surface while a test is in progress will cause changes in the magnitude of the incident heat flux. For this reason, it is recommended that calibration of E 1354 and E 2058 should always include a traverse to simulate expected changes in the elevation of the specimen surface.

References

[1] Eckert, E.R.G., "Radiation Properties of Solids and Liquids," Chapter 14, Part 2, *Handbook of Heat Transfer Fundamentals*, 2nd Edition, W.M. Rohsenow, J.P. Hartnett and E.N.Ganic, Ed., McGraw Hill Book Company, New York, 1985, pp. 14-25.

[2] Mills, A.F., *Heat Transfer*, Section 6.5.3 – Directional Properties of Real Surfaces, Richard D. Irwin, Inc., Homewood, IL, 1992, pp. 540-541.

[3] *Heat Flux Transducer Calibration: Summary of the 2nd Workshop*, W.L. Grosshandler, Ed., NISTIR 6424, National Institute of Standards and Technology, Building and Fire Research Laboratory, November, 1999.

Tom Blanchat,[1] Larry Humphries,[2] and Walt Gill[1]

Sandia Heat Flux Gauge Thermal Response and Uncertainty Models

---

Reference: Blanchat, T. K., Humphries, L. L., and Gill, W., "**Sandia Heat Flux Gauge Thermal Response and Uncertainty Models**," *Thermal Measurements: The Foundation of Fire Standards, ASTM STP 1427*, L. A. Gritzo and N. J. Alvarez, Eds., ASTM International, West Conshohocken, PA, 2002.

Abstract: The Sandia Heat Flux Gauge (HFG) was developed as a rugged, cost-effective technique for performing steady state heat flux measurements in the pool fire environment. The technique involves reducing the time-temperature history of a thin metal plate to an incident heat flux via a dynamic thermal model, even though the gauge is intended for use at steady state. In this report, the construction of the gauge is reviewed. The thermal model that describes the dynamic response of the gauge to the fire environment is then advanced and it is shown how the heat flux is determined from the temperature readings. This response model is based on first principles with no empirically adjusted constants. A validation experiment is presented where the gauge was exposed to a step input of radiant heat flux. Comparison of the incident flux, determined from the thermal response model, with the known flux input shows that the gauge exhibits an noticeable time lag. The uncertainty of the measurement is analyzed, and an uncertainty model is put forth using the data obtained from the experiment. The uncertainty model contains contributions from 17 separate sources loosely categorized as being either from uncontrolled variability, missing physics, or simplifying assumptions. As part of the missing physics, an empirical constant is found that compensates for the gauge time lag. Because this compensation is incorporated into the uncertainty model instead of the response model, this information can be used to advantage in analyzing pool fire data by causing large uncertainties in non-steady state situations. A short general discussion on the uncertainty of the instrument is presented along with some suggested design changes that would facilitate the determination and reduction of the measurement uncertainty.

Keywords: fire testing, heat flux gauge, errors, uncertainty, hydrocarbon fuel fires, fire calorimetry

[1] Principal Member of Technical Staff, Fire Science and Technology Department 09132, Sandia National Laboratories, Albuquerque, NM, 87185.

[2] Principal Member of Technical Staff, Nuclear Safety Testing Department 06423, Sandia National Laboratories, Albuquerque, NM, 87185.

Sandia is a multiprogram laboratory operated by Sandia Corporation, a Lockheed Martin Company, for the United States Department of Energy under contract DE-AC04-94-AL85000.

Introduction

Over the past several years, hydrocarbon fueled pool fire experiments have been performed both at Sandia National Laboratories' (SNL) Lurance Canyon Burn Facility and the Navy's China Lake Large Scale Pool Fire Facility where measurements of radiative heat fluxes were made using the Sandia Heat Flux Gauge (HFG). HFGs were developed by SNL as a rugged, cost-effective technique for performing heat flux measurements in the pool fire environment. The technique involves reducing the time-temperature history of a fire exposed surface as measured by a thermocouple, to a time resolved heat flux via a thermal model that is valid during times of steady-state within the fire environment. Three issues have arisen with respect to the technique. First, the original thermal model that incorporates empirically derived time constants did not perform well in a recent calibration experiment. Second, the original thermal model is not amenable to the formulation of an uncertainty statement that should accompany heat flux measurements in application. And third, it is not always clear from the data as to when steady-state is achieved and the measurement is valid. To address these issues, we herein put forth an alternative thermal model that avoids the use of time constants by allocating, in part, their effect to the uncertainty of the measurement. The uncertainty becomes coupled to the dynamic behavior of the gauge with large values of uncertainty signaling when the gauge is not in equilibrium with the fire environment. We believe this approach results in an improved data reduction technique that is of use in reducing the data collected from previous fires.

Figure 1 shows a typical time-temperature history from an HFG reduced to the incident heat flux. Also in the figure, the uncertainty of the measurement is shown as error bars for each data point. The heat flux was determined by applying the proposed thermal model, and the uncertainty was found from the accompanying uncertainty model. It is worth noting the uncertainty is large during times of dynamic change and can be used to assess the existence of steady state. The thermal model is based on first principles, with no empirically adjusted constants. The uncertainty model contains contributions from 17 separate sources loosely categorized as being either from uncontrolled variability, missing physics, and simplifying assumptions. The uncontrolled variability and simplifying assumptions are the major contributors to the uncertainty during times of steady-state operation, and the missing physics are responsible for the large increase in uncertainty during dynamic changes.

In what follows, the gauge construction is first reviewed. It will be seen that the gauge is essentially a thin metal plate that responds to heating from the fire environment. A thermal model that describes the response is then advanced and it is shown how to determine the heat flux from the fire environment via the time-temperature history of the thin metal plate. A validation experiment is presented where the gauge was exposed to a step input of radiant heat flux. Comparison of the incident flux determined from the thermal model with the known flux input shows that the gauge exhibits a noticeable time lag. The uncertainty of the measurement is analyzed, and an uncertainty model is put forth using the data obtained from the experiment. An empirical constant is found that compensates for the gauge time lag. This compensation is incorporated into the uncertainty model instead of the response model, and it is shown how this information can be used to advantage in analyzing pool fire data. Finally, a short general discussion

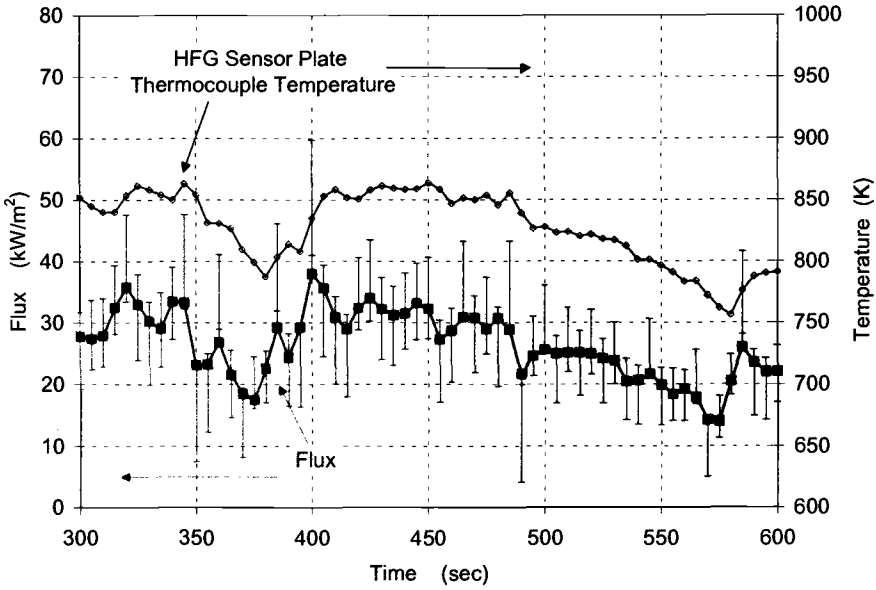

Figure 1 – *Example of a measurement and associated uncertainty using the HFG in a pool fire. Note the uncertainty limits may not always contain the measurement.*

on the uncertainty of the instrument is presented along with some suggested design changes to the HFG that would facilitate the determination and reduction of the measurement uncertainty associated with the HFG.

The HFG

The HFG is intended to function by exposing one side of a thin metal plate to the fire environment and observing the temperature response. Ideally, the plate is perfectly isolated, i.e., the unexposed side and the edges of the plate are thermally insulated. Furthermore, if the plate is assumed to be thermally thin, gradients through the plate and along the lateral direction can be ignored. These assumptions allow interpreting the temperature measured at a single point on the unexposed surface as the one-dimensional response of a heated composite wall.

To meet the requirements of a one-dimensional response, the gauge shown in Figure 2 was developed. The assembly is essentially a hollow cylinder filled with thermal insulation that is fitted with sensor plates on each end. The body of the HFG is a 10-cm long cylinder of 10.2-cm diameter schedule 40 steel pipe. The body is filled with Cerablanket® ceramic fiber insulation to minimize heat transfer inside the HFG. The entire assembly is held together with four 14-cm stainless steel bolts.

The sensor plates are 10.2-cm squares of 0.025-cm thick 304 stainless steel shim-stock. The plates are held in place on the cylindrical body by endplates that are 10.2-cm square by 0.32-cm thick 304 stainless steel with a centered 5.0-cm hole. The sensor surfaces are thermally isolated from the remainder of the HFG by two layers of Lytherm®

ceramic fiber insulation. The front sides of the sensor surfaces are coated with Pyromark® paint to achieve a diffuse gray surface. A 0.16-cm diameter Inconel-sheathed type-K thermocouple is used as the sensor thermocouple. The sensor thermocouple is attached to the sensor surface with 0.01-cm thick retainer straps that are spot-welded to the back of the sensor surface.

For most of the data taken to date, the gauge has been constructed with only one sensor plate. Only one end was exposed to the fire, and the sensor plate on the other end was replaced with a flat plate (304 stainless steel, 10.2-cm square, 0.32-cm thick).

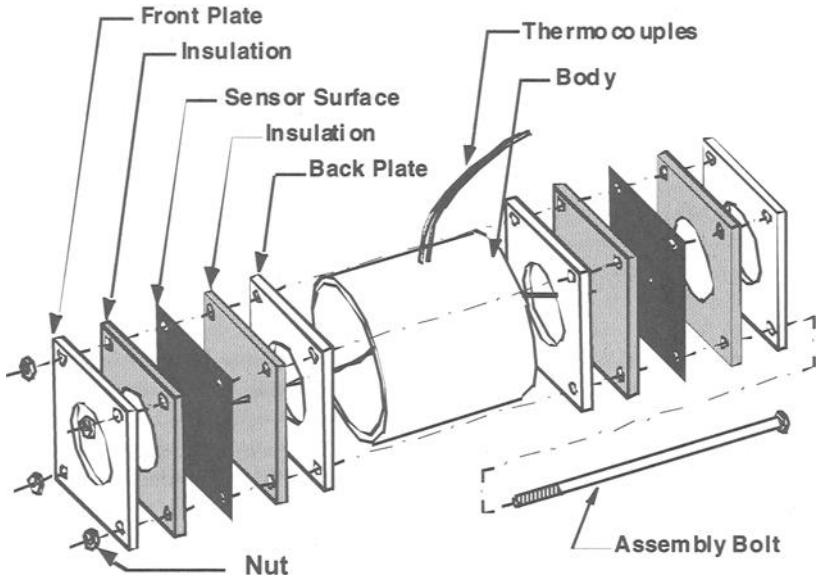

Figure 2 – *The Sandia HFG.*

Thermal Model

The heat balance on the heated surface of an idealized one-dimensional heat flux gauge (Figure 3) can be summarized in the following equation

$$\alpha q_{surf}(t) = \varepsilon \cdot q_{rad}(t) + q_{conv}(t) + q_{steel}(t) + q_{insul}(t) \quad (1)$$

where $q_{surf}(t)$ is the heat flux incident to the heated surface, $q_{rad}(t)$ represents the heat re-radiated from the sensor surface, $q_{conv}(t)$ is the convective heat loss at the sensor surface, $q_{steel}(t)$ is the sensible heat stored in the thin 304 stainless steel sensor plate, and $q_{insul}(t)$ represents the heat conducted into the insulated backing. Absorptivity and emissivity of the steel surface are represented by α and ε, respectively.

To implement this model in a data reduction scheme, each one of the loss terms is related to the instantaneous temperature of the sensor plate. Since the data is normally

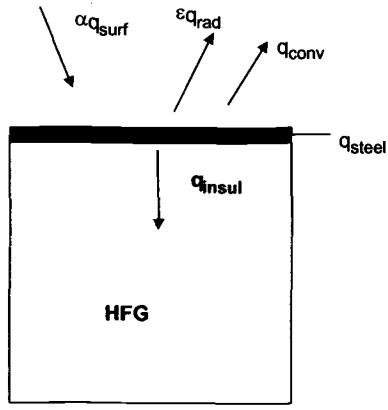

$$q_{surf} = q_{rad} + q_{conv}/\alpha + q_{steel}/\alpha + q_{insul}/\alpha$$

Figure 3 – *The one-dimensional thermal model of the HFG.*

acquired digitally, and temperatures other than the observed sensor plate have to be considered, the following nomenclature is adopted. T_i^N is the temperature at the end of the N^{th} time step (corresponding to the time t_N) at the i^{th} location. The sensor plate corresponds to $i=1$, and increasing values of i are in-depth positions within the thermal insulation. Thus, T_1^N is the observed temperature of the sensor plate at time step N. In what follows, the loss terms are calculated in terms of T_1^N and added to provide a "reading" of the heat flux, $q(t_N)$, on the surface from the fire environment.

Re-radiation Loss Term - q_{rad}

The re-radiation term is based on the Stefan-Boltzmann law

$$q_{rad}(t_N) = \sigma \cdot (T_1^N)^4 \tag{2}$$

with $\sigma = 5.67 \times 10^{-11}$ kW/m^2 K^4.

Convective Loss Term - q_{conv}/α

The convection term is modeled as

$$\frac{q_{conv}(t_N)}{\alpha} = \frac{h(T_1^N - T_{amb})}{\alpha} \tag{3}$$

where the heat transfer coefficient h must be determined from knowledge of the gauge installation, the temperature of the ambient fluid in contact with the sensor face T_{amb}, and flow conditions over the surface.

Storage Loss Term - q_{steel}/α

The heat flux absorbed into the thin steel sensor plate is calculated using the surface plate thermocouple temperature derivative using a central difference, i.e.

$$\frac{q_{steel}(t_N)}{\alpha} = \frac{\rho \cdot C_p(T_1^N) \cdot L}{\alpha} \frac{dT_1^N}{dt} \approx \frac{\rho \cdot C_p(T_1^N) \cdot L}{\alpha} \cdot \frac{(-T_1^{N+2} + 8 \cdot T_1^{N+1} - 8 \cdot T_1^{N-1} + T_1^{N-2})}{12 \cdot (t_{N+1} - t_N)} \tag{4}$$

The 304 stainless steel sensor plate density and specific heat properties are temperature dependent and can be calculated using the following equation (temperature in K) [1].

$$\rho \cdot C_p(T) = 1215.769 + 14.969 \cdot T - 0.029 \cdot T^2 - 2.991\text{e-}5 \cdot T^3 - 1.472\text{e-}8 \cdot T^4$$

$$+ 2.818\text{e-}12 \cdot T^5 \quad \left[kJ/m^3/K\right] \tag{5}$$

L, the thin steel HFG sensor plate thickness is 0.0254 cm.

Insulation Loss Term - q_{ins}/α

The relation between the sensor plate temperature and the heat loss into the insulation is obtained by considering the response of the surface of a thick wall subject to a time varying temperature on one surface and perfect insulation on the other surface. An algorithm for calculating the heat flux into the insulated backing given the thermocouple response at the surface has been derived by numerically modeling the transient thermal response of the insulating material. The one-dimensional heat conduction equation with no internal heat generation and temperature dependent properties is written as

$$\rho c_p \frac{\partial T(z,t)}{\partial t} = \frac{\partial}{\partial z} k \frac{\partial T(z,t)}{\partial z} \tag{6}$$

where k, ρ, and c_p are functions of the temperature field. This equation can be cast in finite difference form as follows (time is designated as superscript *N* and location as subscript *i*)

$$\rho_i c_{p_i} \frac{T_i^{N+1} - T_i^N}{dt} = \frac{k_{i-1/2}}{dz_{i+1}} T_{i-1}^{N+1} - \left(\frac{k_{i-1/2}}{dz_{i+1}} + \frac{k_{i+1/2}}{dz_i} \right) T_i^{N+1} + \frac{k_{i+1/2}}{dz_i} T_{i+1}^{N+1}. \tag{7}$$

Note that the conductivity is evaluated at the average mid-point temperature between nodes while density and specific heat are evaluated at the nodal temperature for the preceding time step. This equation is implicit since the heat flux (right hand side of the equation) is evaluated at the advanced time step *N+1*. This equation results in the following linear system of equations.

$$
\begin{aligned}
c_{1,1}T_1 + c_{1,2}T_2 &= d_1 \\
c_{2,1}T_1 + c_{2,2}T_2 + c_{2,3}T_3 &= d_2 \\
c_{3,2}T_2 + c_{3,3}T_3 + c_{3,4}T_4 &= d_3 \\
&\cdots \\
c_{i,i-1}T_{i-1} + c_{i,i}T_i + c_{i,i+1}T_{i+1} &= d_i \\
&\cdots \\
c_{I-1,I-2}T_{I-2} + c_{I-1,I-1}T_{I-1} + c_{I-1,I}T_I &= d_{I-1} \\
c_{I,I-1}T_{I-1} + c_{I,I}T_I &= d_I
\end{aligned}
\tag{8}
$$

In these equations, the coefficients c are functions of material properties (and time step along the diagonal), the values of d are functions of material property, time step, and the temperature at the preceding time step, and the vector T is the temperature field at the end of the time step. This system is a tri-diagonal set of equations, which can be solved by Gaussian elimination. The resulting algorithm can then be summarized with the following set of equations.

$$T_I = \gamma_I$$

$$T_i = \gamma_i - \frac{c_{i,i+1}T_{i+1}}{\beta_i}, \quad i = I-1, I-2, \ldots, 1 \tag{9}$$

$$\beta_1 = c_{1,1} \quad \gamma_1 = d_1 / \beta_1$$

$$\beta_i = c_{i,i} - \frac{c_{i,i-1}c_{i,i+1}}{\beta_{i-1}}, \quad i = 2,3,\ldots,I$$

$$\gamma_i = \frac{d_i - c_{i,i-1}\gamma_{i-1}}{\beta_i}, \quad i = 2,3,\ldots,I$$

The nodalization is chosen such that node spacing is much finer near the heated surface than through the bulk of the insulation. This objective is achieved by prescribing a geometrically increasing node spacing, i.e.

$$dz_i = dz_{i-1}r^i \tag{10}$$

For 20 nodes, and r = 1.2, and 7.62 cm Kaowool® insulation thickness, the nodalization is shown in Figure 4.

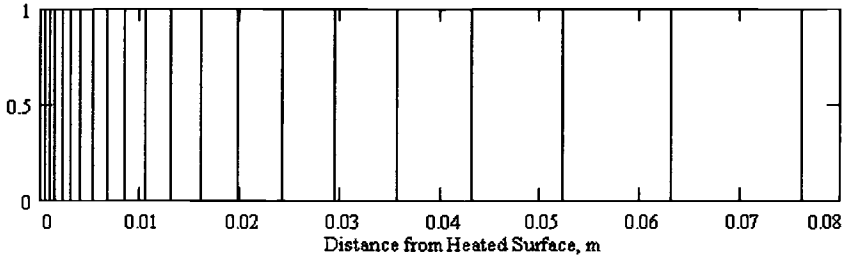

Figure 4 – *A 20-node nodalization.*

Note that the number of nodes and the geometric ratio, r, can be varied to optimize the nodalization. When the number of nodes is very large, care should be taken in selecting the ratio r, since a large ratio will result in very large nodes through the bulk of the insulation. When r = 1, the nodalization collapses to the uniform case.

Thermal properties are evaluated from polynomial curve fits to the manufacturer's data. For 128 kg/m^3 (8 lb/ft^3) Kaowool® blanket (typically used interchangeably with Cerablanket® in the SNL HFG)

$$k(T) = -6.05 \cdot 10^{-3} + 6.98 \cdot 10^{-5} T + 1.04 \cdot 10^{-7} T^2 \quad [kW/m/K] \qquad \text{and}$$

$$\rho c_p(T) = 128 \cdot (739.72733 + .2483608T) \quad [J/m^3/K] \qquad (11)$$

as plotted in Figure 5 and Figure 6. Note that Kaolin is the raw, mineral material melted to form the fibers of both the Kaowool® and Cerablanket® insulation. Because temperatures at the surface of the heat flux gauge can vary widely in a fire test and thermal properties, such as thermal conductivity in particular, are strongly dependent on temperature, it is important to use temperature-dependent properties in this evaluation.

For data reduction, this algorithm is implemented in a computer subroutine, which calculates the temperature field in the insulation at the end of a time step for a prescribed temperature boundary condition on the heated surface. The instantaneous thermocouple reading is used as the surface boundary condition to the insulation. Since the insulation is assumed to be thick, an adiabatic boundary condition is chosen for the opposite side. For the single sided gauge, this surface is located at a distance equal to the total length of the gauge. For the double-sided gauge, this surface is located at a distance equal to half the length of the actual gauge.

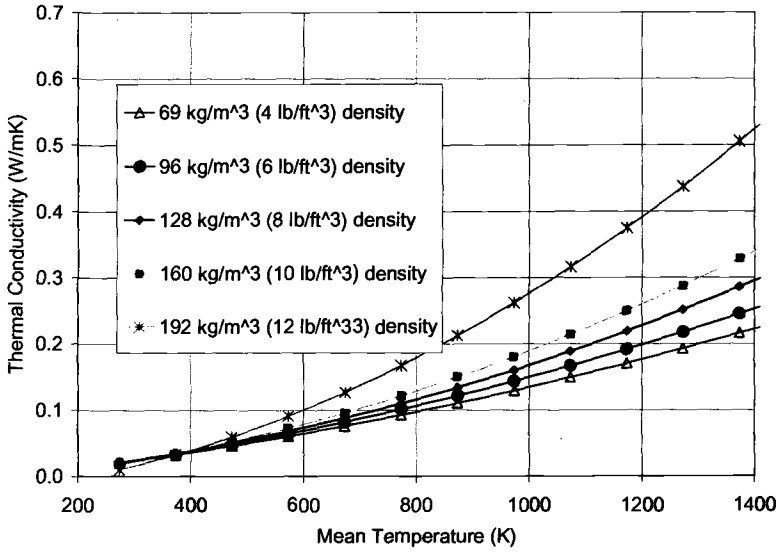

Figure 5 – *Thermal conductivity of Kaowool® at various blanket densities.*

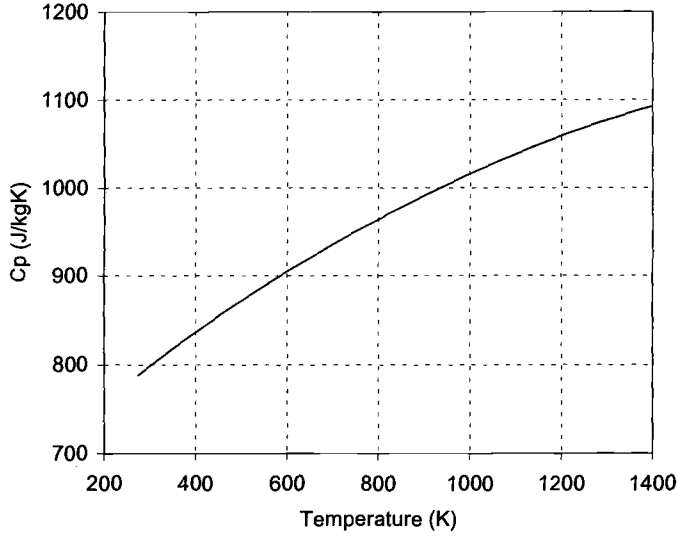

Figure 6 – *Specific heat of Kaolin.*

The heat flux to the insulation is then calculated from the derived temperature field by taking the derivative of the temperature gradient at the surface, i.e.

$$\frac{q_{ins}(t_N)}{\alpha} = \frac{k(T^N_{1+1/2})}{\alpha} \cdot \frac{(T^N_1 - T^N_2)}{dz_1}. \tag{12}$$

Data Reduction - $q_{surf}(t_N)$

Summing the losses for any time, t_N, results in

$$q_{surf}(t_N) = \sigma \cdot \left(T^N_1\right)^4 + \frac{h \cdot \left(T^N_1 - T_{amb}\right)}{\alpha}$$

$$+ \frac{\rho \cdot C_p(T^N_1) \cdot L}{\alpha} \cdot \frac{(-T^{N+2}_1 + 8 \cdot T^{N+1}_1 - 8 \cdot T^{N-1}_1 + T^{N-2}_1)}{12 \cdot (t_{N+1} - t_N)}$$

$$+ \frac{k(T^N_{1+1/2})}{\alpha} \cdot \frac{(T^N_1 - T^N_2)}{dz_1} \tag{13}$$

where T^N_1 is the thermocouple reading in K at the N^{th} time step. $T^N_{1+1/2}$ and T^N_2 are determined by running the thick wall subroutine using T^{N-1}_i as the initial values.

Microsoft® Visual Basic macros have been written to perform heat flux gauge analysis for data in MS Excel® spreadsheets. The subroutine *hflux* calculates the various heat flux terms found in the energy balance to arrive at a total incident heat flux. Time and temperature arrays are passed to this subroutine as real arrays in the argument list, and the incident heat flux is returned as a real array. The dimension of the arrays is calculated within *hflux* and variable array sizes are allowed.

Currently there are certain assumptions or specifications inherent in these macros that may be peculiar to the specific heat flux gauges tested, i.e.:

- The stainless steel sensor plate is .0254 cm thick;
- The emissivity, ε, of the sensor plate is .85;
- ρc_p for the sensor plate is specified for 304 stainless steel;
- Convection is modeled with a specific expression (discussed below) that is not applicable in a general sense; and
- The insulation is a 7.62-cm-thick Kaowool® blanket.

Heat losses to the insulation are calculated in the subroutine *insul* as described in the preceding section. Currently the insulation is modeled as 7.62-cm-thick Kaowool® blanket material and transverse heat losses are ignored, i.e., one-dimensional heat transfer. The model has 20 nodes that are geometrically spaced with a ratio of 1.2.

Model Validation

Experimental Setup and Operation

To validate the model, we chose to subject the gauge to a step input of radiant heat flux to a level commensurate with that found in typical fire experimentation. Response to a step input is particularly desirable in that shortcomings in the data reduction technique are revealed, and global characteristics of interest such as instrument order and response time are directly observable.

To accomplish the step input, the HFG was placed below and facing up into a heated cavity whose walls are maintained at a constant temperature (Figure 7). The cavity, 1 m in diameter by 1.3 m deep, is formed from a cylindrically shaped Inconel shroud with heat lamps directed toward the outside of the shroud to control the temperature of the cavity. A cover is placed over the HFG while the cavity is brought to the desired temperature (typically 1000°C). The step input to the HFG is initiated by removing the cover. A Gardon gauge is positioned next to the HFG to observe the same flux and provide a standard for comparison.

Figure 8 shows the average temperature of the shroud and the response of the Gardon gauge as a function of time. In that figure, heating of the cavity began at about three minutes and steady state at 1000°C was achieved at about seven minutes. At that time, the gauges were uncovered resulting in a step change in heat flux from 0 to about 110 kW/m^2. This flux level was held constant for a 30 minute period, at which time the gauges were covered and the power to the heat lamps turned off. Further details on the setup and operation of this system are given in [2].

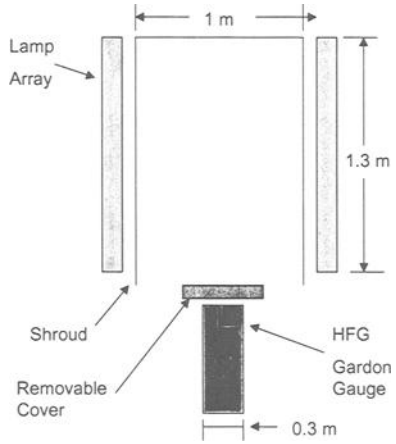

Figure 7 – *Experiment setup for realizing a step increase of radiant heat flux to the HFG.*

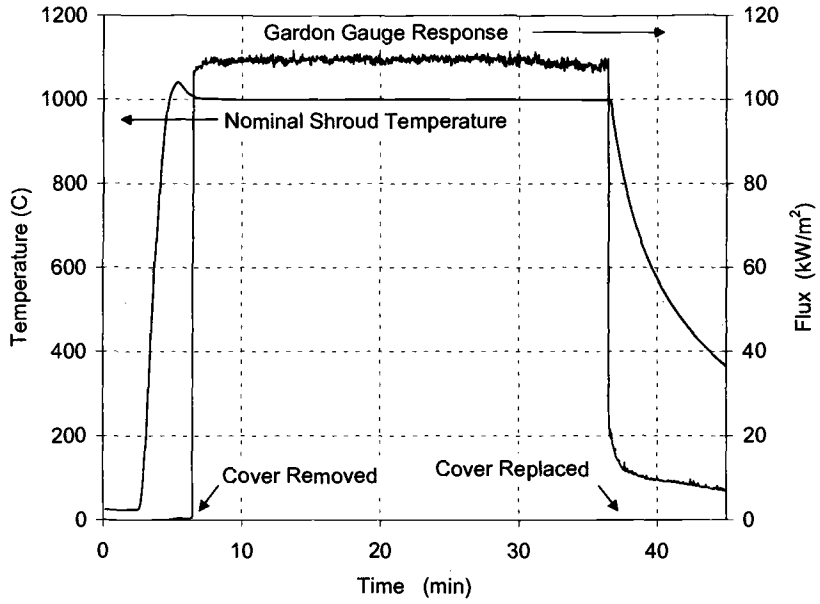

Figure 8 – *Operation of the experimental setup showing the heat-up of the cavity and the step input of heat flux as recorded by the Gardon gauge.*

Correction for Convective Heat Transfer

For comparing the Gardon reading to the HFG response, the convection heat transfer between the ambient air in the cavity and the Gardon gauge must be taken into account. To do this, it is assumed that a convection cell forms in the cavity as shown in Figure 9.

The general correlation shown in Figure 9 has been developed for vertical surfaces, but is directly applicable to an upward facing surface that is being heated by the flow [3]. Evaluating the general correlation for an air temperature of 1000°C and a surface size of 0.3 m (nominal size of the pedestal holding the gauges) gives results shown in Figure 10.

For purposes in this experimentation, it is convenient to fit the results to a curve:

$$h = \frac{\left(21.02 - 0.002144 \cdot T \cdot \ln(T)\right)^{\frac{1}{2}}}{1000} \cdot \frac{kW}{m^2 \cdot K} \quad \text{for } T \text{ in } K. \tag{14}$$

It is worth pointing out that this curve is valid only for the experimental setup and is not intended for use in application of the HFG in other flow situations.

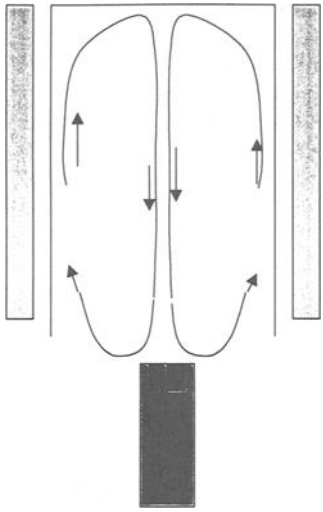

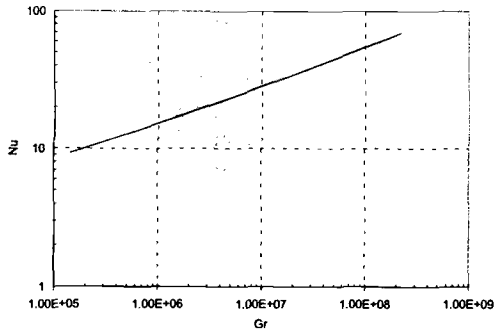

$$Nu^{\frac{1}{2}} = 0.825 + \frac{0.387 \cdot (Gr \cdot Pr)^{\frac{1}{6}}}{\left[1 + \left(\frac{0.492}{Pr}\right)^{\frac{9}{16}}\right]^{\frac{8}{27}}}$$

Churchill-Chu General Correlation for
Flat Plate Free Convection

Figure 9 – *An assumed convection cell in the test cavity results in convective heat transfer from the air to the gauges located in the mouth of the cavity.*

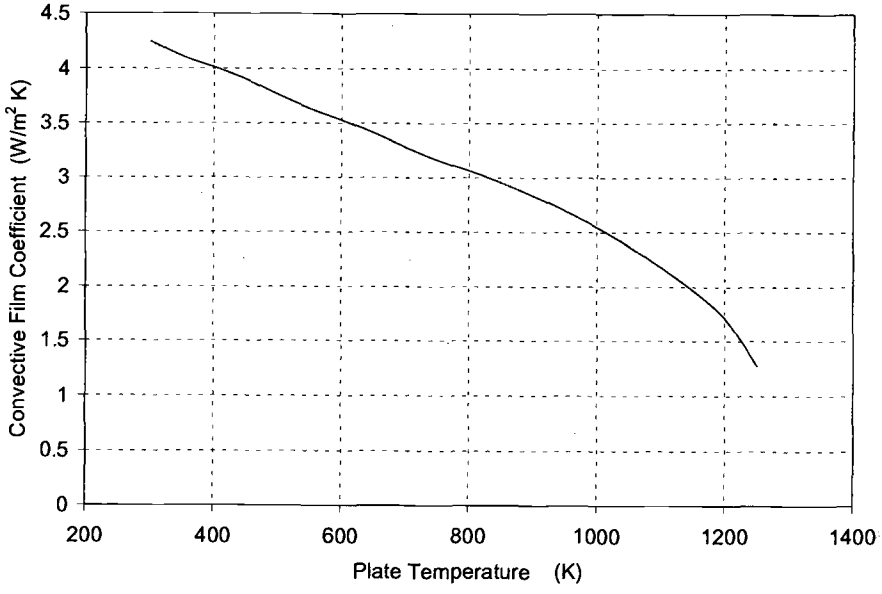

Figure 10 – *Estimated convective heat transfer coefficient for a surface facing up into the cavity as a function of surface temperature (air temperature = 1000°C).*

Radiant Heat Flux Step Input

Figure 10 indicates that the Gardon response in the experiment can be corrected for the convective contribution by subtracting 4 kW/m^2, since the Gardon gauge is water cooled and operated at about 400 K. Because the Gardon gauge is calibrated using a purely radiative source to provide a measurement of incident flux, the Gardon gauge surface absorptance (≅0.85) has to be applied to the correction value (4/0.85 = 4.7). The uncertainty in this correction value is about 50%.[1] Thus, the radiant heat flux step input to the HFG is taken to be

$$(Gardon\ Response - 4.7) \pm 2.4\ kW/m^2 \tag{15}$$

and a plot of it is shown in Figure 11.

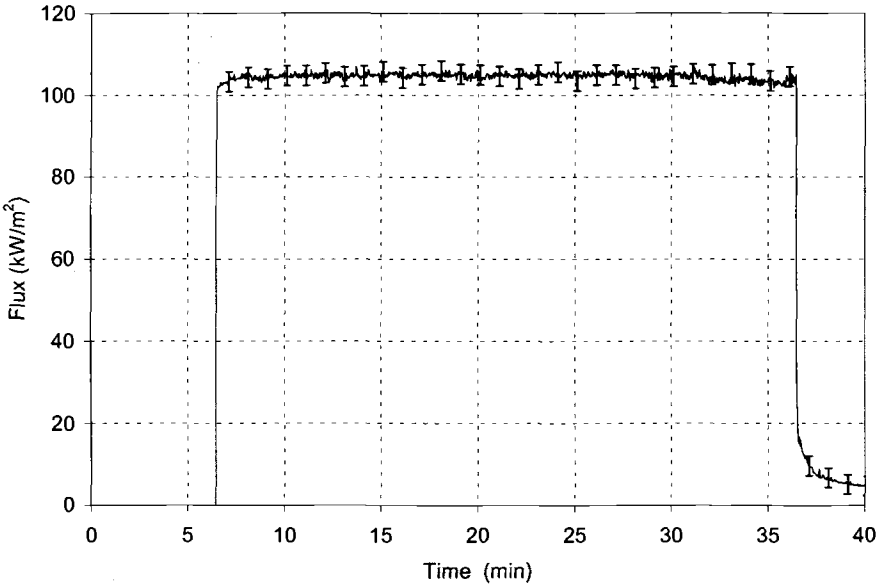

Figure 11 – *Step input of radiant heat flux to the HFG.*

HFG Response

The incident heat flux for the heat flux gauge test, as determined by the Gardon gauge and HFG, is plotted in Figure 12. The various heat losses to the insulation (q_{ins}/α), the sensible heat stored in the sensor plate (q_{steel}/α), heat re-radiated from the steel cover (q_{rad}), and convective heat losses (q_{conv}/α) for the SNL HFG are also plotted in Figure 12.

[1] Nicolette, V., Private Communication, Org. 9132, Sandia National Laboratories, Albuquerque, NM.

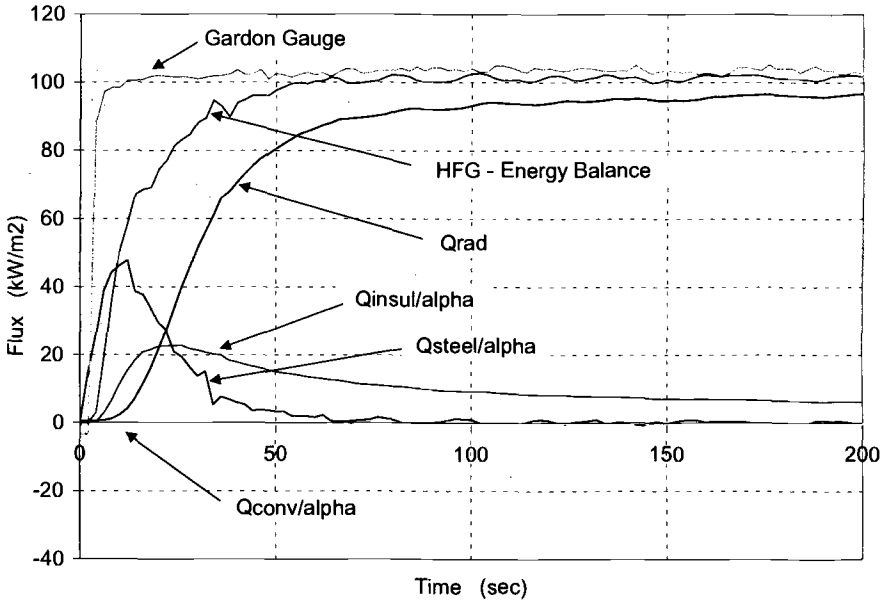

Figure 12 – *Measured versus calculated incident heat flux.*

Temperature profiles calculated in the insulation for the calibration test are plotted in Figure 13. Note that for this insulation thickness, saturation has not occurred even at 1700 seconds. The numerical technique described in this paper provides a convenient means of modeling heat losses to the insulating material yielding improved agreement between measured and imposed heat flux. As seen in Figure 14, heat losses to the insulation are significant at times long after the storage term (sensible heat of the steel cover) has become negligible. By modeling heat losses to the insulation, the time response of the heat flux gauge is greatly improved. It is believed that the difference between the Gardon gauge response and the HFG response early on (< 40 sec) is due to the thermocouple attachment to the HFG sensor plate since this is a known source of time lag and has not been accounted for in the model.

Uncertainty

The uncertainty has been found to be a function of the flux level, rate of change of flux level, time, and heating history. Thus, it is not appropriate to report the uncertainty as a single percentage value, rather, it is required to report it point by point as an observational error bar. As an example, our estimate of the uncertainty of the measurement realized with the flux step input is shown in Figure 15. The measurement as determined from the response of the thermocouple via the response model is indicated with a solid blue line in that figure. The upper and lower bounds of the uncertainty are indicated with horizontal tick marks. These bounds were determined from the

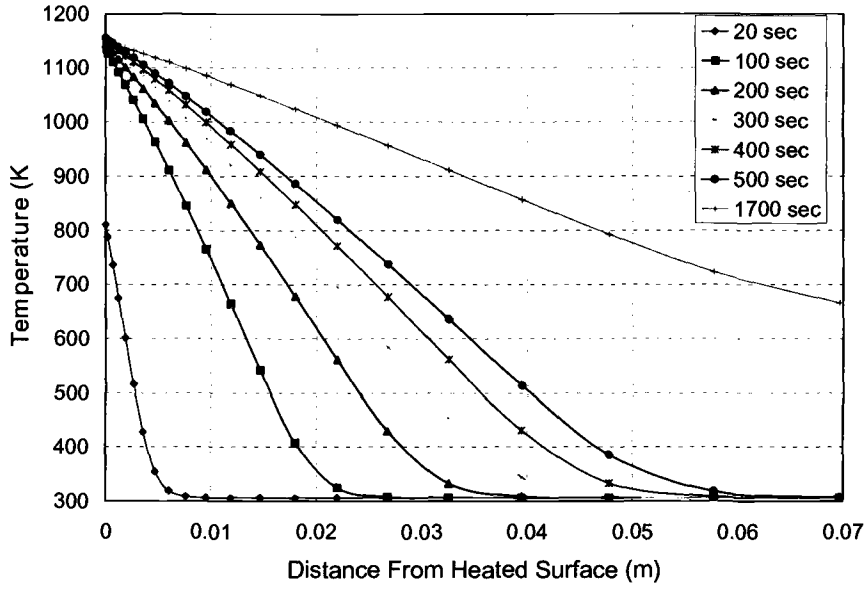

Figure 13 – *Calculated temperature profile in Kaowool® insulation.*

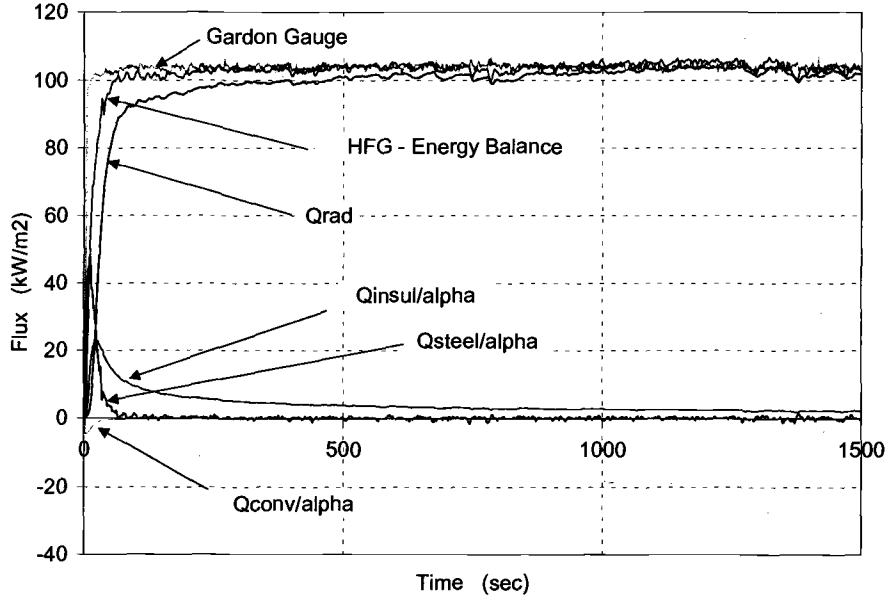

Figure 14 – *Long-term insulation heat loss.*

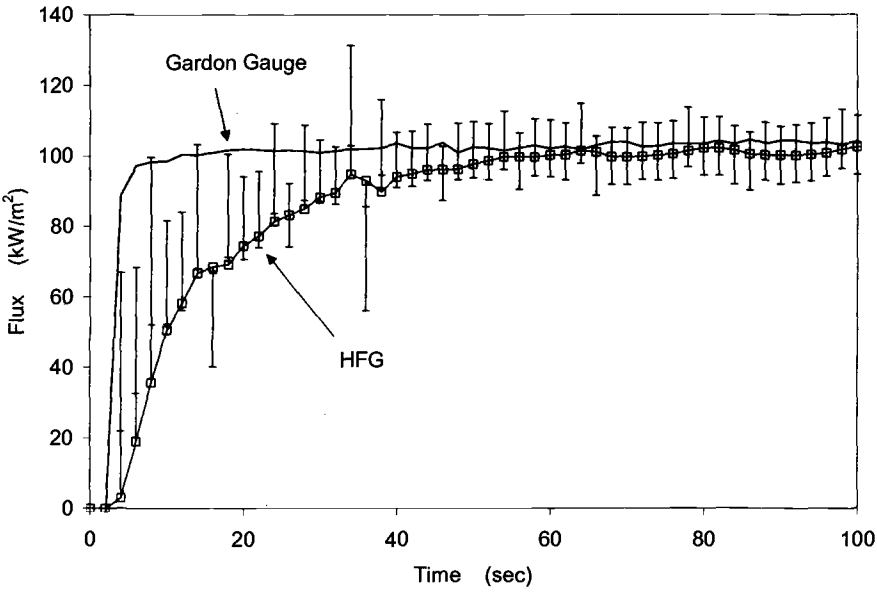

Figure 15 – *Estimate of the uncertainty of measurement of the step input.*

uncertainty model that is developed in the following sections. For comparison purposes, the input incident heat flux as recorded by the Gardon gauge is also shown in Figure 15.

In application, the slow response of the gauge means the heat flux measurement is likely to be unreliable during and after fluctuations in flux. Nearly one minute is required before the measured flux approaches the steady state value of the step input. However, it can be seen the uncertainty is relatively large during the early times of the response to the step input, and approaches a constant value as the gauge comes to equilibrium with the step input. This can be used to advantage in assessing heat flux measurements in actual fires. Figure 1 shows a five-minute segment of a measurement made in a 5 m outdoor pool fire with a HFG facing upward and located near the fuel pool surface. The heat flux varied with time during this test, presumably because of wind shifts, and is typical of most fire data. The error bars shown are calculated from the uncertainty model and their variation with the flux level, rate of change of flux level, time, and heating history are evident. Times of near constant uncertainty signal the attainment of steady-state where the measurement can be assumed valid.

Uncertainty Model

Uncertainty in the heat flux measurement arises from: (1) uncontrolled variability in the gauge characteristics, (2) missing physics in the model, and (3) simplifying assumptions taken on in formulating the instrument response model. The uncontrolled variability includes material thermal properties, geometrical dimensions, data acquisition system hardware, thermocouple uncertainty, etc. Examples include the specific heat and thickness of the stainless steel sensor plate. Estimating uncertainty from this source is

relatively straightforward, requiring only knowledge of the variability of the properties and dimensions. As for the missing physics, these phenomena are commonly buried under empirical constants that are created to bring the modeled instrument response into agreement with the observed experimental response to a known input. An example of this would be the empirically determined time constant derived to account for the thermocouple attachment to the HFG sensor plate. Simplifying assumptions include either sub-scale phenomena or phenomena believed to be of secondary importance. An example of the former is the assumption of no temperature gradient through the sensor plate; and of the latter, the assumption of negligible lateral conduction in the gauge. Uncertainties arising from this source are usually set to zero and justified by appealing to more complicated models or experimental evidence. Here, we adopt the same approach for the sensor plate, however, we do attempt to account for the effect of making the 1-D assumption.

Uncontrolled Variability – The uncontrolled variability includes material thermal properties and geometrical dimensions. Estimating uncertainty from these sources is straightforward by evaluating:

$$\delta U_{UV}^2 = \sum_{e=1}^{14} \left(\frac{\partial q_{surf}}{\partial S_e} \cdot \delta S_e \right)^2 \tag{16}$$

where the first seven sources S_e, the sensitivities $\frac{\partial q_{surf}}{\partial S_e}$, and the source uncertainties δS_e are identified in Table 1 (the other seven sources are identified in a following section entitled Missing Physics).

The sensitivity terms in the table are obtained by performing the indicated partial differentiations on the data reduction expression

$$q_{surf}(t_N) = \sigma \cdot \left(T_1^N\right)^4 + \frac{q_{conv}}{\alpha} + \frac{\rho \cdot C_p(T_1^N) \cdot L}{\alpha} \cdot \frac{(-T_1^{N+2} + 8 \cdot T_1^{N+1} - 8 \cdot T_1^{N-1} + T_1^{N-2})}{12 \cdot (t_{N+1} - t_N)} + \frac{q_{ins}}{\alpha} \tag{17}$$

The source term uncertainties for the first four sources are simply fixed percentages of the pertinent term. For example, the uncertainty in the sensor plate thickness L is taken to 20%, the uncertainty in $\rho \cdot C_p$ is 5%, and so on.

The uncertainty of the derivative, $\frac{dT_1^N}{dt}$, is due to random noise introduced to the recorded temperature time history via the data acquisition system. The noise is constant at 0.1°C regardless of the temperature reading. Its impact on the uncertainty of time derivative is found from

$$\delta\left(\frac{dT_1^N}{dt}\right) = \sqrt{\sum_{i=N-2}^{N+2}\left[\frac{\partial\left(\frac{dT_1^N}{dt}\right)}{\partial T_1^i}\cdot 0.1\right]^2} = \frac{0.1\cdot\sqrt{130}}{12\cdot(t_{N+1}-t_N)} \tag{18}$$

For the uncertainty of the term, $\frac{q_{ins}}{\alpha}$, the data reduction model was run with 20% changes in the thermal properties of the insulating material and it was found the maximum effect on the calculated heat flux was less than 3%; hence the uncertainty level has been conservatively set at the 3% value.

The uncertainty due to convection is more difficult to evaluate as it is dependent on the actual installation of the gauge in use. The flow conditions and local gas temperatures (which in practice are not known) contribute to this uncertainty. VULCAN calculations have indicated in general convective fluxes in fires are about 3% of the radiant flux [4], although this can vary with location. Therefore, the value of 3% of the radiant flux has been adopted for the uncertainty value.

Table 1 – *Uncontrolled variability as uncertainty sources.*

e	**Source** S_e	**Sensitivity** $\frac{\partial q_{surf}}{\partial S_e}$	**Source Uncertainty** δS_e
1	L	$\frac{\rho\cdot C_p(T_1^N)}{\alpha}\frac{dT_1^N}{dt}$	$0.20\,L$
2	$\rho\cdot C_p$	$\frac{L}{\alpha}\frac{dT_1^N}{dt}$	$0.05\rho\cdot C_p(T_1^N)$
3	α	$-\frac{\rho\cdot C_p(T_1^N)\cdot L}{\alpha^2}\frac{dT_1^N}{dt}$	0.05α
4	T_1	$4\cdot\sigma\cdot(T_1^N)^3$	$0.05\cdot T_1^N$
5	$\frac{dT_1^N}{dt}$	$\frac{\rho\cdot C_p(T_1^N)\cdot L}{\alpha}$	$0.10\cdot\sqrt{\frac{130}{144\cdot(t_{N+1}-t_N)^2}}$
6	$\frac{q_{ins}}{\alpha}$	1.0	$0.03\cdot q_{surf}$
7	$\frac{q_{conv}}{\alpha}$	1.0	$0.03\cdot q_{surf}$

Missing Physics – These phenomena are commonly buried under empirical constants that are created to bring the modeled instrument response into agreement with the observed experimental response to a known input. An example of this would be the empirically determined time constant derived to account for the thermocouple attachment to the HFG sensor plate.

It is known the thermocouple lags the sensor plate temperature due to the thermal mass of the thermocouple and the thermal resistance between the thermocouple and the plate. An experimental evaluation of the lag was accomplished by attaching an intrinsic junction thermocouple next to the existing thermocouple and exposing the HFG to a step input. The results are shown in Figure 16. In that figure, the temperature measured by the intrinsic junction is assumed to be the sensor plate temperature. It can be seen the difference between the thermocouple reading and the plate approaches 200°C.

Thermocouple lag is commonly corrected via a first order model that incorporates an empirical time constant

$$T_{Plate} = T_{TC} + \tau \cdot \frac{dT_{TC}}{dt} \tag{19}$$

The value of the time constant is found by plotting the difference between the plate and thermocouple versus the time rate of change of the thermocouple reading. This is shown in Figure 17, where it can be seen the value of τ is just over 5 seconds. The correction is then applied to the thermocouple reading and shown in Figure 16.

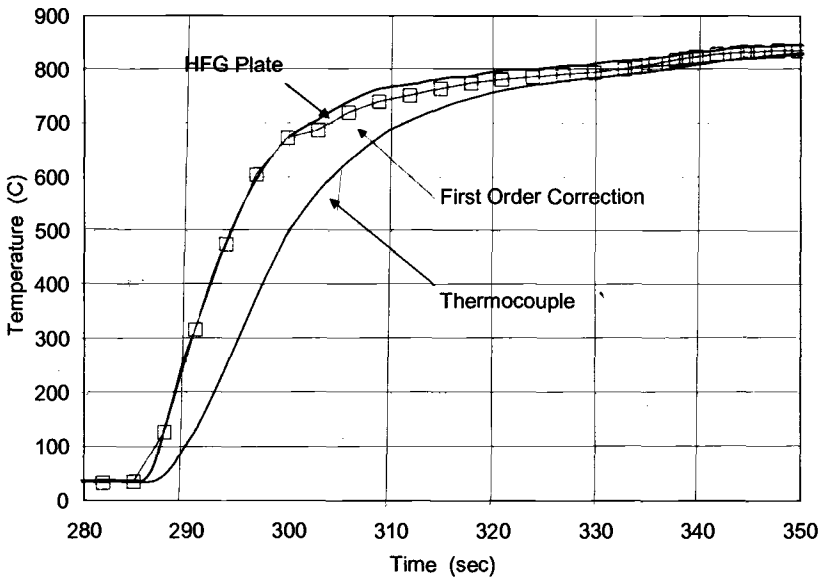

Figure 16 – *The thermocouple lags the actual plate temperature. The lag can be corrected with a first order model.*

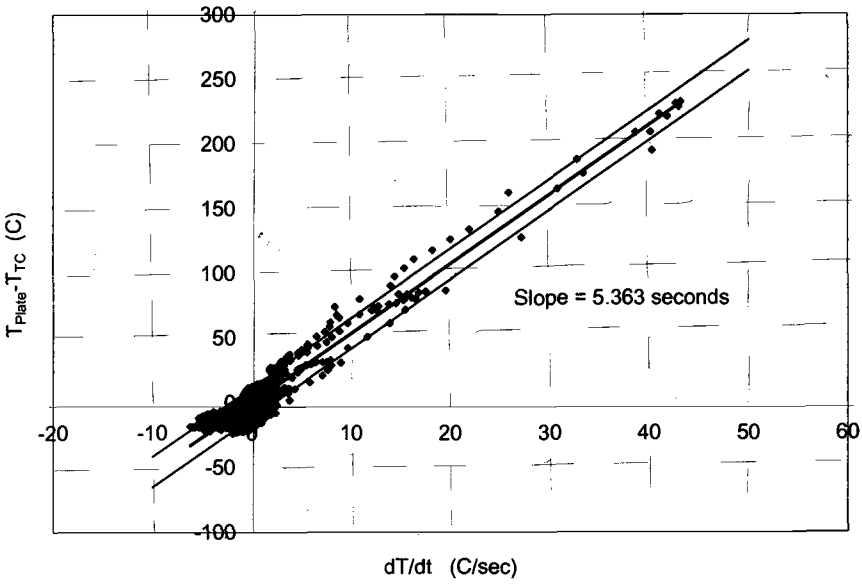

Figure 17 – *Experimental determination of the time constant for the first order correction to the thermocouple reading.*

The correction can be implemented into the data reduction scheme by substitution

$$q_{surf}(t_N) = \sigma \cdot \left(T_1^N + \tau \cdot \frac{dT_1^N}{dt} \right)^4 + \frac{q_{conv}}{\alpha} + \frac{\rho \cdot C_p (T_1^N + \tau \cdot \frac{dT_1^N}{dt}) \cdot L}{\alpha} \cdot \frac{d}{dt} (T_1^N + \tau \cdot \frac{dT_1^N}{dt}) + \frac{q_{ins}}{\alpha} \tag{20}$$

which after rearranging and assuming that $\rho \cdot C_p (T_I^N + \frac{dT_I^N}{dt}) \approx \rho \cdot C_p (T_I^N)$ gives

$$q_{surf}(t_N) = \sigma \cdot \left(T_1^N\right)^4 + \frac{q_{conv}}{\alpha} + \frac{\rho \cdot C_p (T_1^N) \cdot L}{\alpha} \cdot \frac{dT_1^N}{dt} + \frac{q_{ins}}{\alpha} + \frac{\rho \cdot C_p (T_1^N) \cdot L}{\alpha} \cdot \tau \cdot \frac{d^2 T_1^N}{dt^2} + \sigma \cdot \left[4 \cdot (T_1^N)^3 \cdot \tau \cdot \frac{dT_1^N}{dt} + 6 \cdot (T_1^N)^2 \cdot \tau^2 \cdot \left(\frac{dT_1^N}{dt} \right)^2 \right] + \sigma \cdot \left[4 \cdot T_I^N \cdot \tau^3 \cdot \left(\frac{dT_I^N}{dt} \right)^3 + \tau^4 \cdot \left(\frac{dT_I^N}{dt} \right)^4 \right] \tag{21}$$

which is seen to be the original response model plus a systematic correction for the thermocouple installation.

Normally, the systematic correction would be included in the response model. Here, we choose to put the correction in the uncertainty because it is based on τ, an empirical constant that covers the missing physics for the thermocouple installation. Therefore, a systematic error term for the missing physics is defined

$$\delta U_{MP} = \frac{\rho \cdot C_p(T_1^N) \cdot L}{\alpha} \cdot \tau \cdot \frac{d^2 T_1^N}{dt^2} + \sigma \cdot \left[4 \cdot (T_1^N)^3 \cdot \tau \cdot \frac{dT_1^N}{dt} + 6 \cdot (T_1^N)^2 \cdot \tau^2 \cdot \left(\frac{dT_1^N}{dt} \right)^2 \right]$$

$$+ \sigma \cdot \left[4 \cdot T_1^N \cdot \tau^3 \cdot \left(\frac{dT_1^N}{dt} \right)^3 + \tau^4 \cdot \left(\frac{dT_1^N}{dt} \right)^4 \right] \qquad (22)$$

The uncontrolled variance of the different sources enter into the total uncertainty via this error term as well. Table 2 shows the sources, sensitivities, and source term uncertainties as the remaining six entries for the total uncontrolled uncertainty expression.

Table 2 – *Uncontrolled variability as uncertainty sources from the systematic error term.*

e	**Source** S_e	**Sensitivity** $\frac{\partial q_{surf}}{\partial S_e}$	**Source Uncertainty** δS_e
8	L	$\frac{\rho \cdot C_p(T_I^N)}{\alpha} \cdot \tau \cdot \frac{d^2 T_I^N}{dt^2}$	$0.20\,L$
9	$\rho \cdot C_p$	$\frac{L}{\alpha} \cdot \tau \cdot \frac{d^2 T_I^N}{dt^2}$	$0.05 \rho \cdot C_p(T_I^N)$
10	T_I	$\sigma \cdot \left[12 \cdot (T_1^N)^2 \cdot \tau \cdot \frac{dT_1^N}{dt} \right]$ $+ \sigma \cdot \left[12 \cdot T_I^N \cdot \tau^2 \cdot \left(\frac{dT_I^N}{dt} \right)^2 + 4 \cdot \tau^3 \cdot \left(\frac{dT_I^N}{dt} \right)^3 \right]$	$0.05 \cdot T_I^N$
11	$\frac{dT_I^N}{dt}$	$\sigma \cdot \left[4 \cdot (T_1^N)^3 \cdot \tau + 12 \cdot \left(T_1^N\right)^2 \cdot \tau^2 \cdot \frac{dT_1^N}{dt} \right]$ $+ \sigma \cdot \left[12 \cdot T_I^N \cdot \tau^3 \cdot \left(\frac{dT_I^N}{dt} \right)^2 + 4 \cdot \tau^4 \cdot \left(\frac{dT_I^N}{dt} \right)^3 \right]$	$0.10 \cdot \sqrt{\frac{130}{144 \cdot (t_{N+1} - t_N)^2}}$

12	τ	$\frac{\rho \cdot C_p(T_1^N) \cdot L}{\alpha} \cdot \frac{d^2 T_1^N}{dt^2} + \sigma \cdot \left[4 \cdot (T_1^N)^3 \cdot \frac{dT_1^N}{dt} \right] + \sigma \cdot \left[12 \cdot (T_1^N)^2 \cdot \tau \cdot \left(\frac{dT_1^N}{dt} \right)^2 \right] + \sigma \cdot \left[12 \cdot T_1^N \cdot \tau^2 \cdot \left(\frac{dT_1^N}{dt} \right)^3 + 4 \cdot \tau^3 \cdot \left(\frac{dT_1^N}{dt} \right)^4 \right]$	$0.50 \cdot \tau$
13	$\frac{d^2 T_I^N}{dt^2}$	$\frac{\rho \cdot C_p(T_I^N) \cdot L}{\alpha} \cdot \tau$	$0.10 \cdot \sqrt{\frac{1414}{144 \cdot (t_{N+1} - t_N)^4}}$
14	α	$-\frac{\rho \cdot C_p(T_I^N) \cdot L}{\alpha^2} \cdot \tau \cdot \frac{d^2 T_I^N}{dt^2}$	$0.05 \cdot \alpha$

The sensitivities and source uncertainties are, as before, with only the time constant and the second derivative being new terms. The second derivative is approximated from a five-point central difference scheme as

$$\frac{d^2 T_I^N}{dt} = \frac{-T_I^{N+2} + 16 \cdot T_I^{N+1} - 30 \cdot T_I^N + 16 \cdot T_I^{N-1} - T_I^{N-2}}{12 \cdot (t_{N+1} - t_N)^2} \tag{23}$$

which allows the source term uncertainty to be calculated as explained in the previous section.

Simplifying Assumptions – Simplifying assumptions include either sub-scale phenomena or phenomena believed to be of secondary importance. Three assumptions have been adopted in formulating the gauge thermal response model: (1) negligible temperature gradient through the sensor plate, (2) the sensor plate surface emissivity and absorptivity are the same, i.e. $\frac{\varepsilon}{\alpha} = 1$, and (3) the heat conduction within the gauge is adequately modeled as 1-D. Uncertainties arising from these sources are usually set to zero and justified by appealing to more complicated models or experimental evidence. Here, we adopt this same approach for the sensor plate gradient, however, we do attempt to account for the effect of equating ε and α, and for making the 1-D assumption.

The effect of assuming the sensor is a lumped thermal mass is found by analyzing the dynamic response of a semi-infinite wall [4]. For Biot numbers less than 0.1, all temperatures through the thickness of the plate will be within a percentage f percent of the sensor plate temperature

where

$$f = 50 \cdot Biot\,\% \text{ of } T_N^I \tag{24}$$

and

$$Biot = \frac{h \cdot L}{k_s} \quad \text{with} \quad h \approx 4 \cdot \sigma \cdot (T_N^I)^3 \tag{25}$$

and k_s is the thermal conductivity of the sensor plate. This leads to

$$f(T_N^I) = 50 \cdot \frac{4 \cdot \sigma \cdot (T_N^I + 273)^3 \cdot L}{k_s} \quad \% \tag{26}$$

being the uncertainty of T_N^I due to the lumped mass assumption. To evaluate the expression, k_s is set to 0.03 kW/m K (nominal value for stainless steel) and L to 0.000254 m. For the worst case condition, $T_N^I \approx$ 1000°C, $f(T_N^I) \approx$ 0.2%, and there is no appreciable contribution to the uncertainty from the assumption of no temperature gradient through the sensor plate.

The assumption of equal ε and α is evaluated from

$$q_{surf}(t) = \frac{\varepsilon}{\alpha} \cdot q_{rad}(t) + \frac{q_{conv}(t) + q_{steel}(t) + q_{insul}(t)}{\alpha} \tag{27}$$

where the sensitivity is found to be

$$\frac{\partial q_{surf}(t)}{\partial\left(\frac{\varepsilon}{\alpha}\right)} = q_{rad}(t) = \sigma \cdot \left(T_I^N\right)^4 \tag{28}$$

The uncertainty in the ratio, $\delta\left(\frac{\varepsilon}{\alpha}\right)$, is estimated from measurements made on the normal emittance of Pyromark Black [5], the coating on the fire side of the sensor plate. Figure 18 shows that data, and it can be seen that the uncertainty in the ratio (i.e. hot source/cold surface or cold source/hot surface) is about 4%.

The systematic correction for the missing physics also generates an additional term to the simplifying assumptions uncertainty due to the ratio $\frac{\varepsilon}{\alpha}$. This additional term is included in the summary of the total uncertainty shown in Table 3.

To investigate the third assumption, time histories of two thermocouples installed in the insulation along the centerline of the gauge were recorded in the validation experiment. In comparing their response to the step input, it was noted that a 2-D conduction model gave better comparisons. However, the resulting flux from the front sensor plate was at most 5% higher than the flux determined from the 1-D model.

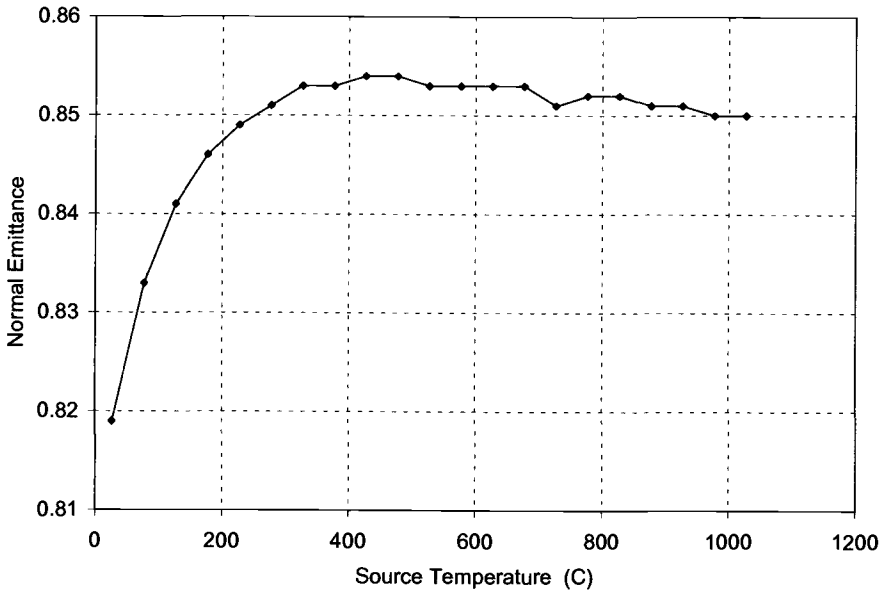

Figure 18 – *The normal emittance of Pyromark as a function of source temperature [5].*

Table 3 – *Simplifying assumptions as uncertainty sources.*

e	**Source** S_e	**Sensitivity** $\frac{\partial q_{surf}}{\partial S_e}$	**Source Uncertainty** δS_e
15	$\left(\frac{\varepsilon}{\alpha}\right)$	$\sigma \cdot \left(T_1^N\right)^4$	$0.04 \cdot \left(\frac{\varepsilon}{\alpha}\right)$
16	$\left(\frac{\varepsilon}{\alpha}\right)$	$\sigma \cdot \left[4 \cdot (T_1^N)^3 \cdot \tau \cdot \frac{dT_1^N}{dt} + 6 \cdot (T_1^N)^2 \cdot \tau^2 \cdot \left(\frac{dT_1^N}{dt}\right)^2\right]$ $+\sigma \cdot \left[4 \cdot T_1^N \cdot \tau^3 \cdot \left(\frac{dT_1^N}{dt}\right)^3 + \tau^4 \cdot \left(\frac{dT_1^N}{dt}\right)^4\right]$	$0.04 \cdot \left(\frac{\varepsilon}{\alpha}\right)$
17	*1-D*	1.0	$0.05 \cdot q_{surf}$

In the interest of parsimony, it was decided to maintain the 1-D model and add 5% to the uncertainty to account for the assumption. Thus, the total uncertainty for the simplifying assumptions becomes

$$\delta U_{SA}^2 = \sum_{e=14}^{16} \left(\frac{\partial q_{surf}}{\partial S_e} \cdot \delta S_e\right)^2 \quad . \tag{29}$$

Application to Validation Experiment – The expression for the total uncertainty is given as

$$\delta U = \delta U_{MP} \pm \sqrt{\delta U_{UV}^2 + \delta U_{SA}^2} \tag{30}$$

where:

$$\delta U_{MP} = \frac{\rho \cdot C_p(T_1^N) \cdot L}{\alpha} \cdot \tau \cdot \frac{d^2 T_1^N}{dt^2} + \sigma \cdot \left[4 \cdot (T_1^N)^3 \cdot \tau \cdot \frac{dT_1^N}{dt} + 6 \cdot (T_1^N)^2 \cdot \tau^2 \cdot \left(\frac{dT_1^N}{dt}\right)^2 \right]$$

$$+ \sigma \cdot \left[4 \cdot T_1^N \cdot \tau^3 \cdot \left(\frac{dT_1^N}{dt}\right)^3 + \tau^4 \cdot \left(\frac{dT_1^N}{dt}\right)^4 \right] \tag{31}$$

and

$$\delta U_{UV}^2 = \sum_{e=1}^{14} \left(\frac{\partial q_{surf}}{\partial S_e} \cdot \delta S_e\right)^2 \tag{32}$$

and

$$\delta U_{SA}^2 = \sum_{e=15}^{17} \left(\frac{\partial q_{surf}}{\partial S_e} \cdot \delta S_e\right)^2 \quad . \tag{33}$$

The relative importance of each source varies with time and are shown in Figure 19. In that figure, it can be seen at early times, the uncertainty due to the missing physics of thermocouple installation and the variability in the thickness of the sensor plate dominate. At later times when steady state is reached, the error due to the simplifying assumptions and the uncontrolled variability are most important. Referring back to Figure 15, it is of interest to see that during fast rise of the thermocouple, the uncertainty bars do not capture the reported "measured value." The same effect can also be seen in Figure 1. It can be deduced that this behavior is due to the correction term from the missing physics uncertainty.

Effect of Sampling Frequency on Calculated Error – The heat flux was calculated for the model validation experiment at three different sampling frequencies. The results, plotted in Figure 20 and Figure 21, indicate that the calculated heat flux and the associated error are dependent on the sampling frequency. The sampling frequency exercises effect in two ways. First, before the step change in heat flux, the 4-second and6-second sampling curves predict heat fluxes in advance of the Gardon gauge. This is because the time derivative uses data subsequent to the step change in heat flux in

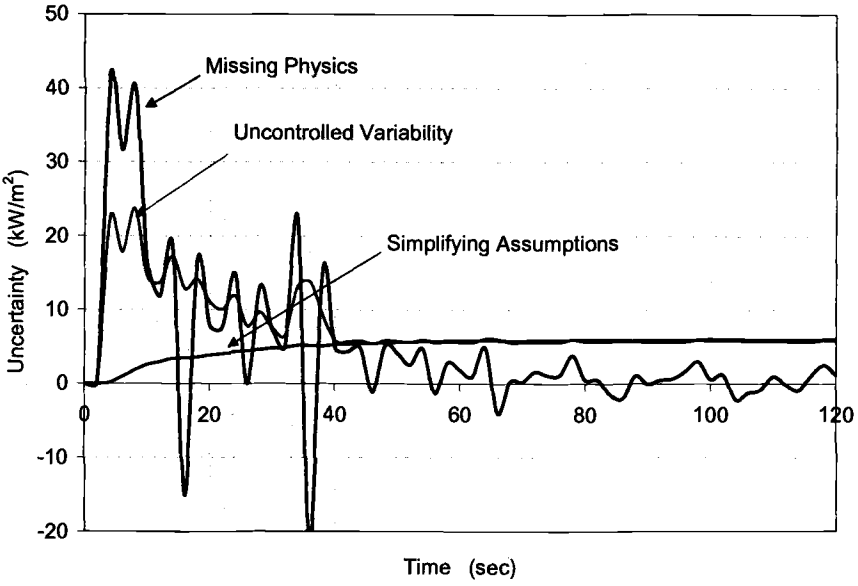

Figure 19 – *Relative importance of the different sources of uncertainty during a step input of 100 kW/m^2.*

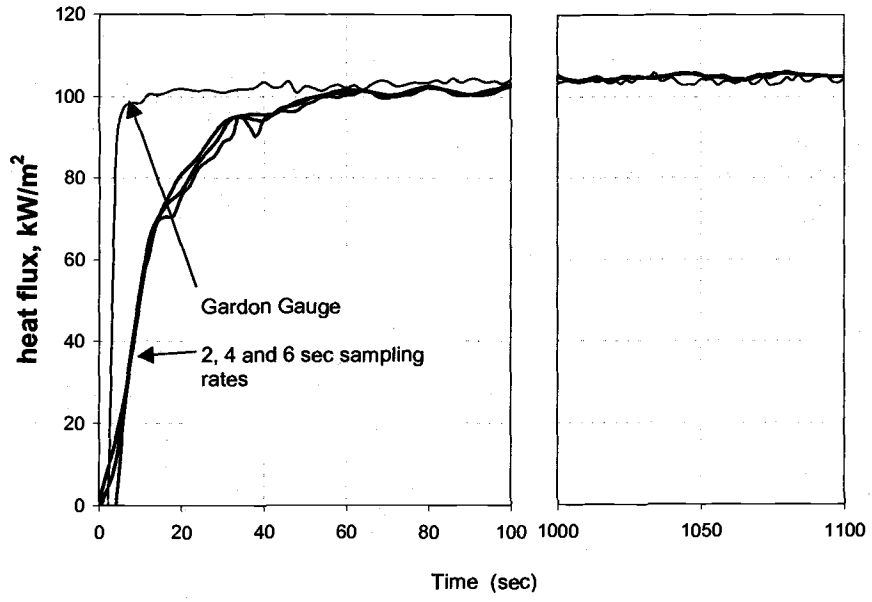

Figure 20 – *Heat flux calculated for various sampling frequencies.*

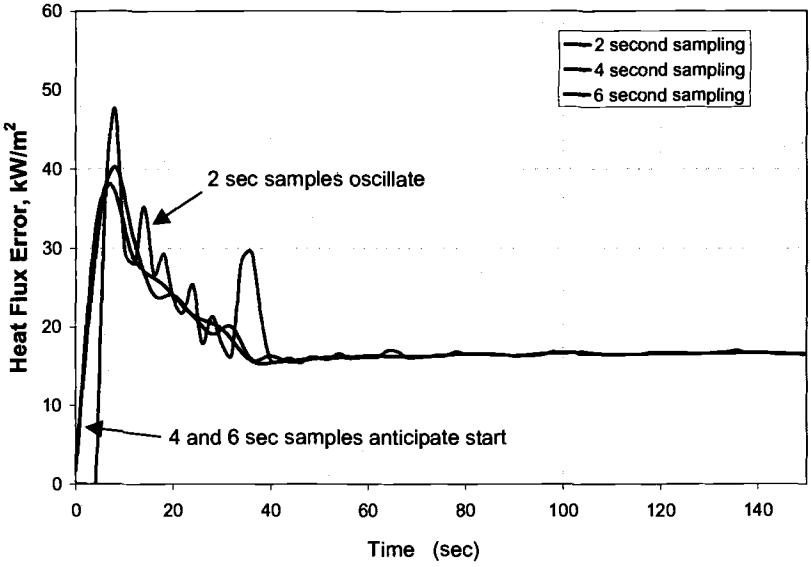

Figure 21 – *Heat flux error range calculated for various sampling frequencies.*

determining the temperature derivative. This "prediction" in the model is observed in the calculated uncertainty for these curves. The second effect appears later in time. As temperatures rise from the imposed heat flux, the 2-second sampling curve shows much larger oscillations in the calculated heat flux. This is reflected as increased uncertainty during the temperature rise. Both effects disappear at steady state; all three curves show agreement and the uncertainty becomes independent of the sampling rate.

The source of the uncertainty associated with sampling rate during high rates of change is the uncertainty contribution from the time derivative. This can be seen by considering a simple three-point central difference equation for the time derivative of temperature

$$\frac{dT}{dt} = \frac{(T_{N+1} - T_{N-1})}{(t_{N+1} - t_{N)}} \tag{34}$$

The equation for the associated uncertainty would be given by

$$\delta\left(\frac{dT_1^N}{dt}\right) = \sqrt{\sum_{i=N-2}^{N+2}\left[\frac{\partial\left(\frac{dT_1^N}{dt}\right)}{\partial T_1^i}\cdot 0.1\right]^2} = \frac{\sigma_T \cdot \sqrt{2}}{(t_{N+1} - t_N)} \tag{35}$$

Note that as the sampling frequency increases, (or $t_{N+1} - t_N$ decreases), the uncertainty in the time derivative also increases. The equation for the derivative is based on differences from discretely measured values of temperatures, each with statistical uncertainty that does not depend on the time step size. Therefore the noise associated with thermocouple measurement can result in excessive error in the derivative term for small time steps.

To reduce some of this error, the raw data can be filtered. In fact, the five-point central difference expression for computing the derivative used in this model represents such an error reduction technique. The error associated with the five-point central difference equation

$$\delta\left(\frac{dT_1^N}{dt}\right) = \sqrt{\sum_{i=N-2}^{N+2}\left[\frac{\partial\left(\frac{dT_1^N}{dt}\right)}{\partial T_1^i}\cdot 0.1\right]^2} = \frac{\sigma_T\cdot\sqrt{130}}{12\cdot(t_{N+1}-t_N)}, \tag{36}$$

is 33% less than the three-point central difference equation. However, the price for smoothing is an increase in the "prediction" source, as the five-point central difference will anticipate changes in rise rate.

In the final analysis, the sampling rate should be commensurate with the expected temperature rise rate and the end use of the time derivative. This is to say, the data sampling rate is an important parameter in the design and use of these heat flux gauges and merits special attention prior to incorporating them in any experiment.

Closure

It has been seen that the HFG is essentially a thin metal plate that responds to heating from the fire environment. A thermal model that describes the response has been advanced and it was shown how to determine the heat flux from the fire environment via the time-temperature history of the thin metal plate. A validation experiment was presented where the gauge was exposed to a step input of radiant heat flux. Comparison of the incident flux determined from the thermal model with the known flux input showed the gauge exhibited a noticeable time lag. The uncertainty of the measurement was analyzed, and an uncertainty model was put forth using the data obtained from the experiment. An empirical constant was found that compensated for the gauge time lag. This compensation was incorporated into the uncertainty model instead of the response model. As a result, the uncertainty does not capture the measurement at certain times due to the systematic error created by the missing physics.

We believe the missing physics model is incomplete and are not willing to include it in the response model. The out-of-bounds response is a signal to the user that the measurement is likely to be wrong because of the thermocouple installation. An example can be seen in Figure 1. There are alternating periods of rapidly changing heat flux and periods of steady heat flux. The uncertainty bars clearly show when it would be appropriate to use the data and when it would be better to ignore it.

If it were desirable to reduce the uncertainty, clearly the missing physics needs to be corrected. We do not believe that complicating the model with a detailed heat transfer analysis of the thermocouple installation is appropriate. The HFG should be modified so it physically meets the assumptions in the model. The obvious first step would be to replace the existing thermocouple with a fine wire intrinsic junction.

It is also felt that the early time discrepancy may be due in part to inadequate thermal properties of the insulation. These properties were developed from steady state measurements where small temperature differences are imposed across a known thickness. It is not known if properties determined this way are appropriate in dynamic heating situations with high gradients. A different insulation material may be more appropriate. Experiments, similar to the model validation step input test, will be required to verify improved response using the suggested design modifications and to revise the uncertainty model.

References

[1] Incropera, F., and DeWitt, D., *Fundamentals of Heat and Mass Transfer*, John Wiley & Sons, Inc., New York, 1995.

[2] Verner, D., and Blanchat, T.K., *Sandia Heat Flux Gage Calibration Experiment*, Sandia National Laboratories, Albuquerque, NM 87185, August 1998.

[3] White, F. M., *Heat and Mass Transfer*, Addison Wesley, New York, 1988.

[4] Kreith, F., *Principles of Heat Transfer*, Intext Educational Publishers, New York, 1976.

[5] Longenbaugh, R.S., L.C. Sanchez, and A.R. Mahoney, *Thermal Response of a Small Cask-Like Test Article to Three Different High Temperature Environments*, SAND88-0661, Sandia National Laboratories, Albuquerque, NM, 1988.

M. Alex Kramer,[1] *Miles Greiner,*[2] *J. A. Koski,*[3] *and Carlos Lopez*[4]

Uncertainty of Heat Transfer Measurements in an Engulfing Pool Fire

Reference: Kramer, M., A., Greiner, M., Koski, J. A., and Lopez, C., **"Uncertainty of Heat Transfer Measurements in an Engulfing Pool Fire,"** *Thermal Measurements: The Foundation of Fire Standards, ASTM STP 1427,* L. A. Gritzo and N. J. Alvares, Eds., ASTM International West Conshohocken, PA, 2002.

Abstract: A series of experiments were performed to measure heat transfer to a cylindrical steel calorimeter engulfed in a 30-minute pool fire. The calorimeter inner surface temperature history was measured at 46 locations. A one-dimensional inverse heat conduction technique was used to determine the net heat flux to the calorimeter as a function of time and location. The uncertainty in heat flux caused by three-dimensional effects is estimated using finite element computer simulations. A Monte Carlo uncertainty simulation is used to estimate the uncertainty in heat flux from propagated uncertainties in dimensions, temperature measurements, and material properties. The estimated uncertainty in the measured heat flux over the 30-minute fire test and the entire calorimeter was found to be ±18 kW/m2, or 27% of the average heat flux of 66.6 kW/m2. The uncertainties for the early times of the fire test are less than those at later times in the test due to the instability of the inverse conduction calculations caused by the Curie effect of the carbon steel calorimeter material.

Keywords: Heat Transfer, Pool Fire, Uncertainty, Inverse Heat Conduction, Engulfing, Finite Element, Heat Flux.

Background

The goal of this work was to measure heat transfer versus time and location to a massive cylindrical object engulfed in a round pool fire [1]. The object is roughly the same size as a high level nuclear waste package transported by tractor trailer truck. It is a 3800 kg (8400 lb) cylindrical carbon steel calorimeter of length L = 4.6 m (15 ft), diameter D = 1.2 m (4 ft), and wall thickness W = 2.54 cm (1 in). The entire setup was located above a 7 m (23 ft) diameter concrete fire pool at the Sandia National Laboratories Burn Site. The 30 minute fire was designed to comply with the 10CFR71.73 regulations [2] used to license such packages. The collected data is believed to be well suited for benchmarking fire simulation codes. Figure 1 (a) shows the calorimeter and the locations where thermocouples were attached to the interior surface. The right side of the section views is toward the west direction during the experiment. Figure 1 (b) shows the method used to attach the thermocouples to the calorimeter wall. Nichrome metal strips were spot welded to the calorimeter wall and were used to hold the thermocouple against the surface. The time response of the 1.6 mm diameter thermocouple is much faster than the response of the 2.54 cm thick calorimeter wall, therefore the thermocouple and interior wall surface are assumed to be isothermal. The interior of the calorimeter was insulated, allowing heat

1 Research Assistant, Mechanical Engineering Department M.S. 312, University of Nevada, Reno, NV 89557.
2 Professor, Mechanical Engineering Department M.S. 312, University of Nevada, Reno, NV 89557, greiner@unr.edu corresponding author.
3 Principal Member of Technical Staff, Sandia National Laboratories, P.O. Box 5800, Albuquerque, NM 87185-0718.
4 Member of Technical Staff, Sandia National Laboratories, P.O. Box 5800, Albuquerque, NM 87185-0718.

Fig 1 (a)

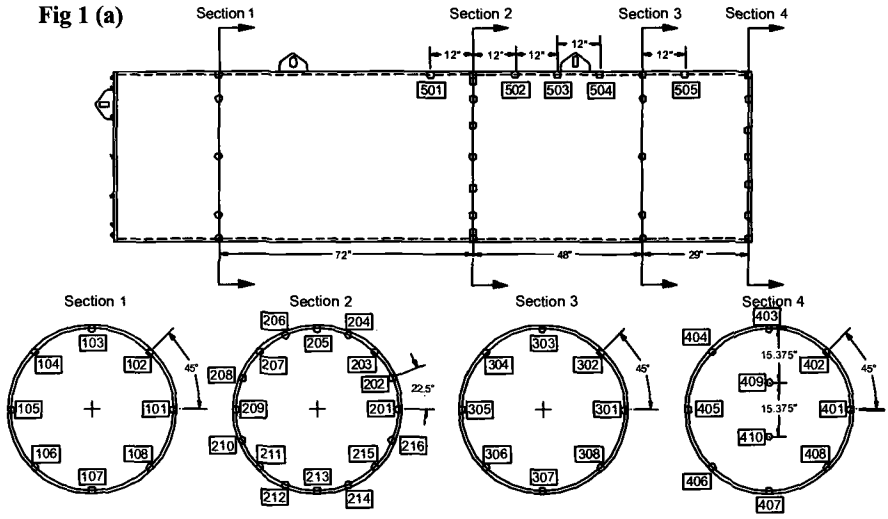

Fig 1 (b)

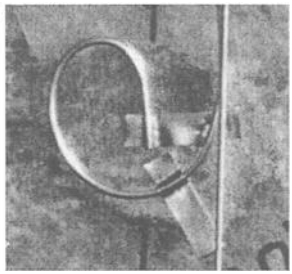

Figure 1. Thermocouple locations and mounting procedure. (a) shows the thermocouple locations on the calorimeter interior. (b) photograph of a thermocouple strapped to the calorimeter wall.

transfer inside the cylinder to be neglected.

Wind fences were used to shield the fire from the ambient wind. They were located in a circle of radius 12.2 m centered around the calorimeter. The wind direction and speed were monitored with propeller type anemometers attached to wind vanes. The measurements were taken outside of the wind fences due to the high temperatures inside the barriers. The anemometers were located 30 m (100 ft) to the northwest of the fire pool, with the intention of measuring the wind speed independent of the fire effects.

The Sandia One-Dimensional Direct and Inverse Thermal (SODDIT) code [3] was used to estimate the heat flux to the outer surface from the inner surface temperature measurements. Temperature versus time data, material properties (specific heat and thermal conductivity versus temperature and a constant density), and the dimensions of the conduction domain were given to SODDIT as input. SODDIT uses this kind of data along

with sensitivity coefficients and the future time method to determine a unique heat flux versus time trace for one-dimensional heat conduction problems. SODDIT has the ability to calculate one-dimensional conduction heat transfer in planar, cylindrical, and spherical coordinates.

Because SODDIT is a one-dimensional code, conduction in the axial or azimuthal directions in the calorimeter wall affects the accuracy of the SODDIT heat flux prediction. This happens because the heat flux from the fire to the outer surface of the calorimeter is not uniform [4]. SODDIT is also adversely affected by material properties that vary sharply with temperature. For the case of carbon steel, a solid-solid phase change known as the Curie point occurs at about 768°C. The latent heat of this phase change is approximated in SODDIT as a sharp rise in the specific heat in the range of 726°C to 768°C. This approximation causes the SODDIT heat flux prediction to become unstable and inaccurate while the calorimeter is inside this temperature range. This problem is addressed by bridging the SODDIT heat flux prediction when the calorimeter passes through this temperature range.

Figure 2 illustrates the use of the SODDIT computer code to quantify the time dependent heat flux to the calorimeter. The solid line marked T_{inner} shows the measured interior surface temperature on the west side of the central thermocouple ring (thermocouple 201). The line marked T_{outer} is the corresponding outside surface temperature predicted by SODDIT. The line with square symbols is the SODDIT-predicted net heat flux to the exterior surface of the calorimeter, q". Positive values of q" indicate heat transfer from the fire to the calorimeter (this does not necessarily mean a negative heat flux indicates the calorimeter is hotter than the fire). Two horizontal lines (labeled Curie Region) show the temperature range of the Curie solid-solid phase change

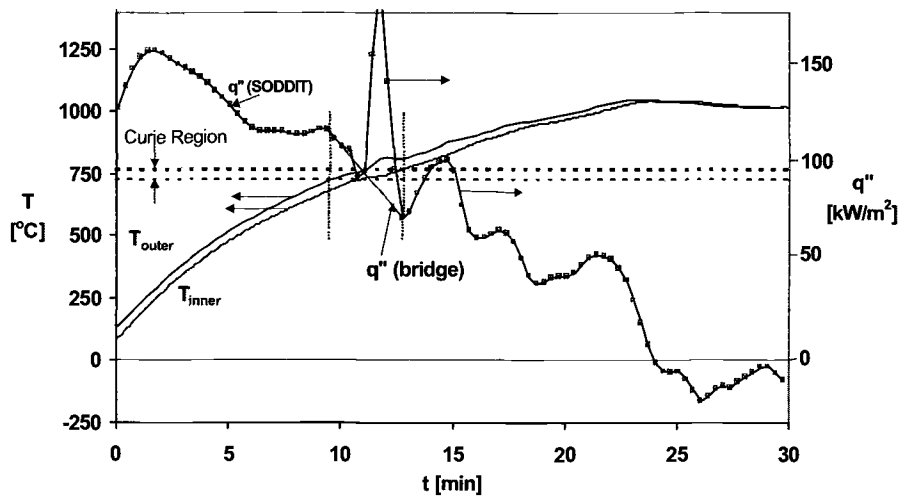

Figure 2. Inner surface temperature trace and sample SODDIT output.

(726-768°C) for the calorimeter steel.

During the time the inner surface temperature is rising (t = 0 to 24 minutes), the net heat flux is from the fire to the calorimeter. The direction of the heat transfer causes the exterior temperature to be greater than the interior value. The outer surface temperature first passes into the Curie Region at t = 9 minutes and the inner surface temperature does not pass out of that range until t = 13 minutes. The SODDIT predicted heat flux exhibits a sharp oscillation between time t = 11 and 13 minutes due to the spike in the effective specific heat (Curie effect). A straight line is used to bridge the heat flux data at t = 9 and 13 minutes to eliminate this oscillation. This technique is applied to all heat flux data used in this experiment.

The thermal mass of the calorimeter wall causes a delay and attenuates interior surface response and acts as a low pass filter. The thermal diffusion time for the 2.54 cm thick steel calorimeter is roughly $W^2/\alpha = 80$ sec, where α is the steel thermal diffusivity and W is the wall thickness. As a result, a given temperature versus time response does not specify a unique heat flux versus time trace. The intent of these heat flux measurements is to measure the time averaged heat flux, as it pertains to the heating of a massive engulfed object. The uncertainty in these heat flux measurements is measured against this time averaged fire heat flux, not instantaneous values.

SOURCES OF UNCERTAINTY

There are several sources of uncertainty in the SODDIT heat flux predictions. One source comes from the assumption of one-dimensional conduction. In reality the conduction in the calorimeter wall is three-dimensional. The heat flux from the fire is non-uniform over the calorimeter surface. This causes temperature gradients, and therefore conduction, in the axial and azimuthal directions. In using SODDIT it is assumed that the dominant direction of conduction in the calorimeter wall is in the radial direction.

Another possible source of uncertainty in heat flux comes from the random and systematic (bias) temperature measurement errors. These errors come from the random thermocouple errors, electrical interference, calibration errors, linearity errors, thermocouple and extension wire impurities, and data acquisition system resolution errors. Because SODDIT is an inverse code, small but rapid changes in the input temperatures can result in large changes in the heat flux prediction. SODDIT uses the slope of the temperature data with time (dT/dt) to calculate a heat flux. The magnitude of the temperature data is used only to calculate the slope and for the evaluation of material properties. An offset in the temperature data (a bias error) does not affect the slope of the temperature with time. Therefore, the systematic inaccuracies associated with thermocouples, which are usually much greater than the random errors, do not significantly contribute to the uncertainty in heat flux. The effects of both random and systematic thermocouple errors were examined.

The last source of heat flux uncertainty comes from the material properties of the calorimeter steel. The SODDIT conduction model is supplied with the thermal properties of the material. Uncertainties in these material properties will propagate through the code and into the heat flux calculations.

QUANTIFYING UNCERTAINTY

One-Dimensional Conduction Assumption

The heat flux uncertainty contribution from the one-dimensional conduction assumption made by SODDIT was determined by using a computer model to simulate both the fire heat flux and the conduction in the calorimeter wall.

The CAFE code calculates fire heat flux boundary conditions that can be applied to a finite element (FE) computer model. These heat flux boundary conditions were coupled to a commercial finite element computer code and applied to a detailed model of the calorimeter. CAFE has recently been adjusted using the fire test data discussed in this work; therefore the heat flux predicted by CAFE is similar to the heat flux predicted by SODDIT for this experiment [6].

The computer simulation has somewhat different heat fluxes than the actual experiment, however the non-uniform and transient characteristics of the simulated and actual heat fluxes are assumed to be similar, as well as the total heat absorbed by the model and experiment. Because of this the heat flux error determined by the computer model serves as a reasonable estimate of the probable error in the experimental heat flux.

A two-dimensional finite element computer model of a section of the calorimeter was used for this analysis. The model was a circular ring with an insulated interior, and the CAFE heat flux boundary condition applied to the exterior surface. The material properties used for the finite element model were the measured properties used in the SODDIT

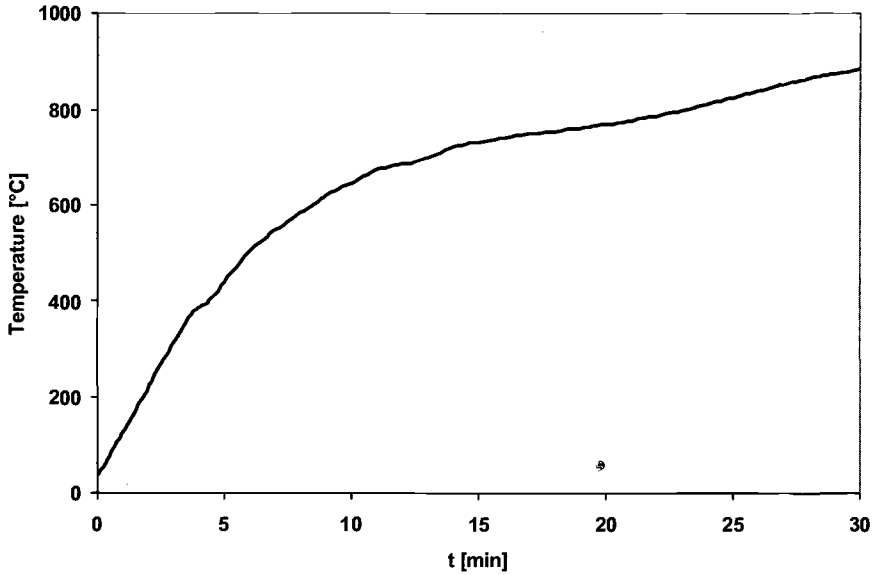

Figure 3 – Inner surface temperature versus time from the CAFE/FE computer simulation

model. The two-dimensional finite element model can simulate radial and azimuthal conduction, but not axial conduction. The uncertainty caused by axial conduction is believed to be small relative to the uncertainty from the azimuthal conduction due to the highly non-uniform heat flux around the circumference of the calorimeter. The computer simulation was run with a 30-minute duration CAFE fire. The temperature versus time data of the interior surface of the ring was extracted from the finite element model, the data from the west side is shown in Fig. 3. This interior temperature data is a simulation of what a thermocouple would measure during the experiment.

The interior temperature versus time data from the CAFE/FE model was used to predict the model outer surface heat flux using SODDIT. This was done using the same technique as for the actual fire experiment heat flux. The difference with the computer model is the actual heat flux applied to the FE model by CAFE is known. Figure 4 shows both the CAFE and SODDIT heat fluxes for the CAFE/FE model on the west side. The CAFE heat flux has been window averaged over 80 seconds to reduce the high frequency oscillations typical of fires. The flat section of the SODDIT curve shows where the heat flux was linearly bridged while the steel was in the Curie temperature range.

The difference between the SODDIT heat flux prediction and the window averaged CAFE heat flux is the error in SODDIT due to the one-dimensional conduction assumption, as well as the inherent errors associated with an inverse conduction algorithm [4]. The

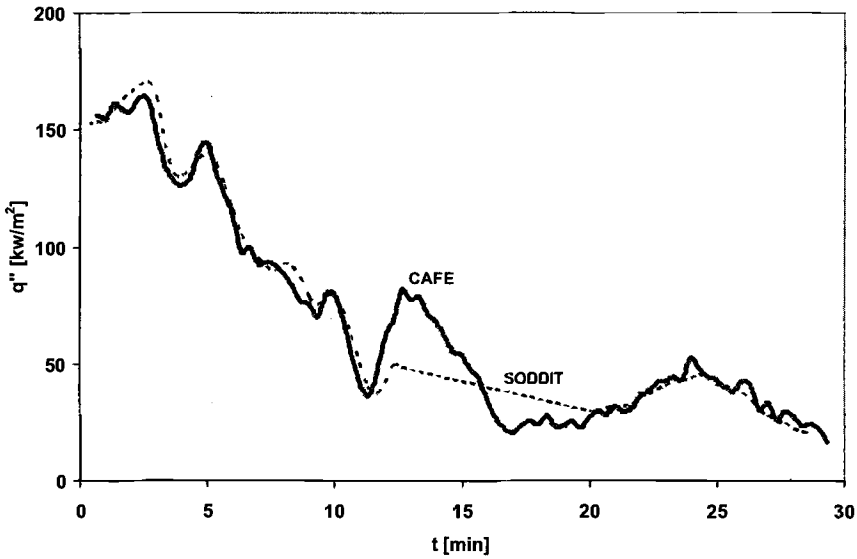

Figure 4. SODDIT and CAFE heat flux versus time from the CAFE/FE computer simulation

SODDIT heat flux error versus time on the west side only is shown in Fig. 5. The SODDIT error is shown as a function of time, however the error at any given time cannot be assigned to the real fire test at that time because of the differences in the actual heat fluxes. However, the error can be quantified statistically over a given time period and used as an estimate for the heat flux error during that time period of the experiment.

Two standard deviations (2σ) of the error over the given time period are used to find the probable one-dimensional contribution of uncertainty with a 95% confidence level. Figure 5 also shows the 2σ estimate of the one-dimensional heat flux uncertainty contribution for the entire 30-minute test on the west side, $U_{q''1} = 19.4\ kW/m^2$. The error on the west side becomes large as the Curie heat flux interpolation is approached. The error is smaller at the beginning of the simulation and at the end. If a shorter time period is used, instead of 30 minutes, a more accurate estimate of uncertainty can be made for that time period. For example, the 2σ error limit for the west side uncertainty (one-dimensional contribution only) from 0 to 5 minutes is reduced by half to $U_{q''1} = 9.6\ kW/m^2$.

Thermocouple Errors

The accuracy reported by the manufacturer of the thermocouples used in this experiment was ± 1.1°C or 0.4% of reading whichever is greater[2]. The extension wires, data acquisition system, calibration curve, and recording procedure all contribute an

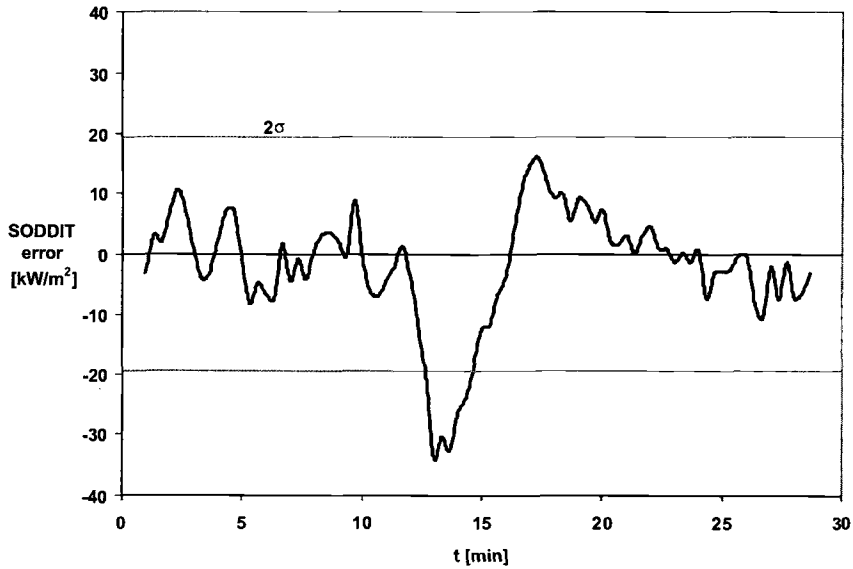

Figure 5. SODDIT heat flux error versus time on the west side only

[2] Pyromation Inc. Report of Calibration, June 26th, 2000

unknown amount of uncertainty to the temperature measurements. For this experiment the thermocouple uncertainty is assumed to be 1% of the reading to account for the additional errors. This implies that the temperature measurements made during the experiment could be in error by as much as 14°C. If a ± 14°C random noise is added to a set of temperature data, the inverse conduction code predicts highly erratic heat fluxes. This is due to the fact that SODDIT uses the slope of the temperature history data (change in temperature with time) to calculate heat flux, not the temperature magnitude. This method of uncertainty estimation for inverse heat flux calculation was used in reference [5]. The temperature magnitude is used to evaluate material properties, which for the most part change slowly with temperature. Fortunately this uncertainty specification includes both the systematic and random errors that occur with thermocouples. It was desirable to know how much of the thermocouple uncertainty is random. Therefore pre-test thermocouple data was used to determine the magnitude of the random component of thermocouple errors in this experiment. To reduce random thermocouple errors, the data acquisition system sampled the temperature inputs at 300 Hz, then it recorded 1 second averages of these samplings.

Shown in Fig. 6 are three thermocouple traces from the experimental setup that were collected in an 8-minute period before one of the fire tests. A total of 43 thermocouples were used for this analysis, only three are shown for clarity. The pre-test temperatures are almost constant, rising about 0.1°C in 8 minutes. A linear fit was made for each temperature trace, shown in Fig. 6. The deviations from the linear fits are assumed

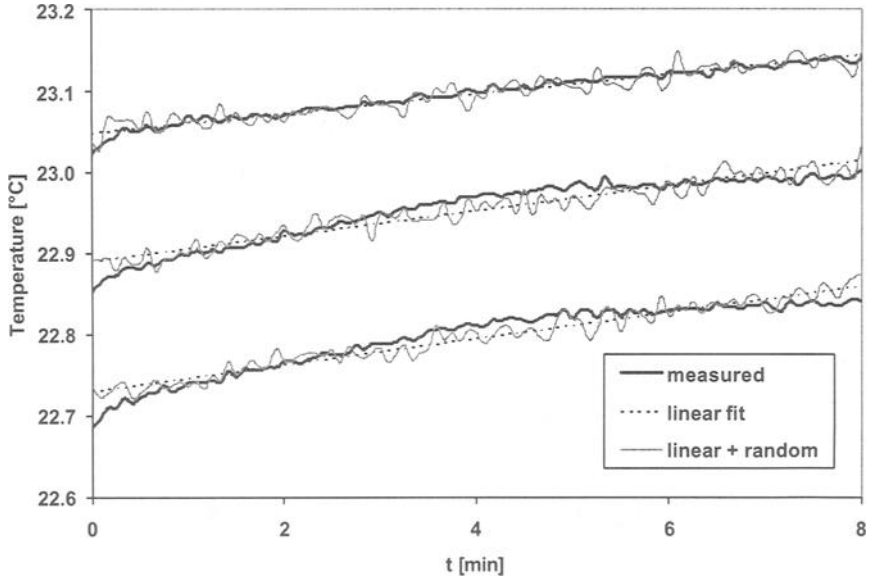

Figure 6. Pre-test thermocouple temperature versus time data, linear fits, and random noise with $\sigma = 0.009°C$

to be the random error for each thermocouple at each time step. A standard deviation was found for the error of each thermocouple trace. The standard deviation from all 43 traces was found to be $\sigma_n = 0.009°C$. Because some of the temperature traces are slightly curved instead of linear, the random error estimation is conservative. Normally distributed random noise with a standard deviation of σ_n was added to the linear temperature fits to show a comparison of generated noise versus measured noise (also in Fig. 6). This analysis was done with data that was recorded by the data acquisition system used for the fire tests. Therefore this random error estimate includes the random components of error added by the thermocouples, thermocouple extension wires, and the data acquisition system. The extremely small random error is likely due to the time averaging technique that was implemented in the data collection algorithm.

Normally distributed random noise was generated with a standard deviation equal to that of the thermocouple random noise. This noise was added to a temperature versus time trace from the CAFE/FE simulation described previously to create 20 separate temperature versus time traces with random noise. The CAFE/FE simulation data was used because it did not already have random noise superimposed on the temperature data. SODDIT was used to predict heat flux versus time using the clean temperature data trace as well as the 20 noisy traces. The deviations of each noisy heat flux trace from the clean heat flux trace were found at every time step. The two standard deviation limit (95% confidence) of the heat flux uncertainty due to random thermocouple noise was found to be 0.038 kW/m^2. Considering the small magnitude of this uncertainty, it is assumed to be negligible.

The systematic thermocouple uncertainties were assumed to be the full 1% error as discussed above. A Monte Carlo simulation was performed to determine the sensitivity of the heat flux error to the systematic thermocouple error. As expected, it was found that the systematic thermocouple error also produced a negligible uncertainty component in the measured heat flux. These uncertainties are negligible in comparison to the large uncertainty due to 1-dimensional and transient effects.

Material Properties and Wall Thickness

The thermal properties of the calorimeter steel were measured prior to the fire tests. The thermal diffusivity was measured as a function of temperature using the laser pulse diffusivity technique. The estimated uncertainty in the thermal diffusivity measurement was estimated to be ± 10% with a 95% confidence level[3]. Differential scanning calorimetry was used to measure the specific heat as a function of temperature. The estimated uncertainty in the specific heat measurement was estimated to be ± 5% with a 95% confidence level[3]. The density of the calorimeter steel was measured using a small cylindrical sample, which was measured using a micrometer and weighed using a calibrated digital scale. The uncertainty in the density measurement was estimated using the method described by Coleman and Steele [7] and was found to be ± 0.75% with a 95% confidence level. The thermal conductivity can be found once the density, specific heat, and diffusivity are known, where $k = \alpha \rho c_p$. The ± 11.2% uncertainty in thermal

[3] Personal communication with Terrence Aselage of Sandia National Laboratories, the expert who performed the measurements

conductivity was also found using the method described in [7]. The steel plate manufacturer supplied the ± 3.5% uncertainty in the 2.54 cm calorimeter wall thickness with a 95% confidence level. These uncertainties in material properties and wall thickness propagate through SODDIT as uncertainties in the predicted heat flux.

SODDIT was used to find the effect of each material property's uncertainty on the SODDIT predicted heat flux. This was done using a numerical Monte Carlo technique. The CAFE computer simulation that was used to determine the one dimensional conduction errors was also used here. For each material property and dimension variable, random values for the error were found using a Gaussian random number generator. These were then scaled with the specified standard deviations. The individual errors were then added to the true values of the variables to yield simulated random noise of the same magnitude as what was estimated for each variable. The SODDIT code was used with the temperature versus time data from the leeward side of the calorimeter simulation to determine a heat flux trace based on the material properties and dimensions with simulated errors. The resulting deviations in the predicted heat flux represent the uncertainty in the heat flux measurements. This process was repeated for 250 iterations. It was found that 1000 iterations yielded similar results.

Figure 7 shows the SODDIT predicted heat flux versus time from the CAFE simulation without simulated errors, and data points that represent the SODDIT predictions of heat flux based on the simulated errors. The resulting relative uncertainty in heat flux due to material property and dimension uncertainties from the Monte Carlo simulation is 6% with a 95% confidence level.

$$\frac{U_{q''mat}}{q''} = 6\% \tag{1}$$

where

$U_{q''mat}$ = absolute uncertainty in heat flux from material properties
q" = heat flux

The simulation described above determines the uncertainty in heat flux caused by all material property and dimension variables. It is also desirable to know how much uncertainty is contributed by each individual variable. This was accomplished using a similar method, however the simulation was performed by adding random noise to only one variable at a time. In this way the uncertainty contribution from each variable can be examined individually. A normalized sensitivity coefficient can be used to describe the influence of the variable uncertainty on the heat flux uncertainty. The definition for a normalized sensitivity coefficient is shown in Eq. 2 below.

$$NSC_i = \frac{X_i}{q''} \frac{U_{q''i}}{U_{X_i}} \tag{2}$$

where

X_i = measured variable with uncertainty
q" = SODDIT predicted heat flux
$U_{q"_i}$ = uncertainty in heat flux (95% confidence)
U_{X_i} = uncertainty in variable X_i (95% confidence)

A normalized sensitivity coefficient greater than 1 indicates the influence of the uncertainty in the variable is magnified as it propagates through the data reduction into the heat flux result. This technique was used to find normalized sensitivity coefficients for the four variables associated with material properties and dimensions. The calculated values for the sensitivity coefficients are shown in Table 1.

The normalized sensitivity coefficients for density, wall thickness, and specific heat are close to one. This means that a 5% uncertainty in specific heat, for example, would yield almost the same level of uncertainty in heat flux. The coefficient for thermal conductivity is less than one, meaning the 11.2% uncertainty in thermal conductivity will result in a smaller uncertainty contribution in heat flux. A verification of the individual components of heat flux uncertainty can be done by a combination using the root sum of the squares method described in [7]. Equation 3 shows this result is the same as what was determined by the full Monte Carlo simulation.

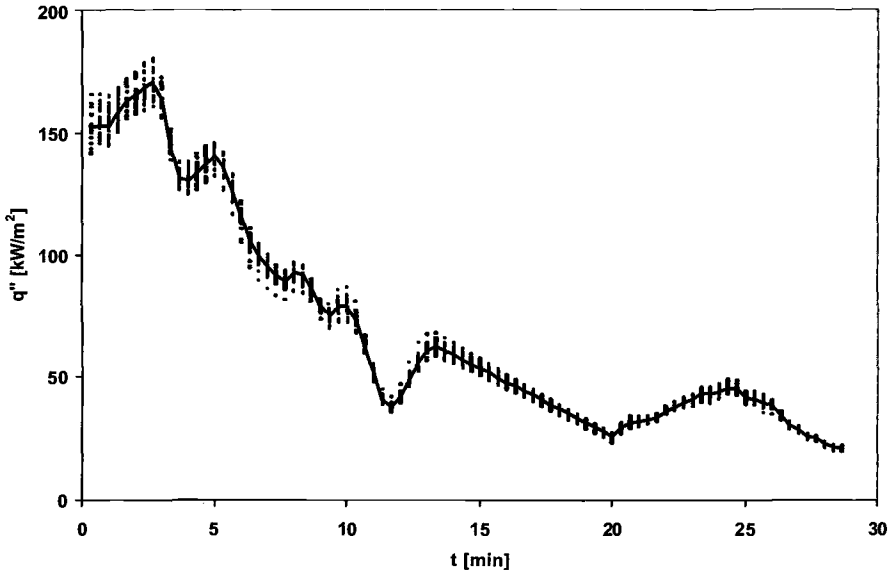

Figure 7 – Heat flux versus time from the west side, and material property Monte Carlo errors.

Table 1 – Material property uncertainties

i	variable name	variable uncertainty $\left(\frac{U_{X_i}}{X_i}\right)$	relative uncertainty in q" due to variable *i* $\left(\frac{U_{q"i}}{q"}\right)$	NSC_i
1	density	0.75%	0.72%	0.96
2	wall thickness	3.5%	3.1%	0.90
3	thermal conductivity	11.2%	2.8%	0.25
4	specific heat	5.0%	4.3%	0.86

$$\frac{U_{q"mat}}{q"} \approx \left(\sum\left(\frac{U_{q"i}}{q"}\right)^2\right)^{\frac{1}{2}} \approx 6\% \tag{3}$$

where

$\frac{U_{q"mat}}{q"}$ = relative uncertainty in heat flux from material properties

COMBINING SOURCES OF UNCERTAINTY

The uncertainties in heat flux resulting from the uncertainties in material properties and wall thickness are relative uncertainties, expressed as a percentage of the total heat flux. The uncertainty resulting from the one-dimensional assumption is an absolute uncertainty, independent of the magnitude of the heat flux. The combination of these uncertainties follows the same method used earlier, outlined in [7]. The method is shown by Eq. 4.

$$U_{q"} = \left(\left(\frac{U_{q"mat}}{q"}\overline{q"}\right)^2 + U_{q"1}{}^2\right)^{\frac{1}{2}} \tag{4}$$

where

$U_{q"1}$ = absolute uncertainty in heat flux from the one-dimensional assumption over a given time period

$\overline{q"}$ = mean heat flux over a given time period

$U_{q"}$ = total absolute uncertainty in heat flux

The estimate for the one-dimensional assumption uncertainty is based upon a standard deviation over a period of time. For a given period of time, 0 to 5 minutes for example, the 1-dimensional uncertainty is evaluated using the CAFE simulation data from 0 to 5 minutes. The absolute uncertainty contribution from material properties and wall thickness is found using the average heat flux over that time period at a given location.

RESULTS

Figure 8 shows the total estimated absolute uncertainty in heat flux, $U_{q''}$, on the center section of the calorimeter versus angle and for several time periods. For most of the locations on the center section, the uncertainty is always below 20 kW/m^2. The uncertainty on the west side during the first five minutes of the experiment is 13.0 kW/m^2, or 9.0% of the mean heat flux during this interval. The uncertainty for the entire center section is below 20 kW/m^2 for the first 10 minutes of the fire test. This is important because the heat fluxes were greater in magnitude in the first 10 minutes than the 20 minutes afterward.

Figure 9 shows the total heat flux uncertainty $U_{q''}$ as a function of angle on the center section with uncertainties calculated over the entire 30 minutes. Most of the calorimeter is still under 20 kW/m^2 absolute uncertainty. The location at 45° is at less than 10 kW/m^2 absolute uncertainty. If the uncertainties are calculated over the entire 30 minutes, and over the entire center section of the calorimeter, the absolute heat flux uncertainty is $U_{q''} = \pm 18$ kW/m^2, or ±27% of the average heat flux of 66.6 kW/m^2. All

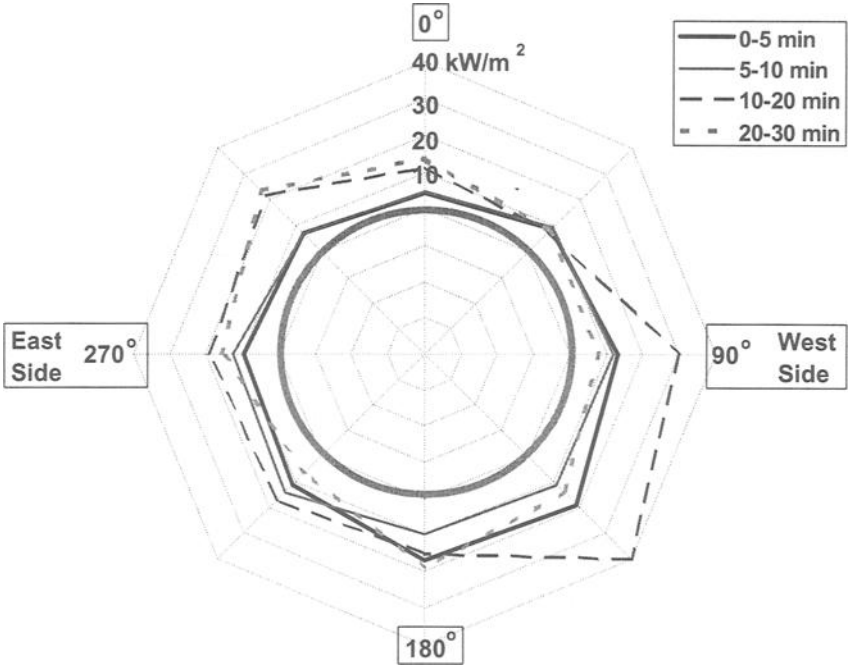

Figure 8. Total estimated absolute uncertainty in heat flux, $U_{q''}$, on the center section of the calorimeter versus angle for several time periods.

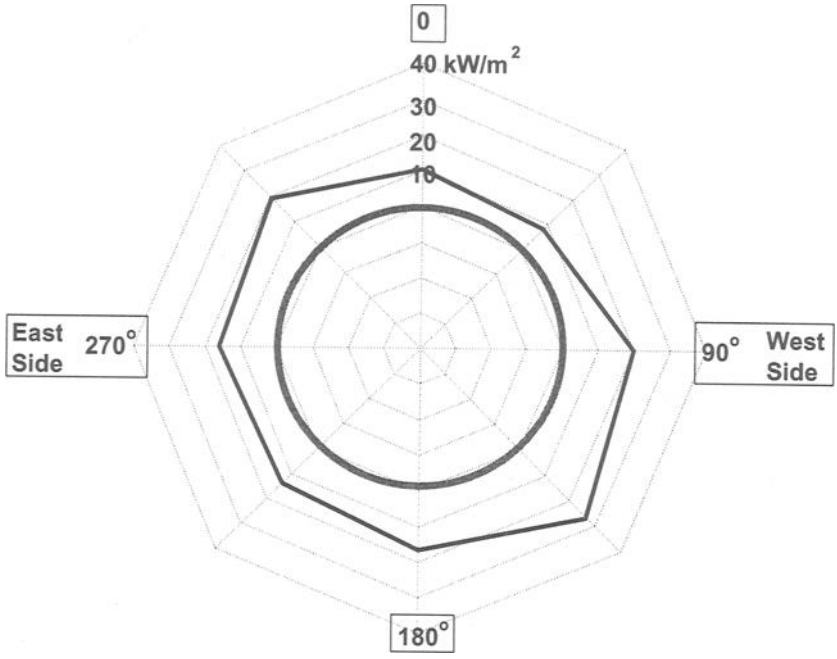

Figure 9. Total estimated absolute uncertainty in heat flux, $U_{q''}$, on the center section of the calorimeter versus angle, averaged over the full 30 minutes.

uncertainties are at a 95% confidence level.

Figure 10 shows the west (leeward) side heat flux measured in the experiment plotted versus time with predicted error bars. The vertical bars indicate the time periods used to calculate uncertainties. The uncertainty is greatest near the time when the calorimeter is passing through the Curie temperature range.

The accuracy of the SODDIT heat flux calculation is greatly affected by the Curie phase change in steel. Heat flux estimates made while the calorimeter material is in the Curie temperature range have much greater uncertainties than measurements made earlier in the test. Because of this, heat flux data measured early in the test, when the calorimeter material is relatively cool, is better suited for the benchmarking of computer codes.

CONCLUSIONS

The uncertainties of heat flux measurements made in a large scale fire test were estimated using traditional uncertainty analysis techniques as well as computer simulations.

The cylindrical calorimeter heat fluxes were calculated using an inverse conduction technique based on interior surface thermocouple measurements.

The heat flux uncertainties due to the one-dimensional conduction assumption made by the inverse conduction code were estimated through the use of computer simulations. The CAFE computer code simulated a fire environment similar to what was measured in the experiment. The CAFE heat flux was applied to a two-dimensional finite element model of the calorimeter. The finite element model simulated the conduction inside the calorimeter wall and supplied the interior temperature versus time. This temperature data was used to run SODDIT, the inverse conduction code, and predict external heat fluxes. These heat fluxes were then compared with the CAFE heat fluxes to find the errors. The deviations are statistically determined over given time intervals and presented as absolute uncertainties, in kW/m^2. For example, the uncertainty due to the one-dimensional assumption in SODDIT on the west side during the first five minutes of the experiment is ± 13.0 kW/m^2, or $\pm 9.0\%$ of the mean heat flux during this interval.

The uncertainties due to material properties were estimated using a Monte Carlo technique. For each material property and dimension variable, random values for the random error were found using a Gaussian random number generator. These were then scaled with the specified standard deviations. The individual errors were then added to the true values of the variables to yield simulated random noise of the same magnitude as what

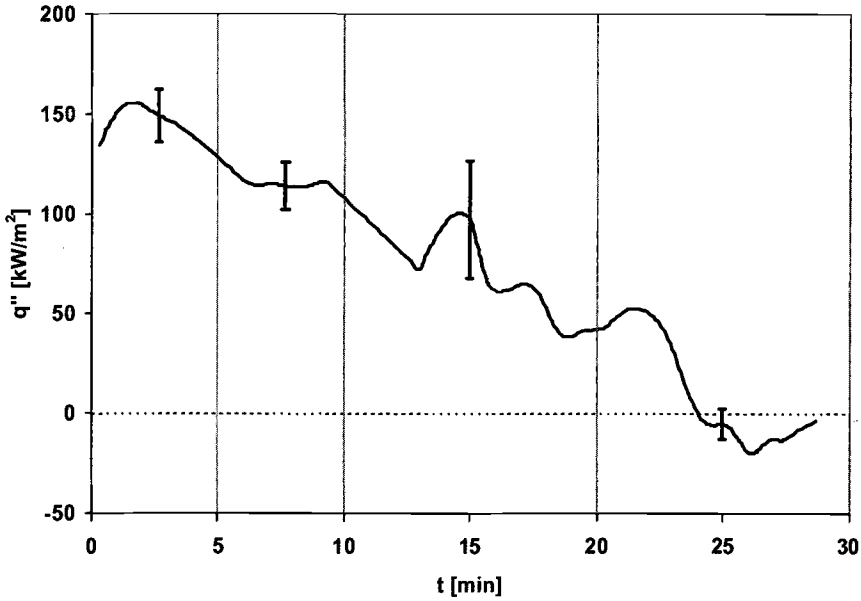

Figure 10. West (leeward) side heat flux versus time with error bars. Averaging times are shown with vertical lines.

was estimated for each variable. The SODDIT code was used with the temperature versus time data from the leeward side of the calorimeter simulation to determine a heat flux trace based on the material properties and dimensions with simulated errors. The resulting deviations in the predicted heat flux represent the uncertainty in the heat flux measurements. These uncertainties were found as percentages of the heat flux magnitude, or relative uncertainties. The uncertainty predicted by the Monte Carlo method is very similar to the uncertainty that was predicted by the sensitivity coefficient method.

The random errors of the thermocouples were measured using pre-test data; the standard deviation of the random thermocouple errors is 0.009°C. The effects of noisy temperature data on SODDIT were examined; the result was a very small uncertainty in heat flux due to the measured random thermocouple errors and the systematic uncertainties reported by the manufacturer. Therefore the thermocouple error effects were neglected.

The total heat flux uncertainty on the center section was calculated for given time intervals and locations. The average heat flux uncertainty calculated over the entire 30 minutes is less than 20 kW/m^2 for most of the center section. The location at 45° is at less than 10 kW/m^2 absolute uncertainty. If the uncertainties are calculated over the entire 30 minutes, and over the entire center section of the calorimeter, the absolute heat flux uncertainty is $U_{q''} = \pm 18$ kW/m^2, or ±27% of the average heat flux of 66.6 kW/m^2. All uncertainties were calculated at a 95% confidence level.

REFERENCES

[1] Kramer, M.A., M. Greiner, Koski, J.A., C. Lopez and A.J. Suo-Anttila, 2001, " Measurements of Heat Transfer to a Massive Cylindrical Object Engulfed in a Regulatory Pool Fire," Paper NHTC01-11466, in Proc. 2001 Nat. Heat Transfer Conference, ASME, Anaheim, June 10-12.

[2] U.S. Nuclear Regulatory Commission, "Packaging and Transportation of Radioactive Material," Rules and Regulations, Title 10, Part 71.73, *Code of Federal Regulations*.

[3] Blackwell, B.F., R.W. Douglass and H. Wolf, 1987, *A User's Manual for the Sandia One-Dimensional Direct and Inverse Thermal (SODDIT) Code*, issued by Sandia National Laboratories, SAND85-2478, 136 pages.

[4] Lopez, C., J. A. Koski, and A. Razani, 2000, Estimates of Error Introduced when One-Dimensional Heat Transfer Techniques are Applied to Multidimensional Problems, Paper NHTC2000-12037, in Proc. 2000 Nat. Heat Transfer Conference, ASME, Pittsburgh, Aug 20-22.

[5] Nakos, J. T, Rosinski, S. T., 1994, *1-Dimensional Simulation of Thermal Annealing in a Commercial Nuclear Power Plant Reactor Pressure Vessel Wall Section*, issued by Sandia National Laboratories, SAND94-0135.

[6] Ju, Hyun Chul. "Computer Simulation of a Spent Nuclear Fuel Transport Package Engulfed in a Pool Fire Using the Cask Analysis Fire Environment", MS Thesis, University of Nevada, Reno, August 2001.

[7] Coleman, Hugh, W. and Steele, W. Glenn, 1999, Experimentation and Uncertainty Analysis for Engineers, John Wiley & Sons, New York.

Ned Keltner,[1] Louis Nash,[2] Jesse Beitel,[3] Art Parker,[3] Steve Welsh,[3] Brian Gilda[4]

Fire Safety Test Furnace Characterization Unit

Reference: Keltner, N., Nash, L., Beitel, J., Parker, A., Welsh, S., and Gilda, B., **"Fire Safety Test Furnace Characterization Unit,"** *Thermal Measurements: The Foundation of Fire Standards, ASTM STP 1427*, L. A. Gritzo and N. J. Alvares, Eds., ASTM International, West Conshohocken, PA, 2002.

Abstract: In standardized fire safety tests such as IMO Res. A 754 (18), ASTM E119, or ISO 834, the furnace temperature is controlled to a standard time-temperature curve [1, 2]. The assumption is made that thermal exposure in these tests will be repeatable and can be described by the measured furnace temperature. The significant variations that occur in test results indicate this assumption is not well founded.

Fire safety test results are influenced by both the temperature of the furnace and by heat transfer in the furnace. The heat transfer depends not only on the furnace temperature and how it is measured but also on the design of the furnace and the test unit. In developing engineering models of fire performance and performance-based codes, there is a need to understand both aspects of thermal exposure - temperature and heat transfer.

To begin to address these problems, the U. S. Coast Guard's Research and Development Center authorized a study of furnace tests. The study documented important factors in current test methods that lead to large uncertainties in the fire safety test results.

To attempt to understand and reduce these large uncertainties, the Coast Guard authorized the development of a Furnace Characterization Unit (FCU). The FCU was built, calibrated using a special electric heater at Sandia National Laboratories, and then used to characterize temperature and heat transfer in a large, gas-fired test furnace at Underwriters Laboratories. This paper reports the results of this multi-year effort.

Key Words: fire testing, furnaces, thermocouples, heat flux, measurement errors

[1] Ktech Corporation, 2201 Buena Vista SE – Suite 400, Albuquerque, NM 87106.
[2] U. S. Coast Guard R & D Center, 1082 Schennecossett Rd., Groton, CT 06340.
[3] Hughes Associates, 3610 Commerce Drive – Suite 817, Baltimore, MD 21227.
[4] U. S. Coast Guard, 2100 Second St. SW, Washington D.C. 20593.

Introduction

In 1996, the U. S. Coast Guard was preparing to change from using national fire safety test standards to International Maritime Organization (IMO) standards [1]. As part of this changeover, the U. S. Coast Guard's Research and Development Center authorized a study of furnace tests to try to understand the important factors that produce large uncertainties in current fire safety test methods and address any differences between national and international standards.

The Coast Guard's study is documented in "Analysis and Comparison of Marine Fire Testing Regulations and Procedures" by N. A. Wittasek, Master of Science Thesis, Worcester Polytechnic Institute, 1996 [3]. The study concluded there are several important factors that can lead to large uncertainties in the fire resistance test results. The most important was that heat transfer in the tests could not be predicted solely from furnace temperature measurements. This thesis is very valuable reading.

In standardized fire safety tests, the assumption is made that thermal exposure will be repeatable and can be described solely by the measured furnace temperature. However, the severity of thermal exposure during these tests and thus the test results themselves are influenced by both the temperature of the furnace and by heat transfer in the furnace. The heat transfer depends not only on the furnace temperature but also on the size of the furnace, the wall lining, the burner design, the fuel, the test unit design, and so on.

In fire safety tests using furnaces, the furnace temperature is controlled to a standardized time-temperature curve. For example in IMO A 754, the furnace temperature (°C) is controlled to a curve described by $345 * \log_{10}(8*t+1) + 20$ where t is the time in minutes [1]. However, studies have shown the measured furnace temperature depends both on the design of the thermocouple and how it is installed [4]. One effort to harmonize test exposures led to the development of the Plate Thermocouple in Europe [5].

To evaluate temperature measurements as a source of uncertainty, Omega Point Laboratories ran a furnace test according to the ISO 834 method (similar to IMO A 754) using two sets of identical thermocouples [1, 6]. However, the thermocouples were installed with orientations that were 90° apart; one set was parallel to the test unit wall and one was mounted normal to it. During the initial rapid temperature ramp, variations occurred in the measured temperatures of up to 100°C. The maximum variation corresponded to 17% of the nominal furnace temperature (580°C at 5 minutes); this translates into a 65% difference in predicted radiant heat transfer rates, which are proportional to the fourth power of the absolute temperature. All of this uncertainty was introduced by simply changing the orientation of the furnace control thermocouples.

Thermocouples can only provide a measure of their own temperature; the thermocouple output is the result of a continuous energy balance [7]. The measured temperatures are different than but related to the furnace temperature. In the ISO 834 tests, both sets of thermocouples are probably giving accurate indications of their own temperatures. Unfortunately, they are different measurements because the heat transfer to them is different. It is different because they have different views of the burner and test unit walls of the furnace. Thus, the energy balance is different.

All of this indicates it is a very difficult to characterize thermal exposure in a fire safety test in terms of just temperature measurements. As a result, it is not surprising that significant variations occur in fire safety test results. These variations make it difficult to use data from current test methods to develop engineering models of fire performance and performance based building codes.

Based on the furnace study findings and experimental results like those described above, the Coast Guard Research and Development Center authorized the development of a Furnace Characterization Unit (FCU). The FCU is designed to characterize the heat transfer in furnaces to aid in understanding the relationship between furnace temperatures, furnace design, and heat transfer levels. The initial goal is to use this understanding to reduce the test-to-test variations and harmonize standardized fire safety tests. Longer term, this effort should provide test data more amenable for developing engineering models of furnace performance to define thermal exposure.

Furnace Characterization Unit Design

The furnace characterization unit was designed for installation in a furnace to make these measurements as a surrogate for a test unit. It is designed to be able to withstand repeated exposures to the high temperatures and the temperature rise rates typical of standardized tests. The basic concept involves a segmented or tiled, all-metal, multi-layer design that:

a) has thermal inertia similar to a marine bulkhead
b) can accommodate significant thermal expansion due to the large temperature excursions and gradients
c) provides a means for checking and calibrating the system; and,
d) provides two-dimensional measurements of heat transfer for mapping purposes.

The FCU has an active area of one square meter to provide a representative size for the Coast Guard's thermal insulation tests. The exposed surface of the unit is a five by five array of Inconel tiles, which are five millimeters thick. In back of the Inconel tiles, there are two layers of sintered metal felt tiles made of Hastelloy-X, with each layer nominally 12.5 mm thick. The stainless steel wool layer was compressed to a nominal thickness of approximately 6 mm during assembly; the thickness at each tile location varies depending on the thickness and flatness of the Hastelloy-X pieces. The mild steel back plate is 5 mm thick.

A U-shaped air duct system with a variable speed fan is used to cool the back plate. The cooling air flows down behind the plenum divider and then up between the plenum

divider and the back-plate. The flow arrangement was designed to try to minimize the temperature variation across the plenum divider to provide a uniform boundary condition. The design is shown in Fig. 1.

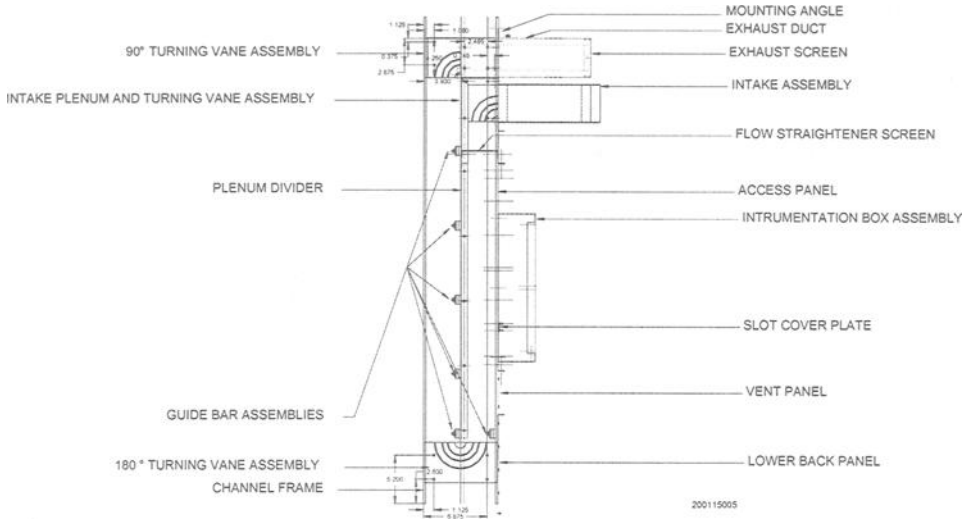

Fig. 1— *Cross-section sketch of the Furnace Characterization Unit.*

There are thirteen (13) instrumented tile locations. A partially expanded cross-section sketch of an instrumented tile location is shown in Fig. 2. A summary of the installed instrumentation is:

a) On the tiled panel assembly Inconel sheathed, Type K thermocouples were 1) attached to the unexposed side of the Inconel tile, 2) set in a groove in the second layer of the Hastelloy-X metal felt, and 3) attached to the back plate. The thermocouples were attached to the Inconel and the steel surfaces using a Nichrome ribbon material. It is formed over the hot junction of the thermocouple for about 20 mm and then spot welded to the substrate. These temperature measurements are used with the parameter estimation and inverse heat conduction codes.
b) Nine of the tile locations have a thermopile type of heat flux sensor attached to the back plate, (EpiSensor from Vatell Corp.). The self-adhesive sensors were attached to the back surface. Then, the surface was painted with Zynolyte 0635, a high temperature, high emissivity paint (data from AEDC show the spectral emissivity is 90 ± 5 % over a range from 1 to 12 microns). These heat flux measurements are used with the parameter estimation code and for comparison with the inverse heat conduction code results.

c) Thermocouples were mounted on the plenum divider panel in the airflow channel. These thermocouples and the heat flux gauges provide boundary conditions for some of the thermal analysis.
d) Double sided, Directional Flame Thermometers (DFTs) were installed ten centimeters from the front (heated) surface on Inconel posts. These were used to estimate the effective radiation temperature of the furnace and to predict the heat transfer or radiosity on the exposed tile surface of the FCU for comparison with the inverse heat conduction calculations.
e) Metal-sheathed thermocouples (6.25 mm OD) were also installed ten centimeters from the tile surface to provide a more traditional type of furnace temperature measurement.
f) A bi-directional velocity probe was installed to provide a future capability for measuring velocity inside a furnace.
g) Two mass flow (velocity) sensors were installed in the down-flow part of the air duct system for estimating convective heat transfer coefficients.

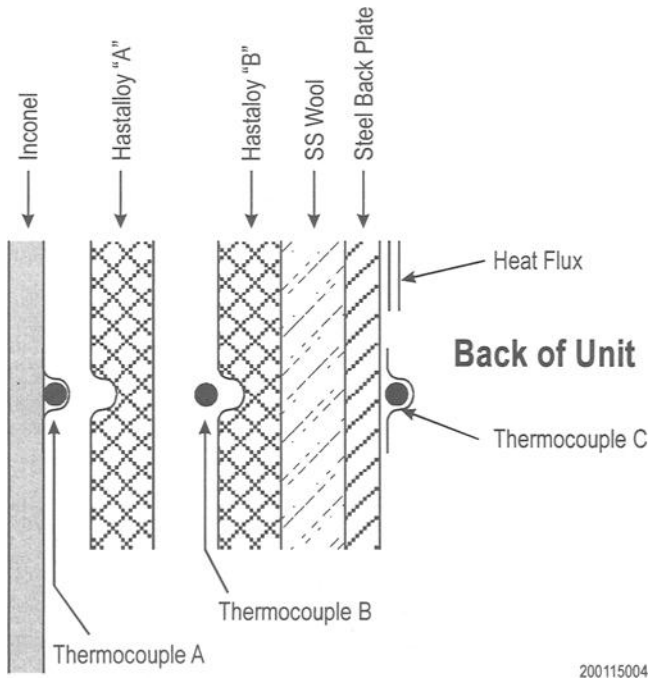

Fig. 2 — *Cross-section of an instrumented Tile location, as built there are minimal gaps between the layers.*

Somewhat redundant techniques are used in the multi-layer design to determine the heat transfer on the instrumented tiles.

a) To meet the Coast Guard's needs, the thickness of Inconel surface tiles was specified to provide a thermal inertia product similar to a marine bulkhead in order to provide a similar heating rate. The tiles absorb energy from the furnace and the temperature rises. Part of this absorbed energy is radiated back into the furnace; part of the energy is stored in the tiles as with a slug calorimeter (ASTM E457); and part of it is conducted towards the unexposed surface [8]. An energy balance on a tile can be used to estimate the total heat flux exposure in a particular furnace for comparison with others.

b) The Hastelloy-X metal felt is used as the main insulation layer. It is expected to withstand repeated cycling to 1000°C without serious degradation. A nonlinear parameter estimation program (PROP1D) is used to estimate local thermal properties from temperature and heat flux measurements at a given tile location [9]. These temperature dependent property estimates are compared with estimates from earlier tests to check unit performance and used as inputs to a nonlinear, inverse heat conduction program. The inverse heat conduction program (IHCP1D) is used to calculate transient heat transfer rates (e.g., heat fluxes) through the different layers [10]. These are used in the energy balances, such as for the Inconel tiles.

c) The back-plate was also designed to provide a thermal inertia product similar to a marine bulkhead. The original intent was to have the back plate respond in a manner similar to an unexposed bulkhead surface. This would provide representative "cold wall" boundary conditions for the total heat transfer through the FCU.

d) Due to problems uncovered during a series of subscale design issue tests, the back plate is separated from the Hastelloy-X by a layer of lightly compressed, stainless steel wool. This helped mitigate two problems. During the initial tests, the back plate temperature rise was twice that allowed in the Coast Guard regulations. The wool added thermal resistance and lowered heat transfer through the FCU. This in turn reduced the back-plate temperature rise to conform more closely to the regulations. Because the wool is compliant, it helped accommodate dimensional variations neither in the Hastelloy-X metal felt tiles, which were not particularly flat nor of uniform thickness.

e) The back-plate is air-cooled. The air duct system was designed to try to provide relatively uniform total heat loss from the back plate. The total heat loss would be from radiation heat transfer to the middle wall of the duct and forced convection to the flowing air stream. Using the thermopile sensors, total heat flux measurements are made at nine (9) locations on the plate.

f) A device called the Plate Thermocouple was developed at SP in Sweden to harmonize furnace control by providing a more representative measure of the furnace temperature [5]. A similar device called a Directional Flame Thermometer was developed by AEA Technologies in the UK for characterizing flame thickness in large pool fires. A new double-sided design of the Directional Flame Thermometers (DFTs) was mounted 10 cm in front of the tile face. Early in a test, the DFTs function as calorimeters in a manner similar to the Inconel tiles but with faster response. Later on when the furnace temperature is varying slowly, the DFTs can be used to estimate the

effective radiation temperature of the test furnace. As will be described later, the DFTs were used to successfully predict the tile heat flux values during furnace tests at Underwriters Laboratories.

A picture of the active face of the FCU is shown in Fig. 3. The Directional Flame Thermometers (DFTs) and furnace thermocouples can be seen in front of the tiles. A bi-directional velocity probe can be seen on the left hand side. The instrumentation is keyed to the tile number.

Calibration Tests

A total of six FCU calibration tests were conducted using the Radiant Heat Facility at Sandia National Laboratories in Albuquerque. The tests used a radiant enclosure built into a very fast, programmable electric furnace, known as Dial-a-Fire. Three of the tests were run using the logarithmic time-temperature curve specified in International Maritime Organization (IMO) Resolution A 754 (18).

The basic setup resembles a shallow box. A high power density, quartz lamp array heats an Inconel shroud, which forms one large face of the box. The tiled face of the FCU forms the other large face of the box. An instrumented transition piece was constructed of mild steel with ceramic fiber insulation covering the outer surface. It provides a more uniform heat flux distribution across the face of the FCU. The overall design provides tight thermal coupling between the heater shroud and the FCU. Having all of the surfaces instrumented with thermocouples provided data for an enclosure analysis of radiation heat transfer.

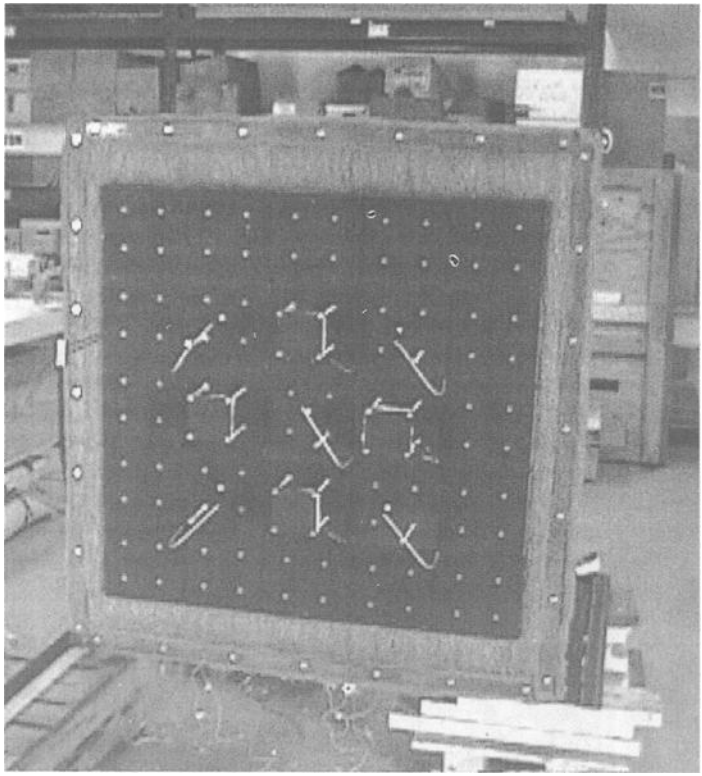

Fig. 3 — *Active Face of the Furnace Characterization Unit.*

A photo of the heater shroud and insulated transition piece is shown in Fig. 4; the photo was taken during a checkout test with the shroud at a temperature of about 1000°C. Although it is difficult to judge in gray-scale, it demonstrates good color (temperature) uniformity.

Sandia National Laboratories (SNL) fabricated the shroud for the Dial-a-Fire heater array. Three rows of seven metal-sheathed thermocouples were attached to the shroud; the locations corresponded to the middle of the top, center, and bottom rows of FCU tiles. As part of the test setup, Sandia National Laboratories provided a set of intrinsic junction thermocouples adjacent to the metal-sheathed thermocouples on the heater shroud. Another paper in this symposium compares the results of the two surface temperature measurement techniques [11].

During the heater system checkout, an infrared (IR) camera was used to generate a digital map of the shroud temperature. Preliminary correlation of the IR camera data with the thermocouple measurements indicated the emissivity of the shroud was approximately 0.84 [12].

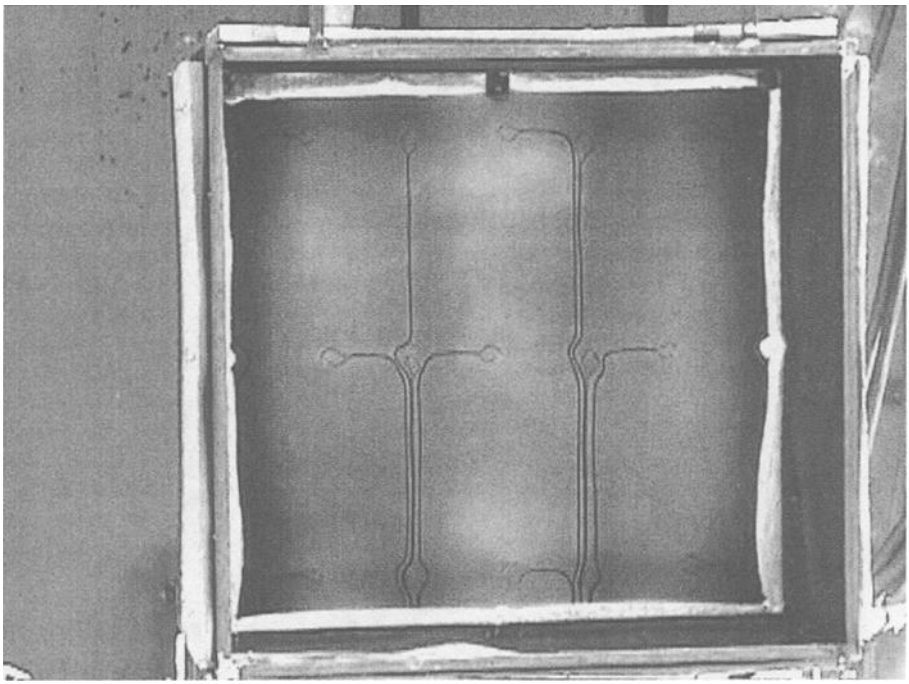

Fig. 4 — *Heater Shroud and Transition Piece.*

In the first series, four calibration tests were run. The first run used a stair-step profile; it served as both a system checkout and a calibration run. The second run followed the logarithmic IMO time temperature curve [1]. The third and fourth runs followed stair-step profiles with 100°C increases in the heater shroud temperature between each step. The duration of each step was approximately eight minutes in one run. In the other, the shroud temperature was held until quasi-steady conditions were attained, typically fifteen to twenty five minutes for each step.

The air-flow system was designed to try to provide a low, uniform temperature across the divider panel. During the checkout run, all of the thermocouples on the divider-panel were monitored; the spread across the panel was approximately 5°C. The maximum rise on the back plate during this test was approximately 100°C.

A temperature transmitter was used with a variable frequency inverter to control the fan speed to try to simulate total heat loss from a full size marine bulkhead. The pressure drop in the air-flow system was much higher than predicted. The maximum attainable velocity was approximately 4.2 m / s with the blower speed set to 125% of the motor rating. This was more than twice the estimate of the velocity needed to provide a total heat transfer coefficient of 15 W / m^2 K needed to simulate the total expected heat loss for a full size, insulated bulkhead.

During the design phase of this project, the total heat loss (radiation plus natural convection) on the unheated surface of a full size, insulated marine bulkhead was estimated to be approximately 2100 W / m^2 at the limit temperature of 164°C. This is based on a total heat transfer coefficient of 15 W / m^2 K with a temperature difference between the back-plate and the air stream of 139°C. During the preliminary design issue tests, temperatures on the back-plate rose faster than expected. The property estimates indicated the thermal conductivity of the Hastelloy-X metal felt insulation layer was approximately twice the value in the manufacturer's literature. This indicated that heat transfer through the FCU would be higher than expected. As noted earlier, a layer of stainless steel wool was added between the Hastelloy-X felt and the back-plate to reduce the heat transfer.

Even with the stainless steel wool layer, the airflow system could not remove heat from the unexposed surface fast enough to control the unexposed surface temperature during the calibration tests. During a calibration test using the IMO time-temperature curve, the peak temperature of the Inconel tiles was limited to approximately 800°C to minimize damage to the heat flux sensors mounted on the steel back plate [1]. When the unexposed surface temperature at the center tile location (Tile 13) reached 164°C (the regulatory limit), the measured heat transfer rate was 3950 W / m^2. The higher velocity and turbulence generated in part by the U-turn resulted in a heat transfer rate that is 88% higher than estimated for an actual bulkhead. The estimated total heat transfer coefficient is approximately 28 W / m^2 K; this is 12% above the predicted level at the measured velocity of 4.2 m / s.

The fifth and sixth calibration tests followed a logarithmic time temperature curve [1]. For these tests, a second fan was installed in series with the original one; this increased the flow rate by approximately 40%. The increased flow allowed the test to run for an additional 6 to 8 minutes before the back surface temperature reached levels that risked serious damage to the heat flux sensors. The test durations were approximately 46 and 48 minutes. All of the calibration test data will be available from the Coast Guard on a CD-ROM.

Test Results

Parameter Estimation Procedures: Estimating the thermal properties of the Hastelloy-X metal felt and stainless steel wool was much more difficult than expected. The original plan called for estimating as a function of temperature the thermal conductivity and volumetric heat capacity of the Hastelloy-X metal felt and the effective

thermal conductance of the stainless steel wool layer at each instrumented tile location for use in the inverse heat conduction analysis. However, we could not obtain consistent results for this many variables with only three or four measurements at a given tile location.

Part of the problem appears to be due to correlation between the sensitivity coefficients calculated in PROP1D when trying to estimate this many parameter values [9].

In reviewing these calculations, it is important to remember that because these property estimates are for 'as built' installations, each one is unique. The as-built nature is a result of the fact that:

a) the metal felt tiles were rigid but not perfectly flat (the curvature was as much as 10% of the thickness) and the thickness varied by as much as +3% / -4% for the individual tiles and ± 4 % overall; plus,
b) due to a), the torque on the different tile bolts were used to produce a uniform assembled thickness which resulted in compression of the stainless steel wool layer (and thus density) that varied from tile to tile.

The thermal property estimates for the individual tile locations reflect this as-built nature. The average thickness was entered for each tile and the stainless steel wool thickness was calculated to give the same overall thickness.

In addition to the curvature, estimates of the effective (as-built) thermal conductivity of the Hastelloy-X were also felt to be influenced significantly by gaps between the Inconel tiles and / or the two Hastelloy-X layers. As a result, an alternate approach started from an assumption that the volumetric heat capacity (density * specific heat) of the Hastelloy-X metal felt could be defined from manufacturers and/or literature data because the composition and density are known.

However, there were large differences between manufacturers and literature data. As a result, both were used as input for estimating other parameters. Evaluating the results indicated temperature dependent data from the Metals Handbook, published by ASM International (formerly the American Society of Metals), and other open literature sources was more representative. This volumetric heat capacity data was then used in PROP1D for estimating the thermal conductivity of the Hastelloy-X metal felt and the stainless steel wool [9].

For a slightly lower density sample of Hastelloy-X, preliminary data from the supplier showed the conductivity varied in an approximately linear fashion out to 500°C – then it changed slope and was nearly linear up to 700°C – the upper limit of the data. Full analysis of the data from the calibration tests was limited due to budget considerations. Data for all three logarithmic tests were analyzed for Tile 15, which is vertical center on one side of the array. Two things to note: A) for three test runs, the thermal conductivity of Hastelloy-X metal felt was set to 0.59 and then a second run was made with it set to 0.7. (Unfortunately, we were never able to get a good estimate of the conductivity at 693°C from analyzing test data.) B) For Tile 15, the confidence intervals overlap for the thermal conductivity estimates at 25°C and 493°C for the second and third tests but they are outside of the intervals for the first test. For all of the other tiles, the

results were selected on the basis of which of the 693°C values produced the "best overall result." The best overall result is a combined score based on the number of iterations, the shape of the sequential estimates, the confidence intervals (as a percentage of the estimate), the amplitude and shape of the residuals, and the RMS or standard deviation between calculated and measured temperatures. As might be expected, this requires making a subjective judgement.

Three temperature dependent, thermal conductivity values were generated for Hastelloy-X. Two of these were estimated using PROP1D and the third based on selection as described above [9]. When there is more than one value given for a thermal property, both PROP1D and IHCP1D use linear interpolation (or extrapolation if needed) to generate temperature dependent values for their calculations [9, 10].

Inverse Heat Conduction Analysis: The property estimates for the individual tiles were used in the inverse heat conduction program (IHCP) to estimate heat transfer rates during the calibration tests. The heat flux distribution across the face of the FCU peaks in the center, falls at the edges, and falls further going into the corners.

Peak absorbed heat fluxes are between 18 and 23 kW /m^2 and occur approximately 12-15 minutes into the time-temperature curve. The highest values occur in the central portion of the tile face, as expected. The lowest values occur at the bottom corners, Tiles 21 and 25, which have a smaller radiation configuration with the heater shroud. Based on differences between the upper and lower corner tiles, it appears that a significant natural convection cell was established. When the heating was terminated (at approximately 40 minutes), the absorbed heat flux was between 10 and 12 kW /m^2.

In all, three tests were controlled to the IMO logarithmic time-temperature curve [1]. For Tile 15, the peak absorbed heat flux was estimated to be approximately 21 kW / m^2; it occurred about 900 seconds (15 minutes) into the test. At this time, the furnace temperature should be about 745°C and the measured Tile 15 temperature was about 400°C. Assuming the measured furnace temperature agrees with the curve and the heat transfer is totally radiant, this implies an effective furnace emissivity of approximately 0.6. Plots of temperatures and heat fluxes from Calibration Test #1 for Tile 15 are shown in Fig. 5. Between the three logarithmic curve tests, the repeatability of the peak heat flux at Tile 15 was 3-4%.

For evaluation of the calibration test data, a simplified radiation enclosure analysis was developed using the MATHCAD analysis software. The enclosure analysis uses the heater shroud, the transition piece, and the FCU tile face as boundaries along with the temperature measurements and emissivity values to calculate the radiosities. Under quasi-steady conditions, the Directional Flame Thermometer (DFT) data provide measures of the equivalent radiation temperatures of the shroud and the tile face of the FCU; these measures are based on the radiosity and were used to compare with the analysis.

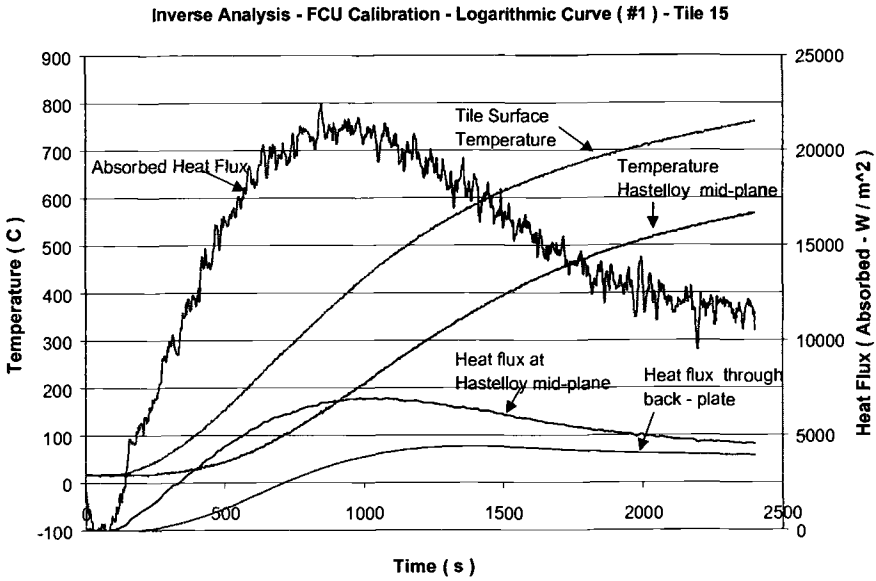

Fig. 5 — *Tile 15 data from Calibration Test #1*

Near the end of heating in the first calibration test using the IMO logarithmic curve, the temperature measurements on both sides of the Directional Flame Thermometers agreed nicely with predictions from the three surface radiosity model [1]. At 2460 seconds, the average heater shroud temperature was 1142 K, the average transition piece temperature was 1065 K, and the average temperature of the central nine Inconel tiles was 1047 K. Using the radiosity model, the predicted DFT readings were 1124 K for the A side, which faces the heater shroud, and 1058 K for the B side which faces the FCU. The measured temperatures for the DFT located at Tile 8 were 1131 K on the A side and 1056 K on the B-side. Both estimates are within the Type K thermocouple calibration limits.

Overall, the calibration test results were excellent. Post-test inspection of the FCU showed no apparent warping, and little or no degradation of the high absorptivity paint on the face of the Inconel tiles.

Furnace Tests

The FCU was used for heat transfer measurements during two tests in the large wall furnace at Underwriters Laboratories (UL) in Northbrook, IL. In the preliminary evaluation, the property estimation code, PROP1D, was used to analyze data from the middle tile (Number 13) for both furnace tests. The conductivity of the Hastelloy-X at

25°C and 493°C plus that of the stainless steel wool was estimated. The estimates used data out to a maximum tile surface temperature of about 600°C.

In each case, the Hastelloy-X conductivity estimates dropped a bit. Estimates for UL Run 01 were lower than the estimates from an early calibration test at Sandia. Estimates for UL Run 02 were lower than UL Run 01.

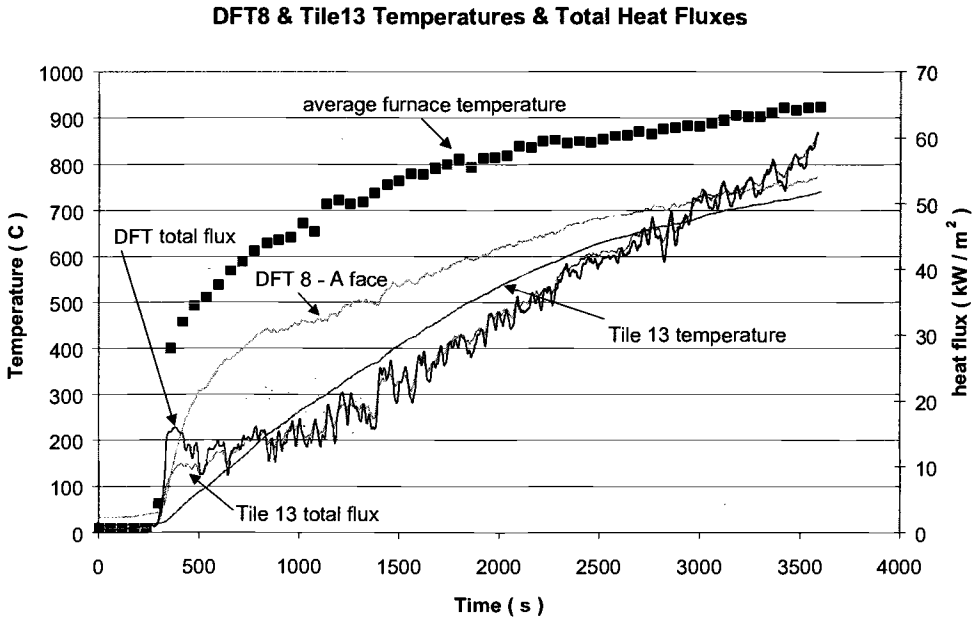

Fig. 6 — *Temperatures and Total Heat Flux Exposures for DFT 8 and Tile 13.*

The estimated thermal properties were used in inverse heat conduction code – IHCP1D to calculate heat fluxes. Preliminary results show the absorbed heat flux spikes during startup of the gas-fired furnace. The absorbed heat flux then climbs to a peak of 15-20 kW / m^2 around 1400 seconds; and, then falls slowly to around 10 kW / m^2 at one hour. The total heat flux (thermal exposure?) was approximated by adding reradiated energy to the absorbed flux. As shown in Fig. 6, total heat flux jumped to over 10 kW / m^2 on startup and then climbs in a fairly linear fashion to 65 kW / m^2 over the course of the one hour test.

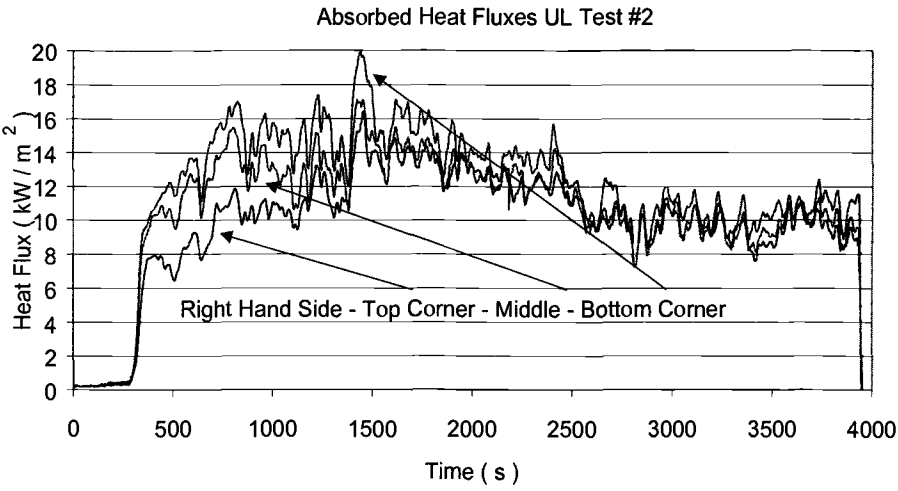

Fig. 7 — *Absorbed Heat Fluxes for 3 Instrumented Tiles – UL Furnace Test #2.*

In looking at the data, there are some interesting features. As shown in Fig. 7, the bottom is hotter than the top, probably due to the firing pattern. There appeared to be good left to right symmetry. This figure gives a sense of the spatial and temporal variations in absorbed heat fluxes Run 01 was hotter than Run 02 in agreement with furnace temperature measurements made by UL

The variation of the heat transfer can also be seen by looking at the spread in the tile temperatures, as shown in Fig. 8. The temperatures of the bottom row of tiles are significantly hotter than the top row. Re-radiation from the bottom row is approximately 50% higher than that from the top row of tiles.

With the exception of the startup pulse, the Directional Flame Thermometer data could be used to predict the FCU heat flux data, see Fig. 6. Calculations for Tile 13 and DFT 8 show that the 'thermal exposure' climbs in a fairly linear fashion; this is different than the expectation of a more 4^{th} power type of relationship. The heat flux absorbed by the tile is

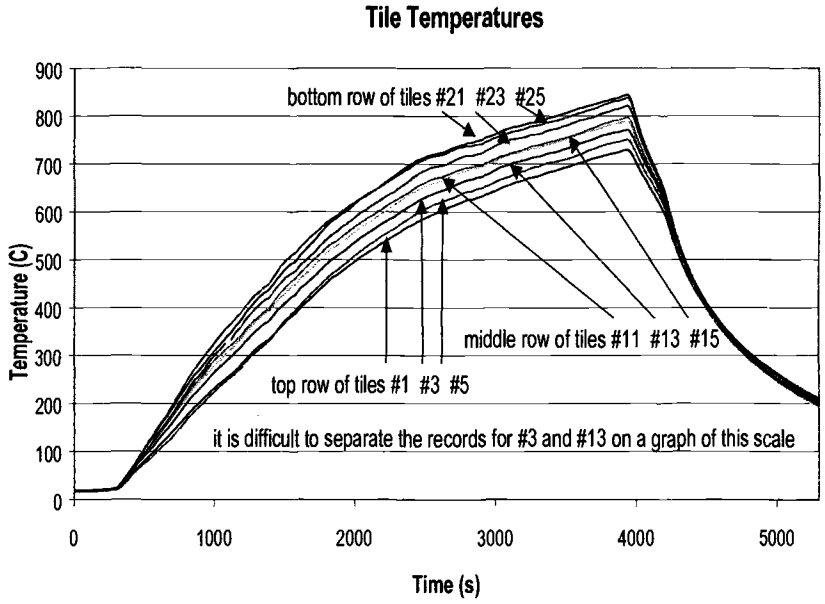

Fig. 8 — *Spread of tile temperature also shows heat transfer variations.*

mildly peaked – it jumps to 10,000 W / m^2 at the start, climbs slowly to 15,000, and then declines slowly into the 8-10,000 range. These results shows the Tile and Directional Flame Thermometer temperature measurements can be used to give a good estimate of the heat flux absorbed by the Inconel tile.

A radiation-only based cold wall correction was added to the absorbed tile heat flux data. It uses the measured temperature of the Inconel Tile and assumed the emissivity of the tile surface, painted with Pyromark 2500 Black, was 0.85. Over the one-hour test, the integrated total heat flux exposures obtained with the FCU and from the DFT differed by less than 3%. The results shown in Figures 6 and 9 give us a start at predicting the total heat flux exposure.

Summary

A Furnace Characterization Unit has been built, calibrated, and tested in a large fire safety test furnace. Nonlinear parameter estimation and inverse heat conduction codes were used to analyze test data.

In calibration tests following the IMO A754 time-temperature curve, peak absorbed heat flux was about 23 kW / m^2 [1]. A three surface radiosity model of these

experiments was developed. It could be used to predict temperature measurements with excellent accuracy and heat flux measurements with good accuracy.

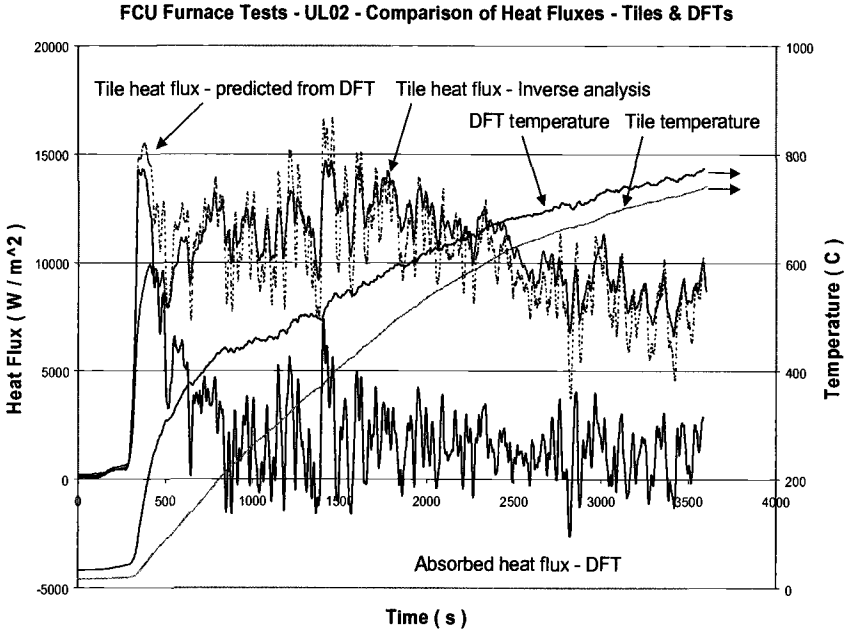

Fig. 9 — *Using the DFT data to predict FCU heat fluxes.*

After calibration, the FCU was tested in the large vertical furnace at Underwriters Laboratories using the IMO A 754 time-temperature curve [1]. Heat fluxes in the furnace tests were lower than in the calibration tests. Peak absorbed heat flux was about 15 kW / m^2. The total heat flux exposure (absorbed plus reradiated heat fluxes) jumped upon furnace ignition to about 10 kW / m2 and then climbed in a nearly linear fashion to approximately 65 kW / m2 at the end of the one hour exposure. This is a very different shape curve than what was expected, namely one which is concave down because it is proportional to the fourth power of the absolute furnace temperature.

The heat fluxes measured with the FCU could be predicted with good accuracy using measurements made with a Directional Flame Thermometer. This suggests the DFTs could be used to improve control of fire safety test furnaces and provide data on heat transfer rates in furnaces in addition to the temperature data.

The results of this work demonstrate the need to understand both the temperatures and the heat fluxes associated with fire safety tests involving furnaces. If both are not considered in evaluation of these tests, it will be almost impossible to harmonize tests

between laboratories. If both are not measured, it will be almost impossible to use the test data to support the development of fire safety performance based building codes.

The U. S. Coast Guard has developed a Furnace Characterization Unit. It offers a way to define the heat transfer component of thermal exposure in individual furnaces. Directional Flame Thermometers are thermocouple-based sensors. Results from the Underwriters Laboratories tests suggest they can be used to control furnaces in a manner that would harmonize the heat transfer. This would reduce the variability between tests.

References

[1] International Maritime Organization Resolution A 754 (18) Recommendation on Fire Resistance Tests for "A", "B", and "F" Class Divisions, 1993.

[2] ASTM E119 – Standard Test Methods for Fire Tests of Building Construction and Materials, ASTM International, West Conshohocken, PA, 2002.

[3] Wittasek, N. A., "Analysis and Comparison of Marine Fire Testing Regulations and Procedures" Master of Science Thesis, Worcester Polytechnic Institute, 1996.

[4] Babrauskas, V. and Williamson, R. B., "Temperature Measurement in Fire Test Furnaces," *Fire Technology*, Vol. 14, pp 226-238, 1978.

[5] Wickstrom, U., "A Proposal Regarding Temperature Measurements in Fire Test Furnaces," Nordtest Project 355-82, SP, Boras, Sweden, 1986.

[6] Priest, D., Omega Point Laboratories, Private communication.

[7] Keltner, N. R., "Thermal Measurements in Fire Safety Testing - Are We Playing with Fire?," Special Symposium of Fire Calorimetry, NIST, July, 1995, *Fire Calorimetry* Proceedings, Editors: Hirschler and Lyon, DOT/FAA/CT-95/46, FAA Tech Center.

[8] ASTM E457 – Standard Method for Measuring Heat Transfer Rate Using a Thermal Capacitance (Slug) Calorimeter.

[9] Beck, J. V., "PROP1D – Program for Estimating Thermal Properties," Beck Engineering Consultants, Okemos, MI, October, 1999.

[10] Beck, J. V., "ICHP1D – Program for Calculating Surface Heat Fluxes from Transient Temperatures Inside Solids," Beck Engineering Consultants, October, 1999.

[11] Nakos, J. T., "The Systematic Error of a Mineral-Insulated, Metal Sheathed (MIMS) Thermocouple Attached to a Heated Flat Surface," *Thermal*

Measurements: The Foundation of Fire Standards, ASTM STP 1427, L. A. Gritzo and N. J. Alvares, Eds., ASTM International, West Conshohocken, PA, 2002.

[12] Nakos, J. T., et al, "Final Report – Summary of Thermal Testing of the Furnace Characterization Unit (FCU) for the Coast Guard," Sandia National Laboratories, SAND2000-1534, June, 2000.

Marc L. Janssens[1]

Variability in Oxygen Consumption Calorimetry Tests

Reference: Janssens. M. L., **"Variability in Oxygen Consumption Calorimetry Tests,"** *Thermal Measurements: The Foundation of Fire Standards, ASTM STP 1427*, L. A. Gritzo and N. J. Alvares, Eds., ASTM International, West Conshohocken, PA, 2002.

Abstract: Oxygen consumption calorimetry has been used for more than twenty years to determine the heat release rate from experimental fires. Several investigators have quantified the theoretical uncertainty of heat release rate measurements. Estimates of the precision of heat release tests based on round robin results suggest that in practice the uncertainty may be much greater, in particular for intermediate and large-scale tests. The objectives of this paper are to examine the reasons for this discrepancy, and to propose actions that will improve the precision of heat release rate measurements to an acceptable level without raising costs beyond the reach of commercial fire testing laboratories. The proposed actions include the establishment of a proficiency program to obtain a realistic measure of the uncertainty of heat release rate measurements in fire tests.

Keywords: Oxygen consumption calorimetry, heat release rate, uncertainty, precision

Nomenclature

A	Constant
B	Constant
C	Flow coefficient ($kg^{½} \times m^{½} \times K^{½}$)
E	Net heat released per unit mass of O_2 consumed (MJ/kg)
m	Mean value
M_e	Molecular mass of gases in the exhaust duct (kg/kmol)
M_{O_2}	Molecular mass of oxygen (32 kg/kmol)
$\dot{q}$	Rate of heat release (kW)

[1] Associate Professor, Department of Engineering Technology, The University of North Carolina at Charlotte, 9201 University City Boulevard, Charlotte, NC 28223-0001.

$\dot{q}''_{180}$ Cone Calorimeter average heat release rate over 180 s following ignition.(kW/m^2)

$\dot{q}_{max}$ Peak heat release rate (kW)

$\dot{q}''_{max}$ Peak heat release rate in the Cone Calorimeter (kW/m^2)

q_{tot} Total heat released (MJ)

q''_{tot} Total heat released in the Cone Calorimeter (MJ/m^2)

r Repeatability value

R Reproducibility value

s_r Repeatability standard deviation

s_R Reproducibility standard deviation

t_{ig} Time to ignition in the Cone Calorimeter (s)

T_e Gas temperature at the orifice or bi-directional probe (K)

$X^a_{O_2}$ Actual mole fraction of O_2 in incoming air (wet)

$X^{A^a}_{O_2}$ Measured mole fraction of O_2 in incoming air (dry)

$X^{A^e}_{O_2}$ Measured mole fraction of O_2 in exhaust flow

u Uncertainty

α Combustion volumetric expansion factor

$\Delta h_{c,eff}$ Effective heat of combustion in the Cone Calorimeter (MJ/kg)

ΔP Differential pressure measured across the orifice or bi-directional probe (Pa)

ϕ Oxygen depletion factor

Technical Terms

Fire terms are defined and discussed in the ASTM Terminology for Fire Standards (E 176). Some important technical terms pertinent to precision of standard tests and uncertainty of measurements in the context of this paper are briefly defined below. These definitions are based primarily on the information provided in the Guide to the Expression of Uncertainty in Measurement (GUM) [1].

accuracy (of measurement) - closeness of the agreement between the result of a measurement and the true value of the measurand (quantity subject to measurement).

error (of measurement) - result of a measurement minus the true value of the measurand; error consists of two components: random error and systematic error.

precision (of a test method) - refers to the repeatability and reproducibility of the measurement.

random error - result of a measurement minus the mean that would result from an infinite number of measurements of the same measurand carried out under repeatability conditions.

relative error - error of measurement divided by the true value of the measurand.

repeatability (of results of measurements) - closeness of the agreement between the results of successive independent measurements of the same measurand carried out under repeatability conditions, i.e., on identical test material using the same measurement procedure, observer(s), and measuring instrument(s) and performed in the same laboratory during a short period of time.

reproducibility (of results of measurements) - closeness of the agreement between the results of measurements of the same measurand carried out under reproducibility conditions, i.e., on identical test material using the same measurement procedure, but different observer(s) and measuring instrument(s) in different laboratories performed during a short period of time.

(experimental) standard deviation - a quantity characterizing the dispersion of the results of a series of measurements of the same measurand; the experimental standard deviation is proportional to the square root of the sum of the squared deviations of the measured values from the mean of all measurements.

systematic error (or bias) - mean that would result from an infinite number of measurements of the same measurand carried out under repeatability conditions minus the true value of the measurand.

uncertainty (of measurement) - half-width of an interval that contains the true value of a measurand with a stated level of confidence.

Introduction

Most accreditation agencies of fire testing laboratories recently adopted the ISO/IEC General Requirements for the Competence of Testing and Calibration Laboratories (17025). This international standard mandates that test reports include a statement of the uncertainty of the measurements. It is therefore necessary that accurate uncertainty estimates be established for all fire test procedures. It is even more critical to carefully quantify the uncertainty of oxygen consumption calorimeter measurements, because heat release rate is the single most important variable in fire hazard assessment [2] and is used more than any other fire test result in support of quantitative fire engineering design and analysis.

Theoretical uncertainty estimates of complex measurements that are a function of several measured and specified variables can be calculated as described below. However, these estimates are typically very optimistic because they do not account for hidden sources of error that cannot easily be quantified. The repeatability estimated from a carefully conducted round robin appears to be a more realistic measure of the uncertainty. Numerous round robins have been conducted over the past 12 years to determine the repeatability and reproducibility of heat release rate measurements. The results from some of these round robins suggest that the uncertainty is much greater than the theoretical value, in particular for intermediate and large-scale tests. The objectives of this paper are to examine the reasons for this discrepancy, and to propose actions that will improve the precision of heat release rate measurements to an acceptable level without raising costs beyond the reach of commercial fire testing laboratories. The proposed actions include the establishment of a proficiency program to obtain a realistic measure of the uncertainty of heat release rate measurements in fire tests based on oxygen consumption. Thus, the author hopes to demonstrate that oxygen consumption calorimetry is not an art requiring a level of detail and care that can only be accomplished in a research laboratory, but a science that can be performed routinely at reasonable cost by any proficient commercial fire testing laboratory.

Oxygen Consumption Calorimetry

History

In 1917, Thornton [3] showed that for a large number of organic liquids and gases, a nearly constant amount of heat is released per unit mass of oxygen consumed for complete combustion. Huggett [4] found this to also be true for organic solids and obtained an average value for this constant of 13.1 MJ/kg of O_2. This value may be used for practical applications and is accurate with very few exceptions to within ± 5%. Thornton's rule implies that it is sufficient to measure the oxygen consumed in a combustion system in order to determine the net heat released.

The first reference to Thornton's rule in the fire literature was made in a report published at the Fire Research Station in England in 1968 [5]. It was suggested in this report that changes in oxygen concentration in the flue gases could be used to determine the heat release rate in the British Fire Propagation test. The oxygen consumption technique was first used by Parker to measure the heat release rate from fires in a study of the Steiner tunnel test [6]. Later, Sensenig applied it to an intermediate-scale room test [7]. During the late 1970's and early 1980's, the oxygen consumption technique was refined at the National Bureau of Standards (NBS, currently the National Institute of Standards and Technology or NIST). The technique is now used extensively in many laboratories all over the world, both in bench-scale and full-scale fire test applications.

Equations

An oxygen consumption calorimeter consists of a hood and exhaust duct to collect and extract all products of combustion generated in the fire. At a distance downstream from the entrance to the exhaust duct sufficient for adequate mixing, both flow rate and composition of the gases are measured. The former is typically determined on the basis of the exhaust gas temperature at, and pressure drop across, an orifice or a bi-directional probe. The gas analysis must include oxygen concentration as a minimum. For the basic gas analyzer configuration, heat release rate is calculated from the following equations:

$$\dot{q} = E\frac{\phi}{1+\alpha(\phi-1)}C\sqrt{\frac{\Delta P}{T_e}}\frac{M_{O_2}}{M_e}X_{O_2}^{a} \tag{1}$$

with

$$\phi = \frac{X_{O_2}^{A^a} - X_{O_2}^{A^e}}{(1-X_{O_2}^{A^e})X_{O_2}^{A^a}} \tag{2}$$

The accuracy of the calculations can be improved by adding instrumentation for measuring the concentration of CO_2, CO, H_2O, and soot. Parker and Janssens derived equations for different gas analyzer configurations [8, 9]. The effect of soot is discussed by Brohez et al. [10].

Standard Test Procedures

Cone Calorimeter - The Cone Calorimeter is standardized as the ISO Reaction to Fire Test Method for Heat Release Rate of Building Products (5660) and the ASTM Test Method for Heat and Visible Smoke Release Rate for Materials and Products Using an Oxygen Consumption Calorimeter (E 1354).

In the Cone Calorimeter, a square sample of 100 × 100-mm (4 × 4-in) is exposed to the radiant flux of an electric heater. The heater has the shape of a truncated cone (hence the name of the instrument) and is capable of providing heat fluxes to the specimen in the range of 10-110 kW/m². An electric spark plug is used for piloted ignition. Heater temperature is measured as an average of the readings of three thermocouples in contact with the coil and is maintained at a preset level during testing. Calibration of heat flux as a function of heater temperature is performed with a total heat flux meter of the Schmidt-Boelter type.

Prior to testing, the heater temperature is set at the appropriate value resulting in the desired heat flux. At the start of a test, the specimen in the appropriate holder is placed on the load cell, which is located below the heater. The electric spark plug is inserted at the start of thermal exposure, and removed when sustained flaming occurs. All combustion products and entrained air are collected in the hood. At a sufficient distance downstream from the mixing orifice at the entrance of the duct, a gas sample is taken and analyzed for O_2. A laser photometer is located close to the gas sampling point to measure light extinction by the smoke. The exhaust gases are removed by a high-temperature blower. The flow rate can be adjusted between 0 and 50 liters per second. For standard testing, the duct flow rate is set at approximately 24 liters per second. Measurements of the differential pressure across and gas temperature at an orifice located downstream from the blower are used to calculate the mass flow of the exhaust gases.

Room/Corner Test - The room/corner test is standardized internationally as the ISO Full-Scale Room Test for Surface Products (9705). There are several domestic room/corner test standards, but precision data have only been obtained for the NFPA Method of Fire Tests for Evaluating Room Fire Growth Contribution of Wall and Ceiling Interior Finish (286).

The apparatus consists of a room measuring 3.6 m (12 ft) deep by 2.4 m (8 ft) wide by 2.4 m (8 ft) high, with a single ventilation opening (doorway) measuring approximately 0.8 m (30 in.) wide by 2 m (80 in.) high in the front wall. The room interior consists of calcium silicate board (ISO 9705 and NFPA 286) or Type X gypsum board (NFPA 286). All walls except the front wall, as well as the ceiling are lined with the test material for experiments according to ISO 9705. For tests according to the NFPA standard, only the walls (except the front wall) are covered with the test material.

The test material is exposed to a propane burner ignition source, located on the floor in one of the rear corners of the room opposite the doorway. The burner is placed directly against the back wall and one of the sidewalls. The ISO burner consists of a steel sandbox measuring $0.17 \times 0.17 \times 0.17$-m ($7 \times 7 \times 7$-in.) Propane is supplied to the burner at a specified rate such that a net heat release rate of 100 kW is achieved for the first 10 min of the test, followed by 300 kW for the remaining 10 min (20 min test duration, unless terminated when flashover occurs). The NFPA burner consists of a steel sandbox measuring 0.3×0.3-m (12×12-in.) $\times$ 0.15 m (6 in.) high, with the top surface positioned 0.3 m (12 in.) above the floor of the room. Propane is supplied at a specified rate such that a net heat release rate of 40 kW is achieved for the first five min of the test, followed by 160 kW for the remaining 10 min (15 min test duration unless terminated when flashover occurs).

Instrumentation for measuring rate of heat release and smoke production is installed in the exhaust duct connected to a fume collection hood located outside the room immediately adjacent to the doorway. The duct instrumentation consists of thermocouples for measuring exhaust gas temperature, a bi-directional probe for measuring exhaust gas velocity, a collimated white light or monochromatic laser light system for measuring smoke obscuration, and probes for sampling O_2, CO_2, and CO. The room contains a single heat flux meter located in the center of the floor. The NFPA standard also specifies that seven thermocouples be installed in the upper part of the room and doorway to measure the temperature of hot gases that accumulate beneath the ceiling and flow through the doorway. In addition to quantitative heat release and smoke production rate measurements,

time to flashover (if it occurs) is one of the main results of a room/corner test. Different criteria are commonly used to define flashover, e.g., upper layer temperature of 600°C (1100°F), flames emerging through the doorway, heat flux to the floor of 20 kW/m², etc.

Single Burning Item Test - The Single Burning Item (SBI) test method is described in a preliminary CEN standard: Reaction to Fire Tests of Building Products Excluding Floorings Exposed to a Single Burning Item (prEN 13823).

Two specimens of the material to be tested are positioned in a specimen holder frame at an angle of 90° to form an open corner section. Both specimens are 1.5 m (5 ft) high. One specimen is 1 m (40 in.) wide, and is referred to as the "long wing." The other specimen is 0.5 m (20 in.) wide and is referred to as the "short wing". During a test, the specimens are exposed to the flame of a triangular-shaped diffusion propane gas burner operating at 30 kW. The specimen holder and primary gas burner are mounted on a trolley that can be moved in and out of an enclosure of 3 ± 0.6 m (10 ± 2 ft) wide, 3 ± 0.6 m (10 ± 2 ft) deep, and 2.4 ± 0.1 m (8 ft ± 4 in.) high. The enclosure walls consist of non-combustible materials (concrete block, calcium silicate board, etc.) or gypsum board, and have windows to allow the operator to observe the test.

Prior to a test, the specimens are placed in the holder, and the trolley is rolled into the enclosure, and positioned under an insulated hood. During a test, the products of combustion are collected in the hood, and are extracted through an exhaust duct. Instrumentation is provided in the duct to measure temperature, velocity, gas composition (O_2, CO_2, and CO), and smoke obscuration. A secondary gas burner, identical in shape to the primary burner, is located permanently under the hood. This burner is primarily used for calibration and reference measurements. A sheet of calcium silicate board is attached to the secondary burner, to shield the specimens from radiation emitted by the secondary burner flame.

Temperature, velocity, gas composition, and smoke obscuration data are taken at 3-second intervals during the entire test. Baseline data are obtained during the first two minutes of a test. Two minutes after the start of a test, the secondary burner is ignited and operated at 30 kW for the next three minutes. Five minutes after the start of the test, the propane gas supply to the secondary burner is shut off. At the same time, the primary burner is ignited. During the next 20 minutes, visual observations are made of the time to ignition and upward and lateral flame spread over the surface of the long wing specimen. At the end of this 20-minute period, the gas supply to primary burner is shut off. Data are collected and observations continue for another five minutes. Hence, the standard SBI test duration is 30 minutes. A test can be terminated sooner if the heat release rate or the gas temperature rise in the exhaust duct is excessive. Materials are tested in triplicate.

The heat release and smoke production rate measurements are used to calculate two indices for product classification. The heat release and smoke production rate indices are called FIGRA and SMOGRA respectively. SBI Euroclass limits have been established on the basis of correlations between the values of the indices and performance in the ISO 9705 room/corner test.

Intermediate Scale Calorimeter - One of the limitations of the Cone Calorimeter is that only relatively small samples can be evaluated. As a result, products that have joints or layered materials with a thickness exceeding 50 mm (2 in.) can generally not be tested in the Cone Calorimeter in a representative manner. For those types of products or assemblies, a larger calorimeter is required. An example of such a calorimeter is the

ASTM Test Method for Determination of Fire and Thermal Parameters of Materials, Products, and Systems Using an Intermediate Scale Calorimeter (E 1623).

The test apparatus in ASTM E 1623 consists of an array of gas heaters, forming a vertical radiant panel with a height of approximately 1.33 m (4 ft 4 in.) and width of approximately 1.54 m (5 ft). The test specimen measures 1 × 1-m (40 × 40-in.), and is positioned parallel to the radiant panel. The heat flux to the specimen is preset to a maximum of 60 kW/m^2 by adjusting the distance to the panel. Gas flow to the panel is controlled to maintain the temperature of the panel, and consequently the heat flux to the specimen. The products of pyrolysis from the specimen are ignited with hot wires located close to, but not in contact with, the specimen at its top and bottom. The specimen is placed in a holder that is put on a load cell to measure mass loss during testing. Panel and specimen are positioned beneath the hood of a standard room/corner test.

Furniture Calorimeter - ASTM has developed three similar furniture calorimeter test standards. Precision data are available for two of the three methods: the ASTM Test Method for Fire Testing of Upholstered Furniture (E 1537) and the ASTM Test Method for Fire Testing of Stacked Chairs (E 1822).

The test item, a single piece of upholstered furniture (ASTM E 1537) or a stack of five stacking chairs (ASTM E 1822), is placed on a weighing platform and exposed to a gas burner ignition source for 80 s. ASTM E 1537 specifies that a 19.3 kW square propane burner be applied to the furniture seating surface. ASTM E 1822 requires that a 17.8 kW T-shaped propane burner be placed below the seat cushion frame of the bottom chair.

Both standards allow for three test configurations: A. the 2.4 × 3.6 × 2.4-m (8 × 12 × 8-ft) test room described in NFPA 286, B. the slightly larger 3.0 × 3.6 × 2.4-m (10 × 12 × 8-ft) test room described in California Test Procedure for Seating Furniture for Use in Public Occupancies (CAL TB 133), or C. an open calorimeter.

In the open configuration, the weight platform is located directly beneath the hood of the exhaust system. In the other configurations, the weighing platform is located in a corner of the room opposite the doorway. The construction and instrumentation of the exhaust system are identical to those specified in NFPA 286.

Precision of Heat Release Rate Measurements

Procedures for Estimating the Precision of Standard Test Methods

The repeatability and reproducibility, collectively referred to as the precision of a standard test method can be determined on the basis of an interlaboratory test program, also called a round robin. Samples of the same material are tested by a number of laboratories according to the standard test procedure. A number of replicates are tested by each laboratory under repeatability conditions.

Procedures for conducting a round robin and analyzing the results to quantify the precision of a standard test method are described in the ASTM Practice for Conducting

an Interlaboratory Study to Determine the Precision of a Test Method (E 691) and the ISO Method for Determination of Repeatability and Reproducibility of a Standard Measurement Method (5725-2). Round robins have been conducted on many standard fire test methods according to either ASTM E 691 or ISO 5725. Precision estimates obtained from oxygen consumption calorimeter round robins are summarized in subsequent sections.

Precision Estimates of Oxygen Consumption Calorimeters from Round Robins

Cone Calorimeter - More round robins have been conducted with the Cone Calorimeter than with all other oxygen consumption calorimeters combined. Since 1989, at least six interlaboratory test programs were performed. Important information concerning these round robins is summarized in Table 1. Resulting repeatability estimates for different parameters measured in the Cone Calorimeter are given in Table 2. Only repeatability is reported, because it is a measure of measurement uncertainty as will be explained below.

In the first edition of ISO 5725 published in 1986 it is recommended to report repeatability as 2.8 times the within-laboratory standard deviation. The factor 2.8 accounts for the fact that the repeatability is expressed at a 95% confidence level and refers to the difference between two single test results. However, in the second edition (ISO 5725-2: 1994), it is recommended that the repeatability standard deviation be reported. Most references in Table 1 give repeatability as a linear function of the mean, which complicates the comparison of results from different round robins. The results are therefore presented in Table 2 as the range and average of relative repeatability standard deviations obtained for the same materials and test conditions (heat flux and orientation) at different laboratories.

The repeatability estimates from rr3 are the worst for all parameters. This is due to the fact that an unusually large fraction of the materials (4 of the 6) were treated with fire retardant chemicals. It is well known that such materials lead to a higher variation of fire test results than untreated materials, in particular if the tests are conducted at heat fluxes close to the critical flux for ignition.

Table 1 - *Cone Calorimeter round robins*

ID	Reference	Year	Labs	Materials	Flux, kW/m^2	Orientation	Replicates
rr1	ISO [11]	1989	8	6	25, 50	Hor & Vert	3
rr2	ASTM [12]	1990	6	6	25, 50	Hor & Vert	3
rr3	ISR [13]	1995	4+13[1]	6	25, 35, 50	Horizontal	3-6
rr4	SAA [14]	1995	3	2	25, 50, 75	Horizontal	5
rr5	BRI [15]	1996	8	5	30, 50	Horizontal	3
rr6	BDMC [16]	2001	4	16	75	Horizontal	3

[1] Four U.S. laboratories active in ASTM and 13 member laboratories of ISO/TC92/SC1

Table 2 - *Relative repeatability standard deviation of Cone Calorimeter round robins, %*

Parameter		rr1	rr2	rr3	rr4	rr5	rr6
t_{ig}	Range	2.6-18	3.5-28	9.1-67	3.1-9.4	3.2-8.4	0.8-70
	Mean	6.5	11.6	22.8	5.6	5.9	16
$\dot{q}''_{max}$	Range	2.6-9.2	2.5-12	4.3-23	3.4-8.0	2.4-21	2.2-29
	Mean	6.2	7.1	13	5.4	6.4	10
$\dot{q}''_{180}$	Range	1.9-21	3.1-11.4	5.7-38	NR[1]	1.7-27	1.6-15
	Mean	6.6	7.4	15		12	5.5
q''_{tot}	Range	2.4-14	2.4-19	4.2-42	NR	1.8-25	2.0-32
	Mean	5.4	5.6	16		11	8.7
$\Delta h_{c,eff}$	Range	1.8-18	1.8-9.3	5.1-23	1.5-5.7	2.0-27	1.3-31
	Mean	5.3	4.5	12	3.1	14	9.5

[1] NR = not reported

Intermediate and Large Scale Calorimeters - Round robins have also been conducted with various intermediate and large-scale calorimeters. Important information concerning these round robins is summarized in Table 3. Resulting relative repeatability standard deviation estimates for different parameters are given in Table 4. These values are again presented in the form of ranges and averages. Since the materials and products evaluated in a round robin are usually representative of the range of performance for which the test method was designed, the average relative repeatability standard deviation appears to be a reasonable parameter to quantify the expected within-laboratory dispersion of test results.

Note that the average relative repeatability standard deviations are significantly higher than for the Cone Calorimeter, with RR2 being the exception. This is partly due to the fact that it is much more difficult to perform large-scale fire tests in a consistent manner, but may also be due to the small number of participating laboratories. ASTM E 691 and ISO 5725 recommend that a minimum of 8 laboratories participate. Due to the high cost associated with interlaboratory testing, which usually has to be absorbed by the laboratories, it is very difficult in practice to meet this recommendation. A smaller number of participating laboratories tend to adversely affect the precision estimates, partly because it is more difficult to identify statistical outliers.

Table 3 - *Full scale oxygen consumption calorimeter round robins*

ID	Reference	Year	Labs	Test Method	Materials	Replicates
RR1	ISR [17]	1994	12	Room/Corner (NFPA 286)	7	2
RR2	CEU [18]	1997	15	SBI (prEN 13823)	30	3
RR3	ASTM [19]	1999	3	ICAL (ASTM E 1623)	6	3-5
RR4	ASTM [20]	2000	4	Furniture (ASTM E 1537)	4	3
RR5	ASTM [20]	2000	4	Stacked Chairs (E 1822)	3	3

Table 4 - *Relative repeatability standard deviation of full scale calorimeters, %*

Parameter		RR1	RR2	RR3	RR4	RR5
$\dot{q}_{max}$	Range	14-83	4.6-28	7.0-56	16-58	29-37
	Mean	41	13	22	40	32
q_{tot}	Range	11-51	5.2-41	5.0-34	34-69	54-94
	Mean	28	17	21	50	68

Uncertainty of Heat Release Rate Measurements

Procedures for Estimating the Uncertainty of Measurements

Procedures for estimating uncertainty of measurements are described in detail in the GUM [1]. In many cases a measurand is not measured directly, but is a function of a number of specified and measured quantities. For example, according to equation (1), heat release rate is a complex function f of some specified quantities such as E and α, and a number of measured quantities such as ΔP and T_e. The uncertainty of the heat release rate can then be estimated on the basis of the uncertainties associated with the specified and measured quantities according to the following equation:

$$u_{\dot{q}} = k\sqrt{\left(\frac{\partial f}{\partial E}u_E\right)^2 + \left(\frac{\partial f}{\partial \alpha}u_\alpha\right)^2 + \left(\frac{\partial f}{\partial \Delta P}u_{\Delta P}\right)^2 + \left(\frac{\partial f}{\partial T_e}u_{T_e}\right)^2 + \ldots} \qquad (3)$$

where k is a "coverage factor" to adjust the uncertainty estimate to the desired confidence level. The "standard" uncertainty ($k = 1$) gives a confidence level of 63%. A coverage factor of 2 corresponds to a confidence level of 95%. As far as the uncertainties of the specified and measured quantities are concerned, the GUM makes a distinction between two types. Type A uncertainties pertain to random variables and are estimated on the basis of statistical analysis of repeat measurements. Type B uncertainties are based on judgment or specifications.

Oxygen Consumption Calorimetry Uncertainty Estimates

Several investigators have estimated the uncertainty of heat release rate measurements for different oxygen consumption calorimeters according to the procedure specified in the GUM. The main results and some additional information concerning theses studies are presented in Table 5.

Table 5 - *Theoretical uncertainty estimates of oxygen consumption calorimeters*

Test Method	Standard uncertainty[1]	Reference
10 MW calorimeter	3.5 - 6%	Dahlberg [21]
Cone Calorimeter	≥ 2.5%	Enright and Fleischmann [22]
ISO 9705 room test	5.5% at 150 kW 3.55% at 1 MW	Axelsson et al. [23]
prEN 13823 SBI Test	7% at 35 kW 5% at 50 kW	Axelsson et al. [23]

[1]The values in [21-23] are based on a coverage factor of 2 and have been divided by 2

Discrepancies Between Precision and Uncertainty

Intuitively it is clear that there is a relationship between the precision of a test method and the uncertainty of its measurements. The left-hand side in Figure 1 depicts the results of a hypothetical round robin performed under ideal conditions. Systematic errors have been eliminated and a very large (infinite) number of repeated measurements have been performed in each laboratory. Under such ideal conditions, the repeatability would be the same in each laboratory, and s_r would also be identical to the standard uncertainty of the measurement.

In the real world it is not possible to completely eliminate systematic errors, and each laboratory has some bias. Moreover, it is usually not feasible to conduct a large number of repeat measurements due to cost and time constraints. The right-hand side in

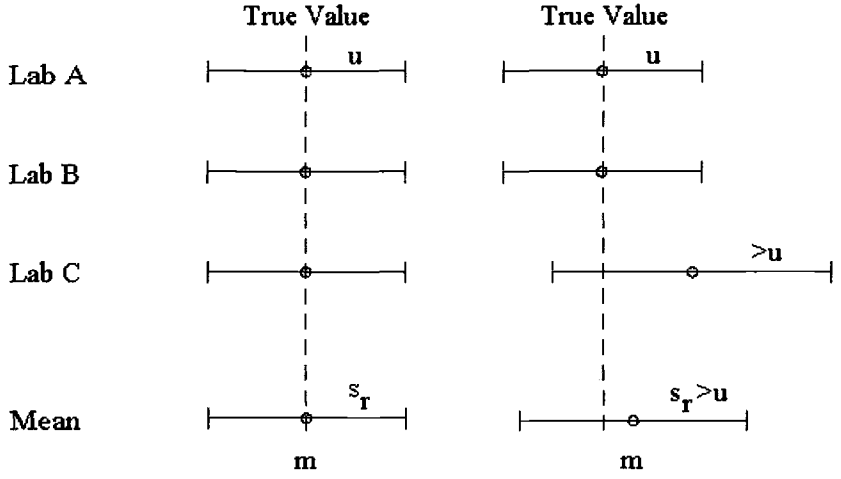

Figure 1 - *Relationship between repeatability and uncertainty*

Figure 1 shows the results of a round robin where the measurements in one of the three participating laboratories have a systematic error and a larger random error than the measurements in the other two laboratories. The situation in the real world would be even worse, with systematic errors and increased random errors in all laboratories. It is obvious from this picture that the repeatability standard deviation under those conditions must exceed the theoretical standard uncertainty.

In practice it is not possible to achieve the theoretical uncertainty, and the repeatability standard deviation from a carefully conducted round robin involving competent laboratories should give a much more realistic measure of the uncertainty.

A comparison between Tables 2, 4, and 5 confirms that the repeatability standard deviation of oxygen consumption calorimeters is indeed larger than the theoretical uncertainty estimates. The discrepancies are actually even larger because the theoretical uncertainty estimates account for uncertainties in specified quantities, while the repeatability standard deviations do not (every laboratory uses the same values for E and α). However, the theoretical uncertainties in Table 5 are significantly underestimated because they do not account for variations in the thermal exposure conditions (cone heater in the Cone Calorimeter, ignition burner in the full-scale tests), material variability, and dynamic effects. The latter is in our opinion a major source of uncertainty. Dynamic uncertainties can be reduced by accounting for the response characteristics of the instruments [24], or by accounting for the transport time and specifying limits for the response time of each instrument [25].

Proposed Procedure for Establishing Uncertainty of Heat Release Rate Measurements

Again, in looking at the data presented in Tables 2, 4, and 5 it is clear that some repeatability standard deviations are reasonably close (within a factor of 2 or 3) to the theoretical uncertainty estimates, while others are way off (by as much as a factor of 12, assuming the ISO 9705 uncertainty estimates are representative for the ICAL and the furniture calorimeters). Most of the Cone Calorimeter round robins and the SBI round robin are of the first category. These are examples of carefully conducted round robins with competent participating laboratories. The room/corner and furniture calorimeter round robins are of the second category. The disappointing results of these round robins may be attributed to material selection (too many fire-retardant-treated materials) or the fact that some participating laboratories may not have followed the standard.

It is proposed that a proficiency program be established by ASTM Committee E05 to obtain realistic uncertainty estimates for these and future heat release methods for which reliable round robins have not yet been conducted. The idea of using proficiency programs to determine the uncertainty of standard test methods is used with success by other committees in ASTM. The proposed proficiency program would be similar to the pre-round-robin calibrations and measurements that were performed prior to rr6 [16] and RR2 [18], and could involve the following steps:

- Determine transport times, response characteristics, noise, and drift of individual instruments;
- Perform multiple gas burner and/or liquid pool fire calibrations to reduce bias systematic errors and determine uncertainty; and
- Perform tests with standard reference materials, if available, to verify the uncertainty estimates.

References

[1] "Guide to the Expression of Uncertainty in Measurement," International Organization for Standardization, Geneva, Switzerland, 1993.

[2] Babrauskas, V., and Peacock, R., "Heat Release Rate: The Single Most Important Variable in Fire Hazard," *Fire Safety Journal*, Vol 18, 1992, pp. 255-272.

[3] Thornton, W., "The Relation of Oxygen to the Heat of Combustion of Organic Compounds," *Philosophical Magazine and J. of Science*, Vol. 33, 1917.

[4] Huggett, C., "Estimation of the Rate of Heat Release by Means of Oxygen Consumption," *Journal of Fire and Materials,* Vol 12, 1980, pp. 61-65.

[5] Hinkley, P., Wraight, H., and Wadley, A., "Rates of Heat Output and Heat Transfer in the Fire Propagation Test," Fire Research Note No. 709, Fire Research Station, Borehamwood, England, 1968.

[6] Parker, W., "An Investigation of the Fire Environment in the ASTM E-84 Tunnel Test," NBS Technical Note 945, National Bureau of Standards, Gaithersburg, MD, 1977.

[7] Sensenig, D., "An Oxygen Consumption Technique for Determining the Contribution of Interior Wall Finishes to Room Fires," NBS Technical Note 1128, National Bureau of Standards, Gaithersburg, MD, 1980.

[8] Parker, W., "Calculations of the Heat Release Rate by Oxygen Consumption for Various Applications," NBSIR 81-2427, National Bureau of Standards, Gaithersburg, MD, 1982.

[9] Janssens, M., "Measuring Rate of Heat Release by Oxygen Consumption," *Fire Technology*, Vol. 27, 1991, pp. 234-249.

[10] Brohez, S., Delvosalle, C., Marlair, G., and Tewarson, A., "Measurement of Heat Release from Oxygen Consumption in Sooty Fires," *Journal of Fire Sciences*, Vol. 18, 2000, pp. 327-353.

[11] Janssens, M., "Report to ISO on Cone Calorimeter Inter-Laboratory Trials," ISO/TC92/SC1/WG5, 1989.

[12] Babrauskas, V., "Report to ASTM on Cone Calorimeter Inter-Laboratory Trials," ASTM E05.21.60, ASTM, Philadelphia, PA, 1990.

[13] Janssens, M., "Inter-Laboratory Test Program on ASTM E 1354 Standard Test Method for Heat and Visible Smoke Release Rates for Materials and Products Using an Oxygen Consumption Calorimeter," International Fire Standards Project Report PCN 33-000015-31, ASTM Institute for Standards Research, Philadelphia, PA, 1995.

[14] Apte, V., "A Report on Preliminary Inter-Laboratory Trials on Cone Calorimeter," Workcover Authority, Londonderry Occupational Safety Centre, Londonderry, NSW, Australia, 1995.

[15] Marchal, A., Yoshida, M., Hasemi, Y., "Asia-Oceania ISO 5660 Cone Calorimeter Inter-Laboratory Trials," *Thirteenth Meeting of the UJNR Panel on Fire Research and Safety, March 13-20, 1996, Volume 2, NISTIR 6030*, K. A. Beall, Ed., National Institute of Standards and Technology, Gaithersburg, MD, 1997, pp. 173-214.

[16] Urbas, J., "BDMC Interlaboratory Cone Calorimeter Test Program," *Journal of Fire and Materials,* in press.

[17] Beitel, J., "Inter-Laboratory Test Program on Proposed ASTM Standard Method for Room Fire Test of Wall and Ceiling Materials," International Fire Standards Project Report PCN 33-000012-31, ASTM Institute for Standards Research, Philadelphia, PA, 1994.

[18] Van Mierlo, R., "Development of the Single Burning Item Test - Results of the SBI Round Robin Tests," European Commission, Directorate General III, Brussels, Belgium, 1997.

[19] Hirschler, M., "An Intermediate Scale Calorimetry Test: ICAL (ASTM E 1623) Precision (Repeatability and Reproducibility) and Applications," *New Advances in Flame Retardant Technology, October 24-27, 1999, Tucson, AZ,* Fire Retardant Chemicals Association, Lancaster, PA, 1999, pp. 117-149.

[20] Fritz, T., "Test Methods E 1537 & E 1822 Inter-Laboratory Precision Study," ASTM E05.15, ASTM, West Conshohocken, 2000.

[21] Dahlberg, M., "Error Analysis for Heat Release Rate Measurements with the SP Industry Calorimeter," SP Report 1994:29, Swedish National Testing and Research Institute, Borås, Sweden, 1994.

[22] Enright, P., and Fleischmann, C., "Uncertainty of Heat Release Rate Calculation of the ISO 5660-1 Cone Calorimeter Standard Test Method," *Fire Technology*, Vol. 35, 1999, pp. 153-169.

[23] Axelsson, J., Andersson, P., Lönnermark, A., and Van Hees, P., "Uncertainty of HRR and SPR Measurements in SBI and Room/Corner Test," *Interflam 2001,September 17-19, 2001*, Interscience Communications, London, England, 2001, pp. 507-518.

[24] Dietenberger, M., and Grexa, O., "Analytical Model of Flame Spread in Full-Scale Room/Corner Tests (ISO 9705)," *Fire and Materials '99, February 22-23, 1999, San Antonio, TX*, Interscience Communications, London, England, 1999, pp. 211-222.

[25] Messerschmidt, B., and van Hees, P., "Influence of Delay Times and Response Times on Heat Release Rate Measurements," *Journal of Fire and Materials*, Vol. 24, 2000, pp. 121-130.

J. Randall Lawson[1] and Robert L. Vettori[2]

Thermal Measurements for Fire Fighters' Protective Clothing[3]

Reference: Lawson, J. R. and Vetton, R. L., **"Thermal Measurements for Fire Fighters' Protective Clothing,"** *Thermal Measurements: The Foundation of Fire Standards, ASTM STP 1427,* L. A. Gritzo and N. J. Alvares, Eds., ASTM International, West Conshohocken, PA, 2002.

Abstract: Current test methods used for quantifying the thermal performance of fire fighters' protective clothing are not providing information needed to understand why fire fighters are being burned. Many of the thermal exposures where fire fighters receive serious burn injuries are much lower than those specified in current test methods. In addition, current test methods do not provide a means to measure performance changes associated with wet garment systems. New test apparatus have been developed for measuring thermal performance of protective clothing systems. A wide range of thermal exposures can be replicated. These test apparatus can measure the thermal performance of protective clothing systems that are dry or wet and also measure performance changes associated with garment compression. This is an overview of measurement issues critical to the development of standards for fire fighters' protective clothing and the safety of fire service personnel. Research efforts addressed in this document have been supported in part by the United States Fire Administration and the National Institute for Occupational Safety and Health.

Keywords: burns, fire fighters, heat flux, predictive models, protective clothing, sensors, temperature measurements, test methods, thermal properties

Thousands of fire fighters are seriously burned each year and many lose their lives while exposed to fire fighting environments [1]. Work is underway at the National Institute of Standards and Technology (NIST) to identify measurement needs for developing a better understanding of thermal performance for fire fighters' protective clothing and equipment. This research is not only providing insight related to thermal performance measurements, it is addressing important safety issues for the fire fighters that use this equipment. Thermal measurements in protective clothing systems are complex as a result of fabric movement, compression, changes in spacing and garment ease, and the dynamic

[1] Physical Scientist, Building and Fire Research Laboratory, National Institute of Standards and Technology (NIST), Gaithersburg, MD 20899.
[2] Fire Protection Engineer, Building and Fire Research Laboratory, National Institute of Standards and Technology (NIST), Gaithersburg, MD 20899.
[3] Contribution of the National Institute of Standards and Technology. Not subject to copyright.

of fabric movement, compression, changes in spacing and garment ease, and the dynamic movement of moisture in protective clothing while it is being used and heated from fire environments. It is documented that the current thermal measurement method used for fire fighter protective clothing product certification is overestimating performance related to the potential for human burn injury. The ability to accurately measure the thermal response of fire fighters' protective clothing to well controlled and quantified thermal environments is the primary function that provides critical information needed for understanding the actual field use performance of the clothing. Development of these measurement data and the analysis of these data should be an initial step in designing protective clothing systems. In addition, the accurate measurement of protective clothing material's thermal properties is essential for accurately predicting the thermal behavior of the protective clothing systems when exposed to a wide range of fire fighting thermal environments. The analysis of these measurement data and thermal performance predictions generated from thermal property measurements should be used to develop materials for training fire fighters in the proper use and limitations of their protective clothing systems. Currently, the understanding of how fire fighters' protective clothing systems really work in the field is only discovered through field use. Unfortunately, learning how protective clothing really works by use in the field sometimes leads to serious injury. This document provides an overview of current measurement technology that is assisting in the advancement of thermal performance for fire fighters' protective clothing.

Fire Fighting Thermal Environments

The primary thermal exposures that a fire fighter must be concerned with are thermal radiation from flames, smoke, hot gas convection, and conduction from high temperature surfaces [2]. Each of these heat transfer modes has an impact on the thermal performance of fire fighters' protective clothing, and they all can independently cause burn injuries. However, in actual fire fighting situations these different components of heat transfer will likely be combined in varying fractions depending on the location and position of the fire fighter in relation to the fire's varying thermal environment. The fact that the component fractions of heat transfer vary during an exposure complicates the measurement process and increases the measurement uncertainty.

Another factor that varies during the process of measuring heat transfer through fire fighters' protective clothing systems is the amount of moisture in the system. Moisture is often a significant factor in the creation of fire fighter burn injuries. The moisture in fire fighters' protective clothing originates from human perspiration, hose spray, and weather. Moisture levels can be controlled to some degree when making thermal measurements in laboratory test environments. These laboratory environments initially provide a stable level of control over wetting and moisture conditions at the beginning of a thermal exposure. The protective clothing systems then respond to heating processes and begin to dry. Controlling moisture input to the protective clothing system after heating begins is difficult and accurately replicating wetting processes that take place in the field environment is difficult. However, basic information on wet thermal performance can be

gained by studying the drying processes of wet protective clothing systems and applying this knowledge to physics based predictive models.

Sensors and Measurements

To understand the thermal performance of fire fighters' protective clothing one must first measure the thermal environment around the fire fighter at any point in time while the person is doing their fire fighting job. Thermal radiation, total heat flux, and gas temperature measurements are used to quantify these environments. In addition, the impact of the surrounding environment on the fire fighter is measured by instrumenting the thermal protective clothing. This protective clothing instrumentation is located on the exterior surface of the clothing and inside the garment. Measurements inside the garment provide insight into not only how heat moves through the garment system but also help to understand how moisture moves through the protective clothing upon being heated. These interior measurements are typically made using thermocouples, thermistors, and small heat flux sensors. Use of each measurement device mentioned above varies with whether it is applied in the laboratory or the field.

Laboratory versus Field Measurements

Laboratory tests alone do not provide all of the information needed for accessing the thermal performance of fire fighters' protective clothing. Certain measurements must be made while protective clothing systems are actually being used by fire fighters or worn by an instrumented manikin. Making thermal response measurements for protective clothing in field environments generally adds difficulty to the measurement process. Field measurements are often much more complicated to conduct than laboratory based measurements. Issues associated with these two means of measurement are:

Laboratory:

- Measurements are usually made under highly controlled conditions.
  Laboratory temperature, humidity, and air circulation
- Instrumentation is easily maintained and calibrated.
- Measurements are typically made in fixed test facilities using standardized test apparatus.
- Data logging is typically accomplished with the use of fixed data logging systems.

Field Measurements:

- Environmental conditions vary with the test location, time of day and year, and changing local weather conditions.
- It is more difficult to maintain and keep instruments calibrated.
- Providing cooling fluids for sustained heat flux measurements is much more difficult.
- Measurements are often made where humans or manikins experience dynamic movement. Instrument placement and attachment becomes critical.

- Data logging systems are small and often carried by humans or placed on manikin test subjects.
- Because field operated data loggers have limited capability fewer data channels are usually available.

From the above list, it is apparent that an accurate log of changing weather conditions is necessary while conducting field experiments. Issues associated with maintaining adequate fluids at appropriate temperatures for cooling heat flux gauges are important since test subjects may have to carry the fluids that produce the needed cooling. This additional weight may actually influence the performance of the individual taking part in the protective clothing test and may alter the results. Also since fewer data channels are usually available for recording measurements in the field, it is important to develop a logical set of measurements that may be correlated with other experiments, including those made in the laboratory.

Temperature Measurements

To understand the thermal performance of fire fighters' protective clothing, thermal measurements must be made to quantify the thermal environment around the individual wearing the protective clothing. In addition, thermal measurements must be made on the surface of the protective clothing and inside of the protective clothing systems in order to quantify heat transfer through the clothing. In many cases, these measurements are used to predict if and when a fire fighter will receive a burn injury. The selection of temperature measurement devices is important for obtaining data that is appropriate for its final use. In addition, temperature measurements for protective clothing are strongly affected by the way the temperature measurement device is attached to and placed on or within the protective clothing system. Thermocouples have been the primary means of measuring temperature since modern forms of data logging came into existence.

Thermocouples are often selected for measuring temperature changes in fire testing. They are used to measure gas temperatures, surface temperatures, and the temperature of liquids and solids. The American Society for Testing and Materials (ASTM) Manual on the Use of Thermocouples in Temperature Measurement [3] suggests that a heat collecting pad attached to a thermocouple may be the best way to obtain an accurate surface temperature for materials that have a low thermal conductivity. Experiments with a range of thermocouple types, attachment methods and configurations, including heat collecting pads have been done [4][5]. These tests were conducted on the radiant panel apparatus described in the following section on test methods. One successful thermocouple attachment method, figure 1, is compared with temperature measurements made with a small heat collecting copper pad, figure 2.

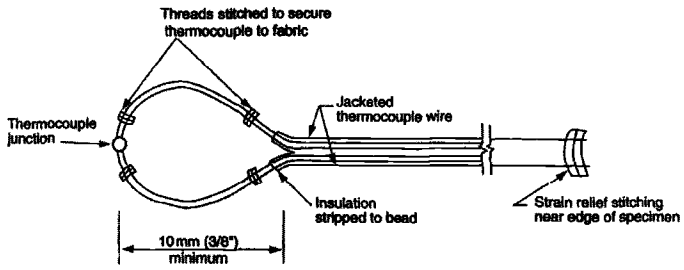

Fig. 1 — *Thermocouple attachment to protective clothing fabrics [4].*

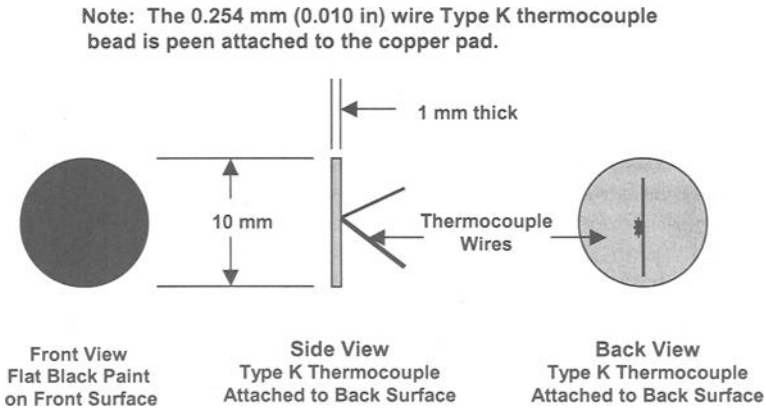

Fig. 2 — *Heat collecting pad thermocouple.*

Each of the thermocouple measurement systems shown above used 0.254 mm (0.010 in) diameter type K thermocouples. The thermocouple attachment method shown in figure 1 is described in detail in NISTIR 6400 [4]. Basically, the thermocouples were held in place against the fabric by making loop stitches across the bare thermocouple wires at the four places shown. Heat resistant thread was used. In addition, strain relief stitches were formed around the insulating jacket of the thermocouple wire. The heat collecting pad thermocouple was attached to the fabric by stitching across the back of the copper pad

with heat resistant thread. The stitch pattern formed an X across the back side of the pad and held it flush with the fabric. Results of these measurements from a square wave exposure at 2.5 kW/m^2 are shown below in figure 3.

From these data it is clear that the temperature lag associated with the copper heat collecting pad is a significant disadvantage when attempting to measure rapidly changing temperatures that are affecting the performance of protective clothing and producing burn injuries. It should be noted that the copper pad is exhibiting slightly higher temperatures at the peak value and significantly higher temperatures when cooling. Another series of tests, reported in NISTIR 6750 [5], showed similar results. In this work a type K and a type J thermocouple are compared to a larger copper pad thermocouple system. The copper pad used a 0.254 mm (0.010 in) diameter wire type J thermocouple. The 39.9 mm (1.6 in) copper pad thermocouple system is described in reference [5]. The bare bead type K and type J thermocouples were also 0.254 mm (0.010 in) diameter wires. The copper pad thermocouple is shown in figure 4, and the test setup for the measurement experiments is shown in figure 5.

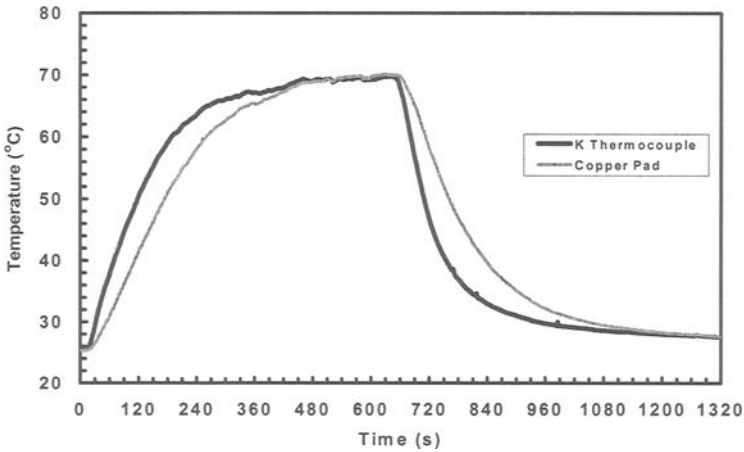

Fig. 3 — *Comparison of bare thermocouple to a heat collecting pad thermocouple.*

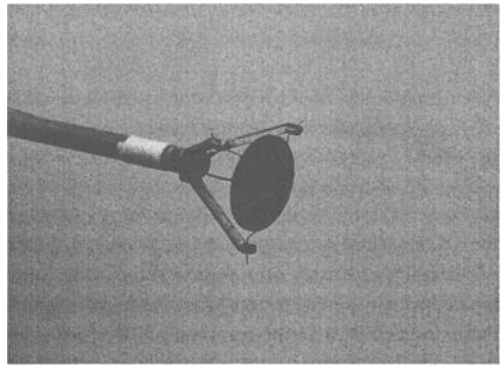

Fig. 4 — *Large heat collecting copper pad thermocouple system [5].*

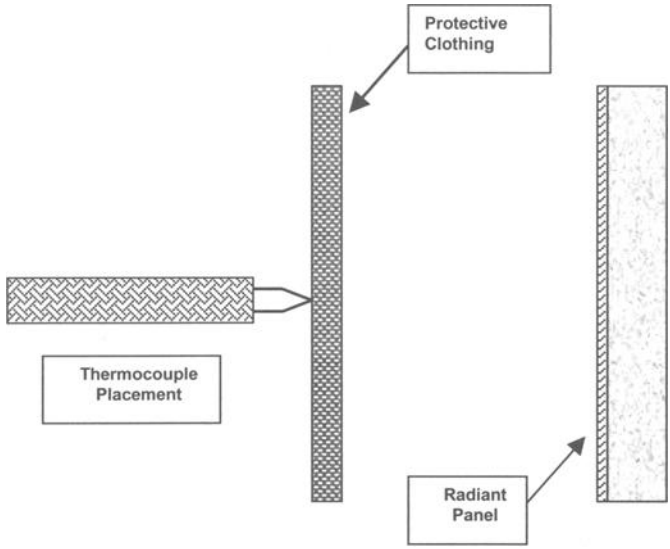

Fig. 5 — *Arrangement for thermocouple and copper pad tests [5].*

Data plots from these experiments exhibiting thermocouple temperature increase, not the actual test temperature rise as presented in figure 3, are given in figure 6. The total heat flux exposure for the tests shown in figure 6 was 5.0 kW/m^2. These plots show, as would be expected, that the more massive copper pad has a significantly longer thermal lag. In

addition, it is shown that the type K thermocouple appears to provide a faster response time as compared to the type J thermocouple and the copper pad. However, the copper pad system does show a significantly higher temperature after about 200 s. These data suggest that the faster response measurements produced by the type K thermocouple may be more useful when studying rapid temperature changes that produce burn injuries. Although when looking at longer heating periods, the copper pad thermocouple system is likely to provide a more accurate peak temperature measurement.

One additional issue that has become apparent while measuring the thermal performance of fire fighters' protective clothing is that temperature measurements made on fabrics show significant variation. Much of this measurement variation has been found to be associated with fabric movement. Fabric movement easily changes the air space between garment layers, and this movement can result in temperature measurement variations of about ±8 °C (±14 °F) or more [4].

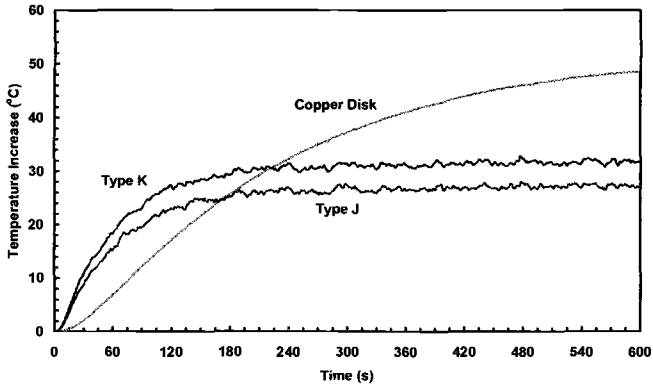

Fig. 6 — *Comparison of bare thermocouples to a copper pad thermocouple system [5].*

Heat Flux Measurements

Heat flux measurements in the evaluation of thermal performance of fire fighters' protective clothing are needed for determining heat transfer rates through the garment systems and also for predicting the potential for burn injury. The measurements have traditionally been accomplished using copper slug calorimeters. These calorimeters have been useful in laboratory measurements for ASTM and National Fire Protection Association (NFPA) standards for thermal protective clothing. The primary use of these calorimeters has been with the TPP (Thermal Protective Performance) test. The original test method, ASTM D 4108, Standard Test Method for Thermal Protective Performance

of Materials for Clothing by Open-Flame Method, led the way for development of additional test methods using the same measurement techniques. NFPA 1971 [6] modified D 4108 and applied it to fire fighters' protective clothing. The result of the test method development made a significant improvement in the thermal performance of fire service protective clothing. But more recently, a number of research efforts have shown that the copper calorimeter has design problems and that the results can be misleading [7][8].

According to findings from NISTIR 6750 [5], water cooled Schmidt-Boelter gauges may provide a solution to the accuracy and time limitations associated with proper use of the copper calorimeter measurements. At times, the copper calorimeter used with the NFPA 1971 TPP test has been referred to as a skin simulant sensor. However, the thermal properties of the copper calorimeters do not replicate human tissue properties.

Skin Simulant Sensors

Currently, there are several thermocouple based heat flux gauges that are referred to as skin simulant sensors. These are primarily sensors that are being used with instrumented manikin test systems. The sensors by themselves do not actually replicate human tissue thermal properties. These sensors are linked to complex computer programs that are designed to collect results from the sensors and then mathematically calculate predictions for burn injury. New sensor systems being developed by Keltner [8][9] and North Carolina State University (NCSU) [10] are attempting to improve the measurement capabilities for protective clothing systems. The sensor by Keltner is being designed to closely replicate the thermal properties of human skin relative to its heating rate. The NCSU sensor is designed to improve measurement capabilities with instrumented manikin testing.

Test Methods

NFPA 1971 specifies one test method for measuring heat transfer through fire fighters' protective clothing [6]. This test method is recognized as the TPP test (Thermal Protective Performance test). It uses a bank of quartz radiant tubes and two Meeker burners as a heat source. According to the standard, these two modes of heating are balanced to provide a 50/50 radiant and convection heat source for the protective garment test specimens. A copper disk slug calorimeter is placed against the back surface of the test specimen and the outer shell material is directed toward the heat source. This method has been instrumental in providing a means for estimating thermal performance. However, there are several issues related to the test apparatus and method that have caused technically heated discussions. Some of the important issues are: 1) the quartz heaters do not provide a sufficient range of infrared radiant energy to replicate actual fire exposures; 2) the copper slug calorimeter is constructed with multiple thermocouples attached to it, and its wiring connections create inaccurate data output; 3) the copper calorimeter is being used to make test measurements in excess of 30 s where the instrument output is questionable because of nonlinear performance; 4) the test method does not provide enough data to determine the thermal response of each component of the

protective system; 5) the test method is only designed to measure the thermal response of specimens exposed to a mid-range (84 kW/m^2) post-flashover fire environment; and 6) the burn prediction estimates generated by the test predict a longer time to burn injury than is actually the case in real fire fighting environments [9][10]. As a result of these issues, NIST has developed two new test apparatus that provide more detailed information on the thermal performance of fire fighters' protective clothing. These test apparatus are described in two NIST reports NISTIR 6400 [4] and NISTIR 6502 [11]. The first report, NISTIR 6400, describes a test apparatus that can be used to measure the thermal response of protective clothing systems while exposed to a wide range of thermal environments. Radiant heat for this test is generated from a gas fired radiant panel that produces an infrared spectrum extending across the full range produced by common structural and liquid pool fires. In addition, the specimens may be tested over a range of exposures from a low-level solar flux to a post-flashover fire. The post-flashover fire exposure may also include the addition of flames sweeping over the specimen's surface.

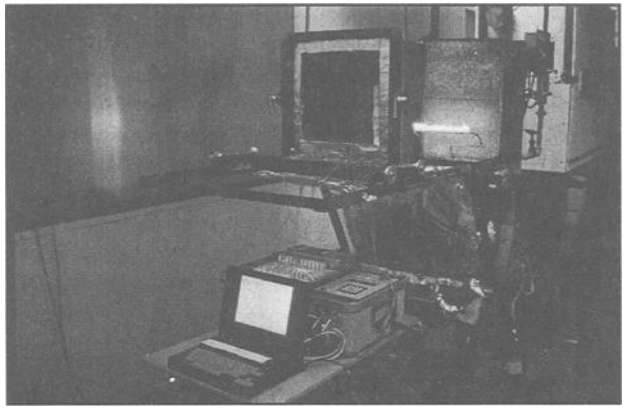

Fig. 7 — *Protective clothing thermal response test apparatus [4].*

The second test apparatus measures the thermal response of protective clothing systems to hot water or hot surfaces. This test apparatus allows the protective clothing specimens to be evaluated while undergoing dynamic compression. The apparatus compresses the protective clothing system against a flooring material submerged in a hot liquid or against a dry hot surface, and it is focused on measuring the thermal response of protective clothing systems to heat conduction. However, in the hot water bath tests, moisture absorption by protective clothing has been shown to significantly influence test results. Each of these test apparatus allows for specimens to be evaluated while wet or dry.

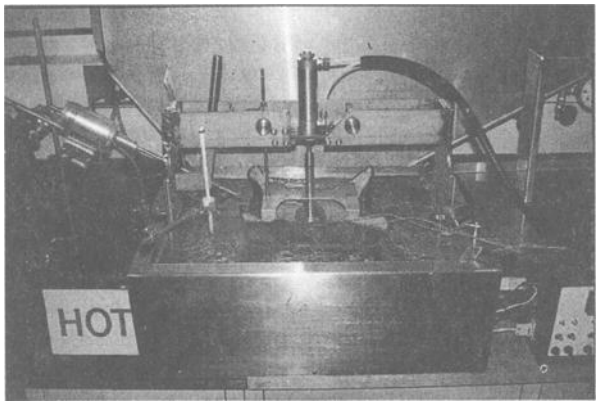

Fig. 8 — *Wet protective clothing dynamic compression test apparatus [11].*

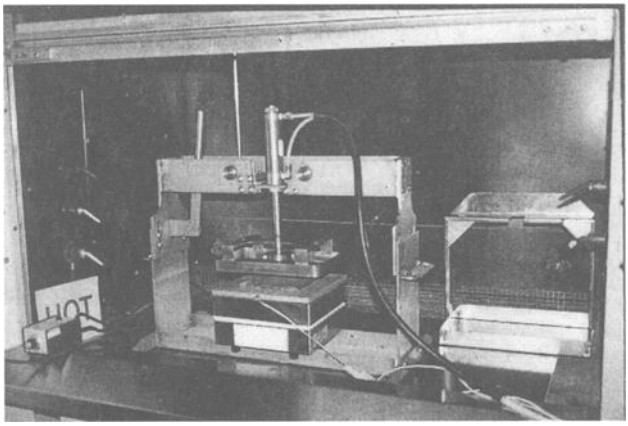

Fig. 9 — *Dry protective clothing dynamic compression test apparatus [11].*

Test data from the radiant panel test apparatus, figure 7, are shown in figures 3 and 6. A set of compressive test data exhibiting thermal response results for two different knee pad designs for fire fighters' protective clothing are shown in figure 10. These data were generated using the test apparatus assemblies shown in figures 8 and 9. Each of the tests, wet and dry, was conducted using the same compression sensor with a surface area of 3710 mm^2 (5.75 in^2) and the same compression force, 133 kPa (19.3 lbf/in^2). Surface temperatures for the tests were different. The wet test was conducted with a water temperature of 90 °C ± 2 °C (194 °F ± 4 °F). The dry test was conducted with a copper

plate surface temperature of 260 °C ± 2 °C (500 °F ± 4 °F). The knee pad designs, 3 and 4, were basically identical except that they had different types of thermal padding. Each of the knee pad designs had an impermeable moisture barrier material incorporated in the system that prevented hot water and hot water vapors from penetrating the padding system and entering the inside of the garment. These data plots in figure 10 show that thermal response of protective clothing systems can vary significantly depending on the type of thermal exposure. Design 4 performs very well when tested in the hot water bath, but it exhibits a significantly higher rate of temperature rise than design 3 when compressed on the dry hot surface [11]. The thermal protective padding in design 4 was made from a material that would degrade when exposed to dry heat test conditions. These data demonstrate the importance of measuring the thermal performance of thermal protective clothing systems while exposed to a range of thermal environments, including wet and dry test conditions.

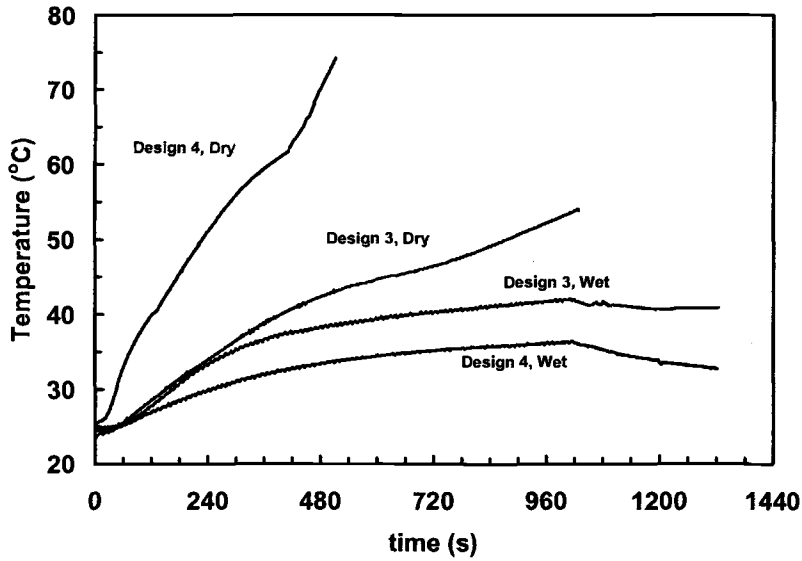

Fig. 10 — *Comparison of wet and dry compressive thermal performance [11].*

Thermo-physical Properties Measurements

Another area where measurement technology is important to the study of fire fighters' protective clothing is the measurement of thermo-physical properties and the application of these measurement data to predicting thermal performance. A greater understanding of thermal performance is often gained by modeling the thermal response of materials to elevated temperature conditions or simulated fire exposures. Computer models are being

developed to assist industry in the design of new protective clothing systems, assist as a tool for the fire service in selecting protective clothing, and will assist in training fire fighters concerning the thermal performance of their equipment. The models will also play a role in the investigation of fire fighter injury cases. One thermal protective clothing heat transfer model was recently developed by NIST and is described in NISTIR 6299 [12]. This one-dimensional model predicts changes in temperature gradient through thermal protective clothing as it heats from exposures to thermal radiation. The model currently predicts heat transfer for dry clothing systems and is being updated to include garment compression and moisture predictions. The following thermo-physical properties are currently being measured and used for predicting the thermal performance of fire fighters' protective clothing: density, thermal conductivity, specific heat or heat capacity, and the thermo-optical properties of transmissivity, reflectivity, and absorptivity. All of these properties are relatively easy to measure when the materials are dry and are at room temperature, and this is a reasonable starting point for developing the data sets. However, fire fighters don't typically work in this type of environment when they are fighting fires. Fire fighters are typically wet and their protective clothing is heated from thermal radiation and hot gas convection when fire fighting. Thermal property measurements become extremely difficult when materials are wet or degraded from thermal exposure, and confidence levels for measurements of wet or thermally degraded materials are low. As a result, NIST is in the process of developing measurement methods and analytical techniques that are expected to improve the measurement uncertainty and thermal performance predictions for wet materials. This work is currently underway and will be discussed in future reports.

Uncertainty

Measurement uncertainty for each of the above test results is described in detail in the associated reference. The uncertainties listed here represent maximum measurement deviations that are expected from the measured data and are obtained from instrument literature or the referenced reports. See NISTIR 6400 [4] for a detailed description of uncertainty for the radiant panel test apparatus. The maximum estimated deviation for the measured values for the radiant panel test apparatus discussed above fell within a range of ±8 °C (±14 °F). Uncertainty for test results from the compression test apparatus described in NISTIR 6502 [11] was estimated to be less than ±5 °C (±9 °F) when the compressive force of 133 kPa (19.3 lbf/in^2) is applied. Temperature measurement variations are expected to be larger if compression force is varied by more than ± 14 kPa (± 2 lbf/in^2). Measurements presented in this document from NISTIR 6750 [5] for incident radiant flux had an uncertainty estimate of ± 3 % with an increased variation of ± 0.6 % with a ± 2 mm (± 0.1 in) change in sensor distance from the desired measurement location.

Summary and Conclusions

Advances in materials, design, and construction of fire fighters' protective clothing and the aggressive use of the protective clothing in fire fighting has led to the need for a better understanding of the gear's thermal performance. This need for a better

understanding is primarily driven by the fact that thousands of fire fighters are continuing to be seriously burned. NIST with the support of the United States Fire Administration and the National Institute for Occupational Safety and Health has been studying the application of current measurement methods used to certify protective clothing systems. In addition, NIST is advancing measurement technology through the development of new test apparatus, measurement techniques, and methods for predicting thermal response of the gear to a wide range of thermal environments. Conclusions from this effort are: 1) fire fighters' protective clothing thermal performance must be evaluated while dry, when wet, in full loft and when fully compressed, 2) it is apparent that thermocouple pad temperature measurement devices can create significant errors when attempting to measure heat transfer in protective clothing systems, and 3) a greater understanding of thermal performance may be gained by using materials thermal properties to model the behavior of protective clothing systems. These new measurement techniques and approaches to predicting thermal performance will provide opportunities for improving fire fighters' protective clothing. In addition, their application to the design of protective clothing and training in the fire service has the potential for reducing the number of serious burn injuries experienced by fire fighters.

Acknowledgements

Appreciation is extended to Mr. Robert T. McCarthy of the United States Fire Administration for assistance with this project. The United States Fire Administration, the National Institute of Occupational Safety and Health, and the National Institute of Standards and Technology provided funding for this work. Appreciation is extended to Mr. William Twilley of the Building and Fire Research Laboratory (NIST) for his assistance in the development of the experimental test apparatus and test data for this report.

References

[1] Karter, Michael J. Jr., and Badger, Stephen G., *1999 United States Firefighter Injuries*, NFPA Journal, Quincy, MA, November/December, 2000.

[2] Lawson, J. Randall, *Fire Fighter's Protective Clothing and Thermal Environments of Structural Fire Fighting*, NISTIR 5804, National Institute of Standards and Technology, Gaithersburg, MD, August 1996.

[3] American Society for Testing and Materials, *Manual on the Use of Thermocouples in Temperature Measurement*, Fourth Edition, Philadelphia, PA 1993.

[4] Lawson, J. Randall and Twilley, William H., *Development of an Apparatus for Measuring the Thermal Performance of Fire Fighters' Protective Clothing,* NISTIR 6400, National Institute of Standards and Technology, Gaithersburg, MD, October 1999.

[5] Vettori, Robert L., Twilley, William H., Stroup, David, W., *Measurement Techniques for Low Heat Flux Exposures to Fire Fighters Protective Clothing*, NISTIR 6750, National Institute of Standards and Technology, Gaithersburg, MD, June 2001.

[6] National Fire Protection Association, *NFPA 1971 Standard on Protective Ensemble for Structural Fire Fighting 2000 Edition,* Quincy, MA, 2000.

[7] Krasny, John F.; Rockett, John A.; Huang, Dingyi, *Protecting Fire Fighters Exposed in Room Fires: Comparison of Results of Bench Scale Test For Thermal Protection and Conditions During Room Flashover, Fire Technology*, National Fire Protection Assoiation, Quincy, MA, February 1988.

[8] Keltner, N.R. et al, "New Methods for Evaluating Thermal Performance of Protective Clothing for Fire Fighters," Ktech Document TR98-01, Ktech Corporation, Albuquerque, NM. Submitted to United States Department of Commerce, Small Business Innovative Research Program, Contract Number 50-DKNB-7-90134, 1998.

[9] Gagnon, Brian David, *Evaluation of New Test Methods for Fire Fighting Clothing, A Thesis,* Worcester Polytechnic Institute, Worcester, MA, May 2000.

[10] North Carolina State University, *Evaluating the Effects of Moisture on the Thermal Performance of Firefighter Protective Clothing in Low Level Heat Exposures,* The Center for Research on Textile Protection and Comfort, Raleigh, NC, 2001.

[11] Lawson, J. Randall, Twilley, William H., and Malley, Kevin S., *Development of a Dynamic Compression Test Apparatus for Measuring Thermal Performance of Fire Fighters' Protective Clothing*, NISTIR 6502, National Institute of Standards and Technology, Gaithersburg, MD, April 2000.

[12] Mell, William E. and Lawson, J. Randall, *A Heat Transfer Model for Fire Fighter's Protective Clothing*, NISTIR 6299, National Institute of standards and Technology, Gaithersburg, MD, January 1999.

Kirk J. Staggs,[1] Norman J. Alvares,[2] and Daniel W. Greenwood[3]

The Difference Between Measured and Stored Minimum Ignition Energies of Dimethyl Sulfoxide Spray at Elevated Temperatures

Reference: Staggs, K. J., Alvares, N. J., and Greenwood, D. W., **"The Difference Between Measured and Stored Minimum Ignition Energies of Dimethyl Sulfoxide Spray at Elevated Temperatures,"** *Thermal Measurements: The Foundation of Fire Standards, ASTM 1427*, L. A. Gritzo and N. J. Alvares, Eds., ASTM International, West Conshohocken, PA, 2002.

Keywords: dimethyl sulfoxide spray, sprayed flammable fluids, high explosives

Introduction

The use of sprayed flammable fluids as solvents in dissolution and cleaning processes demands a detailed understanding of ignition and fire hazards associated with these applications. When it is not feasible to inert the atmosphere in which the spraying process takes place, then all possible ignition sources must be eliminated. If operators are involved in the process, the potential for human static build-up and ultimate discharge is finite, and nearly impossible to eliminate.

The specific application discussed in this paper involved the use of heated dimethyl sulfoxide (DMSO) to dissolve high explosives (HE). The search for DMSO properties yielded data on flammability limits and flash point, but there was no published information pertaining to the minimum energy for electrical arc ignition. Because of the sensitivity of this procedure, the Hazards Control Department of Lawrence Livermore National Laboratory (LLNL) was tasked to determine the minimum ignition energy of DMSO aerosol and vapor.

Because there were no electrical sources in the spray chamber, human electro-static discharge (HESD) was the only potential ignition source. Consequently, the electrostatic generators required for this investigation were designed to produce electrostatic arcs with the defined voltage and current pulse characteristics consistent with simulated human capacitance. Diagnostic procedures required to ensure these characteristics involve specific data gathering techniques where the voltage and current sensors are in close proximity to the electrodes, thus defining the arc energy directly between the electrodes. The intriguing finding derived from this procedure is how small these measured values are relative to the arc energy as defined by the capacitance and the voltage measure at the capacitor terminals. The suggested reason for this difference is that the standard

[1] Scientific Associate, Lawrence Livermore National Laboratory, Chemistry and Materials Science, 7000 East Ave., Livermore CA 94550

[2] Consultant to Lawrence Livermore National Laboratory, Fire Science Applications, 751 Laurel St.., San Carlos, Ca 94070

[3] Electrical Engineer, Lawrence Livermore National Laboratory, Defense Science Engineering Division, 7000 East Ave., Livermore, CA 94550

Introduction

The use of sprayed flammable fluids as solvents in dissolution and cleaning processes demands a detailed understanding of ignition and fire hazards associated with these applications. When it is not feasible to inert the atmosphere in which the spraying process takes place, then all possible ignition sources must be eliminated. If operators are involved in the process, the potential for human static build-up and ultimate discharge is finite, and nearly impossible to eliminate.

The specific application discussed in this paper involved the use of heated dimethyl sulfoxide (DMSO) to dissolve high explosives (HE). The search for DMSO properties yielded data on flammability limits and flash point, but there was no published information pertaining to the minimum energy for electrical arc ignition. Because of the sensitivity of this procedure, the Hazards Control Department of Lawrence Livermore National Laboratory (LLNL) was tasked to determine the minimum ignition energy of DMSO aerosol and vapor.

Because there were no electrical sources in the spray chamber, human electro-static discharge (HESD) was the only potential ignition source. Consequently, the electrostatic generators required for this investigation were designed to produce electrostatic arcs with the defined voltage and current pulse characteristics consistent with simulated human capacitance. Diagnostic procedures required to ensure these characteristics involve specific data gathering techniques where the voltage and current sensors are in close proximity to the electrodes, thus defining the arc energy directly between the electrodes. The intriguing finding derived from this procedure is how small these measured values are relative to the arc energy as defined by the capacitance and the voltage measure at the capacitor terminals. The suggested reason for this difference is that the standard procedure for determining arc energy from the relation $E = 1/2\ CV^2$ does not account for the total capacitance and impedance of the system.

Background: Dissolution Project

As a matter of policy it is necessary to dismantle tactical weapons to ensure their safety and reliability. Similar dismantling procedures are employed to retire units. During this process, the HE must be removed from critical components by dissection or by dissolution processes. However, dissolution processes require the application of combustible solvents. One unique dissolution project involves the use of heated DMSO.

The known properties of DMSO are listed in (Table 1) [1]. Because of its low vapor pressure, no published data of minimum electrical arc ignition energy (M_i) were found.

Table 1 - *Physical–Chemical Data for DMSO*

Parameter	Value
Melting Point, T_m	18.55°C (65.4°F)
Boiling Point, T_b	189°C (372°F)

Flash Point, T_f	95°C (203°F)
Auto Ignition, T_a	300–302°C (572–576°F)
Lean Limit Conc, C_{LL}	3.0–3.5% volume
Rich Limit Conc, C_{RL}	42–63% volume
Lean Limit Pres, P_{LL}	22.8–26.6 mm Hg, computed
Rich Limit Pres, P_{RL}	319–479 mm Hg, computed
Lean Limit Conc, C_{LL}	95.8–111.8 g/m3, computed
Rich Limit Conc, C_{RL}	1342–2013 g/m3, computed

The dissolution process employs a specially designed glove box fabricated with a ventilation system that maintains a negative pressure within the box during all phases of operation as shown in (Figure 1). A pneumatically powered re-circulating pump sprays the DMSO through ring-like manifolds with rows of spray nozzles directed inwards toward the HE and associated components. The DMSO is heated to 150°F by pumping it through a heat exchanger that uses hot water as the heating medium. The glove box, ventilation system, manifolds, and supporting hardware are electrically bonded to minimize electrostatic charge development during spraying cycles.

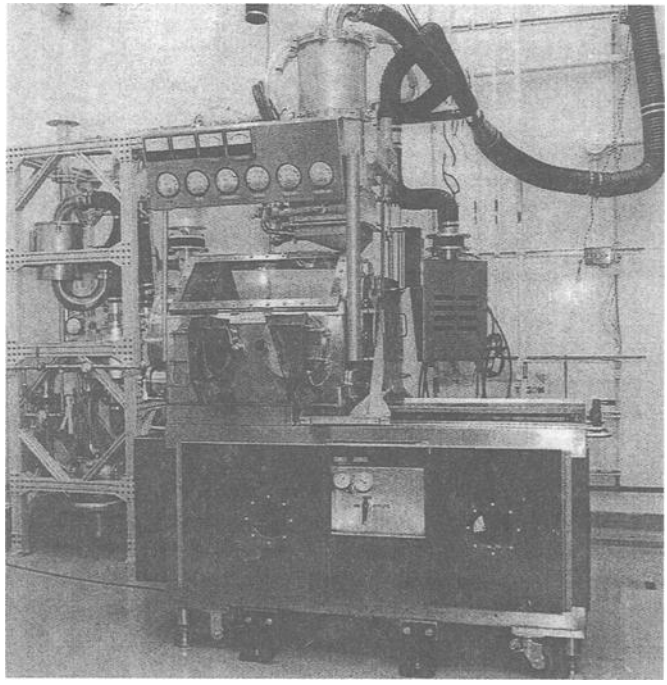

Fig. 1 - *Dissolution Workstation*

At selected intervals during the dissolution process the manifolds are systematically moved to provide complete coverage of the HE. These adjustments are performed manually by accessing the glove box through the glove ports. Specified procedures mandate that the pump be turned off, the mist from the spraying action allowed to clear,

and that operators bond themselves to the glove box prior to reaching into the box via the attached gloves. Initially, however, there was resistance to bonding the operator because of procedural control issues and the difficulties in performing the work while wearing bonding straps.

During development of the dissolution workstation, safety studies predicted that arcs from electrostatic discharge (ESD) were extremely unlikely because of the engineered electrical bonding and the conductive nature of DMSO. However, without bonding operators there was concern that ignition of the DMSO spray could result from HESD. Thus, to meet necessary safety criteria the minimum ignition energy ignition had to be defined.

ESD and HESD Ignition Study of DMSO Spray

An extensive series of tests was conducted to evaluate the minimum ignition energies for spray aerosols of DMSO and DMSO/HE solutions from HESD electrical arcs [2]. (Figure 2) shows a schematic of a test conducted in a metal glove box.

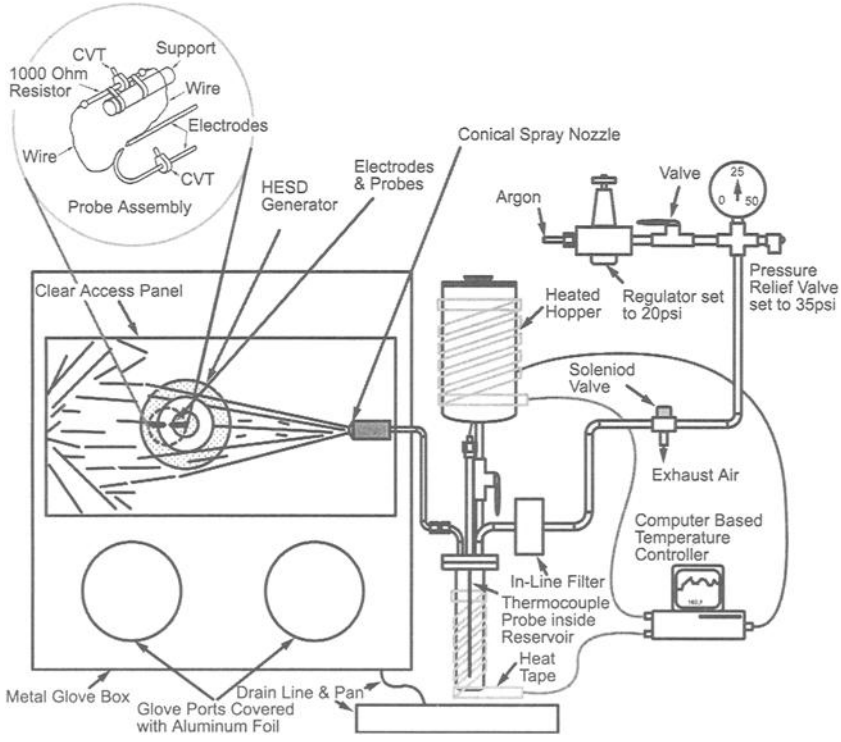

Fig. 2 - *Test setup used for human electrostatic spark tests*

The following parameters were controlled:

- DMSO flow rate and delivery pressure {416ml/min (0.11gpm) @20psi}
- DMSO average droplet size (154μm)
- DMSO temperature {71°C (160°F)}
- Spark generator stored ignition energy (Table 2)
- Ambient room temperature {23°C (74°F)}
- Glove box temperature {54°C (130°F)}.

Two types of ESD generators were used as a source for the arc energy in this study. One of the generators, obtained from Sandia National Laboratory (SNL) and called the Sandia Severe Human Body Electrostatic Discharge Tester (SSET), could have provided arc energy levels up to 7 millijoules (mJ). However, this unit was designed to evaluate the effect of ESD on electrical components and was not adequate for developing the power levels of electrical arcs required for ignition studies. In addition, tests were conducted at the Combustion Research Center (CRC) to determine spark ignition profiles for DMSO vapors at elevated temperatures [3]. The results of these tests are shown in (Figures 8 and 9).

The energy produced within an electrical arc is primarily a function of the circuit resistance, capacitance, and the medium that the arc transverses. The difference between ESD and HESD is the resistance of the human body. LLNL developed an ESD generator that closely simulates the charge capacitance and resistance of a human body. The initial design consisted of ceramic capacitors, resistors, and an EGG high-voltage Gap switch in a small cylindrical package. This package was placed behind a test chamber and attached to electrodes inside the chamber using high-voltage cable commonly used for pulse power systems. The probes used to measure current and voltage were mounted on the backside of the test compartment. However, this configuration produced questionable results that indicated a significant difference in the stored energy and the measured results. To address this issue, independent electrical analysis was conducted by the Pulse Power Systems Group at LLNL to study the electrical arc energy and the stored energy within the system. As a result of these studies, we decided to minimize or eliminate the cable between the generator and electrodes, and to install the current and voltage probes as close as possible to the end of the electrodes [2].

(Figure 3) shows the final design with the unit attached to the back wall of the test chamber. Aluminum disks that support internal components were also used as electrical conduits. One electrode was directly attached to the aluminum disk on the test chamber, and the other electrode was directly attached to the EGG Gap switch. This eliminated the need for cables between the generator and electrodes.

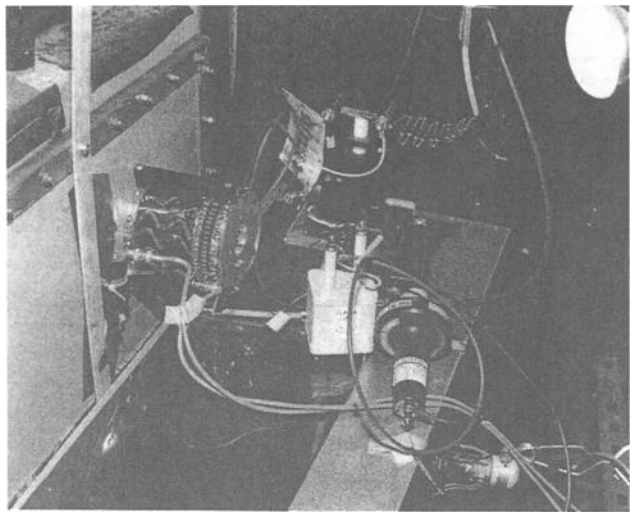

Fig. 3 - *HESD generator*

(Figure 4) shows a schematic of the HESD generator circuit including the generator components and probes. (Figure 5) is a schematic of the HESD generator.

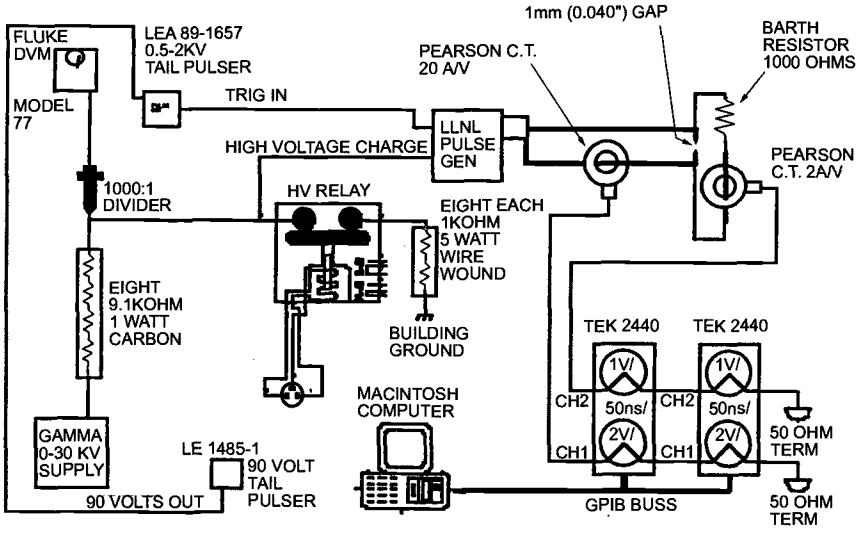

Fig. 4. Schematic of LLNL HESD generator circuit.

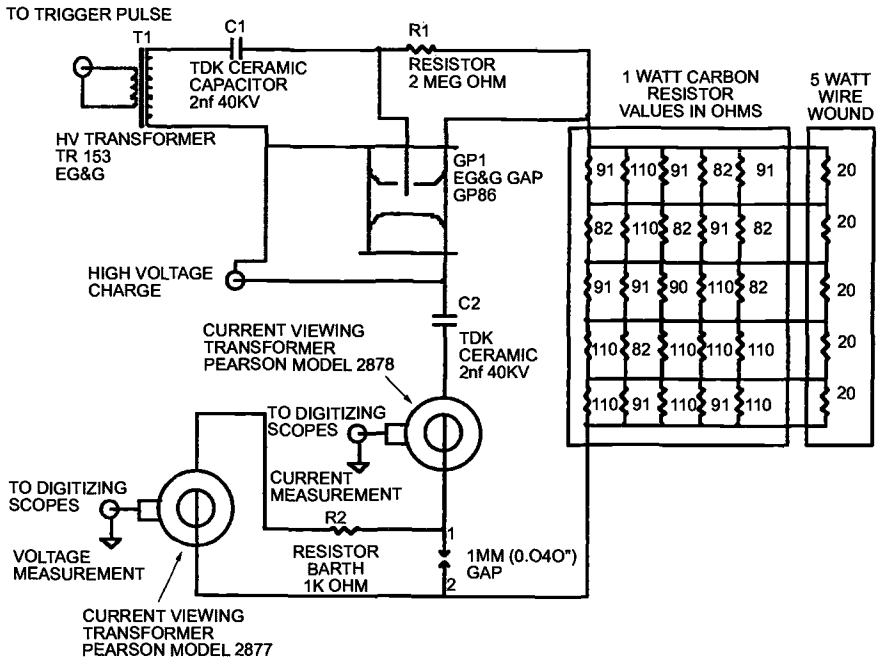

Fig. 5 - *LLNL HESD generator and sensors*

The two electrical parameters measured were the voltage across the arc gap and the discharge current. Because the arc voltage rise time is relatively fast (on the order of 5 to 10 ns), series resistance and inductive components presented by the leads connecting the arc gap to the pulse source will adversely affect the measurement. A ground reference for this measurement would involve very high common mode voltage and introduce the possibility of ground loops. To address these problems, we used a floating voltage probe with a connection as close to the arc gap as possible. The arc voltage was impressed across a Barth 1 kilo-ohm high-voltage resistor with known response and voltage vs. resistance coefficient characteristic. A Pearson current transformer (model 2877, 0.5 volts/ampere, 2 ns response, 1% accuracy) was then used to measure the current in the 1 kilo-ohm resistor. The normal sensitivity of this probe configuration was:

Resistor: I = 1 kV/1K Ω
Current transformer: I = 2 amperes/volt (when terminated in 50 ohms)
Probe system: Ep = 2 kV/volt

We used another Pearson current transformer (model 2878, 5 ns response, 0.05 volts/ampere, 1% accuracy) to measure the arc discharge current. Because the current in a series circuit is common to all elements, the current transformer can be placed in any location in the discharge circuit. The nominal sensitivity of this probe was 20 ampere/volt.

Both the arc voltage probe and the circuit current probe were attached to a Tektronix 2440 transient digitizers oscilloscope, which captures the signal voltage from the probes.

These transient digitizers have a minimum rise time of 3 ns and a maximum sample rate of 2 ns per point. A computer and custom written LabView application provided transient digitizer control and raw data collection.

The recorded voltage was converted to the appropriate arc-gap voltage and current. Any baseline shift was removed from raw current and voltage data to normalize each waveform to an initial zero. Voltage and current waveforms were multiplied to generate power in Watts. This power waveform was trimmed to provide limits for the energy derived from the resulting area under the power curve according to Eq. (1) below.

$$E = \int_0^t (vi)\ dt \qquad (1)$$

Where v is the spark gap voltage and i is the current at time t.

(Figure 6) shows an example of the voltage and current waveform recorded during the arc process. In this example, the voltage builds up on the ends of the electrodes to 6000 volts before ionizing the air in the gap between the electrodes. At point (t = 0), the current flow starts to increase, the resistance across the electrode gap drops, and the voltage drops. (Figure 7) shows the curve of the power derived from the voltage and current from point t = 0.

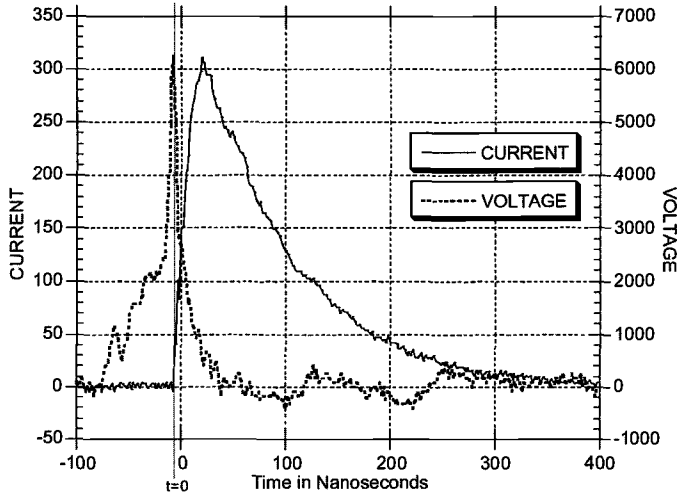

Fig. 6 - *Test "DMSO 96 Spray 33" voltage and current*

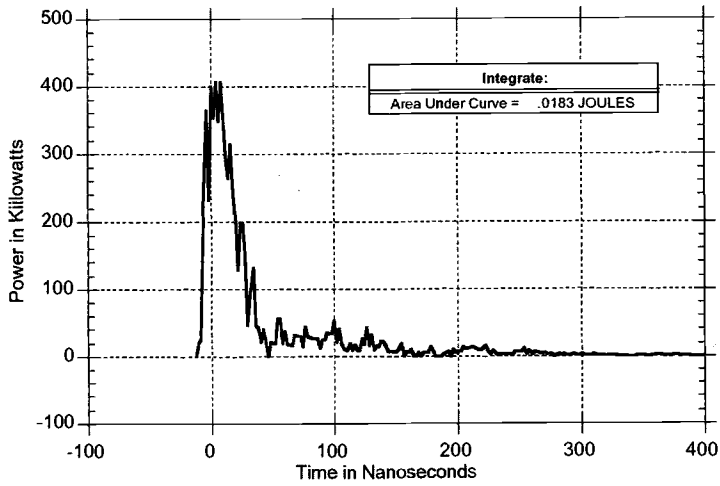

Fig. 7 - *Test "DMSO 96 spray 33" Watts*

The current/voltage transformers (CVT) have a specified accuracy of 1% with a usable rise time of 2 or 5 ns depending on the model. They were calibrated using a Tektronix PG508 pulse generator with a 5 ns rise time, a Tektronix 2465 oscilloscope with a 1.16 ns rise time, and a HP 3458A multimeter. The connecting cables used during calibration were the same as those used for the experimental runs. Any rise time and bandwidth losses were a part of the calibration when these cables were used. The results of the calibration achieved 2% accuracy in voltage and current probes. The voltage probe had a calibration value of 2084 volts/volt. The current probe had a calibration value of 21.6 amperes/volt.

The Tektronix 2440 transient digitizer calibration was verified to 0.5%. Voltage steps from 0–5 volts were applied to the input and simultaneously monitored on the HP 3458A multimeter. The data values were then input into a LabView routine that calculated Mean Squared Error and Slope. The accuracy of these data using this procedure was 0.45%.

The error calculations below include the calibration error of the voltage and current probes, non-linearity of the transient digitizers and the timing error of the signal cables. The probes and scope errors were calculated using calibration techniques described in the calibration section.

The transmission lines used in this diagnostic setup have a stated accuracy of 0.5 nanoseconds. The effect of this error was evaluated with the following process:

- Using Labview, linear interpolated points were added to scaled current and voltage waveforms to yield a 500-picosecond sample rate.
- Each interpolated waveform was time shifted with respect to the other by the amount of the possible signal cable error, 0.5 nanoseconds.

- The remainder of the numerical processes which yield power and energy were then performed on the two time shifted waveforms.
- The resulting energy magnitudes were then compared and found to vary by 10 percent maximum.

A geometric calculation including all the possible system errors is:

$$\text{Error}_{\text{total}} = \text{SQRT}((2.0\%\text{probe1})^2 + (0.45\%\text{digitizer1})^2 + (2.0\%\text{probe2})^2 + (0.45\%\text{digitizer2})^2 + (10.0\%\text{timing})^2)$$

$$\text{Error}_{\text{total}} = + \text{ or- } 10.4\%$$

A simple sum of the errors yields + or - 14.9%. This bounds the total error and, was used as a conservative, worst case figure.

The test parameters and results are summarized in (Table 2). Minimum ignition energy of the DMSO spray obtained with the LLNL HESD unit ranged between 15 mJ M_i 18 mJ. This range is substantially greater than the highest credible HESD arc of 7 mJ. Review of the data reveals the interesting observation that there is a significant difference between the stored energy and the energy measured within the arc (i.e., the stored energy calculation averaged 15 to 17 times more than energy measured at the spark gap by the LLNL HESD unit). This is interesting because the current standard (ASTM E-582) determines M_i in gases and vapors by calculating $E = 1/2\ CV^2$, where C is the capacitance of the system capacitor and V is the stored voltage.

Table 2 - *Test conditions for spray ignition tests*

Test	DMSO (wt%)	HE (wt%)	Atmo-sphere	Generator voltage (kV)	Spark Energy (mJ)	Calc Energy (mJ)	No. of ignitions	No. of sparks per ignition	Comments
19	100.0		Air	10-13	est. >20	100–170	3	5, 3, 1	LLNL Gen w/ 2nf cap
20	100.0		Air	18	?		0	10	LLNL Gen w/ 1nf cap
21	100.0		Air	19	?		0	10	LLNL Gen w/ 1nf cap
22	100.0		Air	30	3.1	212	0	10	Sandia Gen w/470pf cap
23	100.0		Air	30	6.5	212	0	21	Sandia Gen w/470pf cap
24	75.0	25.0	Air	30	5.7	212	0	29	Sandia Gen w/470pf cap
25	100.0		Air	20	> 13.0	200	0	12	LLNL Gen w/1nf cap
26	100.0		Air	20	26–29	400	3	8, 1, 5	LLNL Gen w/ 2nf cap
27	100.0		Air	12	8.6	144	0	21	LLNL Gen w/ 2nf cap
28	100.0		Air	15	?	225	multiple	unknown	LLNL Gen w/ 2nf cap
29	75.0	25.0	Air	12	8.8	144	0	13	LLNL Gen w/ 2nf cap
30	75.0	25.0	Air	12	8.3	144	0	13	LLNL Gen w/ 2nf cap
31	100.0		Air	15	15	225	0	17	LLNL Gen w/ 2nf cap

Vapor Ignition Study

We contracted CRC survey the ignition propensity of DMSO vapor at elevated temperatures using a modified version of the Bureau of Mines ignition apparatus [3]. This apparatus is similar to the unit described in ASTM E-582. The procedure was to inject a small quantity of the DMSO liquid into a container heated to slightly less the test set point temperature. The temperature of the container was then heated to the set point, and the internal atmosphere was stirred to ensure appropriate mixing. The pressure in the

chamber was reduced to 664 mm Hg to simulate negative pressure conditions in the workstation and ignition of the mixture was attempted over the temperature range of interest. The open cup flash point for DMSO (Table 1) is 95 C (203 F). Thus, ignition response was not expected at temperatures below the flash point

Using two strong ignition sources (a chemical match of approximately 130 J nominal energy and a carbon electrode spark unit of approximately 60 J nominal energy), the lower flammability temperature limit (LFL) of DMSO vapor was found to be 79 C (173 F) and 81 C (178 F), respectively. Positive determination of ignition was indicated by excessive pressure rise in the chamber. (Figure 8) shows these data [3].

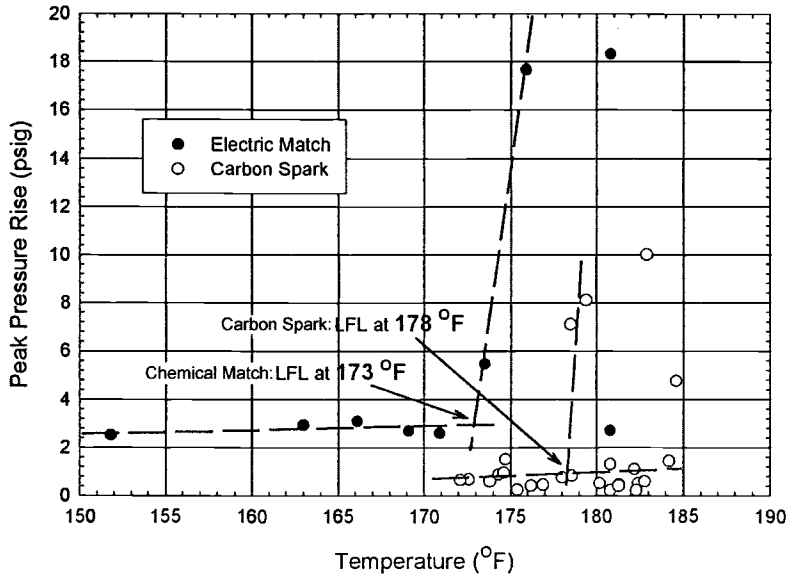

Fig. 8 - *LFL study at 664 mm Hg* [3]

Nominal ignition energies of heated DMSO vapor at increasing temperatures were then determined using two pointed graphite electrodes separated by a 3-mm gap. (Figure 9) plots the nominal ignition energy (mJ) vs the DMSO vapor temperature [3]. It is interesting to note that at the temperature of the published DMSO flash point (95°C 203°F), the nominal ignition energy is above 10 mJ, which is 3 mJ above the maximum potential HESD of 7 mJ. The pressure in which these tests were conducted was about 0.9 bars. Consequently, the measured ignition energy should be approximately 10% higher than the ignition energy at 1.0 bar. However, the data trends should be conserved. Note that the nominal ignition energy calculations are determined using the system voltage and capacitance at electrode gap break over. The actual spark energy of the discharge could be a tenth or less of this value, based on considerations from the spray ignition tests.

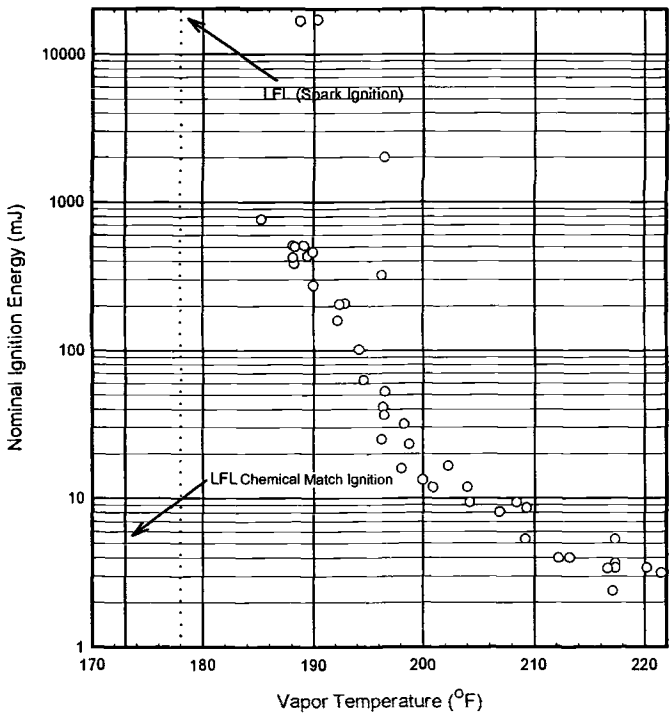

Fig. 9 - *Nominal ignition energy (mJ) vs the DMSO vapor temperature* [3]

Current Standard Minimum Ignition Energy Measurements of Gases and Vapors

The American Society For Testing and Material (ASTM) standard E-582, "Standard Test Method for Minimum Ignition Energy and Quenching Distance in Gaseous Mixture," uses a high-voltage power supply to charge capacitor(s) that are in parallel with the electrode circuit shown in (Figures 10a and 10b). The process involves setting a gap between electrodes and slowly charging the capacitor of a measured or known value until the potential across the capacitors and electrodes reach the break over point of the arc gap. When break over occurs the capacitor discharges its stored energy to the electrodes and across the gap until the voltage drops to a level that will no longer sustain an arc. An isolation resistor limits the amount of current available from the power supply to limit the arc duration. To determine spark energy, the voltage potential developed on the electrodes, which represents the charge voltage on the capacitor, is measured and recorded at break over and the ignition energy is calculated using the formula $E = 1/2\ CV^2$. This standard states that the reproducibility and presumed accuracy of M_i is $\pm 10\%$.

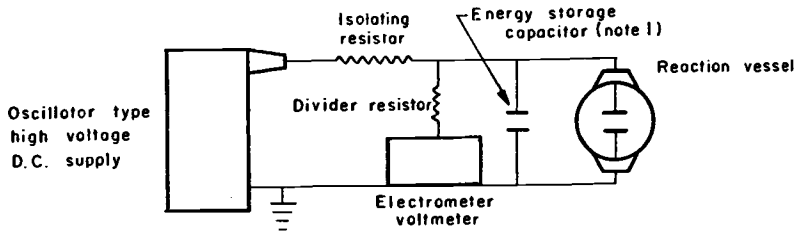

Fig. 10a.

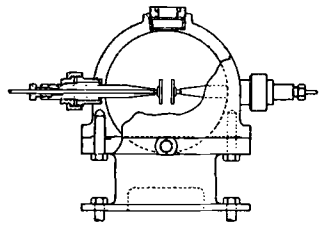

Fig. 10b – *ASTM E-582 Test Apparatus*

There are many different factors that can influence the accurate determination of M_i, particularly in heterogeneous mixtures such as sprays and dust distributions. In fact, it has been acknowledged that it is very difficult to define M_i for systems where air velocity and turbulence must be high to maintain levitation of aerosols [4]. For fluids of low vapor pressure such as DMSO, flammable concentrations of vapor can only be developed at elevated temperatures. Apparatus design can also influence the measurement of M_i (e.g., electrode size, shape, presence of quenching flanges, and composition influence the discharge efficiency). The resistance, inductance and capacitance of the circuit elements can markedly modify the total power to the electrode tips. The diagnostic equipment can directly impact the accuracy and precision of the data. Results from the LLNL HESD ignition tests for DMSO show that the apparatus design and diagnostic procedures have a significant and large effect on determining the magnitude and temporal character of energy delivered to the spark gap. The order of magnitude difference between measured M_i and M_i calculated from $1/2\ CV^2$ calls to question the data produced by current standard methods.

Historical Minimum Spark Ignition Data

Tables that list M_i data are found in handbooks, monographs, standards, and reports that focus on the subject of fire and explosion [5–10]. The lists are generally collections of data from research published in journals or symposium proceedings. Some of these data for selected flammable gases and vapors are listed in (Table 3). The first column of

this table is from Calcote, et al. [5] and lists M_i data for a wide variety of flammable vapors and gasses. These data were determined at the stoichiometric fuel/air ratio to reduce the experimental time required to establish the true M_i, which for most hydrocarbons occur at mixtures that are slightly richer than stoichiometric. The apparatus used to produce these data was designed at the Bureau of Mines and is essentially the same as the unit recommended in the current ASTM E 582-86.

Table 3 - *Minimum spark ignition energy data from various sources. Values given in mJ.*

Fuel	Column 1 [5]	Column 2 [6]	Column 3 [7]	Column 4 [8]	Column 5 [9]	Column 6 [10]
Acetaldehyde	0.38	0.376	0.38		0.38	0.37
Acetone	1.15	1.15	1.15		1.15	1.15, (0.41)
Acrolein	0.137	0.137	0.175			0.13
Benzene	0.55	0.55	0.55	0.22	0.22	0.2
Carbon Disulfide	0.015	0.015	0.015	0.01–0.02	0.015	0.009
Ethane	0.285	0.285	0.42 (0.24)	0.24	0.25	0.24
Heptane	0.7	0.7	1.15, (0.24)			0.24
Hydrogen	0.028	0.02	0.02, (0.018)	0.019	0.017	0.016
Methane	0.47	0.47	0.33, (0.29)	0.29	0.3	0.21, (0.30)
Propane	0.31	0.29	0.305	0.25		0.25, (0.48)
Toluene					2.5	0.24

Columns 2 through 5 [6–9] list M_i data from collections that postdate Calcote, et al. [5]. The data in these columns are for the most part from Ref. 5, or are determinations made from an ignition apparatus essentially identical to the Bureau of Mines design. Two sets of data for ethane, heptane, hydrogen, and methane in column 3 are listed because they include measurements using either different electrode configuration, spark duration, electrode composition or fuel/air ratio. The data in column 6 [10] are from measurements at fuel/air mixture ratios that reflect the true minimum spark energy defined by the ignition apparatus. These data generally indicate M_i magnitudes lower than ignition values at the stoichiometric fuel/air ratio. These data were collected from a paper published in 1992, which we assume to be from measurements more current than data listed in the rest of (Table 1). Background materials in the monograph indicate that the method used to determine M_i was similar to the method described in the current standard.

In most circumstances, the conditions of accidental electrical discharge are such that the released energy is more than adequate to cause ignition of released flammable gases and aerosols. Because of this fact, accurate information about M_i is not a requirement but intrinsically designed safety systems and components are mandated to ensure safe operations in areas defined as "hazardous locations." Sources of electrical energy that are not easily controlled are caused by static processes such as HESD, which can occur because of a broad set of circumstances where charge separation is possible. There are also unguarded, low-voltage systems that are contained in systems containing flammable vapors and aerosols where the circuit characteristics are assumed to either preclude the possibility of electrical discharge or the where the discharge energy is considered to be safely below M_i for the environment. For this set of circumstances, accurate knowledge of M_i is a requirement to ensure safe operations.

It is safe to assume that the historical M_i data from the references in (Table 3) were determined by the classical procedure of calculation using measured values of capacitance and voltage. Moreover, the consistency of the data in (Table 3) suggests that data in the more recent tables, except for Ref. 10, appear to be Blanc, et al. [11] or Calcote, et al. [5]. It also is an established fact that the technology of electrical measurement has vastly improved over the period since Ref. 5 was published. The data produced during the DMSO spray tests using the LLNL HESD unit provides some indication of the improvement in measurement and analysis of spark discharge energy. (Figure 11) is a curve that contrasts the difference in spark ignition energy values determined by measurement and by dependence on the stored energy calculation. It shows that the M_i calculated is 15 times M_i measured. Because of circuit components use to provide the HESD characteristic discharges, some of the difference between Mi calculated and Mi measured was expected. These data are for a much more complicated fuel-spray system at elevated temperatures, however the trend is certain and should be conserved in standard gas and vapor phase environments. For these reasons we ask "Are published minimum vapor phase spark ignition data valid? And, shouldn't these measurements be revisited to insure that they reflect accurate safety limits. "

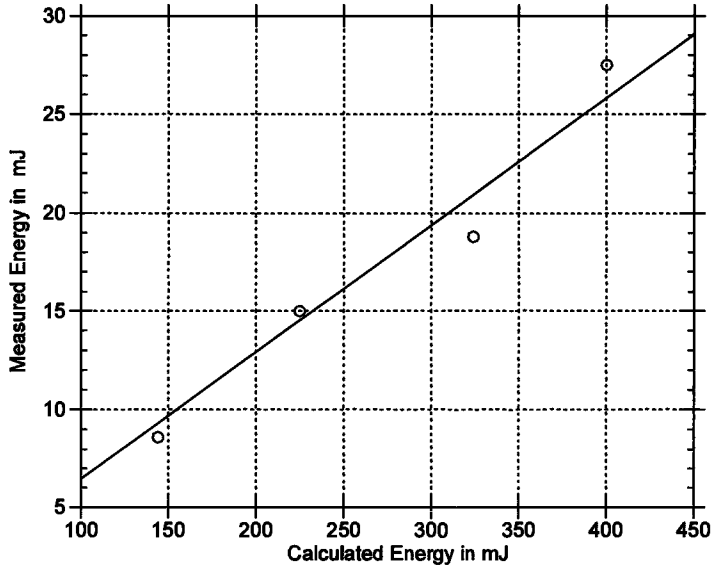

Fig. 11 - *Calculated vs measured spark energy*

Conclusions

- Minimum ignition energy for heterogeneous DMSO sprays of particle size ranging from 0.08 um to 0.4 um and aerosol concentration of 9.4 g/m^3, at average temperature of 71 C (160 F) ranged between 15 mJ M_i 18 mJ.
- Minimum vapor temperature for high-intensity spark ignition is 81 C (178 F).

- Nominal spark ignition energy at the published open cup flash point temperature of DMSO {95 C, (203 F)} is ~ 9 mJ. The actual spark energy is likely to be substantially less than this value.
- Spark energies measured at the electrodes of the LLNL HESD spark generator averaged one order of magnitude lower than the calculated system energy of ½ CV^2 for all of the DMSO spray ignition tests.
- Improved instrumentation has allowed for much better M_i measurements.
- Current method of determining M_i does not provide accurate measure of energy produced in the spark.
- Published M_i energy data may be higher than actual M_i spark energies for many vapor phase ignitable materials.

References

1. D. Martin, H. G. Hauthal, and E. S. Halberstadt, *Dimethyl Sulfoxide*, (Van Nostrand Reinhold Company Ltd., Berkshire, England 1975).
2. W. Bergman, K. J. Staggs, D. E. Turner, D. W. Greenwood, P. D. Wapman, *Spark Ignition Studies of DMSO/HE Sprays, Liquids and Aerosols in the W79 HE Dissolution Workstation,* Lawrence Livermore National Laboratory, Livermore, CA, UCRL-ID-126012 (1996).
3. Erdem A. Ural and William Weisgerber, *Ignitability of DMSO Vapors at Elevated Temperature and Reduced Pressure,* CRC Technical Report SSR-1953/SO-47152, Combustion Research Center, Holliston, MA (1998).
4. Martin Hertzberg, Ronald S. Conti, and Kenneth L. Cashdollar, "Spark Ignition Energies for Dust-Air Mixtures: Temperature and Concentration Dependencies," *20th Symposium (International) on Combustion, The Combustion Institute,* pp. 1681–1690 (1984).
5. H. F. Calcote, C. A. Gregory, Jr., C. M. Barnett, and Ruth B. Gilmer, "Spark Ignition—Effect of Molecular Structure," *Ind. and Eng. Chem.* 44, 11 (1952).
6. *Fire Protection Manual for Hydrocarbon Processing Plants, Vol. 1,* 3rd Ed. (1985).
7. Henry C. Barnett and Robert Hibbard, Eds., *Basic Considerations in the Combustion of Hydrocarbon Fuels with Air NACA,* Report 1300 (1957).
8. Frank P. Lees, *Loss Prevention in the Process Industries, Vol. 1,* (Butterworths, London, 1989).
9. NFPA 53M, Oxygen Enriched Atmospheres (1990).
10. Thomas H. Pratt, *Electrostatic Ignitions of Fires and Explosions,* (Burgoyne Inc., Marietta, GA, 1997).
11. Blanc, et al., *J. of Phys. Chem.* 15, 798–802.